

Electronic Thesis and Dissertation Repository

10-29-2012 12:00 AM

Novel Controls of Photovoltaic (PV) Solar Farms

Shah Arifur Rahman
The University of Western Ontario

Supervisor
Dr. Rajiv K. Varma
The University of Western Ontario

Graduate Program in Electrical and Computer Engineering
A thesis submitted in partial fulfillment of the requirements for the degree in Doctor of
Philosophy
© Shah Arifur Rahman 2012

Follow this and additional works at: <https://ir.lib.uwo.ca/etd>



Part of the [Power and Energy Commons](#)

Recommended Citation

Rahman, Shah Arifur, "Novel Controls of Photovoltaic (PV) Solar Farms" (2012). *Electronic Thesis and Dissertation Repository*. 922.
<https://ir.lib.uwo.ca/etd/922>

This Dissertation/Thesis is brought to you for free and open access by Scholarship@Western. It has been accepted for inclusion in Electronic Thesis and Dissertation Repository by an authorized administrator of Scholarship@Western. For more information, please contact wlsadmin@uwo.ca.

NOVEL CONTROLS OF PHOTOVOLTAIC (PV) SOLAR FARMS

(Thesis format: Monograph)

by

RAHMAN, SHAH ARIFUR

Graduate Program in Electrical and Computer Engineering

A thesis submitted in partial fulfillment
of the requirements for the degree of
Doctor of Philosophy (Ph.D.)

The School of Graduate and Postdoctoral Studies
Western University
London, Ontario, Canada

© Shah Arifur Rahman, 2012

WESTERN UNIVERSITY
School of Graduate and Postdoctoral Studies

CERTIFICATE OF EXAMINATION

Supervisor

Examiners

Dr. Rajiv K. Varma

Dr. Kankar Bhattacharya

Supervisory Committee

Dr. Kamran Siddiqui

Dr. Kenneth Mclsaac

Dr. Kenneth Mclsaac

Dr. Jin Jiang

Dr. Kazimierz Adamiak

The thesis by

Shah Arifur Rahman

entitled:

“Novel Controls of Photovoltaic (PV) Solar Farms”

is accepted in partial fulfillment of the
requirements for the degree of
Doctor of Philosophy (Ph.D.)

Date

Chair of the Thesis Examination Board

Abstract

Solar Farms are absolutely idle in the night and even during daytime operate below capacity in early mornings and late afternoons. Thus, the entire expensive asset of solar farms remains highly unutilized. This thesis presents novel technologies for utilization of PV solar farm inverter in nighttime for providing multiple benefits to power systems, as well as accomplishing the same objectives during the daytime from the inverter capacity left after production of real power. The new technology transforms a solar farm inverter functionally into a dynamic reactive power compensator known as STATCOM, and termed PV-STATCOM.

A novel coordinated control of PV-STATCOMs is proposed for loss reduction in a distribution network. The saved energy is substantial and can be used for powering several homes annually. The second novel PV-STATCOM control involves a temporary curtailment of real power production and utilization of the available reactive power capacity to prevent the instability of a critical induction motor load. The third novel PVSTATCOM control is employed to significantly enhance the power transfer limit of a long transmission line both in the nighttime and also during daytime even when the solar farm is producing a large amount of real power. A new technique for short circuit current management is developed for a conventional PV solar farm that can potentially solve the problem due to which several solar farms have been denied connectivity in Ontario. This thesis has contributed to two patent applications and presented first time implementations of another two filed patents.

A generalized PV solar system model in EMTDC/PSCAD software has been developed and validated with manufacturer's datasheet. Another contribution of this thesis is the first time harmonics impact study of the largest solar farm in Canada, in the distribution utility network of Bluewater Power, in Sarnia, Ontario.

This thesis makes a strong case for relaxing the present grid codes to allow solar farms to exercise these novel controls. This technology can open up new avenues for solar farms to earn revenues apart from the sale of real power. This will require appropriate agreements between the regulators, network utilities, solar farm developers and inverter manufacturers.

Keywords

Photovoltaic (PV) Solar Farms, Inverter Modeling, STATCOM, PV-STATCOM, Flexible AC Transmission System (FACTS), Fault Detection, Short Circuit Current Management, Line Loss, Induction Motor Instability, Transmission Limit, Reactive Power Compensation, Voltage Control, Damping Control, Transient Stability, Harmonics Analysis, Electromagnetic Transients Simulation.

Devoted to:

My Parents

Acknowledgments

I would like to express my sincere gratitude to my supervisor, Dr. Rajiv K. Varma, for his generous support, constructive guidelines, and valuable suggestions in every step of my graduate carrier at Western University. I greatly appreciate his humble and caring attitude that has made me more respectful to him. I feel very proud to have had the opportunity to work under his kind supervision and to have the opportunity to work within the industry that has enriched my knowledge and built my confidence to succeed in my future career. The contribution he made to my academic career is so enormous that it can't be conveyed appropriately in words. I, herewith, convey my sincere and warmest regards to him.

I am highly obliged to Tim Vanderheide, Chief Operating Officer, Bluewater Power Corp. to have provided me the rare opportunity to work closely with industrial people for more than four years. In addition, he has helped to facilitate all of the logistic support to make this work much more meaningful. I am very thankful to him for furnishing me unlimited confidential technical resources. I convey my profound respect to him as well. I would also like to thank Maureen Glaab for her very co-operative and friendly manner which made my working environment much more informal. I am also very grateful to the Bluewater power management, engineering, and technical personnel for their technical and logistic support to make this research successful.

I also acknowledge the Ontario Center of Excellence (OCE), Hydro One Networks Inc., Bluewater Power Corp., London Hydro Inc. and Natural Sciences and Engineering Research Council (NSERC) for their financial support for four years.

I humbly express profound gratitude to my parents for their perpetual blessings and love. Finally, I owe the completion of this thesis to my children who have sacrificed a lot of their own time and to my wife for her sincere encouragement and support in my family.

Shah Arifur Rahman

Table of Contents

CERTIFICATE OF EXAMINATION	ii
Abstract	iii
Acknowledgments.....	vi
Table of Contents	vii
List of Tables	xiv
List of Figures	xvi
List of Appendices	xxii
List of Acronyms	xxiii
List of Symbols	xxiv
Chapter 1	1
1 Introduction	1
1.1 General.....	1
1.2 Modeling of a Grid Connected PV Solar System	1
1.2.1 System description	1
1.2.2 PV Solar Panel/Module.....	2
1.2.3 Maximum Power Point Tracking (MPPT) System.....	5
1.2.4 PV Inverter Modeling	6
1.2.5 Filter Modeling	11
1.2.6 Step Up Transformer.....	11
1.3 Short Circuit Contribution of Grid Connected PV Solar System	12
1.3.1 Techniques for Fault Detection.....	12
1.4 Flexible AC Transmission System (FACTS) Devices	13
1.5 STATCOM	15
1.5.1 Basic Operating Principle:	15

1.5.2	V-I Characteristic of STATCOM	16
1.5.3	Configuration	17
1.5.4	Controller	18
1.5.5	Voltage Control.....	20
1.6	Application of Shunt FACTS Devices:.....	21
1.6.1	Voltage Control and Improvement of Steady State Power Transfer Capability over a Long Transmission line.....	22
1.6.2	Improvement of Transient Stability and Enhancement of System Damping	23
1.7	Enhanced Utilization of Grid Connected PV Solar System.....	26
1.7.1	Nighttime Utilization of PV Solar Farm as STATCOM for Increasing Wind Connectivity	26
1.7.2	Line loss Improvement with PV solar farm	26
1.7.3	Transmission Limits and Damping Enhancement with PV solar farm.....	27
1.8	Impact of PV System Harmonics in the Network.....	28
1.9	Motivation of Thesis	29
1.10	Objective and Scope of the Thesis.....	30
1.11	Outline of Chapters	31
Chapter 2	34
2	Modeling of a Three Phase Grid Connected Photovoltaic (PV) System in EMTDC/PSCAD.....	34
2.1	Introduction.....	34
2.2	System Model	34
2.2.1	System Description	34
2.2.2	PV Source Model.....	36
2.2.3	Maximum Power Point Tracking (MPPT).....	46
2.2.4	Inverter	48
2.2.5	DC Link Capacitor Modeling	50

2.2.6	AC Filter Modeling.....	51
2.3	Case Study	53
2.3.1	Operating Data	53
2.3.2	Model Output.....	53
2.4	Conclusion	57
Chapter 3	58
3	New Fault Detection and Management Technique for Inverter Based DGs.	58
3.1	Introduction.....	58
3.2	System Model	58
3.2.1	System Description.....	58
3.2.2	PV System Model	59
3.2.3	Fault Detection Module	61
3.3	Case Studies.....	66
3.3.1	Symmetrical Fault at PCC	67
3.3.2	Symmetrical Fault at Grid Bus	70
3.3.3	Asymmetrical Fault at PCC and Grid Bus.....	71
3.3.4	Performance comparison of slope detector and magnitude detector in the fault controller.....	73
3.3.5	Load Switching.....	74
3.3.6	Filter Capacitor Ringing Effect.....	75
3.4	Conclusion	77
Chapter 4	78
4	Novel Control of PV Solar System as STATCOM (PV-STATCOM).	78
4.1	Introduction.....	78
4.2	Novel PV-STATCOM Control Concept.....	79
4.2.1	PV-STATCOM Based on “Un-Used” PV Solar Farm Inverter Capacity	79

4.2.2	PV-STATCOM Based on “Used” Solar Farm Inverter Capacity.....	80
4.3	Novel Application of PV-STATCOM Utilizing “Unused” Inverter Capacity.	81
4.3.1	Line Loss Reduction	81
4.3.2	Improvement of Power Transfer Capacity in Transmission Lines	81
4.4	Novel Application of PV-STATCOM Utilizing “Used” Inverter Capacity.	82
4.5	Conclusion	82
Chapter 5	83
5	Reduction of Line Losses Through a Novel Control of PV Solar Farm as PV-STATCOM.....	83
5.1	Introduction.....	83
5.2	Loss Formulation of a Two Bus Network with a Distributed Generator.....	84
5.3	System Model	86
5.3.1	System Description	86
5.3.2	PV System Control	87
5.4	Control Strategy for Line Loss Reduction	88
5.4.1	Single PV System as PV-STATCOM.....	88
5.4.2	Coordinated Control of Multiple PV Systems as PV-STATCOMS.....	89
5.5	Case Study 1: Radial Feeder with Single PV System.....	89
5.5.1	Scenario-1	89
5.5.2	Scenario 2.....	93
5.6	Case Study 2: Radial Feeder with two PV Systems	94
5.6.1	Scenario-3	94
5.6.2	Scenario 4.....	95
5.7	Economic Evaluation and Discussion.....	97
5.8	Conclusion	99
Chapter 6	101

6	Prevention of Instability of Critical Induction Motor Load with a Novel Control of PV Solar Farm as PV-STATCOM.....	101
6.1	Introduction.....	101
6.2	System Model	102
6.2.1	Study System	102
6.2.2	Induction Motor (IM).....	102
6.2.3	Proposed PV-STATCOM Control.....	103
6.3	Study Results	105
6.3.1	Case-1: Conventional PV system disconnected during fault:.....	106
6.3.2	Case 2: Conventional PV system stays connected during fault.....	107
6.3.3	Case 3: PV system operation as PV-STATCOM	110
6.3.4	Determination of maximum size of induction motor stabilized with 7.5 MVA PV-STATCOM.....	113
6.3.5	Reinstatement of a conventional PV solar farm operation following PV-STATCOM operation	114
6.4	Conclusion	118
	Chapter 7.....	119
7	Improvement of Power Transfer Limit Over a Long Transmission Line with a Novel Control of PV Solar Farm as PV-STATCOM.	119
7.1	Introduction.....	119
7.2	System Model	119
7.2.1	Generator and Line Models	121
7.2.2	Distributed Generator Models.....	122
7.2.3	Control System.....	123
7.3	System Studies	124
7.3.1	Case Study 1: Power Transfer Limits in Study System 1	125
7.3.2	Case Study 2: Power Transfer Limits in Study System 2.....	134
7.4	Implementation of PV-STATCOM on Large Scale Solar System	138

7.5 Conclusion	139
Chapter 8.....	142
8 Harmonic Analysis of Distribution Network with Large Scale PV Solar Farm.....	142
8.1 Introduction.....	142
8.2 System Description.....	142
8.2.1 Sarnia Solar Farm	142
8.2.2 St. Andrews Substation and Feeder Capacitors	143
8.2.3 Feeder 18M14 and Major Loads.....	143
8.3 Network Data Acquisition Systems	144
8.3.1 SCADA System	144
8.3.2 GIS System	144
8.4 System Model	145
8.4.1 Grid/Source Model and Capacitor Banks Model.....	145
8.4.2 Feeder Model	146
8.4.3 Loads and Load Capacitor Models	147
8.4.4 PV System Model	148
8.5 Steady State Load Flow Validation of System Model.....	149
8.6 Network Impedance and Resonance.....	150
8.6.1 Case-I: Base Case	151
8.6.2 Case-II: Variation of SCL of Source	153
8.6.3 Case-III: Loss of Substation Transformer.....	156
8.6.4 Case-IV: Loss of Large Distribution Line Segment with Large Customer Load	157
8.7 Impact of PV Solar Farm Harmonics Injection on Network Impedance.....	159
8.7.1 Selection of Worst Network Condition by Varying SCL.....	159
8.7.2 Harmonics Distortion Due to Worst Network Condition	163

8.8 Conclusion	170
Chapter 9	172
9 Conclusion	172
9.1 Introduction.....	172
9.2 Modeling of a Conventional PV Solar Farm	173
9.3 New Fault Detection and Management Technique for PV Solar System.....	174
9.4 Novel Control of PV Solar Farm as PV-STATCOM	175
9.4.1 Utilization of Unused Capacity of a PV Inverter.....	175
9.4.2 Utilization of Used Capacity of a PV Inverter for Prevention of Induction Motor Instability	178
9.5 Harmonic Impact Study of a Large Scale PV Solar Farm in a Distribution Network.....	179
9.6 Contribution and Significance of this Thesis.....	181
9.7 Future Work	182
Patents and Publications from this Thesis:	183
References or Bibliography	186
Appendices.....	196

List of Tables

Table 2.1 FS 272 PV module electrical specification at STC* and at 45 °C, 0.8 Sun.....	36
Table 2.2 Comparison of simulated model with manufacturer’s datasheet for FS 272 PV module at 0.8 radiation level at 45 °C.....	57
Table 5.1 Line Loss Evaluation for Scenario 1.....	92
Table 5.2 Line Loss Evaluation for Scenario 2.....	93
Table 5.3 Line Loss Evaluation for Scenario 3.....	95
Table 5.4 Line Loss Evaluation for Scenario 4.....	96
Table 5.5 Summary of Energy Loss Savings and Cost Savings.....	99
Table 7.1 Power Flows and Voltages for Study System I for Solar DG with Conventional Reactive Power Control and Proposed Damping Control both during Nighttime and Daytime (Vg=1.05 pu).....	126
Table 7.2 Power Flows and Voltages for Study System I for Solar DG with Proposed PCC Voltage Control and Damping Control, both during Nighttime and Daytime.	131
Table 7.3 Increase in Stable Power Transfer Limit (MW) for Study System 1 with Different PV-STATCOM Controls.....	133
Table 7.4 Power Flows and Voltages for Study System 2 for both Solar DG and Wind DG with Conventional Reactive Power Control and Proposed Damping Control both during Nighttime and Daytime (Vg =1.05 pu).....	134
Table 7.5 Increase in Power Transfer Limits for Study System 2 with Different DG Power Outputs.....	137
Table 8.1 Daytime Data on 18M14 (time stamp-25/05/2011 at 12:22PM).....	149
Table 8.2 Nighttime Data on 18M14 (time stamp-7/10/2011 at 12:05 am)	150

Table 8.3 Power, Voltage and Harmonics for Base Case Scenario of Fig. 8.3	160
Table 8.4 Power, Voltage and Harmonics for the Network Impedance of Fig. 8.5	161
Table 8.5 Power, Voltage and Harmonics for the Network Impedance of Fig. 8.7	161
Table 8.6 Power, Voltage and Harmonics for the Network Impedance of Fig. 8.1	162
Table 8.7 Power, Voltage, Harmonics Distortion during the Evening of a Sunny Day	164
Table 8.8 Power, Voltage, and Harmonics Distortion at noon on a Sunny Day.	165
Table 8.9 Power, Voltage, and Harmonics Distortion for High Harmonics Injection on a Sunny Day.....	165
Table 8.10 Power, Voltage, Harmonics Distortion during the Evening on Cloudy Day.....	167
Table 8.11 Power, Voltage, and Harmonics Distortion at noon on a Cloudy Day.....	167
Table 8.12 Power, Voltage, and Harmonics Distortion for High Harmonics Current Injection on a Cloudy Day	168
Table 8.13 Simulated Power, Voltage, and Harmonics Corresponds to Highest Harmonics Injection by the Solar Farm at 1SCL	169
Table 8.14 Simulated Power, Voltage, and Harmonics Corresponds to Highest Harmonics Injection by the Solar Farm at 1/3rd SCL.....	170
Table 8.15 Simulated Power, Voltage, and Harmonics Corresponds to Highest Harmonics Injection by the Solar Farm at 4SCL	170

List of Figures

Figure 1.1 Block Diagram of a Complete Grid Connected PV System.....	2
Figure 1.2 Typical I-V characteristic of a PV module at (a) different solar irradiation levels at 25°C and (b) different temperatures at 1 Sun irradiation.	3
Figure 1.3 Equivalent circuit of PV solar cell (single diode model).	4
Figure 1.4 Typical PV solar farm inverter.	7
Figure 1.5 Generic VSI based PV inverter controller.....	10
Figure 1.6 (a) STATCOM (b) analogous representation of STATCOM and,.....	15
Figure 1.7 STATCOM (a) V-I and (b) V-Q characteristics.....	17
Figure 1.8 IGBT based basic STATCOM configuration.....	18
Figure 1.9 Schematic Diagram of Generic STATCOM Controller.....	18
Figure 1.10 Voltage and current waveforms for (a) 5 MVar inductive and (b) 5 MVar capacitive mode of operation of STATCOM.....	20
Figure 1.11 Relative magnitudes of various power transmission limits.....	22
Figure 1.12 Power flow improvement (a) without compensation and (b) with mid-point compensation.	23
Figure 1.13 Single Machine Infinite Bus (SMIB) system with shunt FACTS devices.	24
Figure 2.1 Single line diagram of grid connected PV system.....	34
Figure 2.2 Detailed system model (a) PV source (b) IGBT inverter (c) filter (d) MPPT module and (e) inverter switching signal controller.	35
Figure 2.3 Circuit model of PV Source and its equivalent representation in EMTDC/PSCAD.	36

Figure 2.4 DC circuit to determine diode ideality factor, n .	44
Figure 2.5 ‘PV Source’ building blocks in EMTDC/PSCAD	45
Figure 2.6 Incremental conductance algorithm flowchart for MPPT.	47
Figure 2.7 MPPT module building blocks for Incremental Conductance algorithm.	48
Figure 2.8 PV system output at different radiation and temperature; PV current and inverter output phase current, DC link and AC voltage and power output.	54
Figure 2.9 Total Harmonic Distortion (THD) at different irradiation & temperature.	55
Figure 2.10 Instantaneous phase voltage and current output of PV system at STC.	56
Figure 3.1 One line diagram of the study system.	59
Figure 3.2 Detailed PV system inverter and conventional controller with incorporated fault detection module.	60
Figure 3.3 Fault detection module.	61
Figure 3.4 Fault detection module implementation in EMTDC/PSCAD.	62
Figure 3.5 Fault detector operation flowchart.	66
Figure 3.6 PV system operation for fault at $t=5$ sec, at rated power output.	67
Figure 3.7 Inverter output current at non-peak fault instant.	68
Figure 3.8 Inverter output current at peak fault instant.	68
Figure 3.9 Inverter output current waveform with 0.4 pu PV solar farm generation	69
Figure 3.10 Inverter output current at non-peak fault instant	70
Figure 3.11 Inverter output current at peak fault instant.	70
Figure 3.12 Different phase currents of PV inverter for fault at PCC.	71

Figure 3.13 Inverter output current for a SLG fault at PCC (peak fault instant).....	72
Figure 3.14 Inverter output current for a SLG fault at Grid Bus (peak fault instant).....	72
Figure 3.15 (a) Inverter output current and (b) generation of trip signals.....	73
Figure 3.16 PV current with (a) 8.9 MVA and (b) 66.7 MVA load switching.....	75
Figure 3.17 Current at PCC with the proposed controller when (a) filter unit uses smaller damping resistor (b) filter unit disconnects and (c) filter unit uses larger damping resistor. .	76
Figure 4.1 PV Solar Farm operation as PV-STATCOM in the night.....	78
Figure 4.2 Reactive power capability of PV-STATCOM.	80
Figure 4.3 PV-STATCOM operation during an event.....	81
Figure 5.1 A two bus network.....	84
Figure 5.2 Detailed PV-STATCOM configuration in the study system (a) PV array model, (b) IGBT matrix of inverter, (c) L-C-L filter, (d) MPPT module, (e) conventional inverter controller, (f) PCC voltage regulator and (g) Optimal Power Flow unit.....	87
Figure 5.3 Schematic diagram of control co-ordination strategy	89
Figure 5.4 Scenario 1: PV system connected at feeder end.....	90
Figure 5.5 Voltage profile with conventional PV solar farm operation.	90
Figure 5.6 Loss profile to identify optimal set point of PCC voltage.....	91
Figure 5.7 Voltage profile with PV-STATCOM operation.....	92
Figure 5.8 Scenario 2: PV system connected in the middle of feeder.....	93
Figure 5.9 Scenario 3: Two PV systems connected at the middle of feeder and at the end of the feeder.....	94
Figure 5.10 Voltage profile with two solar farms for Scenario 3	95

Figure 5.11 Scenario 4: Two PV systems connected at 1/3 rd and 2/3 rd distance.	96
Figure 5.12 (a) PV-STATCOM reactive capability, (b) line loss reduction with PV-STATCOM for scenario 1 and (c) comparison of loss reduction with PV-STATCOMs in different scenarios.	99
Figure 6.1 One line diagram of study system.	102
Figure 6.2 Conceptual block diagram of proposed PV-STATCOM system.	103
Figure 6.3 Detailed system diagram in EMTDC/PSCAD	104
Figure 6.4 Conventional operation of the PV solar farm.....	107
Figure 6.5 Conventional PV solar farm operates during and after the fault.	108
Figure 6.6 PV-STATCOM operation at the motor terminal.....	111
Figure 6.7 PV-STATCOM operation when located 19 km far from motor terminal.	113
Figure 6.8 PV solar farm operating as PV-STATCOM.....	116
Figure 6.9 PV solar farm reinstated following the PV-STATCOM operation.	117
Figure 7.1 One line diagram of Study System 1.....	120
Figure 7.2 One line diagram of Study System-2.....	121
Figure 7.3 Detailed DG control diagram of study systems.....	121
Figure 7.4 Gearless Wind Turbine-Generator-Rectifier (Wind T-G-R) Model	122
Figure 7.5 (a) Maximum nighttime power transfer (731 MW) from a generator when a solar DG remains idle (b) Voltage at generator terminal.	127
Figure 7.6 (a) Maximum nighttime power transfer (850 MW) from a generator with a solar DG using a damping controller, (b) Voltages at generator terminal and PCC.	128

Figure 7.7 Maximum daytime power transfer (719 MW) from generator with solar DG generating 91 MW real power.	129
Figure 7.8 Maximum daytime power transfer (861 MW) from generator with solar DG generating 91 MW real power and using the damping controller.	130
Figure 7.9 (a) Maximum nighttime power transfer (899 MW) from generator while the solar DG uses damping controller with voltage control and (b) Voltages at generator terminal and solar DG PCC (1.01pu).....	132
Figure 7.10 Maximum nighttime power transfer from generator with both DGs using damping controller but with no real power generation.....	135
Figure 7.11 Maximum daytime power transfer from generator where both DGs generate 95MW each while using a damping controller.	137
Figure 8.1 Network Impedance vs. Harmonic Frequencies plot when no capacitor is on 18M14.....	152
Figure 8.2 Network Impedances vs. Harmonic Frequencies plot when only load capacitor is on 18M14.....	152
Figure 8.3 Network Impedance vs. Harmonic Frequencies plot when load capacitor and 20 MVAR station capacitors are on 18M14.....	153
Figure 8.4 Network Impedance vs. harmonic frequencies plot when load capacitor and 40 MVAR station capacitors are on 18M14.....	153
Figure 8.5 Network Impedances vs. Harmonic Frequencies plot when load capacitor and 20 MVAR station capacitors are on 18M14 with 1/3rd SCL of the source.	154
Figure 8.6 Network Impedances vs. Harmonic Frequencies plot when load capacitor and 20 MVAR station capacitors are on 18M14 with 10 SCL of the source.	155
Figure 8.7 Network Impedances vs. Harmonic Frequencies plot when load capacitor and 40 MVAR station capacitors are on 18M14 with 4 SCL of the source.	155

Figure 8.8 Network Impedances vs. Harmonic Frequencies plot when load capacitor and 40 MVAR station capacitors are on 18M14 with 10 SCL of the source.	156
Figure 8.9 Network Impedance vs. Harmonic Frequencies plot when load capacitor and 20 MVAR station capacitors are on 18M14 with the loss of one transformer.....	156
Figure 8.10 Network Impedance vs. Harmonic Frequencies plot when load capacitor and 40 MVAR station capacitors are on 18M14 with the loss of one transformer.....	157
Figure 8.11 Network Impedance vs. Harmonic Frequencies plot when load capacitor and 20 MVAR station capacitors are on 18M14 with the loss of largest load on the feeder.....	158
Figure 8.12 Network Impedance vs. Harmonic Frequencies plot when load capacitor and 40 MVAR station capacitors are on 18M14 with the loss of largest load on the feeder.....	158
Figure 8.13 Harmonics Dataset for High Third Harmonics Injection	160
Figure 8.14 10 MW Solar Farm Output for a Sunny Day	163
Figure 8.15 Harmonics Dataset in the Evening of a Sunny Day	164
Figure 8.16 Harmonics Dataset around noon on a Sunny Day.....	164
Figure 8.17 High Harmonics Dataset on a Sunny Day.....	165
Figure 8.18 10 MW Solar Farm Output for a Cloudy Day.....	166
Figure 8.19 Harmonics Dataset during the Evening on a Cloudy Day.....	166
Figure 8.20 Harmonics Dataset around noon on a Cloudy Day	167
Figure 8.21 High Harmonics Dataset on a Cloudy Day	168
Figure 8.22 Harmonics Spectrum for Highest Harmonics Current Injection Over the Whole Period.	169

List of Appendices

Appendix A: 100kW PV inverter modeling mathematical expression and calculation	196
Appendix B: 7.5 MW PV solar system model parameters, fault detector parameters and calculation	210
Appendix C: Induction motor parameters and calculation	213
Appendix D: SMIB system parameters and 100 MW solar farm parameter calculation.	214
Appendix E: Substation data, SCADA, CYME modeling and GIS snapshots for the feeder networks	217

List of Acronyms

AC	Alternating Current
ATC	Available Transmission Capacity
BWP	Bluewater Power Corporation
DC	Direct Current
DG	Distributed Generation
DVS	Dynamic Voltage Support
EMTDC	Electromagnetic Transient including DC
EMTP	Electromagnetic Transient Program
FACTS	Flexible AC Transmission System
FC	Fuel Cell
FCL	Fault Current Limiter
Fortran	Formula Translation
GIS	Geographical Information System
GTO	Gate Turn Off Thyristor
HONI	Hydro One Network Inc.
HV	High Voltage (winding)
IEEE	Institute of Electrical & Electronics Engineers
IGBT	Insulated Gate Bipolar Transistor
IM	Induction Motor
LV	Low Voltage (winding)
LVRT	Low Voltage Ride Through
MPP	Maximum Power Point
MPPT	Maximum Power Point Tracking
ON	Ontario
OPF	Optimal Power Flow
PCC	Point of Common Connection/Coupling
PI	Proportional Integral (controller)
PLL	Phased Locked Loop
PMSG	Permanent Magnet Synchronous Generator
PSCAD	Power System Computer Aided Design

PV	Photovoltaic
PWM	Pulse Width Modulation
RMS	Root Mean Square
SCADA	Supervisory Control and Data Acquisition
SCL	Short Circuit Level
SMIB	Single Machine Infinite Bus
SPICE	Simulation Program with Integrated Circuit Emphasis
SPWM	Sinusoidal PWM
STATCOM	Static Compensator
STC	Standard Test Condition
SVC	Static VAr Compensator
SVPWM	Sinusoidal Vector PWM
TCR	Thyristor Controlled Rectifier
TCSC	Thyristor Controlled Series Compensation
TDD	Total Demand Distortion
THD	Total Harmonic Distortion
UPFC	Unified Power Flow Controller
VAr	Reactive Volt Ampere
VSC	Voltage Sourced Converter
VSI	Voltage Sourced Inverter

List of Symbols

θ	Theta
δ	Delta
ω	Omega
Δ	Delta (transformer winding configuration)
ξ	Xai
Ω	Sigma (Ohm unit)
μ	Mu (micro unit)

Chapter 1

1 Introduction

1.1 General

Solar energy is the most widely available source of renewable and sustainable energy that can play a leading role in the program of reducing greenhouse gas emissions. One of the established means to transfer this energy and transform it into electricity is Photovoltaic (PV) technology. One of the world's largest PV projects of 80MW, capable of providing electricity for more than 12,000 homes, is located in Sarnia, ON, Canada, and has been generating power since 2010. This is a \$400 million project. The installed PV capacity now exceeds more than 250 MW all over Canada [1]. Although PV technology is expensive, it is receiving strong encouragement through various incentive programs globally [2]-[6]. As a result, PV technology is becoming more popular for connecting to the grid both on large and small scales. PV solar farms are inactive during night and only partially utilized during daytime. Therefore, a huge investment remains unutilized in most of the time over a 24 hours period. This thesis deals with novel technologies for utilizing the unused capacity of the PV solar farm inverter for providing several benefits to power system such as, line loss reduction, prevention of induction motor load instability, improvement of transmission line capacity, etc.

1.2 Modeling of a Grid Connected PV Solar System

1.2.1 System description

A grid connected solar farm system is represented in terms of a block diagram, shown in Fig. 1.1. In a grid connected PV system the PV solar farm is connected to the electrical network at a bus called the Point of Common Coupling (PCC). The AC network consists of a number of loads connected with a typically stiff source, known as 'Grid', which is primarily responsible for supplying its loads when there is no PV power generation. After supplying the neighbouring loads, the additional power generated by the PV solar farm goes back to the grid. The PV solar farm generates DC power with its PV panels based on solar insolation and temperature, as shown in Fig. 1.1. A DC-DC converter is used to

harvest maximum DC power at that solar insolation and temperature by incorporating the Maximum Power Point Tracking (MPPT) algorithm. A DC link capacitor is used to maintain the DC link voltage constant at the inverter DC terminal. The inverter transforms the available DC power to AC power to supply to the AC network. The inverter includes semiconductor devices configured in a ‘matrix’ of switches and a controller which controls the switching of the devices. The power quality at the output terminal of the inverter is maintained with the use of a filter. The output voltage level of the inverter is integrated with the network voltage by using a step up coupling transformer. The details of each subsystem are provided below:

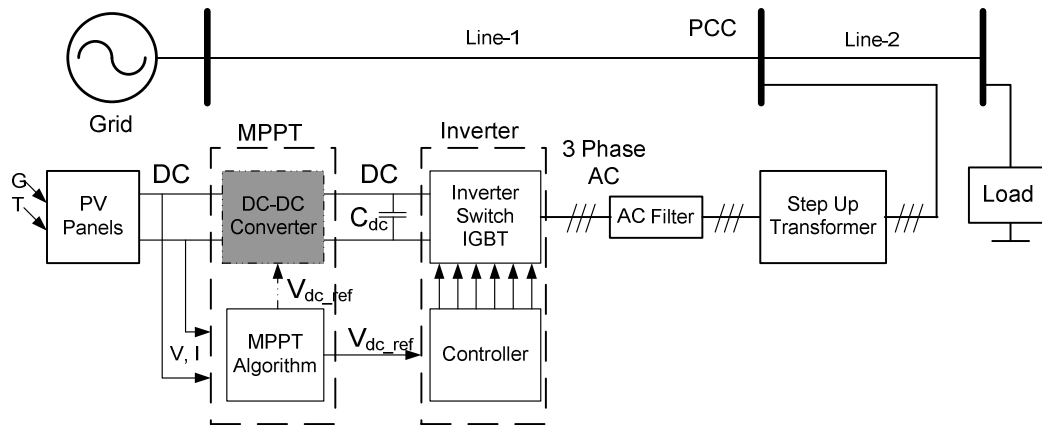


Figure 1.1 Block Diagram of a Complete Grid Connected PV System.

1.2.2 PV Solar Panel/Module

In a PV solar system, the PV modules, often called PV panels, are the power generating devices. For a large scale PV system a number of PV modules are connected in series to form a ‘String’, and these strings connect in parallel to form an ‘Array’. However, the PV modules, or panels, are comprised of a number of PV cells also connected in series and shunt configuration. These PV cells are a formation of p-n junctions from the doping of p-type and n-type substrates that are able to produce DC current and DC junction voltage upon the incidence of light due to the photovoltaic effect on semiconductors. As a result of the series and shunt combination of the cells in a module, the PV module can be equally characterized with an increased level of current and voltage. The current versus voltage (I-V) characteristic of the PV cell, and thereby the PV module, is not linear as shown in Fig. 1.2. For a particular amount of solar irradiation, there is a peak point of

power corresponding to the voltage at which the PV module can supply maximum power for that irradiance level expressed in the units of Sun. One Sun is equivalent to an irradiance level of 1000 watt/m^2 . These I-V characteristics are also temperature dependent. As a result, the maximum power point operation varies depending upon the solar irradiation and temperature as evident from the typical power versus voltage (P-V) characteristic curves, also illustrated in Fig. 1.2.

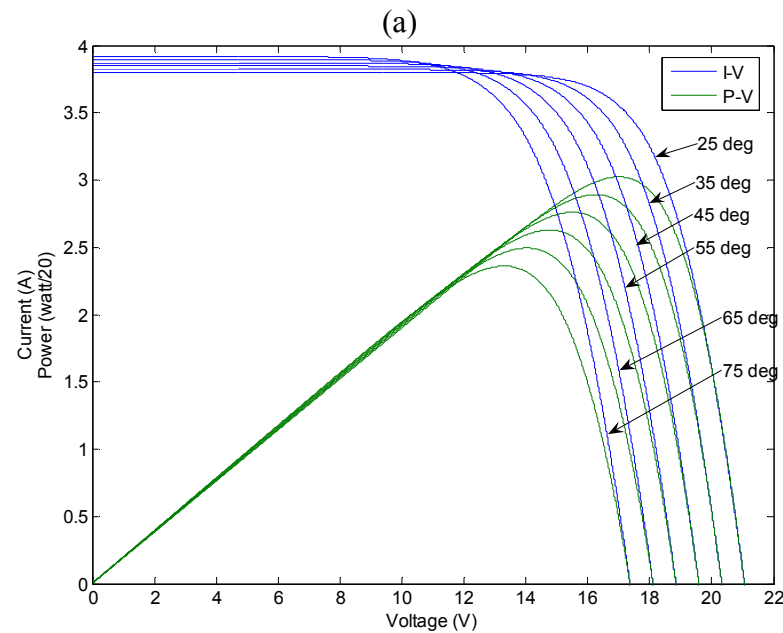
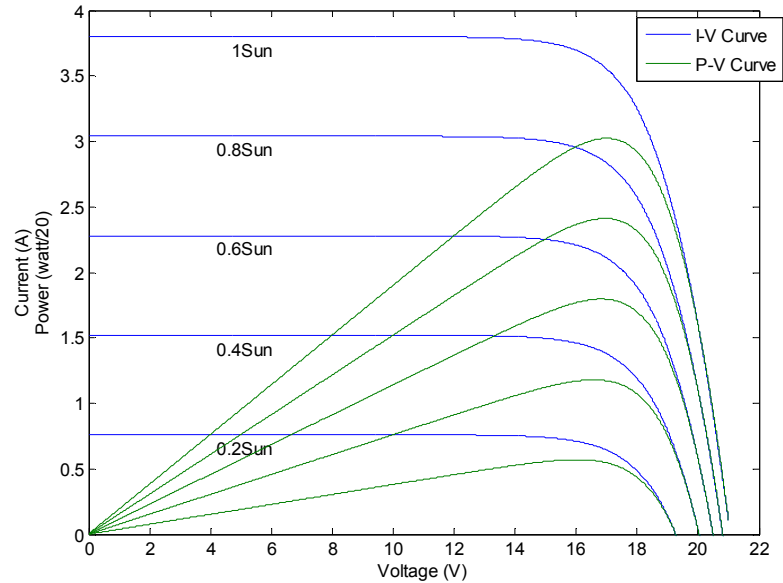


Figure 1.2 Typical I-V characteristic of a PV module at (a) different solar irradiation levels at 25°C and (b) different temperatures at 1 Sun irradiation.

Due to the construction similarity of the solar cells with the p-n junction photodiode, in general, the equivalent circuit of a PV cell can be represented by a current source in parallel with a p-n junction diode, as shown in Fig. 1.3, where G denotes the solar irradiation, T is the temperature, R_s is the equivalent series resistance of the cell, and R_{sh} is the equivalent shunt resistance of the cell [7]. Although there is another equivalent circuit representation of two diodes, known as the double exponential model [8], the single diode model is the simplest representation with respect to accuracy and construction.

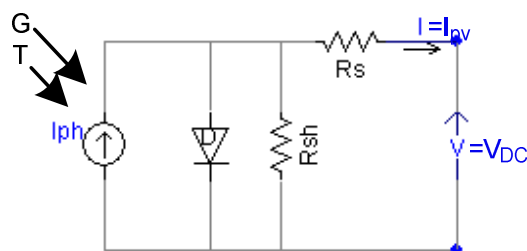


Figure 1.3 Equivalent circuit of PV solar cell (single diode model).

The modeling of solar panels using different commercially available software such as Matlab/Simulink, SPICE, SABER, etc., is reported in [8]-[17]. For modeling PV panels, these software applications utilize lookup tables for the equivalent source current output according to I-V curves [9], approximate diode current equations embedded in an equivalent current source [10], equivalent linear DC voltage source [11], program coding for current output corresponding to equivalent source terminal voltage [12], and a predetermined constant from the I-V characteristic curve of PV cell for the determination of equivalent source parameters [8].

Although the aforementioned papers utilize standard diode equations to model PV cells, it is important to determine precisely the equivalent series resistance R_s and the shunt resistance R_{sh} due to the non-linearity of the equations [18]. The effects of R_s and R_{sh} are illustrated in Appendix-A. Some papers have used I-V characteristic curves [12], [13] to determine equivalent R_s of the PV cell by neglecting R_{sh} of the PV cell as the value of R_{sh} is quite high and the effect of R_s is more dominant than R_{sh} in certain operating regions. Alternatively, they have determined both the resistances through iterative techniques

[14]-[17]. Several models have also been developed in EMTDC/PSCAD software for fault analysis [19], MPPT modeling [20], PV array modeling [21],[22]. These models are developed using approximate equations by neglecting both R_s and R_{sh} [19]. Some models typically use a number of pre-defined constant values with FORTRAN coding [20]. One of them [21] utilizes predefined constants derived from I-V characteristic curves. Another paper [22] has used the circuit based piecewise linearization technique through trial and error method to model the PV source.

However, the above mentioned modeling techniques are based on the use of lookup tables [9] or predetermined constants from the I-V characteristic curve of PV cell and, thereby, the PV module are PV cell manufacturing parameters dependent and require more detailed information for the modules from the manufacturer's datasheet of the PV cell. The determination of both resistances through iterative techniques requires more iterative programming, and eventually slows down the simulation process. Also, the circuit based piecewise linearization technique, through trial and error, requires repetitive refinement for different levels of solar radiation and temperature. It is further noted that the dynamic model of the PV solar modules represented with an equivalent linear DC voltage source is not the proper choice because of the nonlinear I-V characteristics of PV cells, and thereby the modules. In most cases, these models lack accuracy in prediction of output power and current due to a large number of assumptions and approximations.

1.2.3 Maximum Power Point Tracking (MPPT) System

To harvest maximum power from the solar cells or modules as depicted in Fig. 1.2, a Maximum Power Point Tracking (MPPT) system is required to be integrated with the system, as illustrated in Fig.1.1. In modeling the MPPT, two types of topologies are used: one is the use of a DC-DC converter [23], [19] and the other is without a DC-DC converter [24], [25].

1.2.3.1 MPPT with DC-DC converter

In this topology, a DC-DC buck, boost, or buck-boost converter is used to maintain the output DC link voltage across the DC link capacitor constant and allows the PV panels to operate at this maximum power point voltage. It also serves as a decoupling circuit

between PV panels output and inverter input to minimize the effect of inverter operation. A detailed modeling procedure for a DC-DC converter of PV solar cells, thereby, the PV modules can be found in [26].

1.2.3.2 MPPT without DC-DC Converter (Converter-less MPPT)

In a grid connected solar system, it is also possible to maintain the voltage constant across the DC link capacitor by controlling the inverter input current without the use of a DC-DC converter. This technique minimizes the loss and increases the efficiency [27]. The output voltage of PV panels or modules serves as the DC link voltage: and when this voltage is maintained at maximum power point voltage due to inverter control, the PV panels generate maximum power.

1.2.3.3 MPPT Algorithm

To maintain the DC link voltage constant a reference is used by monitoring the output voltage and current of the PV panels based on some established algorithms, e.g. Perturb and Observe [28], Incremental Conductance, [29] etc. such that the PV panels operate at maximum power point voltage to generate maximum power. Among all of the algorithms, incremental conductance algorithm is much more efficient in terms of rapid tracking of changes in the solar irradiation level [26], [30]. The reference obtained from the MPPT algorithm is set in the DC-DC converter switching controller (not shown in figure) for the DC-DC converter based system, or in the inverter controller for the converter-less system as shown in Fig. 1.1.

1.2.4 PV Inverter Modeling

1.2.4.1 PV Inverter Configuration

Two types of inverter configuration are employed presently in solar farms. One is called string technology; [32]-[35] where several modules in string configuration feed in to a single large inverter. These large inverters are grouped together to feed the grid. The other is called the micro-inverter, also known as AC module technology, [32], [33] where each individual module has its own inverter and the outputs of all micro-inverters are integrated together to feed the grid.

There are numbers of inverter topologies used for grid connected PV solar farms. There are single step topology for AC modules [36],[37], two stage topology for multiple modules [38],[39], multilevel inverter topology [40],[41], fly-back type inverter [42],[43], fly-back current fed inverter, [44] all of which are summarized in [45]. Different topologies used by several commercial manufacturers are compared and studied in terms of performances in [46]-[50], [35]. A resonant inverter is also discussed in [51].

To construct inverter circuits, manufacturers use Metal-Oxide Semiconductor Field Effect Transistor (MOSFET) [52], Gate Turn Off (GTO) thyristor, and Insulated Gate Bipolar Transistor (IGBT) switches [53]. The present trend is to use IGBT switches [53], [54] because of their low loss and ease of switching [55]. A typical six pulse inverter using the IGBT switches is depicted in Fig. 1.4 [11], [24] which is comprised of 6 IGBT switches with associated snubber circuits for smooth switching operation [56]. The firing pulses to trigger the IGBT switches are generated from the inverter controller.

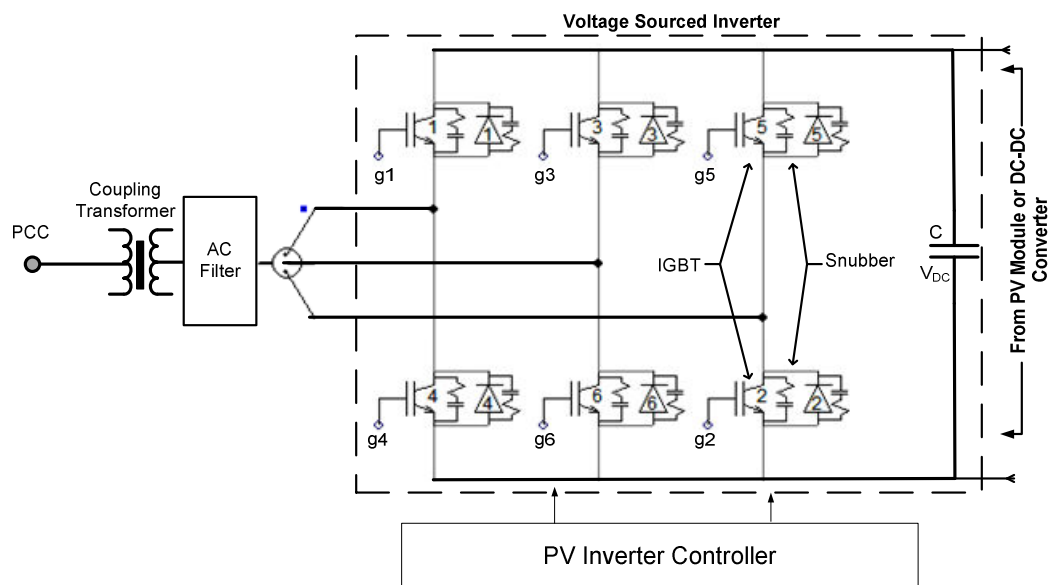


Figure 1.4 Typical PV solar farm inverter.

1.2.4.2 Inverter Firing Strategy

To generate the firing pulses for the IGBTs in the inverter, various technologies such as Pulse Width Modulation (PWM) [52], [53], Sinusoidal Vector PWM (SVPWM) [24], or Hysteresis control [57] techniques are used. Among all of these techniques, the PWM technique is widely used for high power PV inverter applications [52],[53],[58].

1.2.4.3 Inverter Control schemes

The PV solar farm is required to inject power to the grid at close to unity power factor according to several DG inter-connection standards [59],[60],[61]. In modeling the control system, two control schemes are widely used - Current Sourced Inverter (CSI) and Voltage Sourced Inverter (VSI) or, alternately known as Voltage Sourced Converter (VSC). In a CSI scheme, the inverter input is maintained as a constant current source with the use of DC link inductors, whereas the VSI scheme uses the DC link capacitor to maintain constant voltage source at the inverter input. For CSI, the output of the inverter is the controlled voltage. On the other hand, the output of the VSI control scheme is a controlled current. Due to the lower short circuit current contribution to the grid faults, the VSI with current control strategy is preferred by industries [52],[53],[55]. Therefore, the remainder of the work in this thesis is mainly focused on VSI based inverter control schemes.

Fig.1.5 presents the VSI current controller of a typical PV solar farm inverter which uses d-q current and voltage components as a feedback signal of two current control loops: direct axis current control loop and quadrature axis current control loop [24],[52],[54],[62]-[65]. The three phase voltage (V_a, V_b, V_c) and current (I_a, I_b, I_c) measured at PCC (not shown in figure) are converted into d-q components of voltage (V_{sd}^c, V_{sq}^c) and current (I_d, I_q) through the Park's transformation process. In this transformation, it uses the angle obtained from the PCC voltage (V_a, V_b, V_c) through a phase locked loop (PLL) oscillator known as the synchronization angle, θ . For balanced three phase signals,

$$f_a(t) = \cos \theta ; f_b(t) = \cos\left(\theta - \frac{2\pi}{3}\right) ; f_c(t) = \cos\left(\theta - \frac{4\pi}{3}\right) \text{ and } \theta = (\omega t + \varphi)$$

The Park's transformation is as follows [108] as given in Appendix – A for a rotating d-q frame at a speed of ω :

$$\begin{bmatrix} f_d(t) \\ f_q(t) \end{bmatrix} = \frac{2}{3} \cdot \begin{bmatrix} \cos \theta & \cos\left(\theta + \frac{2\pi}{3}\right) & \cos\left(\theta - \frac{2\pi}{3}\right) \\ -\sin \theta & -\sin\left(\theta + \frac{2\pi}{3}\right) & -\sin\left(\theta - \frac{2\pi}{3}\right) \end{bmatrix} \cdot \begin{bmatrix} f_a(t) \\ f_b(t) \\ f_c(t) \end{bmatrix}$$

where, the quantity, f , represents either the instantaneous voltage or current signals. $\omega=2\pi f$ is the angular frequency and φ is the phase angle of the corresponding components. Therefore, the real power, P and the reactive power, Q in d-q co-ordinate system is given by [108],

$$P = \frac{3}{2} [v_d \cdot i_d + v_q \cdot i_q] \text{ and } Q = \frac{3}{2} [-v_d \cdot i_q + v_q \cdot i_d]$$

If the direct axis component v_d is aligned with the space vector, at steady state, the power expression can be decoupled as follows [108]:

$$P = \frac{3}{2} [v_d \cdot i_d] \text{ and } Q = \frac{3}{2} [-v_d \cdot i_q]$$

The d-q components of voltages v_d , v_q and current i_d , i_q are constantly rotating with d-q reference axes. Therefore, v_d , v_q , i_d and i_q are expressed as in Laplace form as V_{sd}^c , V_{sq}^c , I_d and I_q , respectively.

In Fig. 1.5, the direct axis current control loop consists of two proportional integral controllers, PI-1 and PI-3. Whereas, the quadrature axis current control loop consists of PI-2 and PI-4. The direct axis current control loop maintains the DC link voltage constant around a reference set by the MPPT algorithm in a converter-less MPPT technique and injects the balance of the power generated from the PV modules to the inverter output. To perform this control function, the DC link voltage, V_{DC} , is compared with the DC voltage reference, V_{DC_ref} , obtained from the MPPT algorithm and is passed through a PI-3 controller to obtain the direct axis current control loop reference, I_{d_ref} . The measured direct axis current signal, I_d , is compared with this reference signal, I_{d_ref} , to obtain the direct axis modulation signal, m_d , through the PI-1 controller. On the other hand, the quadrature axis current control loop is used to maintain the reactive power output of the inverter around a reference value of zero for unity power factor operation[24],[62]. In this case, the reactive power output is compared with the reference value which gives the quadrature axis current control loop reference, I_{q_ref} , through the PI-4 controller and generates the quadrature axis component of modulation signal, m_q , with the comparison of I_q through the PI-2 controller. The direct axis and quadrature axis voltages act as disturbance signals in these control loops and a decoupling factor of ωL is included to decouple these two control loops where, ω is the angular frequency in rad/sec and L is the

inductance at the output of the inverter. The detailed mathematical manipulation is given in Appendix-A. However, the output two axis modulation signals m_d and m_q from the controller are converted into three phase signals called modulating signals (m_a, m_b, m_c), as follows:

$$m_a = m \cos(\theta + \alpha), m_b = m \cos(\theta + \alpha - 120^\circ), m_c = m \cos(\theta + \alpha + 120^\circ)$$

$$\text{where, } m = \sqrt{m_d^2 + m_q^2}, \alpha = \tan^{-1} \frac{m_q}{m_d}.$$

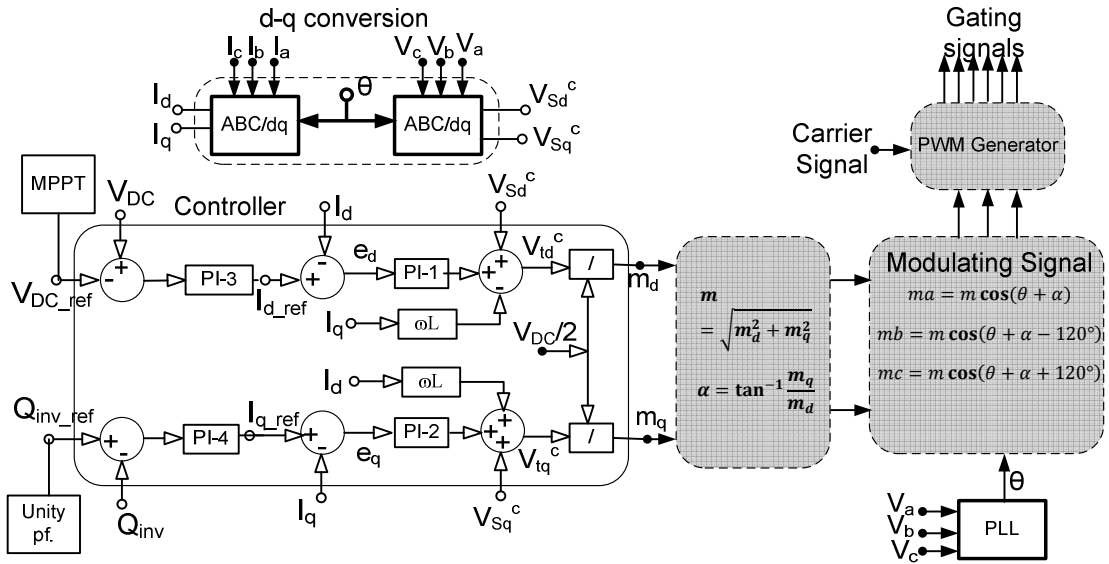


Figure 1.5 Generic VSI based PV inverter controller.

In the PWM technique, these ‘modulating signals’ are compared with high frequency triangular signals called ‘carrier signals’ to generate the gating signals for the IGBT devices to inject PV solar farm power to the AC grid at unity power factor and controls the DC link voltage.

1.2.4.4 DC link Capacitor

In a PV solar system the main role of the DC link capacitor, in addition to holding a constant DC voltage, is to maintain the power quality at the DC side which ultimately influences the power quality at the AC side [66]. For smooth operation of the inverter, a comparatively ripple free DC current and voltage is required at the input of the inverter. While using the DC link capacitor in a converter-less MPPT system, the size of the DC link capacitor must be carefully chosen. Otherwise, pulsating power due to extra high

value of capacitor or a power variation due to a very low value of DC link capacitor will be transmitted to the grid [27]. The sizing of DC link capacitors is reported in [52], [65], [67], [68] based on maximum energy storage capacity and allowable minimum DC voltage.

1.2.5 Filter Modeling

Along with the fundamental component, the inverter generates harmonics depending upon its switching frequency and the size of DC link capacitor. Hence, filters are required at the AC side of the inverters such that the net harmonics output expressed in terms of Total Demand Distortion (TDD) and Total Harmonic Distortion (THD) comply with the grid code requirements as set by several standards, e.g. IEEE 519 [69], IEEE 1547 [59]. To perform the filtration of the output AC power in order to obtain a purely sinusoidal waveform, a number of filter configurations are used [35]; out of which the L-C-L configuration or the L-C filter, in conjunction with the transformer impedance, are chosen widely [70], [71]. The traditional modeling techniques for the L-C-L filter are reported in [64],[68],[70],[71].

1.2.6 Step Up Transformer

A step up transformer is primarily used as the coupling transformer between the inverter and the grid. In most of the inverters, the DC terminal is grounded to apply equal DC link voltage across each IGBT switches. Therefore, in the case of any line to ground fault at the AC side of the inverter, to protect the IGBT valves, the zero sequence current flow through the valves are prevented by using either ungrounded wye winding, or delta winding at the inverter side of the step up transformer. In the case of any overvoltage due to ungrounded winding at the inverter side, the inverter is equipped with protective devices to shut itself down by sensing the voltage and phase angle at its terminal [52],[53],[55]. According to several utility connection requirements, the DG coupling transformer should be delta (at the inverter side) and must be grounded wye at the utility side [72] due to several advantages as discussed in [73],[74]. Therefore, the step up transformer with either delta (at inverter side) - wye grounded (at the utility side) [75] or, floating wye (at the inverter side) - wye grounded (at the utility side) is preferred [76].

1.3 Short Circuit Contribution of Grid Connected PV Solar System

In electric power systems, the integration of more Distributed Generators (DGs) with the network increases the short circuit level due to the current contribution of the DGs to a potential fault [77]-[79]. Hence, utility companies, especially in Ontario, are limiting the connection of DGs into their network [61] which has resulted in the loss of opportunity to integrate more renewable generation into the network. Compared to the synchronous and induction machine based generators, the inverter based generators, such as the Photovoltaic (PV) system, contributes much less fault current to the network due to the characteristics of PV panels and inverter operation. The short circuit current contribution from a PV system inverter is in the range of 1.2 times the rated current for the large size inverter (1MW) [55], [80] 1.5 times (500kW) for the medium size inverter [80], [81] and 2 - 3 times for the smaller inverters [80],[81]. Although each PV solar farm satisfies the standards, the total amount of fault contribution becomes unacceptably large for a feeder that has a large number of PV systems [81], [82]. According to several grid interconnection standards [59], [60], regardless of fault level, it is required to disconnect the PV solar farms or any other DGs upon detection of fault on the system.

Therefore, it is not only important to detect the faults rapidly, but also to disconnect the DGs from the network as quickly as possible to minimize short circuit current contribution. This issue has not been adequately addressed in literature. Although [83] claims that their controller is capable of limiting the short circuit contribution within 1 pu, the details are not yet disclosed to the public.

1.3.1 Techniques for Fault Detection

The traditional relay technologies mainly use the over-voltage, under-voltage, and over-current signals to detect the fault and, subsequently, operate the protective breaker and disconnect the DGs from the network. According to DG interconnection requirements by a utility [61], a DG generating more than 1 MW is required for transfer trip. To detect the fault the utility uses instantaneous over current relay which takes about 17 milliseconds to detect a fault and transfers the trip signal within 5-10 milliseconds [61]. The traditional breaker operating time is considered as 83 milliseconds [61]. Therefore, the current

practice of detecting a fault and disconnecting the DG takes at least 105-110 milliseconds. Within this time the fault current already exceeds its allowable peak limit at least for 7-8 cycles. Techniques have been proposed for quick detection of fault through the monitoring of change in the voltage phase angle [84], combined voltage phase and magnitude [85], positive sequence component of voltage [86], [87], and d-q components of voltage magnitude at the point of common coupling (PCC) [88],[89]. To detect the fault faster current monitoring is chosen in [90]- [92]. According to [90], the speed of fault detection depends on the digital signal processing and sampling rate of the fed back current signal that is able to generate a trip signal within 3-5 ms. Whereas, [91] and [92] use the rate of rise of current and current magnitude to generate a trip signal within 1ms. So far, these fast fault detection techniques are used for power system network protection and unsymmetrical fault detection in Fault Current Limiter (FCL), which uses either solid state breaker to trip faster.

Such techniques have not been applied for fast fault detection in the case of PV solar systems.

1.4 Flexible AC Transmission System (FACTS) Devices

Flexible AC Transmission System (FACTS) is defined by IEEE [93] as:

“Alternating current transmission systems incorporating power electronic-based and other static controllers to enhance controllability and increase power transfer capability.”

FACTS devices can be classified based on the device technology as follows [94]-[96]:

A) Thyristor Based FACTS Devices:

The thyristor based FACTS devices employ thyristor that can only be turned on by gating signals, but cannot be turned off by removing gating signals. They turn off only when the current passing through it becomes zero. This type of FACTS device can be categorized in two groups: Shunt connected, and Series connected thyristor based FACTS devices.

Shunt connected thyristor based FACTS devices include Thyristor Controlled Reactor (TCR), Thyristor Switched Capacitor (TSC), and Static Var Compensator (SVC), etc.

Series connected thyristor based FACTS devices include Thyristor Controlled Series Capacitor (TCSC), Thyristor Switched Series Capacitor (TSSC), and Thyristor Controlled Phase Angle Regulator (TCPAR), etc.

B) Voltage Sourced Converter (VSC) based FACTS devices:

In these VSC based FACTS devices GTO, MOSFET, or IGBT devices are used to form the switches in the VSC. These devices can be turned ON and turned OFF by employing the gating signals. As a result, the controllability increases significantly. In every VSC based FACTS device, a dc link capacitor is used to maintain a constant voltage. Based on the construction and application, these devices are categorized in three different groups: Shunt Connected VSC based FACTS devices, Series Connected VSC based FACTS devices, and Combined Shunt and Series Connected FACTS devices.

Shunt connected VSC based FACTS devices include the Static Synchronous Compensator (STATCOM) which primarily comprises an inverter. The inverter could be either six pulse, twelve pulse, or higher. The higher the pulse level, the lower the harmonic injections but the higher the construction complexity [94]-[96]. Also, the inverter could be single level, two level, or multilevel [94]-[96], [199]-[202].

Series connected VSC based FACTS devices include the Static Synchronous Series Compensator (SSSC) which can effectively modulate the line reactance by introducing into the line a voltage at an appropriate phase angle with respect to current [95], [199]-[202].

Combined Shunt and Series Connected FACTS devices include the Unified Power Flow Controller (UPFC), which is basically the combination of a SSSC and a STATCOM sharing a common DC link capacitor. Therefore, two VSCs are connected on either side of the capacitor; one is connected in shunt, and the other is connected in series. The UPFC performs both the functions of SSSC and STATCOM simultaneously [95], [199]-[202].

FACTS devices, although very expensive, are widely employed in power systems for the following reasons:

The shunt connected FACTS devices exchange controlled reactive power with the grid in order to maintain the bus voltage constant, or to modulate the bus voltage and increase system stability [97] and damping [95], [199]-[202]. The series connected FACTS devices effectively increase, decrease, or modulate the line reactance to control power flow and to increase system stability [94]-[96], [199]-[202].

A distinctive feature of VSC based FACTS devices (STATCOM, SSSC, UPFC) is the capability of real power exchange if they are connected to an energy storage system such as battery [96], [98]-[102],[199]-[202]. However, this thesis focuses on STATCOM operation, thus, the STATCOM is described in detail in the next section.

1.5 STATCOM

1.5.1 Basic Operating Principle:

A STATCOM is analogous to a synchronous condenser [95] and is capable of generating three phase sinusoidal voltages with controllable amplitude and phase angle. Fig. 1.6 shows the one line diagram of a STATCOM with its voltage and current phasors in a power system.

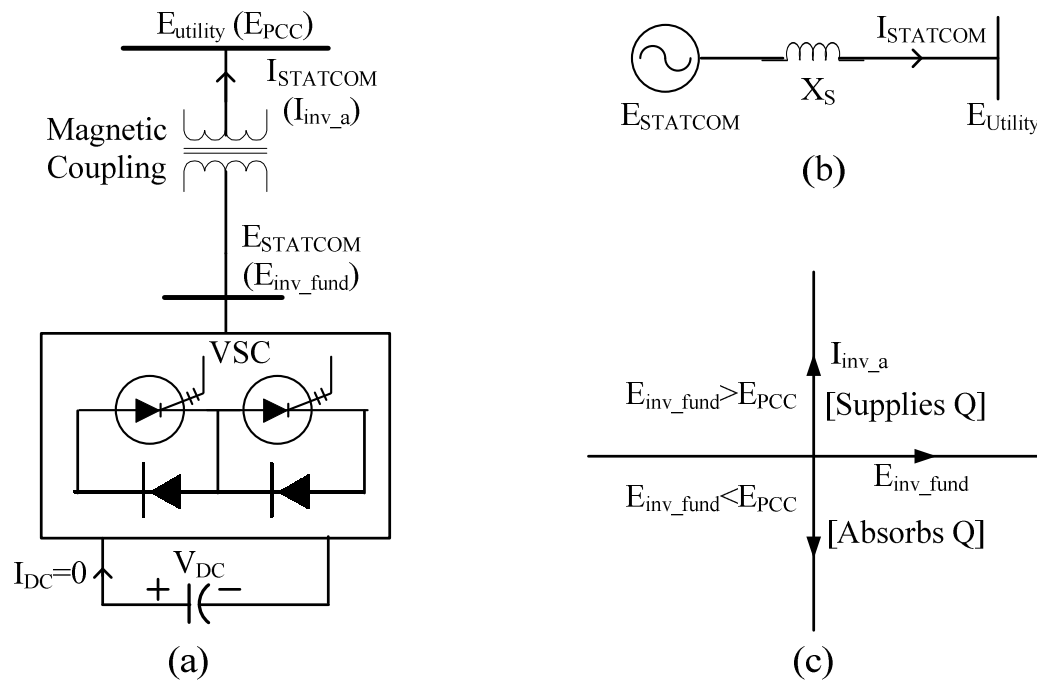


Figure 1.6 (a) STATCOM (b) analogous representation of STATCOM and, (c) STATCOM terminal voltage and current phasor.

The STATCOM is connected with the utility through a coupling reactance or transformer, as shown in Fig. 1.6 (a). Therefore, the STATCOM can be equally represented as an ideal adjustable voltage source connected to a utility network, as shown in Fig. 1.6 (b) where the equivalent reactance X_s is provided by the coupling transformer leakage reactance. Like the synchronous condenser, when the STATCOM inverter output voltage E_{inv_fund} is greater than the utility voltage E_{PCC} , as shown in Fig 1.6 (c), the STATCOM supplies reactive power Q or leading current, and when E_{inv_fund} is less than E_{PCC} it absorbs Q or supplies lagging current. It is noted, when E_{inv_fund} is exactly equal to the E_{PCC} , no current flows from the STATCOM. This condition is known as the floating state. Therefore, the reactive power can be varied from inductive to capacitive range smoothly by varying the STATCOM terminal voltage magnitude E_{inv_fund} .

Since the STATCOM controls reactive power flow through power electronics processing, it does not require any additional capacitor banks or reactors as a SVC that contributes to a compact design, and smaller footprint, as well as low noise and low magnetic impact. The only capacitor used is at the DC terminal of the STATCOM, which provides a constant voltage. As DC power does not have any reactive component and the voltage at the DC terminal is held constant, the DC link capacitor does not participate in any reactive power exchange. Since the STATCOM does not inject any real power to the grid, the DC link provides an instantaneous power-circulating path to satisfy the power balance relation and thus, the converter establishes a circulating reactive power exchange among the phases. However, in a practical STATCOM system there are real power losses that are compensated from the DC link capacitor, thereby reducing the DC link voltage. Thus, some real power must be absorbed from the AC system to keep the DC link capacitor voltage constant. This is accomplished by making the VSC terminal voltage lag the utility system voltage by an angle of θ . The magnitude of this angular difference depends on the amount of charge that needs to be replenished in the DC link capacitor.

1.5.2 V-I Characteristic of STATCOM

The typical V-I characteristic and the V-Q characteristics of a STATCOM are depicted in Fig. 1.7 [95]. According to the V-I characteristics it is observed that the STATCOM is able to provide its rated reactive current even when the voltage at its terminal decreases

as low as 0.1 p.u. Therefore, the Q limit varies linearly with the bus voltage as observed in Fig. 1.7(b). This reveals that the STATCOM can operate effectively even if there is a fault in the network which might cause a low voltage situation. It is also observed that both the maximum inductive and the capacitive current ranges, as well as the inductive and capacitive reactive power ranges are equal, giving the STATCOM twice the dynamic range for the same size of VSC.

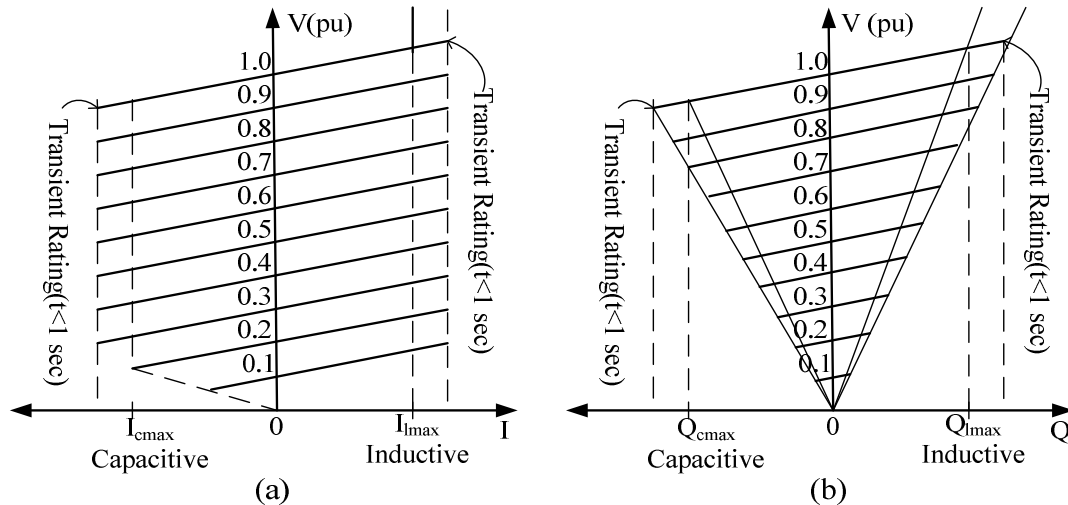


Figure 1.7 STATCOM (a) V-I and (b) V-Q characteristics.

1.5.3 Configuration

A STATCOM is comprised of a voltage sourced converter (VSC) with a DC link capacitor. The sole purpose of the DC link capacitor is to maintain the DC link voltage constant such that the voltage at the AC terminal can be controlled smoothly. The VSC can be based on either Gate Turn Off (GTO) thyristors or Insulated Gate Bipolar Transistors (IGBT) [96]. The IGBT based STATCOMs are becoming more popular due to being more cost effective. Along with the IGBT switches, snubber circuits are incorporated for smooth switching operation of the IGBT devices [103]. The IGBT switches can be controlled through various control techniques among which the Pulse Width Modulation (PWM) technique is widely used in large size STATCOMs. A typical STATCOM is depicted in Fig. 1.8 where the coupling transformer is used for transforming the STATCOM output voltage to the system bus voltage. While using the PWM technique, a filter is needed to eliminate harmonics and maintain the power quality at the AC side of the STATCOM [104], [105].

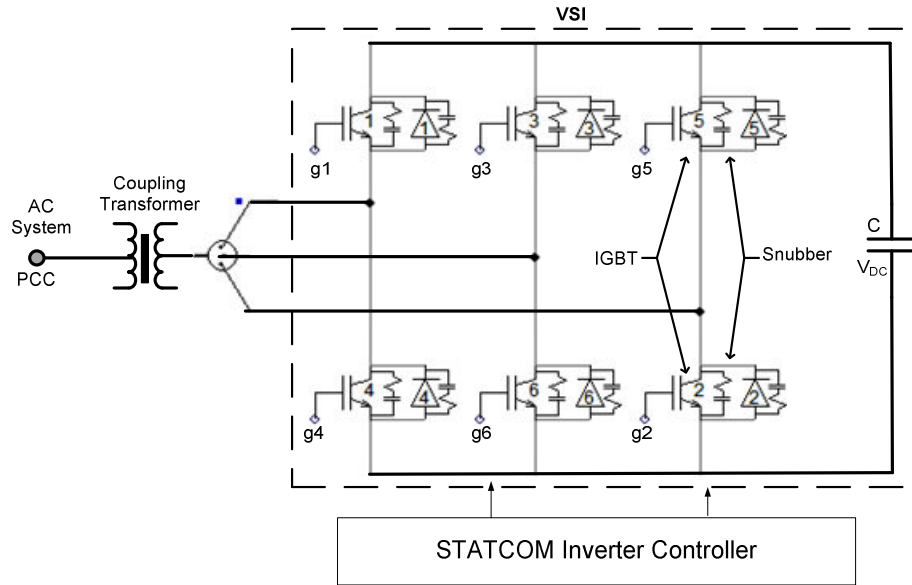


Figure 1.8 IGBT based basic STATCOM configuration.

1.5.4 Controller

The STATCOM controller is used either to control the voltages at the PCC or to control the reactive power flow. Based on the control strategy, the PCC signal is monitored accordingly. A PWM based typical PCC voltage control strategy of a STATCOM is demonstrated in Fig. 1.9 [106] where the controller is implemented with the use of d-q co-ordinate system signals [98], [107].

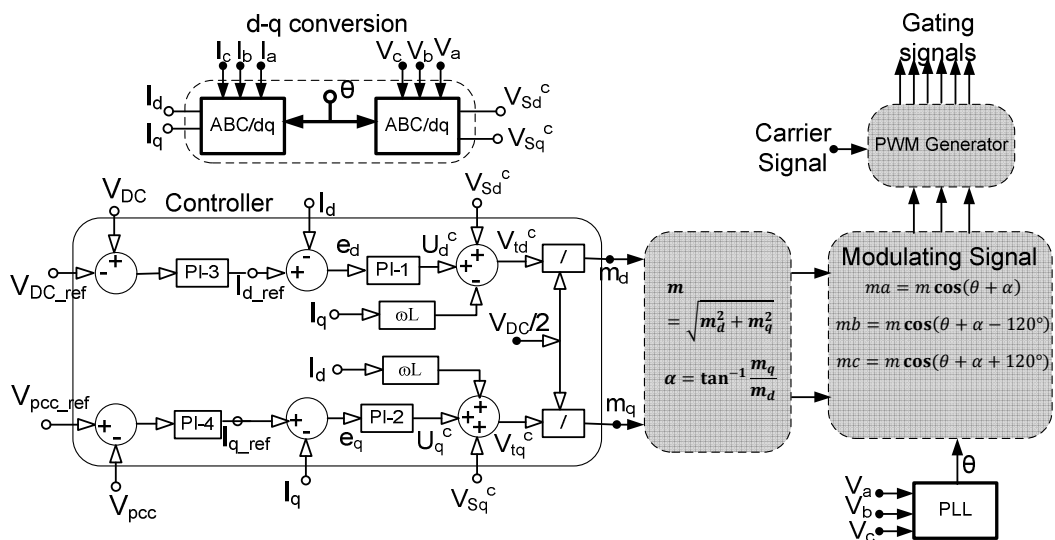


Figure 1.9 Schematic Diagram of Generic STATCOM Controller.

In this control system, all of the measured current and voltage quantities are converted from the ABC co-ordinate system to the d-q co-ordinate system prior to being given as controller input. This controller uses two inner current control loops: direct axis current (I_d) control loop and the quadrature axis current (I_q) control loop. Regardless of the control strategy, in an ideal case, STATCOM does not transfer any real power. However, in a real case, a real power loss associated with STATCOM operation lowers the DC link voltage. Hence to maintain constant DC link voltage the DC bus is monitored and regulated through a controller PI-3 on direct axis current control loop which eventually defines the reference value I_{d_ref} for the direct axis current control loop as shown in Fig. 1.9. On the other hand, to control the voltage at the PCC through reactive power exchange, the PCC voltage is monitored and is compared with the reference value of PCC voltage. The output of the voltage regulator PI-4 on the quadrature axis control loop sets the reference value I_{q_ref} for quadrature axis current control loop. The current signals monitored from the PCC are then compared and passed through two PI controllers, PI-1 and PI-2, to generate desired modulating signals m_d and m_q . These modulating signals, m_d and m_q , are converted back into three phase signals and compared with a high frequency carrier signal which generates a series of gating signals for the IGBT switches of the inverter.

According to the switching of the IGBT devices, the input DC voltage of the inverter appears at the output of the inverter as a high frequency pulsating DC, which includes a fundamental component of AC voltage. It is noted that a phase locked loop oscillator (PLL) is used to synchronize the VSC output with the power system voltage and frequency [106].

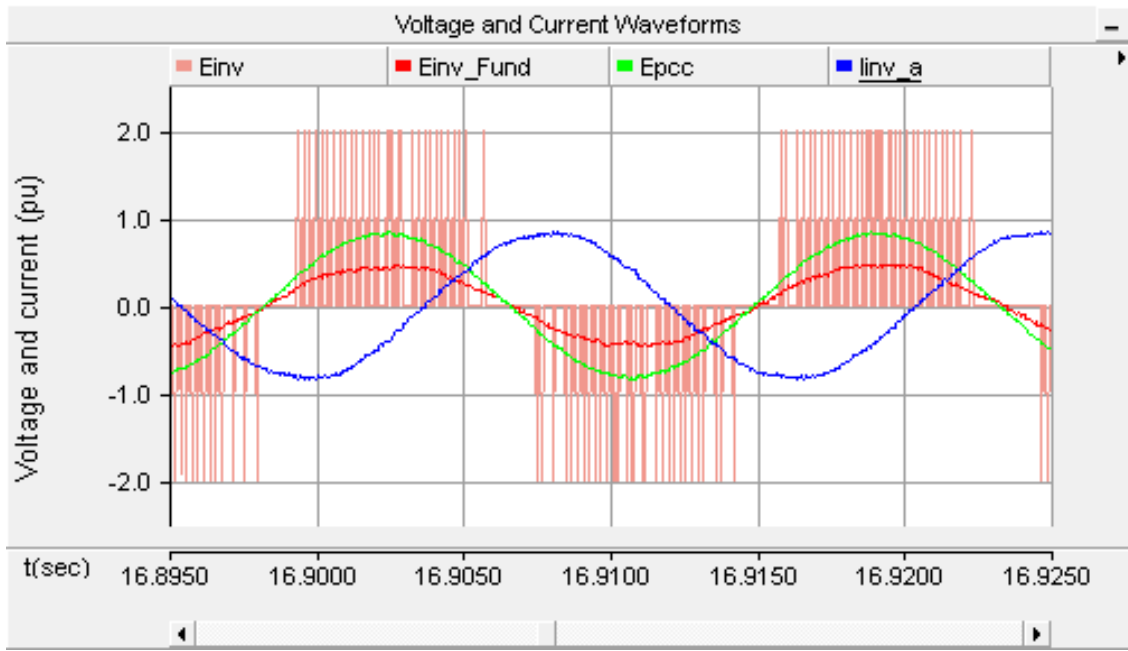
In this PWM technique, the output and input voltage relation in terms of modulation index ‘ m ’ can be expressed as follows [98], [96], [108]:

$$V_{AC(L-N),peak} = m \cdot V_{DC}/2 \dots\dots\dots (1.1)$$

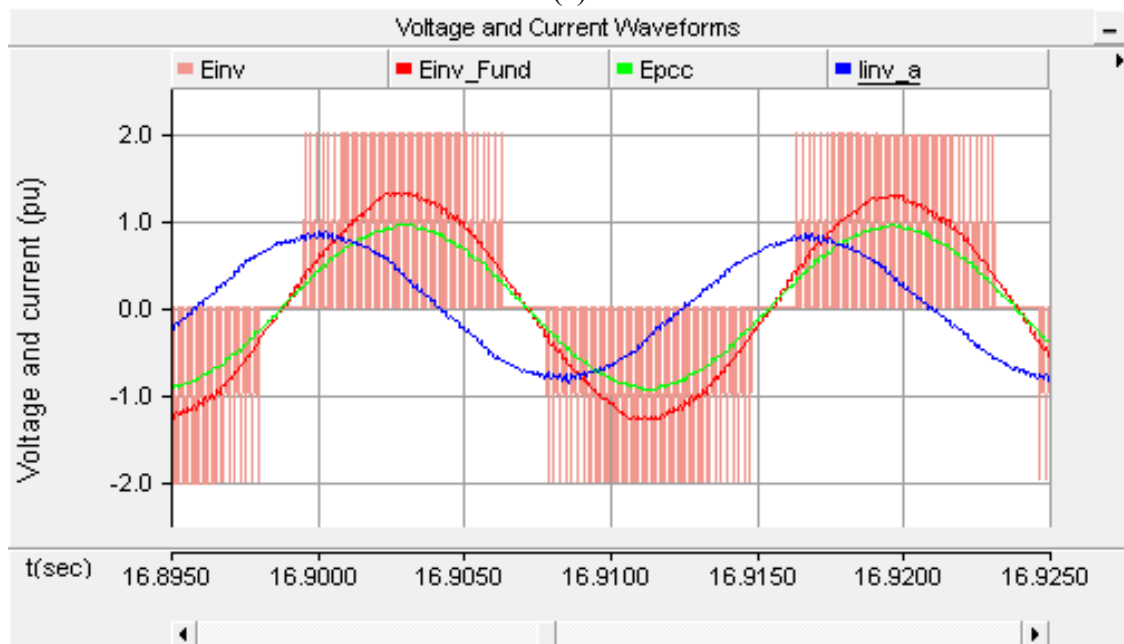
Therefore, by controlling the magnitude of the modulation signal with the controller, the desired AC voltage output from the input constant DC voltage V_{dc} can be achieved. A detailed mathematical analysis of a STATCOM controller can be found in [106],[108].

1.5.5 Voltage Control

This voltage control operation of a STATCOM is demonstrated with an EMTDC/PSCAD software simulation result, presented in Fig. 1.10.



(a)



(b)

Figure 1.10 Voltage and current waveforms for (a) 5 MVAR inductive and (b) 5 MVAR capacitive mode of operation of STATCOM.

The high frequency pulse series signal, E_{inv} , represents the line-to-line pulsating voltage between phase A and B at the STATCOM inverter terminal. The red sinusoidal waveform ($E_{inv_Fund}=V_2$) represents the fundamental component of the line-to-line voltage between phases A and B extracted from the pulsating voltage ‘ E_{inv} ’ with the use of a filter. The green waveform ($E_{PCC}=V_1$) represents the PCC line to line voltage between phases A and B and the blue waveform (I_{inv_a}) represents the inverter output current at phase A. Fig. 1.10(a) represents the voltage and current waveforms for 5MVAR inductive, and Fig. 1.10(b) represents the voltage and current waveforms for 5 MVAR capacitive reactive power supplied by the STATCOM.

It is evident from the waveforms in Fig. 1.10 (a) that when the magnitude of fundamental voltage at the STATCOM terminal is lower than the PCC voltage (V_l), the inverter output current is lagging behind the voltage, indicating that the STATCOM is operating in inductive mode. On the other hand, when the magnitude of fundamental voltage at the STATCOM terminal is higher than the PCC voltage as shown in Fig. 1.10(b), the inverter output current is leading the bus voltage, indicating that the STATCOM is operating in capacitive mode. Based on this principle, the VSC of STATCOM regulates the voltage magnitude at its terminal such that both capacitive and inductive reactive power can be exchanged with the grid as needed. It is noted that the control system is compensating for a very small amount of real power loss by maintaining the DC link voltage constant. Hence, a very small phase angle difference between the voltages is noticed (not visible in figure.)

1.6 Application of Shunt FACTS Devices:

Transmission grids worldwide are presently facing challenges in integrating large-scale renewable systems (wind farms and solar farms) due to their limited power transmission capacity [109]. In a power system, the power transfer over a transmission line is limited by several angular stability limits such as: thermal limit, steady state stability limit, transient stability limit, and damping limit [95], [97]. The relative magnitudes of these various limits are presented graphically in Fig. 1.11 where the vertical length denotes the level of power in MVA.

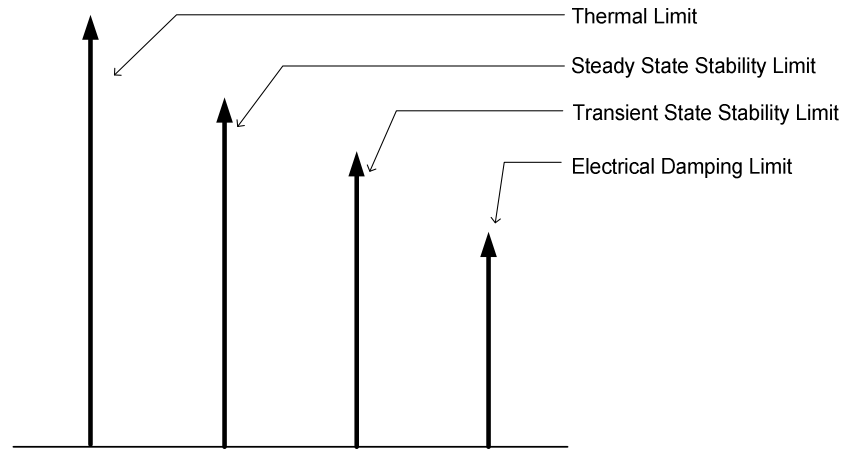


Figure 1.11 Relative magnitudes of various power transmission limits.

To increase the transmission capacity of existing transmission lines, series compensation and various Flexible AC Transmission System (FACTS) devices are utilized [94],[95],[110],[111]. In an extreme situation, new lines may need to be constructed at a very high expense [112].

Among various applications of shunt connected FACTS devices on a transmission network, the following are the most significant applications of these devices that have been considered in this thesis.

1.6.1 Voltage Control and Improvement of Steady State Power Transfer Capability over a Long Transmission line.

In a long transmission line, regulation of midpoint voltage helps to increase the steady state power transfer limit. For instance, assuming a lossless long transmission line as shown in Fig. 1.12 (a), the power transferred over the transmission line can be expressed by :

$$P_{12} = \frac{V_1 V_2}{X} \sin \delta . \dots \dots \dots (1.2)$$

Where, V_1 and V_2 are the magnitudes of sending end and receiving end voltages respectively, δ is the angle difference between two voltages, and X is the reactance between the sending and receiving end.

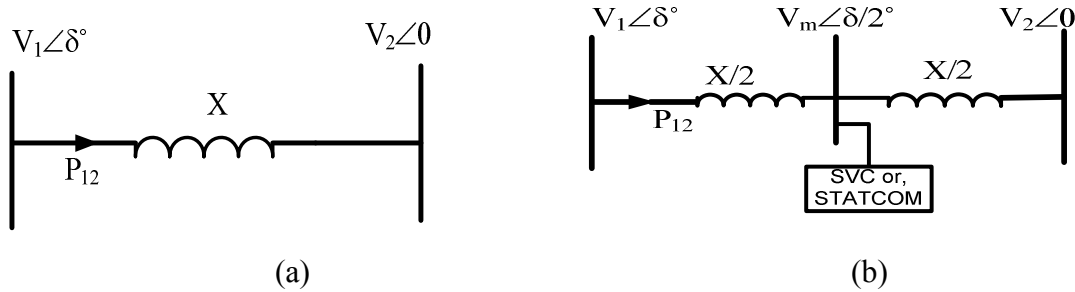


Figure 1.12 Power flow improvement (a) without compensation and (b) with mid-point compensation.

Therefore, for $V_1=V_2=1$ pu, the maximum power transfer over the transmission line is obtained for $\delta=90^\circ$ and at this condition:

$$P_{12_max} = \frac{1}{X} \dots\dots\dots (1.3)$$

In this uncompensated line, for further improvement of power transfer, a parallel transmission line is required to effectively reduce the value of X . Alternately, placement of a shunt FACTS device at the mid-point helps to improve the power flow [65], as demonstrated in Fig. 1.12 (b). In this FACTS device, a compensated system to the power flow equation becomes,

$$P_{12} = \frac{V_1 V_m}{X/2} \sin \delta/2, \dots\dots\dots (1.4)$$

Therefore, for $V_1=V_m=1$ pu, the maximum power transfer over the transmission line is obtained for $\delta=180^\circ$ and at this condition the maximum power flow that can now be achieved becomes [95],

$$P_{12_max} = \frac{2}{X} \dots\dots\dots (1.5)$$

Thus the power transfer limit is increased to twice the capacity of the uncompensated line.

1.6.2 Improvement of Transient Stability and Enhancement of System Damping

The transient stability is limited mainly due to low frequency power oscillation in the power system among which the rotor mode electromechanical oscillation is the significant one, having a frequency oscillation in the band 1-2 Hz. This oscillation can

lead a power system towards instability. This instability can be avoided with the use of a shunt connected FACTS device [95], [113]-[116]:

Consider a single machine infinite bus system as shown in Fig. 1.13, where a shunt FACTS device is connected at the mid-point of the line.

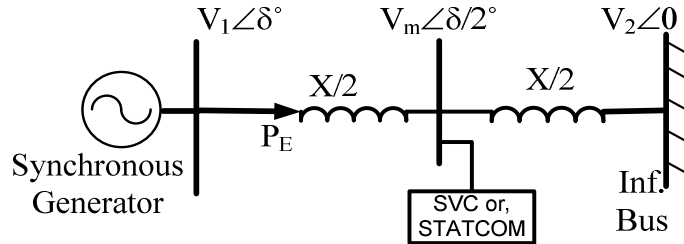


Figure 1.13 Single Machine Infinite Bus (SMIB) system with shunt FACTS devices.

The machine swing equation can be expressed as:

$$M \frac{d^2 \delta}{dt^2} = P_M - P_E \dots\dots\dots (1.6)$$

Here, M is the angular momentum, δ is the generator rotor angle, P_M is the mechanical power and P_E is the electrical power. For a small signal disturbances,

$$M \frac{d^2 \Delta \delta}{dt^2} = \Delta P_M - \Delta P_E \dots\dots\dots (1.7)$$

Considering $\Delta P_M = 0$, since mechanical power input is assumed constant,

$$M \frac{d^2 \Delta \delta}{dt^2} = -\Delta P_E \dots\dots\dots (1.8)$$

For a mid-line compensated system, considering $|V_1|=|V_2|=V$,

$$P_E = \frac{V \cdot V_m}{x/2} \cdot \sin \delta/2. \dots\dots\dots (1.9)$$

For incremental change in electrical power,

$$\Delta P_E = \frac{\partial P_E}{\partial V} \Delta V + \frac{\partial P_E}{\partial V_m} \Delta V_m + \frac{\partial P_E}{\partial \delta} \Delta \delta$$

By considering the sending end voltage constant, i.e., $\Delta V = 0$,

Using equation (1.8) we get,

$$M \frac{d^2 \Delta \delta}{dt^2} + \frac{\partial P_E}{\partial V_m} \Delta V_m + \frac{\partial P_E}{\partial \delta} \Delta \delta = 0 \dots\dots\dots (1.10)$$

This is the expression for small signal dynamic behavior of the system, where the middle term $\frac{\partial P_E}{\partial V_m} \Delta V_m$ is the effect of the FACTS devices. If the FACTS devices are used to

maintain the mid-point voltage V_m strictly constant then, $\Delta V_m = 0$, Hence, the equation (1.10) becomes as follows:

$$M \frac{d^2 \Delta \delta}{dt^2} + \frac{\partial P_E}{\partial \delta} \Delta \delta = 0 \dots\dots\dots (1.11)$$

Or, in Laplace domain,

$$s^2 \cdot \Delta \delta + \frac{1}{M} \cdot \frac{\partial P_E}{\partial \delta} \Delta \delta = 0 \dots\dots\dots (1.12)$$

The characteristic equation becomes,

$$s^2 + \frac{1}{M} \cdot \frac{\partial P_E}{\partial \delta} \Big|_0 = 0 \dots\dots\dots (1.13)$$

Hence the roots are,

$$s = \pm \sqrt{-\frac{1}{M} \cdot \frac{\partial P_E}{\partial \delta} \Big|_0} = \pm j \sqrt{\frac{1}{M} \cdot \frac{\partial P_E}{\partial \delta} \Big|_0} = \pm j \omega_n \dots\dots\dots (1.14)$$

Here, j denotes the imaginary quantity. Therefore, the roots of the characteristic equation lie on the imaginary axis, that results in un-damped oscillations in the rotor angle δ with a frequency of

$$\omega_n = \sqrt{\frac{1}{M} \cdot \frac{\partial P_E}{\partial \delta} \Big|_0} \text{ where, } \frac{\partial P_E}{\partial \delta} \text{ is the synchronizing power coefficient.}$$

Therefore, it is observed that the pure voltage control by the FACTS device does not provide system damping [95]. However, the FACTS device can contribute to the damping by modulating the mid-point voltage instead of keeping it constant. The mid-point voltage is modulated in response to the oscillation in generator rotor as, $\nabla V_m = k \cdot \frac{d(\Delta \delta)}{dt}$ where, k is a constant.

Hence, equation (1.10) can be re-written as follows:

$$M \frac{d^2 \Delta \delta}{dt^2} + \frac{\partial P_E}{\partial V_m} k \cdot \frac{d(\Delta \delta)}{dt} + \frac{\partial P_E}{\partial \delta} \Delta \delta = 0 \dots\dots\dots (1.15)$$

The characteristic equation becomes as,

$$s^2 + s \cdot \frac{k}{M} \cdot \frac{\partial P_E}{\partial V_m} \Big|_0 + \frac{1}{M} \cdot \frac{\partial P_E}{\partial \delta} \Big|_0 = 0 \dots\dots\dots (1.16)$$

$$\text{Or, } s^2 + 2\xi s + \omega_n^2 = 0 \dots\dots\dots (1.17)$$

Hence, the roots become:

$$s = \frac{-2\xi \pm \sqrt{4\xi^2 - 4\omega_n^2}}{2} \dots\dots\dots (1.18)$$

It is clearly evident that the roots lie on the left half of the s plane and the oscillations damp out exponentially, where the damping ratio can be expressed as $\xi = \frac{k}{2.M} \cdot \frac{\partial P_E}{\partial V_m} \Big|_0$

However, to modulate the mid-point voltage various signals can be used as auxiliary signals that reflect the rotor mode oscillation [95]. The main criterion for choosing this signal is to have a better observation as well as good controllability [95],[96]. The following signals can be used to modulate the mid-point voltage:

A) Local signals:

Line current, Real power flow, Reactive power flow, Bus frequency, Bus voltage/angle.

B) Remote signals (synthesized/telecommunicated):

Rotor angle/speed deviation of a remote generator, angle or frequency difference between remote voltages at the two ends of the transmission line.

1.7 Enhanced Utilization of Grid Connected PV Solar System

1.7.1 Nighttime Utilization of PV Solar Farm as STATCOM for Increasing Wind Connectivity

Recent research [57],[117] reported that the PV solar farm can be transformed to act as a STATCOM to increase the connectivity of a neighbouring wind farm during nighttime on a distribution network. This novel concept of PV solar farm control is used to regulate the voltage at PCC during nighttime. The PV solar farm generates power during the day time and provides voltage control during nighttime when it is normally sitting idle.

1.7.2 Line loss Improvement with PV solar farm

Renewable energy sources like Photovoltaic (PV) solar, wind, fuel cell, etc. are connected to the distribution grid as Distributed Generation (DG) sources at different locations in an electrical network. The loads are also distributed on a feeder and the power is supplied to these loads over the network by both conventional generators and

DGs. The flow of current in the lines causes I^2R heating loss due to line resistance. These losses increase as the square of the current. It is always recommended to locate the DGs near the large loads such that, to meet the demand of the load, the whole network is not used to transfer the power; consequently, the line losses are minimized. However, it is not simple to locate DGs close to loads all of the time. Power is always carried over the whole network as DGs only generate a small fraction of the total load demand. For better selection of location and sizing of DGs based on real power generation to minimize the network losses various algorithms have been suggested [118]-[125].

It is also understood that due to the injection of DG real power to the network, the Point of Common Connection (PCC) voltage raises itself [126]-[129] which also helps to reduce the line losses by improving the overall voltage profile along the line. Thus, the PV solar farm, by injecting real power, can indirectly reduce the system losses [130]. Loss reduction through voltage control with a PV solar farm is reported [131] with the use of an external series reactor to provide reactive power. A hybrid system of PV with Fuel Cell (FC) [132] is also able to compensate for the fluctuation in real power generation due to the variability effects of weather on a PV solar system. This is also shown to reduce the network losses by locating the solar system optimally in the network. In addition, it has been demonstrated that network losses can be reduced [133]-[135] by minimizing the voltage fluctuations at the PCC caused by variations of real power output from the PV solar farm, through the use of DG reactive power control.

These papers have considered both power quality in terms of voltage fluctuation and the optimal system losses by a single PV system during only daytime, and also have not addressed the additional internal losses in the inverter due to reactive power support [133]. It is also noticed, that no studies have been reported on the use of multiple PV systems through reactive power compensation for reducing the losses.

1.7.3 Transmission Limits and Damping Enhancement with PV solar farm

A full converter based wind turbine generator has recently been provided with FACTS capabilities for providing improved response during faults and fault ride through

capabilities [136], [137] in a distribution network. Another research is reported to utilize the PV inverter for improving the system stability through the modulation of real power which uses active energy storage devices [107] and is demonstrated for the case of simple load variation. Other papers [138]-[140],[11] have proposed voltage control functionality with PV systems.

Although, it has been reported that the grid connected photovoltaic solar farm has reactive power compensation capability [141], [142]. No research has been reported to enhance the steady state or the transient state power transfer limit of a transmission line with this reactive support capability of PV solar farm.

1.8 Impact of PV System Harmonics in the Network

In a power system, the transmission and distribution lines comprise a combination of resistance, R , inductance, L , and capacitance, C [143]. The combination of L - C of the line can resonate at certain frequencies leading to Network Resonance. The network presents high impedance at these resonant frequencies and these high impedances appear as peaks in the frequency scan of network impedance [144]. Moreover, presence of any capacitors gives rise to additional network resonant modes. Power electronics based generators in the network such as a PV system produce harmonics that are injected into the network [145], [146]. If these injected harmonics match with any one of the resonance peaks, the voltage at that harmonic frequency will be amplified [147]-[149] which may cause failure or damage the customer equipment or protection systems.

A real world case study has been reported for a distribution network [150] which demonstrated the increase of voltage harmonics due to network resonance occurring at low frequencies due to power factor correction capacitors at the substation in the presence of harmonics sources. The network resonance also varies with the loading condition in a transmission and sub-transmission network [151] and with short circuit levels, [152] etc. The impact of a PV solar system on the network is reported in [153]. However, the impact of harmonics generation from a large scale PV solar system has not been reported in literature.

1.9 Motivation of Thesis

- **Basic Model Development of a Grid Connected PV Solar System**

A detailed modeling of the complete PV solar system in electromagnetic transient analysis software, such as EMTDC/PSCAD, is needed to be able to assess its impact on the network. The electrical rating of PV solar panels is mainly dependent upon the manufacturing materials and their physical properties. Many times manufacturers do not disclose detailed physical properties of the PV module, except some electrical quantities like open circuit voltage (V_{oc}), Short Circuit Current (I_{sc}), Maximum Power Point voltage (V_{mpp}) and Current (I_{mpp}), rated power or the maximum Power (P_{mpp}), temperature co-efficient etc. Therefore, to model the PV system comprehensively, it is required to determine other physical parameters, such as series resistance of PV cells (R_s), shunt resistance of PV cells (R_{sh}), or diode ideality factor (n) from these sets of generalized data.

The use of a DC-DC converter based MPPT at the output of a PV panel initiates additional losses and hence, reduces the overall efficiency, whereas, the converter-less MPPT is much more efficient. In EMTDC/PSCAD, implementing the converter-less MPPT with the help of an iteration technique increases the complexity of the model and may enhance the simulation time. The use of graphical approaches that use C++ coding is not user friendly. So, an accurate and efficient user-friendly MPPT implementation technique needs to be developed based on standard library blocks in an EMTDC/PSCAD environment. This has not been disclosed in any literature, so far.

- **Management of Short Circuit Current Contribution from Grid Connected PV Solar Systems**

Solar farms are facing a restriction on their connectivity due to their short circuit current contributions. Also, they need to be disconnected rapidly when a fault is detected in order to conform to technical connection requirements of the utilities. A

better fault current management technique to limit the short circuit current within rated value is therefore needed to ensure effective deployment of solar farms.

- **Novel Controller of PV Solar Farm for New Application in Power System**

The PV system is completely dependent on the sun and, therefore, can generate electricity only during the presence of enough daylight and remains idle during nighttime. It is understood that the PV solar system and a STATCOM both are based on voltage source inverters. Hence, novel controllers' designs could potentially be implemented to transform a PV system into that of a STATCOM to demonstrate new functionalities.

- **Harmonics Impact of a Large Scale Solar Farm**

As discussed earlier, it is important to investigate the potential for network resonance in the presence of harmonics sources and shunt capacitors. In a BWP distribution network, the large scale 80 MW PV solar farm is connected with different feeders which have feeder capacitors, power factor correction capacitors, or load capacitors as well as underground cables. Hence, these feeders need to be modeled and investigated for potential network resonances and harmonic amplification with respect to different network conditions.

1.10 Objective and Scope of the Thesis

The objectives and the scope of the thesis are as follows:

1. To develop a generalized model of PV panels in EMTDC/PSCAD software, regardless of PV module types, size etc. only by knowing the standard parameters provided by the module manufacturers.
2. To develop a fast fault detection technique and to integrate it with the converter based DG systems such that the DGs become disconnected before the peak current exceeds the rated peak value of current due to the fault at any point of the network.

3. To develop novel controls of a PV solar farm as a STATCOM, termed PV-STATCOM for reduction of distribution system loss, prevention of motor load instability, improvement of power transfer capability of a long transmission line through voltage control.
4. To develop novel controls of PV solar farm as STATCOM, termed PV-STATCOM for enhancement of transient stability limit of a typical transmission line through damping control.
5. To determine the potential of harmonic amplification in the BWP distribution network in the presence of a large scale 80 MW PV solar farm. Out of four feeders which connect the large scale solar farm, one of the feeders (18M14) connected to 20 MW solar farm is considered for this study.

1.11 Outline of Chapters

The chapters are organized as follows:

- **Chapter-2:** presents a detailed three phase grid connected PV solar farm modeling technique developed in EMTDC/PSCAD by the use of standard EMTDC/PSCAD library blocks. It includes solar module modeling from manufacturers datasheets, converter-less MPPT modeling, and LCL filter incorporation into conventional grid tied inverter. The simulation results are validated with a commercially available PV solar farm inverter.
- **Chapter-3:** presents a new control concept for fast fault detection on a network and a fault current management technique based on inverter output current magnitude and slope monitoring. The current slope detector and the magnitude detector are developed and incorporated with the conventional solar farm such that a quickest fault detection and best fault management can be achieved. The controller is developed and demonstrated by EMTDC/PSCAD software.

- **Chapter-4:** introduces the innovative concept of PV solar farms to act as a STATCOM, called PV-STATCOM by the utilization of used and unused capacity of the solar farm during both night and day.
- **Chapter-5:** presents one of the novel applications of PV solar farm as PV-STATCOM to improve the distribution line losses through voltage control technique with the remnant reactive power capability of the solar farm at any power generation level of PV solar farm. No PV solar farm generation curtailment is required in this proposed control strategy. The associated control configuration and the network management techniques are proposed by steady state load flow analysis. Finally, a financial analysis is presented to highlight the net loss savings. In this steady state modeling technique, PowerWorld Simulator is used.
- **Chapter-6:** presents another novel operation of a PV solar farm for the prevention of induction motor load instability by using the PV solar farm's used capacity as PV-STATCOM. A load curtailment is required for a very short period of time. In case of any network disturbances, the PV solar farm senses the fault by the developed fast fault detection technique, and disconnects the PV panels. To prevent the motor instability, the PV inverter is immediately turned into a STATCOM and provides voltage support until the motor returns to its nominal operating condition. Once the motor is stabilized, the PV-STATCOM returns to its original solar farm operation. This new controller is developed and demonstrated through EMTDC/PSCAD software.
- **Chapter-7:** demonstrates a novel concept of utilizing a PV solar farm as a PV-STATCOM to enhance the transmission capacity through voltage control and damping control technique. It utilizes the entire solar farm inverter capacity in the night and the remainder inverter capacity after real power generation during the day, both of which remain unused in a conventional solar farm operation. Similar STATCOM control functionality can also be implemented in inverter based wind turbine generators during no-wind or partial wind scenarios for improving the transient stability of the system. Studies are performed for two variants of a Single

Machine Infinite Bus (SMIB) system. One SMIB system uses only a single PV solar farm as PV-STATCOM connected at the midpoint, whereas the other system uses a combination of a PV-STATCOM and another PV-STATCOM or an inverter based wind Distributed Generator (DG) with similar STATCOM functionality. The novel controllers are developed in EMTDC/PSCAD software. Three-phase fault studies are conducted to demonstrate the improvement in stable power transmission limit for different combinations of PV-STATCOM controllers on the solar and wind farm inverters, both during night and day.

- **Chapter-8:** presents a case study of network resonance for a practical utility distribution network connecting a large scale 20 MW PV solar farm. It presents model validation through load flow and SCADA and the network resonance peak through the frequency scan technique for different operating condition of the network. One BWP distribution network feeder 18M14 is studied, connecting 20 MW solar farms. As the feeder 18M14 has reactive power, compensation capacitors on the feeder level and a load capacitor this feeder is studied for potential network resonance peak in detail. The study is accomplished by utilizing SCADA, GIS to construct the network, CYME for load flow validation of the modeled network, and the frequency scan is accomplished in EMTDC/PSCAD. By using the measured data from the large-scale solar farm, the level of voltage distortion is studied for the first time at different times and in worst conditions of the network.
- **Chapter-9:** This chapter concludes the entire thesis, and presents the thesis contribution and recommendation for future work.

Chapter 2

2 Modeling of a Three Phase Grid Connected Photovoltaic (PV) System in EMTDC/PSCAD.

2.1 Introduction

In this chapter, a model of the complete grid connected PV solar system is developed along with the solar panel modeling which uses the standard datasheet values as input parameters. The major contribution is the complete development of a converter-less grid connected PV system in EMTDC/PSCAD software by using its available library blocks. This model is general and applicable for any size and type of PV module. The Maximum Power Point Tracking (MPPT) feature is embedded with four quadrant DC-AC converter controller logic to harvest maximum power from the PV panels. As a result, this model can be used to simulate the maximum available power output for any level of solar irradiation and ambient temperature efficiently.

Section 2.2 describes the study system and modeling of the system. Section 2.3 presents various simulation results for different levels of power output of the solar farm [154]. Section 2.4 concludes the chapter.

2.2 System Model

2.2.1 System Description

The single line diagram of a simple study system is depicted in Fig. 2.1.

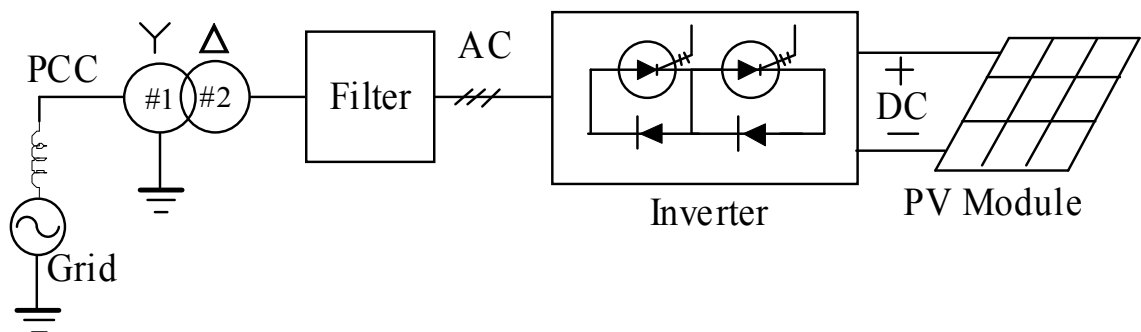


Figure 2.1 Single line diagram of grid connected PV system

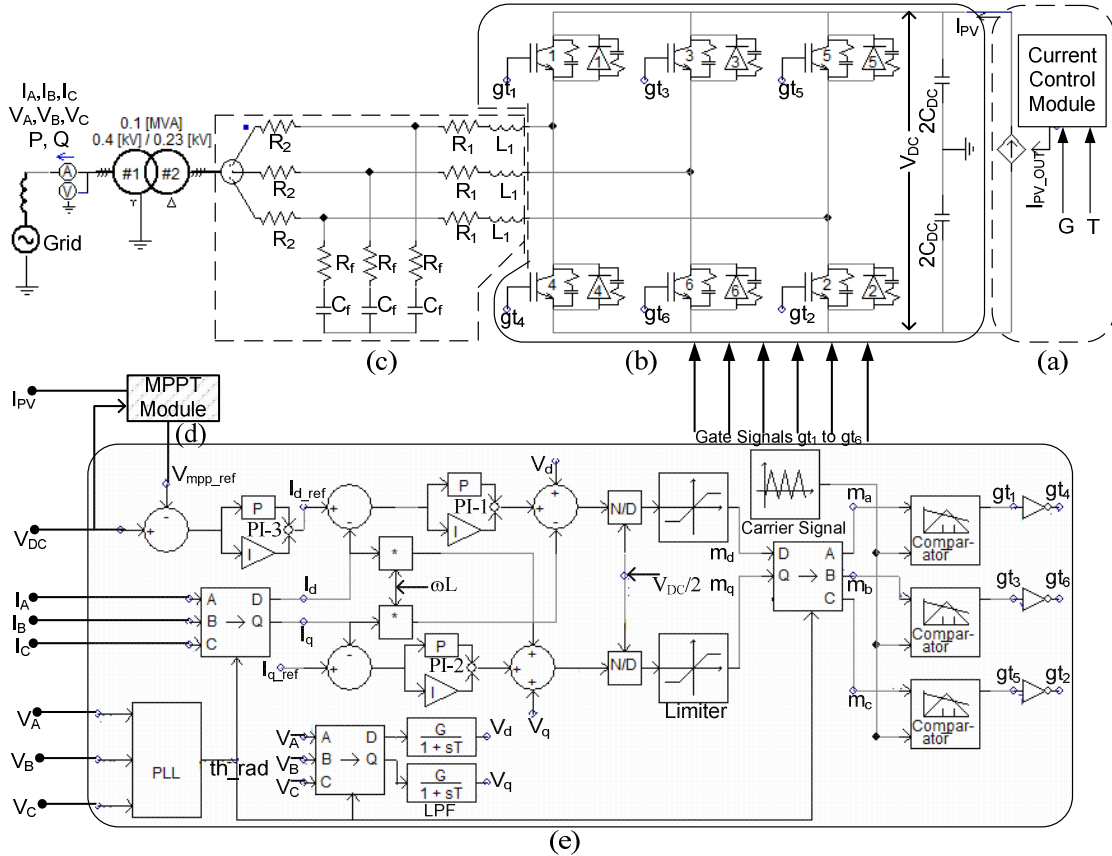


Figure 2.2 Detailed system model (a) PV source (b) IGBT inverter (c) filter (d) MPPT module and (e) inverter switching signal controller.

The study system is comprised of a 100 kW PV solar farm having MPPT capability connected through a transformer with the equivalent grid representation of the distribution network [155]. In this study, the solar farm is connected through the point-of-common-coupling (PCC) to the grid of 400 Volt systems. The short circuit impedance of the grid is considered to be 0.009Ω [155]. The coupling transformer is configured as Δ -Y, grounded with a turn ratio of 1:1. The Δ side of the transformer is connected with the inverter side, as shown in Fig. 2.1. The voltage at the output side of the inverter is 230 V. The PV module is capable of generating a DC voltage of up to 887 Volts [154]. The MPPT can vary the voltage over a wide range of reference values depending upon the solar irradiation. In this study, although the PV system is connected to a specific network [155], the PV system model developed here is general. The detailed system is presented in Fig. 2.2 and described in subsequent sections.

2.2.2 PV Source Model

The equivalent circuit model [7] of a PV cell is shown in Fig. 2.3 (a) where, G denotes the solar irradiation, T is the temperature, R_s is the equivalent series resistance of the cell, and R_{sh} is the equivalent shunt resistance of the cell.

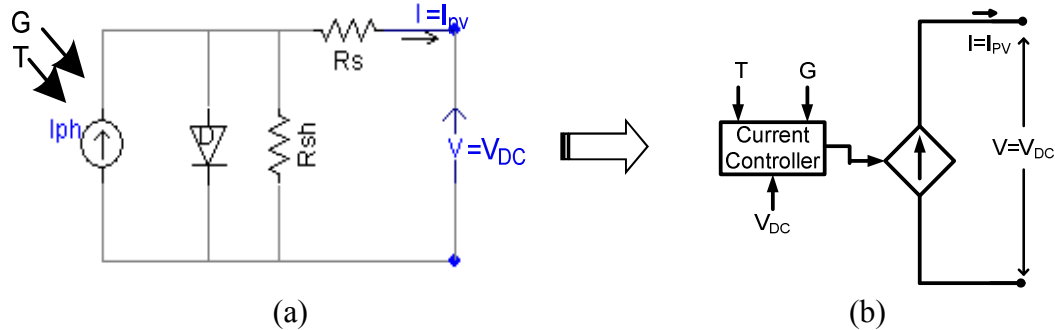


Figure 2.3 Circuit model of PV Source and its equivalent representation in EMTDC/PSCAD.

In this equivalent representation, generally the resistance R_s , R_{sh} are not provided by the manufacturer's datasheet, which is given in the form of Table-2.1 [154] where, Standard Test Condition (STC) is defined as the solar irradiation of 1000W/m^2 equivalently 1 Sun at 25°C . Additional datasheets are available in Appendix A. Therefore, the objective of this section is to determine a general expression to obtain parameters R_s and R_{sh} to be able to perform simulation studies.

Table 2.1 FS 272 PV module electrical specification at STC* and at 45°C , 0.8 Sun.

Item Description	Symbols	AT STC	AT 45°C , 0.8 Sun
Nominal Power ($\pm 5\%$)	P_{MPP} (Watt)	72.5	54.4
Voltage at P_{MPP}	V_{ms} (Volt)	66.6	62.4
Current at P_{MPP}	I_{ms} (Amp)	1.09	0.87
Open Circuit Voltage	V_{OC} (Volt)	88.7	82.5
Short Circuit Current	I_{SC} (Amp)	1.23	1.01
Temperature Co-efficient of P_{MPP}	K_p ($\%/^\circ\text{C}$)	-0.25	
Temperature Co-efficient of V_{OC} High temp $>25^\circ\text{C}$	K_v ($\%/^\circ\text{C}$)	-0.25	
Temperature Coefficient of V_{OC} Low Temp (-40°C to $+25^\circ\text{C}$)	K_v ($\%/^\circ\text{C}$)	-0.20	
Temperature Coefficient of I_{SC}	K_i ($\%/^\circ\text{C}$)	0.04	
Cell Type	CdS/CdTe with 116 active cells.		

* At STC, AM=1.5, $T=25^\circ\text{C}$ and $G=1000\text{ watt/m}^2=1\text{Sun}$ and all ratings $\pm 10\%$, unless specified otherwise.

As discussed in Section 1.2.2, researchers have either neglected both R_s and R_{sh} [19] or R_{sh} [13] only, which reduces the accuracy. Determination of both R_s and R_{sh} through complex iteration technique [14]-[17] may not converge at all times. It is noted that in the determination of the value of R_s and R_{sh} , another parameter named diode ideality factor n , needs to be known [14]-[17], and is not provided by the manufacturer's datasheet.

The model developed below overcomes the above discrepancies. A non-iterative technique has been developed to obtain both R_{sh} and R_s by using the datasheet values given in Table 2.1 and thereby ensuring simplicity and accuracy. In addition, a simple procedure is discussed to obtain n also by using the manufacturer datasheet.

The PV solar farm model is developed for use with EMTDC/PSCAD. For this purpose the circuit model given in Fig. 2.3 (a) is transformed into a controlled current source [10] as presented in Fig. 2.3(b). The current control block embeds all the current equations implemented with the use of EMTDC/PSCAD standard library blocks to determine the current output of the controlled current source according to its terminal voltage. It is noted that the output current from the controlled current source is the current at the terminal of PV circuit model as shown in Fig. 2.3 (a). The equations are derived as below:

The relationship between voltage and current with respect to different solar irradiations and temperatures for a standard PV source can be expressed by a set of basic diode equations [15]:

$$I = I_{ph} - I_0 \left[e^{q(V+IR_s)/nkTn_s} - 1 \right] - \frac{V + IR_s}{n_s R_{sh}} \dots\dots\dots (2.1)$$

where, V and I are the output voltage and current of the PV cell at any temperature and radiation, respectively. In this equation, for an equivalent single string panel, n_s is the number of series cells in the string, R_s is the total series resistance of the string expressed in ohm, k is the Boltzmann's constant, n is the diode ideality factor, q is the charge of electron expressed in 'coulomb', R_{sh} is the leakage or shunt resistance expressed in ohm, I_0 is the reverse saturation current, T is the temperature in °K, and I_{ph} is the photo current, as depicted in Fig. 2.3 (a).

The photo current, I_{ph} , is a direct function of solar radiation, G , and can be expressed as [15]:

$$I_{ph} = I_{ph(STC)} \frac{G}{G_{nom}} \dots\dots\dots (2.2)$$

where, $I_{ph(STC)}$, is the photocurrent at standard insolation level, G_{nom} .

The reverse saturation current I_0 is a function of temperature and is usually expressed with the equation containing the energy band gap function, V_g [12], [8].

$$I_0 = I_0(T_s) \cdot \left(\frac{T}{T_s}\right)^{\frac{3}{n}} \cdot e^{\frac{-qV_g\{1+K_v(T_2-T_s)\}}{n.k.T_s.T_2.n_s}} \dots\dots\dots (2.3)$$

Here, T_s is the temperature at STC and T_2 is other operating temperature. However, this energy band gap is yet another unknown parameter and depends upon the manufacturing material and process. However, at STC; $T=T_s$, $G=G_{nom}$, $I_0=I_0(STC)$, and $I_{ph}=I_{ph(STC)}$. Applying two conditions in (2.1) i.e., (i) short circuit condition where $V=0$ and $I=I_{sc}$ and (ii) open circuit condition where $I=0$ and $V=V_{oc}$ we get:

$$I_{sc} = I_{ph(STC)} - I_0(STC) \left[e^{q(I_{sc}R_s)/nkT_s n_s} - 1 \right] - \frac{I_{sc}R_s}{n_s R_{sh}} \dots\dots\dots (2.4)$$

and,

$$0 = I_{ph(STC)} - I_0(STC) \left[e^{qV_{oc}/nkT_s n_s} - 1 \right] - \frac{V_{oc}}{n_s R_{sh}}$$

$$\text{or, } I_{ph(STC)} = I_0(STC) \left[e^{qV_{oc}/nkT_s n_s} - 1 \right] - \frac{V_{oc}}{n_s R_{sh}} \dots\dots\dots (2.5)$$

Substituting, the value of $I_{ph(STC)}$, in (2.4), we get,

$$I_{sc} = I_0(STC) \left[e^{qV_{oc}/nkT_s n_s} - 1 \right] - \frac{V_{oc}}{n_s R_{sh}} - I_0(STC) \left[e^{q(I_{sc}R_s)/nkT_s n_s} - 1 \right] - \frac{I_{sc}R_s}{n_s R_{sh}}$$

$$\text{or, } I_0(STC) = \frac{I_{sc}n_s R_{sh} + I_{sc}R_s - V_{oc}}{n_s R_{sh} (e^{qV_{oc}/nkT_s n_s} - e^{qI_{sc}R_s/nkT_s n_s})} \dots\dots\dots (2.6)$$

In this procedure, no energy band gap information is required to determine I_0 .

Now using (2.5) in (2.2), the expression of photo current I_{ph} can be obtained as follows:

$$I_{ph} = \left[I_{0(STC)} (e^{qV_{oc}/nkTn_s} - 1) + \frac{V_{oc}}{n_s R_{sh}} \right] \frac{G}{G_{nom}} \dots\dots\dots (2.7)$$

It is noted that the short circuit current I_{sc} and open circuit voltage V_{oc} can be expressed in terms of temperature coefficient to relate them with the quantities at STC as follows [15]:

$$I_{sc} = I_{sc(STC)} \{1 + K_i(T - T_s)\} \dots\dots\dots (2.8)$$

$$V_{oc} = V_{oc(STC)} \{1 + K_v(T - T_s)\} \dots\dots\dots (2.9)$$

Here, K_i is the temperature coefficient of PV short circuit current and K_v is the temperature coefficient of PV open circuit voltage at STC. Both are expressed in %/°C. T_s is the standard temperature at STC, G_{nom} is the solar radiation at STC. Now substituting (2.6)-(2.9) in (2.1), the final expression of the PV output current becomes as follows:

$$I = \frac{\left[I_{sc(STC)} \{1 + K_i(T - T_s)\} \{n_s R_{sh} + R_s\} - V_{oc} \right] \left[e^{\frac{qV_{oc(STC)} \{1 + K_v(T - T_s)\}}{nkTn_s}} - 1 \right] G}{n_s R_{sh} \left[e^{\frac{qV_{oc(STC)} \{1 + K_v(T - T_s)\}}{nkTn_s}} - e^{\frac{qI_{sc(STC)} \{1 + K_i(T - T_s)\} R_s}{nkTn_s}} \right] G_{nom} - \frac{\left[I_{sc(STC)} \{1 + K_i(T - T_s)\} \{n_s R_{sh} + R_s\} - V_{oc} \right] \left[e^{\frac{q(V + IR_s)}{nkTn_s}} - 1 \right]}{n_s R_{sh} \left[e^{\frac{qV_{oc(STC)} \{1 + K_v(T - T_s)\}}{nkTn_s}} - e^{\frac{qI_{sc(STC)} \{1 + K_i(T - T_s)\} R_s}{nkTn_s}} \right]}} + \frac{GV_{oc}}{n_s R_{sh} G_{nom}} - \frac{V + IR_s}{n_s R_{sh}} \dots\dots\dots (2.10)$$

This is the final expression for the output current of the controlled current source in which, once R_s , R_{sh} and n are determined, the output current I denoted as I_{pv} in the circuit can be obtained. The current I is dependent upon the solar irradiation, G , temperature, T and its terminal voltage, V denoted as V_{DC} in the circuit.

- **Determination of shunt resistance (R_{sh}) and series resistance (R_s):**

To determine these parameters, an STC case is considered, as they do not vary significantly with different temperature and insolation. In (2.10) it is assumed that,

$$e^{\frac{qI_{sc(STC)} \{1 + K_i(T - T_s)\} R_s}{nkTn_s}} \cong 1 \dots\dots\dots (2.11)$$

This assumption is validated as below.

It is observed that the magnitude of the exponent will be high, which is the worst case, if the value of n is low and the value of R_s is high with a large temperature difference from the STC. Usually, the temperature variation is considered as $T_s \pm 50^\circ C$ where $T_s = 25^\circ C$. Considering the diode to be ideal gives the lowest value of $n=1$ [156]. As the value of R_s is not yet determined an approximate value of maximum R_s is chosen. In I-V characteristic curve the slope at V_{oc} determines the approximate value of R_s [18]. Therefore, it is justified to make an approximation of R_s by the expression, $R_s = (V_{oc} - V_{mpp})/I_{mpp}$, which calculates an optimistic value of R_s as demonstrated in Appendix-A. By using the parameters given in Table-1, the approximate maximum value of R_s is found as 0.175Ω . Therefore, for the worst case scenario, the left side of (2.11) is calculated as 1.065, which is very close to 1.0 and thus the assumption is justified.

Therefore, the term,

$$\frac{\left[e^{\frac{qV_{oc}(STC)\{1+K_v(T-T_s)\}}{nkTn_s}} - 1 \right]}{\left[e^{\frac{qV_{oc}(STC)\{1+K_v(T-T_s)\}}{nkTn_s}} - e^{\frac{qI_{sc}(STC)\{1+K_i(T-T_s)\}R_s}{nkTn_s}} \right]} \dots\dots\dots (2.12)$$

can be approximated as unity. At STC, by replacing T by T_s and G by G_{nom} , and using the above approximation, (2.10) can be approximated as follows:

$$I = \frac{[I_{sc}(STC)\{n_s R_{sh} + R_s\} - V_{oc}(STC)]}{n_s R_{sh}} - \frac{[I_{sc}(STC)\{n_s R_{sh} + R_s\} - V_{oc}(STC)] \left[e^{\frac{q(V+IR_s)}{nkTn_s}} - 1 \right]}{n_s R_{sh} \left[e^{\frac{qV_{oc}(STC)}{nkTn_s}} - 1 \right]} - \frac{V + IR_s}{n_s R_{sh}} \dots (2.13)$$

Therefore, the expression for shunt resistance can be derived by using the fact that at maximum power point (MPP) the derivative of power with respect to voltage is zero.

As we know, power $P = VI$. Therefore,

$$\frac{\partial P}{\partial V} = I + V \frac{\partial I}{\partial V} = 0|_{at\ mpp} \dots\dots\dots (2.14)$$

Hence, differentiating (2.13), we get:

$$\frac{\partial I}{\partial V} = - \frac{[I_{sc(StC)}\{n_s R_{sh} + R_s\} - V_{oc(StC)}] \left[e^{\frac{q(V+IR_s)}{nkT_s n_s}} \right] \left\{ \frac{q \left(1 + R_s \frac{\partial I}{\partial V} \right)}{nkT_s n_s} \right\}}{n_s R_{sh} \left[e^{\frac{qV_{oc(StC)}}{nkT_s n_s}} - 1 \right]} - \frac{1 + R_s \frac{\partial I}{\partial V}}{n_s R_{sh}}$$

Or,

$$\begin{aligned} \frac{\partial I}{\partial V} \left[1 + \frac{R_s}{n_s R_{sh}} + \frac{[I_{sc(StC)}\{n_s R_{sh} + R_s\} - V_{oc(StC)}] \left[e^{\frac{q(V+IR_s)}{nkT_s n_s}} \right] \left\{ \frac{q R_s}{nkT_s n_s} \right\}}{n_s R_{sh} \left[e^{\frac{qV_{oc(StC)}}{nkT_s n_s}} - 1 \right]} \right] \\ = - \frac{[I_{sc(StC)}\{n_s R_{sh} + R_s\} - V_{oc(StC)}] \left[e^{\frac{q(V+IR_s)}{nkT_s n_s}} \right] \left\{ \frac{q}{nkT_s n_s} \right\}}{n_s R_{sh} \left[e^{\frac{qV_{oc(StC)}}{nkT_s n_s}} - 1 \right]} - \frac{1}{n_s R_{sh}} \end{aligned}$$

Or,

$$\begin{aligned} \frac{\partial I}{\partial V} \left[(n_s R_{sh} + R_s) \left[e^{\frac{qV_{oc(StC)}}{nkT_s n_s}} - 1 \right] \right. \\ \left. + [I_{sc(StC)}\{n_s R_{sh} + R_s\} - V_{oc(StC)}] \left[e^{\frac{q(V+IR_s)}{nkT_s n_s}} \right] \left\{ \frac{q R_s}{nkT_s n_s} \right\} \right] \\ = - [I_{sc(StC)}\{n_s R_{sh} + R_s\} - V_{oc(StC)}] \left[e^{\frac{q(V+IR_s)}{nkT_s n_s}} \right] \left\{ \frac{q}{nkT_s n_s} \right\} \\ - \left[e^{\frac{qV_{oc(StC)}}{nkT_s n_s}} - 1 \right] \end{aligned}$$

Or,

$$\frac{\partial I}{\partial V} = \frac{-[I_{sc}(STC)\{n_s R_{sh} + R_s\} - V_{oc}(STC)] \left[e^{\frac{q(V+IR_s)}{nkT_s n_s}} \left\{ \frac{q}{nkT_s n_s} \right\} - \left[e^{\frac{qV_{oc}(STC)}{nkT_s n_s}} - 1 \right] \right]}{\left[(n_s R_{sh} + R_s) \left[e^{\frac{qV_{oc}(STC)}{nkT_s n_s}} - 1 \right] + [I_{sc}(STC)\{n_s R_{sh} + R_s\} - V_{oc}(STC)] \left[e^{\frac{q(V+IR_s)}{nkT_s n_s}} \left\{ \frac{qR_s}{nkT_s n_s} \right\} \right] \right]}$$

Putting into (2.14) and equating at MPP, we get:

$$\frac{[I_{sc}(STC)\{n_s R_{sh} + R_s\}]}{n_s R_{sh}} = \frac{[I_{sc}(STC)\{n_s R_{sh} + R_s\} - V_{oc}(STC)] \left\{ e^{\frac{q(V_m+I_m R_s)}{nkT_s n_s}} - 1 \right\}}{n_s R_{sh} \left\{ e^{\frac{qV_{oc}(STC)}{nkT_s n_s}} - 1 \right\}}$$

$$= \frac{\frac{V_m + I_m R_s}{n_s R_{sh}}}{\frac{V_m [I_{sc}(STC)\{n_s R_{sh} + R_s\} - V_{oc}(STC)] \left\{ e^{\frac{q(V_m+I_m R_s)}{nkT_s n_s}} \left\{ \frac{q}{nkT_s n_s} \right\} + V_m \left\{ e^{\frac{qV_{oc}(STC)}{nkT_s n_s}} - 1 \right\} \right\}}{\left[(n_s R_{sh} + R_s) \left\{ e^{\frac{qV_{oc}(STC)}{nkT_s n_s}} - 1 \right\} + [I_{sc}(STC)\{n_s R_{sh} + R_s\} - V_{oc}(STC)] \left\{ e^{\frac{q(V_m+I_m R_s)}{nkT_s n_s}} \left\{ \frac{qR_s}{nkT_s n_s} \right\} \right]}}$$

where, V_m and I_m are the maximum power point voltage and current at STC, respectively.

Simplifying the above expression for R_{sh} at STC is obtained as follows:

$$R_{sh} = \frac{[I_{sc}(STC)R_s - V_{oc}(STC)] \left[e^{\frac{q(V_m+I_m R_s)}{nkT_s n_s}} - 1 \right] \frac{q}{n_s T_s k n} + \left[e^{\frac{qV_{oc}(STC)}{nkT_s n_s}} - 1 \right]}{\left[n_s I_m \left\{ e^{\frac{qV_{oc}(STC)}{nkT_s n_s}} - 1 \right\} \right] / (V_m - I_m R_s) - \left[e^{\frac{q(V_m+I_m R_s)}{nkT_s n_s}} - 1 \right] \frac{q I_{sc}(STC)}{T_s k n}} \dots \dots (2.15)$$

Now, to deduce the expression of R_s , the leakage current component in (2.1), $(V+IR_s)/n_s R_{sh}$, can be neglected as the current flowing through the leakage resistance, R_{sh} , is very small. Therefore, at STC using $T=T_s$ and $G=G_{nom}$, $I_0=I_0(STC)$, and $I_{ph}=I_{ph}(STC)$, (2.1) can be re-written as:

$$I = I_{ph}(STC) - I_0(STC) \left[e^{q(V+IR_s)/nkT_s n_s} - 1 \right] \dots \dots \dots (2.16)$$

Again, applying short circuit condition and open circuit condition at STC, we get,

$$I_{sc} = I_{ph(STC)} - I_{0(STC)} \left[e^{q(I_{sc}R_s)/nkT_s n_s} - 1 \right] \dots \dots \dots (2.17)$$

And,

$$0 = I_{ph(STC)} - I_{0(STC)} \left[e^{qV_{oc}/nkT_s n_s} - 1 \right]$$

$$\text{or, } I_{ph(STC)} = I_{0(STC)} \left[e^{qV_{oc}/nkT_s n_s} - 1 \right] \dots \dots \dots (2.18)$$

Substituting, the value of $I_{ph(STC)}$, in (2.17) at STC, we get,

$$I_{sc(STC)} = I_{0(STC)} \left[e^{qV_{oc(STC)}/nkT_s n_s} - 1 \right] - I_{0(STC)} \left[e^{q(I_{sc(STC)}R_s)/nkT_s n_s} - 1 \right]$$

$$\text{or, } I_{0(STC)} = \frac{I_{sc(STC)}}{\left(e^{qV_{oc(STC)}/nkT_s n_s} - e^{qI_{sc(STC)}R_s/nkT_s n_s} \right)} \dots \dots \dots (2.19)$$

Therefore, substituting (2.19) into (2.18) we get:

$$\text{or, } I_{ph(STC)} = \frac{I_{sc(STC)} \left[e^{qV_{oc(STC)}/nkT_s n_s} - 1 \right]}{\left(e^{qV_{oc(STC)}/nkT_s n_s} - e^{qI_{sc(STC)}R_s/nkT_s n_s} \right)} \dots \dots \dots (2.20)$$

Putting the expression (2.19) and (2.20) into (2.16), we get,

$$I = I_{ph(STC)} - I_{0(STC)} \left[e^{q(V+IR_s)/nkT_s n_s} - 1 \right]$$

$$\text{Or, } I = \frac{I_{sc(STC)} \left[e^{qV_{oc(STC)}/nkT_s n_s} - 1 \right]}{\left(e^{qV_{oc(STC)}/nkT_s n_s} - e^{qI_{sc(STC)}R_s/nkT_s n_s} \right)} - \frac{I_{sc(STC)} \left[e^{q(V+IR_s)/nkT_s n_s} - 1 \right]}{\left(e^{qV_{oc(STC)}/nkT_s n_s} - e^{qI_{sc(STC)}R_s/nkT_s n_s} \right)}$$

Simplifying further with the assumption shown in (2.11), we get,

$$I \approx I_{sc(STC)} - \frac{I_{sc(STC)} \left[e^{\frac{q(V+IR_s)}{nkT_s n_s}} - 1 \right]}{\left[e^{\frac{qV_{oc(STC)}}{nkT_s n_s}} - 1 \right]} \dots \dots \dots (2.21)$$

From this expression, by applying the MPP operating condition at STC, by putting $V=V_m$ and $I=I_m$, the expression becomes:

$$\frac{I_m}{I_{sc(STC)}} \left[e^{\frac{qV_{oc(STC)}}{nkT_s n_s}} - 1 \right] = \left[e^{\frac{qV_{oc(STC)}}{nkT_s n_s}} - 1 \right] - \left[e^{\frac{q(V_m+I_mR_s)}{nkT_s n_s}} - 1 \right]$$

Or,

$$\frac{I_m}{I_{sc}(STC)} \left[e^{\frac{qV_{oc}(STC)}{nkT_s n_s}} - 1 \right] = \left[e^{\frac{qV_{oc}(STC)}{nkT_s n_s}} - e^{\frac{q(V_m + I_m R_s)}{nkT_s n_s}} \right]$$

Or,

$$e^{\frac{q(V_m + I_m R_s)}{nkT_s n_s}} = e^{\frac{qV_{oc}(STC)}{nkT_s n_s}} - \frac{I_m}{I_{sc}(STC)} \left[e^{\frac{qV_{oc}(STC)}{nkT_s n_s}} - 1 \right]$$

Or,

$$\frac{q(V_m + I_m R_s)}{nkT_s n_s} = \ln \left[e^{\frac{qV_{oc}(STC)}{nkT_s n_s}} - \frac{I_m}{I_{sc}(STC)} \right]$$

Or,

$$(V_m + I_m R_s) = \frac{nkT_s n_s}{q} \ln \left[e^{\frac{qV_{oc}(STC)}{nkT_s n_s}} - \frac{I_m}{I_{sc}(STC)} \left\{ e^{\frac{qV_{oc}(STC)}{nkT_s n_s}} - 1 \right\} \right]$$

Therefore, R_s is found as follows:

$$R_s = \frac{n_s T_s k n}{q I_m} \ln \left[e^{\frac{qV_{oc}(STC)}{nkT_s n_s}} - \frac{I_m}{I_{sc}(STC)} \left\{ e^{\frac{qV_{oc}(STC)}{nkT_s n_s}} - 1 \right\} \right] - \frac{V_m}{I_m} \dots\dots\dots (2.22)$$

• **Determination of diode ideality factor n :**

It is obvious from output current expression (2.10), shunt resistance R_{sh} expression (2.15), and series resistance R_s expression (2.22) that all are dependent upon the value of diode ideality factor n which differs based on cell type mainly due to the manufacturing process [157]-[159]. Depending upon the value of n , the maximum power point varies [160]. Hence, the value of n is determined such that it satisfies the maximum power point voltage and current. It is noted that the determination of n is done only once for a specific datasheet. Therefore, no repetitive iterative technique is needed while running the simulation for different operating levels. The following technique is used to determine n .

A simple DC circuit is constructed as shown in Fig. 2.4.

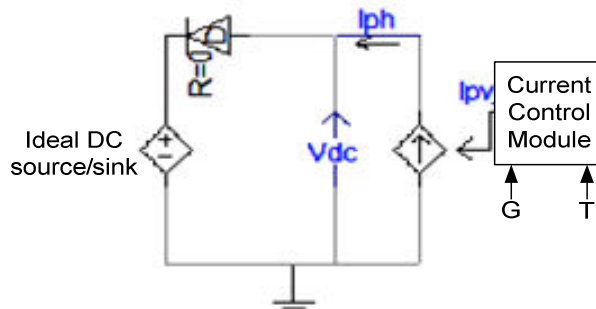


Figure 2.4 DC circuit to determine diode ideality factor, n .

In this Fig. 2.4, the controlled current source shown in Fig 2.3 (b) is connected with an ideal DC source which also acts as a current sink. In the current control module of the controlled current source as shown in Fig. 2.4, expressions (2.10), (2.15) and (2.22) are implemented with the use of EMTDC/PSCAD standard library blocks as shown in Fig. 2.5 by using the ideal value of $n=1$ at initial step.

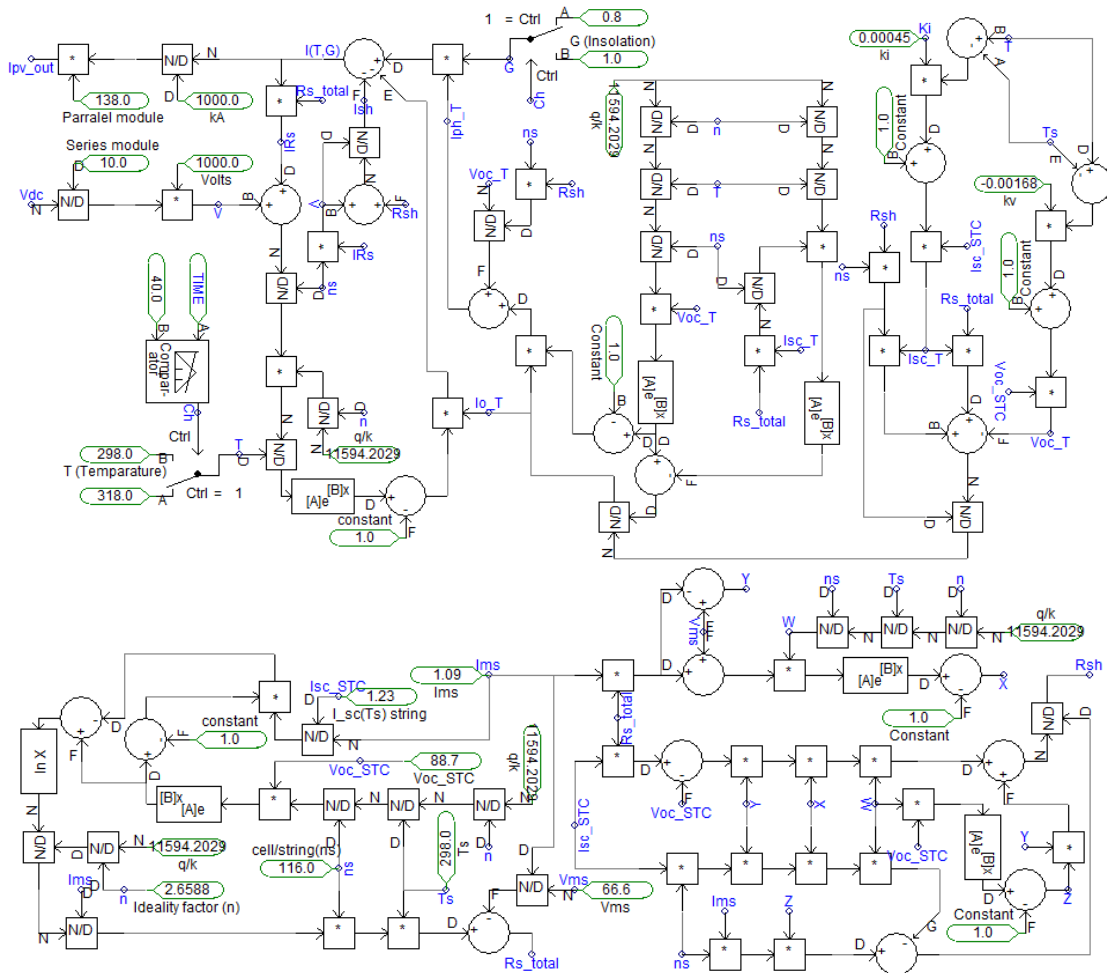


Figure 2.5 'PV Source' building blocks in EMTDC/PSCAD

The ideal DC voltage source is set for V_{mpp} at STC. Now the value of n is increased slowly and the output current is measured to verify if $I_{ph}=I_{mpp}$. When the I_{mpp} corresponding to V_{mpp} matches with the datasheet value for a certain value of n , this value of n is recorded as the actual value of diode ideality factor for that specific PV module datasheet. Thus n is determined accurately through a simulation process by matching V_{mpp} and I_{mpp} at STC. Since n influences the value of R_s and R_{sh} as seen in (2.22) and (2.15), the values of R_s and R_{sh} also become very accurate.

Once the actual value of n is determined by using the above mentioned procedure, the PV module in Fig. 2.2 (a) is modeled by implementing the same blocks as shown in Fig 2.5, but with the actual determined value of n . Therefore, the PV module, modeled as controlled current source in Fig. 2.2(a), generates the desired current output I_{PV} by taking the feedback of its terminal voltage V_{DC} corresponding to the prevalent solar irradiation and temperature.

2.2.3 Maximum Power Point Tracking (MPPT)

The incremental conductance algorithm [161] is utilized to get the reference voltage for MPPT. This algorithm is shown by the flowchart in Fig. 2.6. This MPPT algorithm is implemented in EMTDC/PSCAD software with the mathematical and logical blocks available in the software library, as shown in Fig. 2.7. The MPPT algorithm monitors the change in current and voltage at PV module output with a certain time interval known as sampling time.

In the algorithm presented in Fig. 2.6, two cases are observed while monitoring the change in DC voltage. The first case is when there is no change in voltage, and the second case is when there is a change in voltage.

For first case when there is no change in voltage it examines the change in current. If the change in current is zero then the algorithm assumes that the PV module is already operating at Maximum Power Point (MPP). Therefore, there is no voltage step change. But, if the change in current is a non-zero value then the algorithm assumes that the PV modules are not operating at MPP. Therefore, a small step change in voltage is applied depending upon the +ve or -ve change in current [161]. Due to the change in voltage at the module output the current output from the module also changes. This process continues until the PV module reaches its MPP operating condition.

For the second case, when there is a change in voltage, it examines the relationship $\frac{dI}{dV} = -\frac{I_{PV}}{V_{DC}}$ [161]. If the relationship is satisfied, the algorithm assumes that there is a change in the level of insolation and temperature, but the PV modules are operating at MPP. Therefore, no changes in operating point are required. But, if the relationship is not

satisfied, the PV module is not operating at MPP. Therefore, a small step change in voltage is applied, which changes the current output of the PV module. In this case, as in the first case, the process continues until the MPP operating condition is reached.

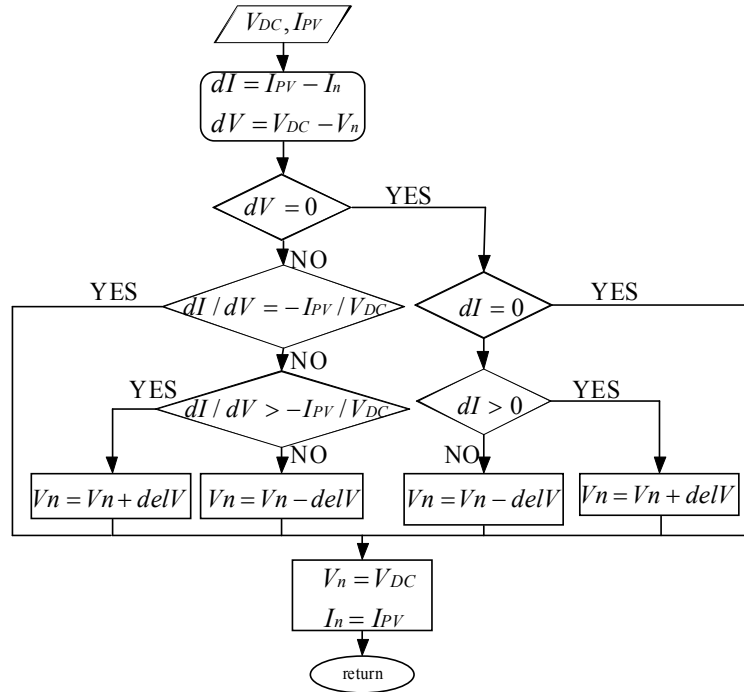


Figure 2.6 Incremental conductance algorithm flowchart for MPPT.

To implement the above algorithm in EMTDC/PSCAD, the sampling time is given in the form of time delay as shown in Fig. 2.7. The PV module output current I_{ph} is compared with the previously sampled output current through a subtraction block S1 to monitor the change in current. Similarly, the change in voltage in V_{dc} is monitored with other subtraction block S2. On the other hand, the ratios of dI/dV and I_{ph}/V_{dc} are compared with another subtraction block S3 which gives an output of 'e' and is passed through a band comparator B3. The outputs S1 and S2 are passed through band comparators B1 and B2, respectively. The band comparators gives +1 output when the input is more +ve value than the upper +ve limit, -ve output when the input is more -ve then the lower -ve limit, and zero output when the input lies within upper +ve and lower -ve limits [165]. However, when there is no change in DC voltage, for example, in the first case as discussed in the algorithm, the output of B2 becomes zero, which inverts to 1 and multiplies with the output of B1. Now, if the change in current is zero, the output of B1

will also be zero. Therefore, there will be no change at the output, V_{mpp_ref} . But if the output of B1 is a non-zero value, either +1 or -1, the voltage step $\text{del}V$ will be added or subtracted with the previously sampled value and will appear at V_{mpp_ref} . It is noted that in this case the output of B3 will be multiplied with zero as the output of B2 is zero, as shown in Fig. 2.7.

If the change in voltage is not zero, as noted in the second case, and discussed in the algorithm, the output of B2 will be 1 after passing through $|X|$ block. It will allow the output of B3 to go at the output, V_{mpp_ref} . On the other hand, the inverted output of B2 will nullify the output of B1. Therefore, in this case, depending upon the output of B3, the change in voltage step will be applied to V_{mpp_ref} . In this MPPT modeling, the sampling time given as a time delay is considered as 0.2 sec and the voltage step is considered as 5 V to get an acceptable output in terms of speed and accuracy. It is noted that V_{mpp_ref} acts as reference DC voltage of the inverter. Therefore, with the control of inverter DC link voltage regulator the Maximum Power Point Tracking is achieved.

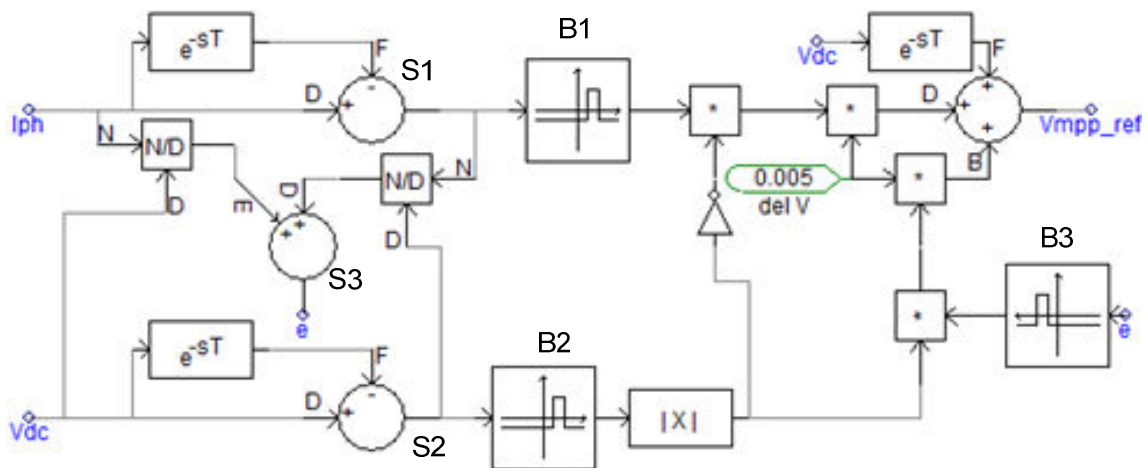


Figure 2.7 MPPT module building blocks for Incremental Conductance algorithm.

2.2.4 Inverter

The inverter is composed of six IGBT devices with associated snubber circuits as shown in Fig. 2.2 (b). This inverter transforms DC power to AC by using sinusoidal pulse width modulation (SPWM) technique [103], [56] which uses a high switching frequency of 5 kHz. This frequency is chosen to avoid excessive switching losses and noise in the

audible range. A series of switching signal pulses of different pulse widths resulting from the comparison between a 5 kHz triangular wave, known as carrier wave, and the sinusoidal modulating signals, are fed from the controller to the inverter. By controlling the modulating signal, the switching pulse width and switching instances can be controlled, which ultimately controls the power output from the inverter [103], [56].

The detailed controller configuration to generate the modulation signals is shown in Fig. 2.2 (e) where two current control loops in a d-q co-ordinate system are used, as explained in section 1.4.2.3. The direct axis current control loop consists of two proportional integral controllers, PI-1 and PI-3. Whereas, the quadrature axis current control loop consists of PI-2 only. The direct axis current control loop maintains the DC link voltage constant around a reference set by the MPPT algorithm in a converter-less MPPT technique. To perform this control function, the DC link voltage, V_{DC} , is compared with the DC voltage reference, V_{mpp_ref} , obtained from MPPT algorithm and is passed through PI-3 controller to obtain the direct axis current control loop reference, I_{d_ref} . The measured AC output current signals I_A , I_B and I_C of the inverter are transformed into a d-q reference frame as a direct axis component, I_d , and quadrature axis component, I_q , as explained in section 1.4.2.3. The direct axis component, I_d , is compared with direct axis reference value of I_{d_ref} and passed through the regulator PI-1 to generate direct axis component of modulation signal, m_d . On the other hand, the quadrature axis current control loop is used to maintain the reactive power output of the inverter around a reference value of zero for unity power factor operation [24],[62]. Therefore, the reference, I_{q_ref} , is set to zero according to the following decoupled power equation at steady state [108].

$$P = V_d I_d \quad \dots\dots\dots (2.23)$$

$$Q = -V_d I_q \quad \dots\dots\dots (2.24)$$

where, P and Q are the real and reactive power output of the inverter, respectively.

The quadrature axis component I_q is regulated through PI-2 controller and generates the quadrature axis component of modulation signal, m_q . It is noted that two limiters are used

to limit the modulation index, $m = \sqrt{m_d^2 + m_q^2}$. The outputs of these current control

loops are transformed back into the ABC reference frame, thereby generating the sinusoidal modulating signals, m_a , m_b and m_c .

A phase locked loop oscillator (PLL) is used for grid synchronization and, therefore, the angle, th_rad , measured from grid voltage is fed into the ABC to the d-q converter. It is noted that while modeling with EMTDC/PSCAD library components, the use of an offset angle of 1.57 rad (90 degree) in the PLL makes the alignment of direct axis component V_d with the voltage vector in ABC frame, V_{ABC} . As a result, the quadrature component of AC voltage V_q can be considered as zero during steady state. Low pass filters are added with d-q voltage transformation to obtain the noise free fundamental measured voltage for feedback.

The corresponding proportional gain, k_p , and integral gain, k_i , in each PI controllers are tuned through simulation process with systematic hit and trial method starting with a base value from the detailed mathematical design procedure of the inverter controller given in Appendix A.

2.2.5 DC Link Capacitor Modeling

As mentioned earlier, the DC link voltage must be maintained constant to achieve high power quality and to minimize the ripples of the PV source current. To fulfill these objectives generally a large size DC link capacitor which is capable of handling maximum power, P_{max} , is used [64]. For maximum power at a frequency f , the total energy for a single cycle is,

$$E_{max} = (P_{max}/f) \dots\dots\dots (2.25)$$

This energy is considered to be supplied by the DC link capacitor in the worst case scenario such that the dc-link voltage does not go below the margin, V_{dcmin} . Therefore, it is expressed by:

$$E_{max} = \frac{1}{2}CV_{dc}^2 - \frac{1}{2}CV_{dcmin}^2 \dots\dots\dots (2.26)$$

By equating (2.25) and (2.26), the size of the DC link capacitor is determined as follows:

$$C = (2P_{max})/[fV_{dc}^2(1 - k^2)] \text{ Farad} \dots\dots\dots (2.27)$$

Where, $k = V_{dc\ min}/V_{dc}$, and is known as ripple factor.

The value of ‘ k ’ is chosen in such a way that the controllability of the source current can be achieved at all operating points through the tuning of inverter controller parameters, k_p and k_i . It is assumed in the determination of the size of DC link capacitor that the output current is ripple free. This assumption is justified as the output power quality is maintained using high switching frequency and AC filter at the output which is discussed in the next section.

2.2.6 AC Filter Modeling

Different filter configurations can be used at the inverter output. Among these, L filter comprised of only series inductor, L-C filter comprised of series inductor with a shunt capacitor, and L-C-L filter comprised of two series inductors at either side of a shunt capacitor in ‘T’ configuration are used widely [35]. Due to certain advantages of the L-C-L filter, it is largely preferred [63], [64] and is presented in Fig. 2.2 (c) for the study system. In modeling the L-C-L filter certain conditions [63] are considered to: (i) avoid excessive voltage drop in the ac side across inductors, (ii) maintain better controllability of output current and, (iii) suppress the ripple in the AC side current. These conditions are,

- a) The capacitor size should be limited such that it can draw a maximum reactive power of not more than 5% of the rated active power in order to maintain almost unity power factor.
- b) The total value of inductance should be around 0.1 pu to limit the AC voltage drop during operation. Otherwise, higher DC link voltage is required to ensure current controllability.
- c) The resonant frequency should be in the range between ten times the line frequency and one-half of the switching frequency, to avoid amplification of unwanted harmonics in the lower parts and upper parts of the harmonics spectrum.

- d) Passive damping must be sufficient to avoid high frequency oscillation known as the ringing effect by taking the losses under consideration.

The expression for filter capacitor can be given as below [63]:

$$C = \frac{\lambda P_{max}}{(6\pi f V_{pn}^2)} \text{ Farad} \dots\dots\dots (2.28)$$

where, nominal frequency, $f=50\text{Hz}$. The constant $\lambda=1.65\%$ is chosen arbitrarily for the study system to operate the inverter very close to unity power factor operation according to condition (a). From (2.28) the value of the filter capacitor is found to be $99 \mu\text{F}$ for the study system. Hence, the capacitive reactance is calculated as 32.15Ω , which draws 1.645 kVAr at 230 volts . This power is 1.6% of the rated power which is very low according to condition (a). Therefore, for the selected capacitor value, condition (b) can be relaxed and slightly higher value of inductances may be chosen [63].

The size of inverter side inductance L_1 can be determined from the following formula [63]:

$$\frac{i_g(h_{sw})}{i(h_{sw})} = \frac{1}{|1 + r(1 - CL_1\omega_{sw}^2)|} \dots\dots\dots (2.29)$$

Where, $i_g(h_{sw})$ is the grid current at switching harmonic and $i(h_{sw})$ is the switching current output from the inverter, $\omega_{sw}=2\pi f_{sw}$, f_{sw} is the switching frequency. The constant r is the ratio of grid side inductance L_2 and the inverter side inductance L_1 , i.e., $L_1/L_2=r$. For the study system, the suppressed switching current harmonic at the grid is considered as 0.1 times the output switching current harmonics. The value of the constant r is chosen as 9.5 , which is reasonable according to the recommendation of [67] and [68] to avoid the overlapping of the cut-off frequency of the L-C-L filter with the bandwidth of the grid connected current controller. This results in a value of $L_1=500 \mu\text{H}$ and $L_2=52.64 \mu\text{H}$. Therefore, the total value of $L_T=L_1+L_2$ is calculated as 0.3 pu (Appendix-A) which is higher than the recommended value given in condition (b). As the DC link voltage is sufficiently higher than $2V_{ac}$, this higher value of L_T does not affect the controllability due to the presence of enough DC link voltage [63]. In addition, the use of larger L_1

suppresses the ripple current more effectively.

The resonance frequency can be calculated with the following expression [63]:

$$f_r = \left\{ \sqrt{(L_T/L_1 L_2 C)} \right\} / 2\pi \text{ Hz} \dots\dots\dots (2.30)$$

For the study system the value of resonance frequency is found $f_r=2317$ Hz, which is within the range of $10f$ and $1/2f_{sw}$ and hence satisfies the condition (c).

It is noted that L_2 includes the transformer leakage inductance. If the leakage inductance of the transformer is large enough then the transformer itself can act as an L_2 branch in the L-C-L filter configuration and is illustrated in Fig. 2.2 (c). The damping resistor in series with capacitor is considered as $1/3^{\text{rd}}$ of the capacitive reactance at resonant frequency [63] to effectively damp the oscillations or the ringing effect.

2.3 Case Study

2.3.1 Operating Data

In this simulation study, 10 x 138 numbers of series-parallel combinations of FS 272 solar modules are connected to make a total capacity of 100kW at STC. Thus, 10 modules in series form a string, whereas the total number of string is 138. Therefore, the voltage represents the string voltage and the current represents the cumulative current of all 138 strings. It is noted that the current in a string is equivalent to the current in a module. On the other hand, the voltage across a single module is the string voltage divided by the number of series modules in a string.

2.3.2 Model Output

In Fig. 2.8 and Fig. 2.9, the DC voltage and current, AC side RMS voltages and currents, PV power output, and the variation of THD are illustrated for a solar radiation of 1 Sun at 25°C (0-40 sec) and solar radiation of 0.8 Sun at 45°C (40-60 sec) while the system is run with MPPT for the duration of 15-60 sec.

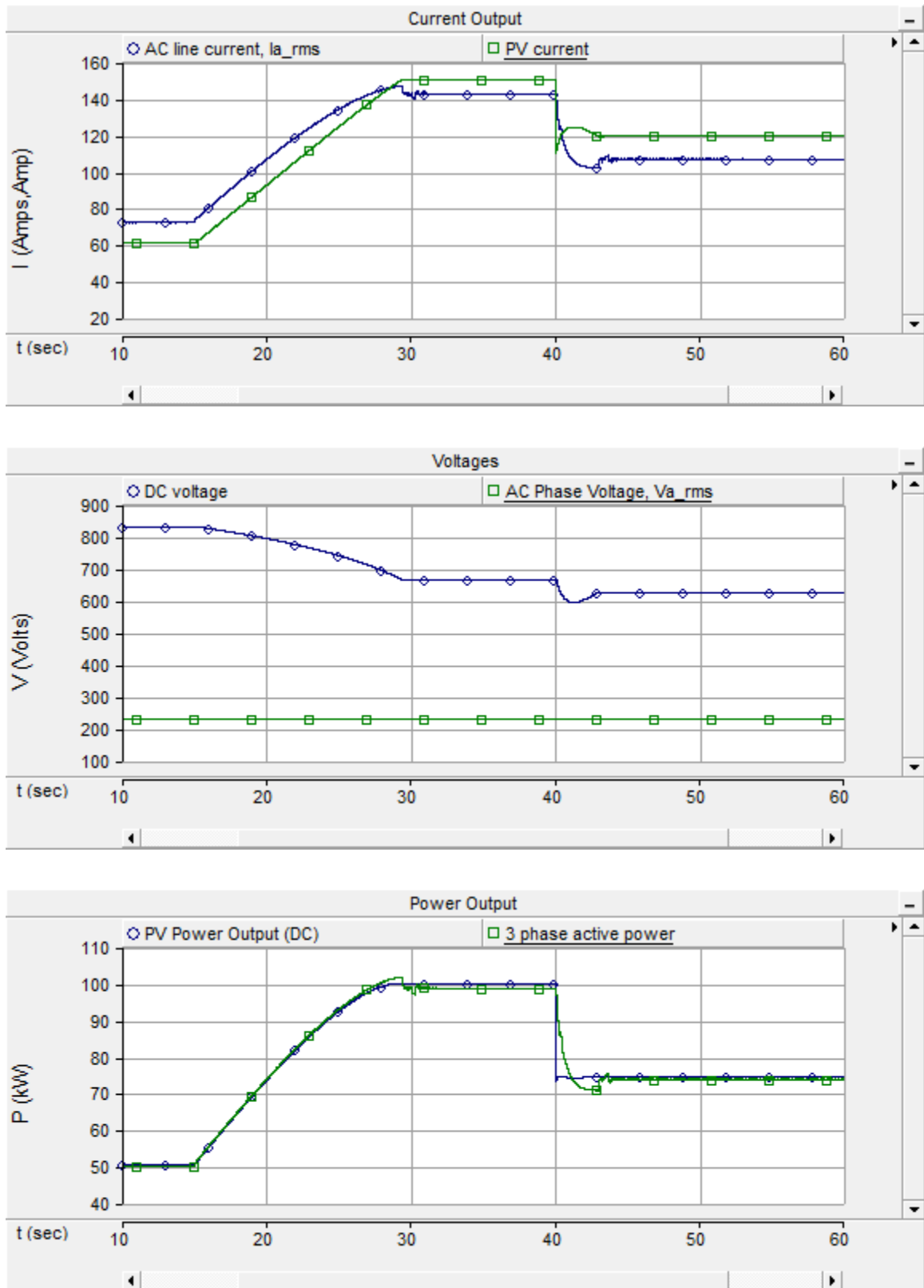


Figure 2.8 PV system output at different radiation and temperature; PV current and inverter output phase current, DC link and AC voltage and power output.

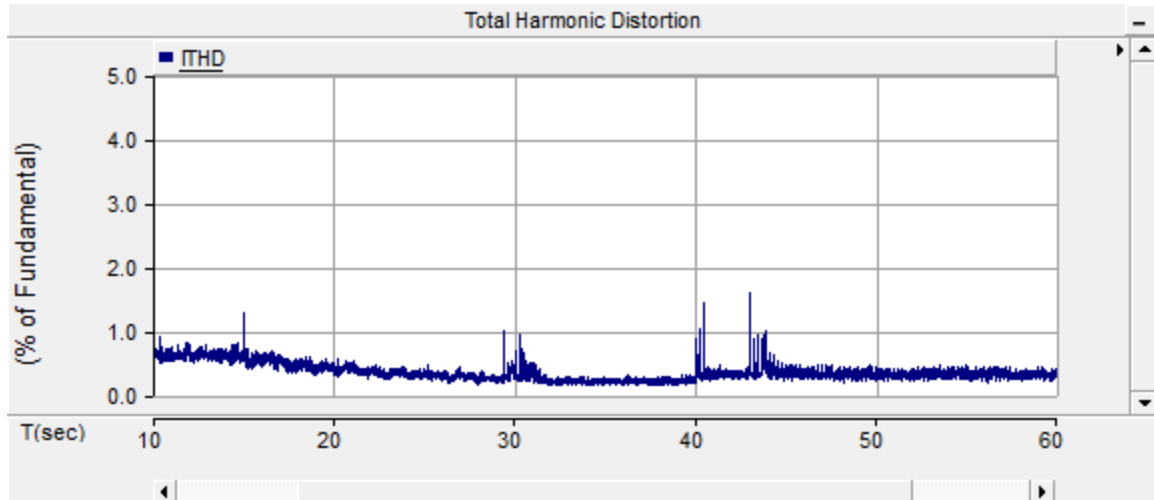


Figure 2.9 Total Harmonic Distortion (THD) at different irradiation & temperature.

It is observed from Fig. 2.8 that while the PV system operates under STC without the MPPT enabled (10-15sec) it generates a low power level of 53.7kW corresponding to 827.7 V DC. After 15 seconds when the MPPT feature is enabled, it reaches its maximum power point within next 10 seconds, which is the time taken by the MPPT module to track the maximum power. This can be made even faster with fine tuning of the controller. Thus, at STC with MPPT enabled, the PV system operates at 100kW at a string voltage level of 666 V, (DC) for the duration of $25 \leq t \leq 40$ seconds. This demonstrates the effectiveness of the modeled MPPT.

After 40 seconds, the solar insolation level changes from 1 Sun to 0.8 Sun and the temperature changes from 25°C to 45°C . Corresponding to this insolation and temperature, the maximum power point decreases to 74.7 kW with a string DC operating voltage of 624 V. This continues until $t=60$ seconds. A small difference between the DC and AC supply occurs due to the losses in the inverter and its associated circuits. The voltage at the AC side is almost constant as it is established by the grid voltage. The level of harmonics remains within the acceptable IEEE 519 standard [69] limit (5% of fundamental) as illustrated in Fig. 2.9, for different operating conditions as mentioned above. This demonstrates the effectiveness of the modeled L-C-L filter and the sizing of DC link capacitor. As illustrated in Fig. 2.10, the instantaneous phase voltage and current are in phase, which demonstrates that unity power factor is maintained at the PCC by the solar inverter.

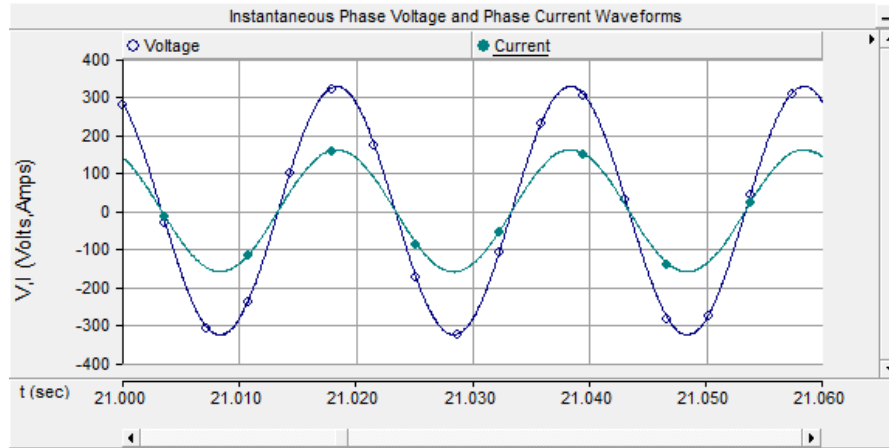


Figure 2.10 Instantaneous phase voltage and current output of PV system at STC.

It is observed from Fig. 2.8 that with the MPPT feature at STC, the operating voltages of each string are 666 V. Therefore, the operating voltage of each series module is (= 666V/number of modules in a string) 66.6 volts. The total solar farm output current is observed to be 150.4 amps. Therefore, the current output from a single string is (=150.4 amp/number of total string) 1.09 amp. The output maximum power point voltage and current matches very closely with the datasheet values provided in Table 2.1.

By using the developed model at STC, the value found for series resistance, R_s , is 0.038Ω , shunt resistance, R_{sh} , is $822.85\ \Omega$ and the diode ideality factor, n , is 2.6588 for the specified datasheet. To validate the developed model with the above determined values of R_s , R_{sh} and n , the quantities as provided by the same manufacturer given in Table – 2.1, at a non STC case (0.8 radiation level and 45°C), are predicted. The comparison of predicted output quantities of the developed model with the manufacturer's datasheet values corresponding to above non-STC case are presented in Table 2.2.

It is obvious from Table 2.2 that the developed model with R_s , R_{sh} and n at STC condition, is also able to predict very closely the output quantities, e.g., maximum power, maximum power point voltage and currents, corresponding to the non STC case.

Table 2.2 Comparison of simulated model with manufacturer’s datasheet for FS 272 PV module at 0.8 radiation level at 45 °C.

Item Description	Symbols	Datasheet value	Model value	Error (%)
Nominal Power ($\pm 5\%$)	P_{MPP} (W)	54.4	54.14	0.49
Voltage at P_{MPP}	V_{ms} (V)	62.4	62.46	0.098
Current at P_{MPP}	I_{ms} (A)	0.87	0.867	0.34
Shunt Resistance	Rsh (ohm)	Not provided	822.85	-
Series Resistance	Rs (ohm)	Not provided	0.038	-
Diode Ideality Factor	n	Not provided	2.6588	-

2.4 Conclusion

In this chapter, a complete generalized model of a grid connected PV solar system in EMTDC/PSCAD has been presented with the necessary mathematical formulas. The PV module is modeled by using only manufacturer datasheet values. The proposed technique determines all of the PV module parameters without any explicit repetitive iteration. This model includes converter-less MPPT controller to get the maximum power output at any level of solar irradiation, and temperature without using any DC-DC converter, thus reducing overall losses. The selection of filter parameters and the size of DC link capacitors are explained. The EMTDC/PSCAD simulation study demonstrates that this model: (i) maintains unity power factor at any level of power; (ii) ensures maximum power point tracking and, (iii) maintains acceptable ranges of harmonics. The EMTDC/PSCAD simulation results for the PV modules have been validated with two levels of solar insolation and temperature levels for a commercial PV system with respect to a manufacturer datasheet’s values of voltage, current, and power quantities. This generalized EMTDC/PSCAD model can be adopted for any other PV module and system operating conditions.

Chapter 3

3 New Fault Detection and Management Technique for Inverter Based DGs.

3.1 Introduction

Inverter based DGs such as PV solar systems use solid state devices such as IGBT switches to convert the DC power harnessed from PV modules into AC power supply for the grid. These IGBT switches are capable of operating within a few hundred nanoseconds [8]. This chapter presents a new fast fault detection technique based on the rate of rise of current together with the current magnitude in a PV solar system based DG. The fault is detected very rapidly and IGBT switches are operated to disconnect the PV inverter before the fault current exceeds the rated output current of the inverter. Implementation of such a strategy can alleviate the problem of short circuit currents from inverter based DGs. It may be mentioned that several PV solar systems have been denied connections in Ontario due to their potential short circuit current contributions [61].

In Section 3.2, the study system model is described with the proposed controller. Section 3.3 presents case studies for symmetrical fault, asymmetrical fault, and fault at different locations. Finally, Section 3.4 concludes the outcome of this work.

3.2 System Model

The study system is comprised of a typical distribution network with a PV solar farm connected at the end of the feeder [162] as shown in Fig. 3.1. The different components of the network are described below.

3.2.1 System Description

The study system consists of a 25 km long 27.6 kV overhead feeder connected to a transmission network through a substation having two 47 MVA transformers [162]. Each set of a three phase transformer is configured with three single phase transformers having an impedance of 18.5%. The equivalent grid system is assumed to have a very large short circuit capacity i.e., very low grid impedance. Hence the equivalent positive sequence

source impedance is modeled with the transformer impedance only. All positive and zero sequence impedances are modeled and referred to the 27.6kV side of the transformers. The system data is given in Appendix-B. In EMTDC/PSCAD, the overhead line is configured as several PI sections for different spans of line lengths between the loads. A total distributed load of 15 MVA is modeled as three groups of fixed impedance three phase static loads, connected with the feeder. The adjacent feeder loads of around 60MW at 0.9 pf. are modeled as a single aggregated fixed P-Q load connected at the beginning of the feeder. A 7.5MW PV solar farm is connected at the end of feeder.

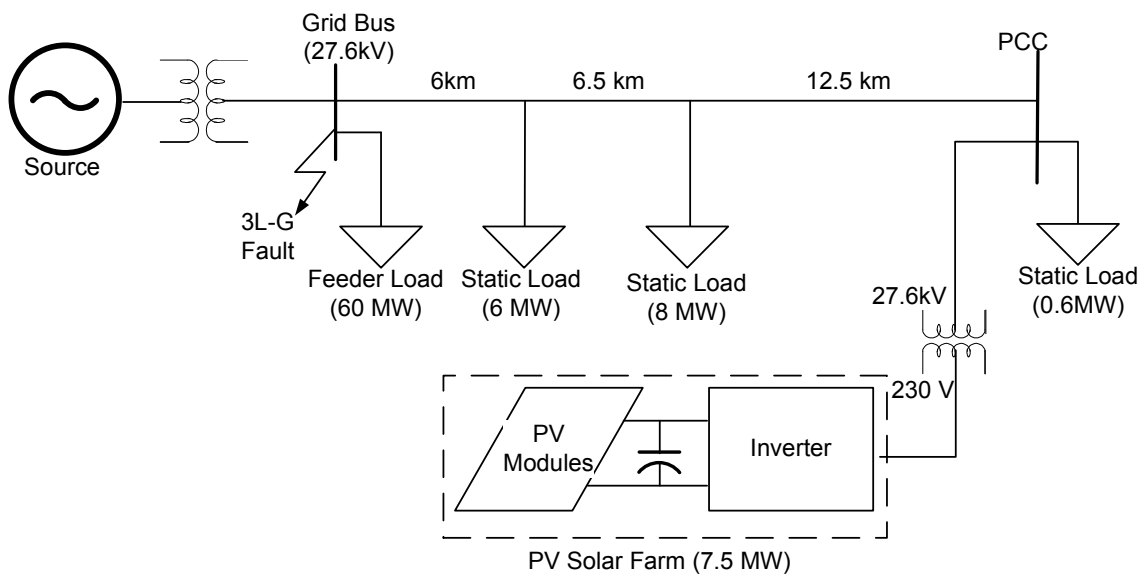


Figure 3.1 One line diagram of the study system.

3.2.2 PV System Model

Fig. 3.2 presents the detailed PV system model. The PV solar system consist of the PV solar modules depicted in Fig. 3.2 (a), inverter shown in Fig. 3.2 (b), AC filter described in Fig. 3.2 (c), MPPT module illustrated in Fig. 3.2 (d), and the inverter controller elaborated in Fig. 3.2 (e). These subsystems are already described in Section 2.2. Therefore, Fig. 2.2, Fig. 2.5, and Fig. 2.7 in Chapter 2 are used to develop a 7.5MW PV solar system with the data provided in [162] and given in Appendix-B. The PV inverter output of 230 V connects to the grid through a 0.23/27.6kV, 7.5MVA step up transformer. The filter parameters are chosen in accordance with the size of the PV solar

farm while satisfying the criterion given in [64], [70], [164]. The controller parameters and L-C-L filter parameter calculation are given in Appendix-B. A novel supplementary control block named ‘*Fault Detection Module*’ is added with the conventional PV solar farm inverter controller as depicted in Fig. 3.2 (f). A solid state GTO or IGBT based switch is incorporated to isolate the solar panels as shown in Fig. 3.2 (g).

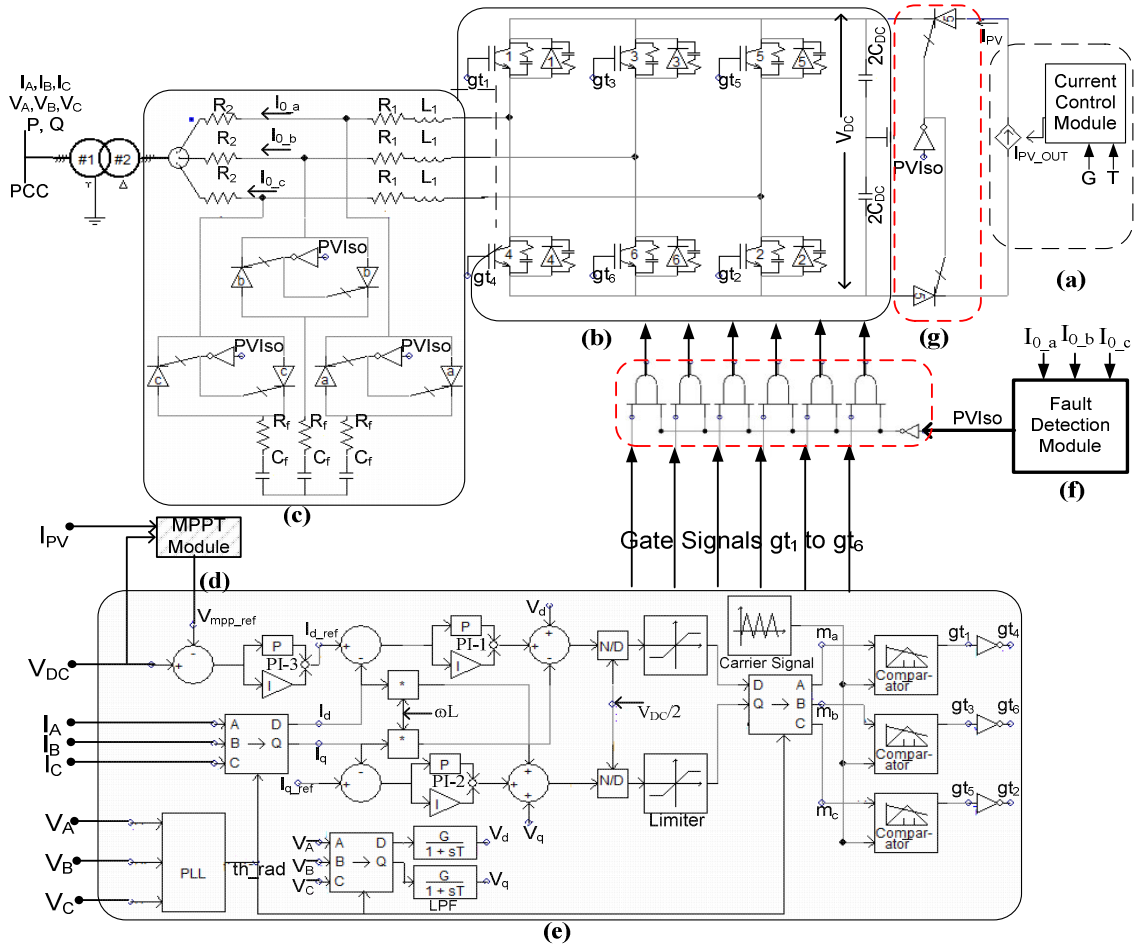


Figure 3.2 Detailed PV system inverter and conventional controller with incorporated fault detection module.

The inverter is a voltage sourced converter which is comprised of IGBT switches and associated snubber circuits. Each phase has a pair of IGBT devices which converts the DC voltage into a series of variable width pulsating voltages, using the sinusoidal pulse width modulation (SPWM) technique. The gating signals ($gt_1, gt_2, gt_3, gt_4, gt_5, gt_6$) of the IGBT switches are generated from the inverter controller which uses two current control loops to control the active and reactive power at the inverter output along with the

regulation of DC link voltage by taking a three phase current signal from the inverter output as feedback signal to the controller. During short circuit scenarios, the firing pulses to the IGBTs are disabled as soon as the “fault detection module” establishes that a fault has occurred.

3.2.3 Fault Detection Module

3.2.3.1 Concept

The concept of the proposed fault detection module in Fig. 3.2 (f) is described in Fig. 3.3.

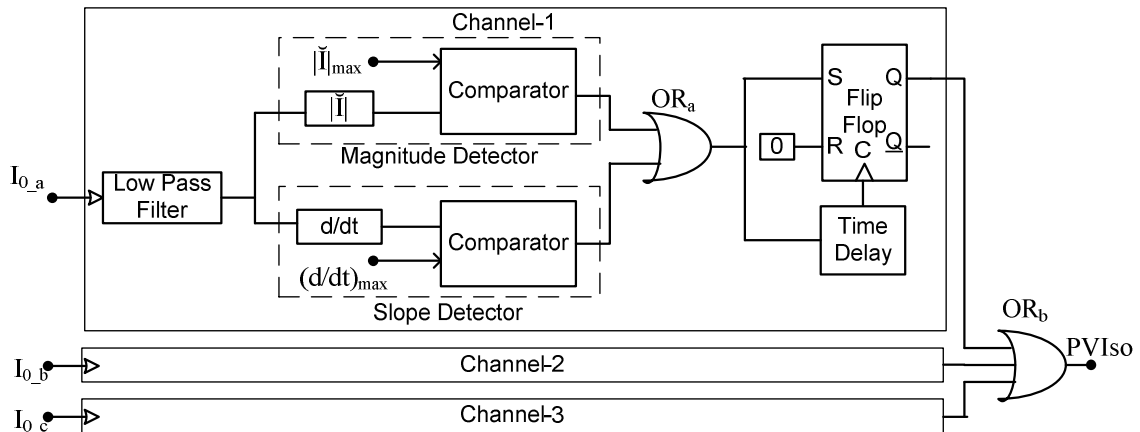


Figure 3.3 Fault detection module.

The proposed fault detector has three separate channels to measure three phase instantaneous inverter output currents (I_{0_a} , I_{0_b} , I_{0_c}) at the PCC. These currents are passed through a low pass filter to reject all the higher order frequencies due to solar inverter injection, feeder capacitor switching, or transformer energization [92]. The filtered current is passed through in two parallel paths in each channel; one is through a slope detector (d/dt), and another is through a magnitude detector $|\dot{I}|$. The slope detector is comprised of a comparator which compares the derivative of the PV system current to determine the slope, and compares with the reference slope $(d/dt)_{max}$. Similarly, the magnitude detector is comprised of a comparator which compares the magnitude of the PV system current with respect to a reference value $|\dot{I}|_{max}$, which is the peak magnitude of instantaneous rated current. The output of these detectors becomes high only if either of the monitored values, (d/dt) or $|\dot{I}|$ exceeds their corresponding reference values, $(d/dt)_{max}$ or $|\dot{I}|_{max}$. The output of the detectors referred to here as ‘trigger signal’ are passed

through the OR_a gate. The OR_a gate output signal is then applied to the RS flip-flop to hold the trigger signal once it becomes high. Finally, the output of all triggering signals from all other channels are passed through a digital ‘ OR_b ’ gate to ensure the output triggering signal, ‘PVIso’, to be high due to the detection of fault with any of the phase signals.

It is noted that in a transient event such as the load switching, transformer energization, or capacitor switching which is not completely filtered out in the low pass filter can cause a high d/dt for a very short period of time. This high d/dt may generate an undesirable trigger signal. Therefore, to avoid the generation of undesired triggering signal in these transient events, a time delay in the clock signal of the RS flip-flop is introduced. This prevents the instant trigger signals generated due to transient action to pass through the RS flip-flop. Once the operation of the fault detector is complete and the fault is cleared a reset signal (not shown here) is used to reset all the triggering signals and as well as all the flip-flops to bring back the PV solar farm to normal operation.

3.2.3.2 Implementation in EMTDC/PSCAD

The proposed fault detector shown in Fig. 3.3 is implemented in EMTDC/PSCAD software as shown in Fig. 3.4 which is divided in two sections: Section-A and Section-B. There are three identical channels corresponding to phase a, phase b, and phase c currents. The channel corresponding to phase a, is described in detail below.

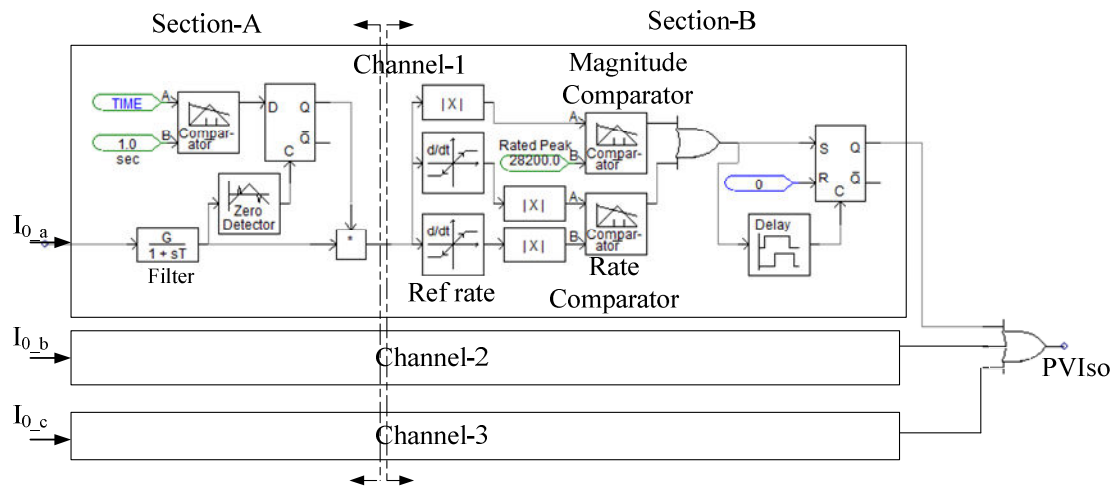


Figure 3.4 Fault detection module implementation in EMTDC/PSCAD.

The fault detector uses a synchronization section labeled as Section-A. In this section the current signals, I_{0_a} , monitored at the PCC, as explained earlier, is passed through a low pass filter. To avoid a false operation of the fault detection module due to a start up transient of the solar farm, a time delay (typically 1 sec) is added through a comparator. The output of the comparator becomes high after this preset time delay of 1 second. It is further required to accomplish a zero crossing synchronization prior to transmitting the filtered current signal to the input of section-B. This synchronization ensures that the section-B operation will start only from the zero crossing instants of the current. Otherwise, the rate comparator in section-B will see a sudden jump in current or, alternately, a high rate of rise of current which will generate a false triggering signal. To synchronize with the zero crossing, a D flip-flop is used at the output of the comparator. The clock signal of the D flip-flop is twice the fundamental frequency which is implemented through a zero crossing detector of the input signal. The clock frequency is twice that of the fundamental frequency so that the synchronization can occur at either of the two positive going or negative going zero crossings. Therefore, when the comparator output becomes high after 1 second, the output of the D flip-flop waits for the zero crossing of the current signal. Until this time, the output of D flip-flop remains zero and thereby, no current signal passes to section B. Once the synchronization with zero crossing is accomplished, the current signals from section-A are transmitted to Section-B.

In Fig. 3.4, the synchronized signals from Section-A are passed through two parallel paths in section-B, in each channel as explained in the previous section 3.2.3.1. In EMTDC/PSCAD, the rate limiters replicate the input signals as long as the rate of change of the input (d/dt) does not exceed the specified threshold limits [165]. Therefore, the output of the rate limiters is based on the slope of the input signal. During a system fault the rate of change of input current (d/dt) becomes more than the threshold limit. The threshold limit can be determined approximately with the magnitude of (d/dt) of the rated current as shown in the following expression [91].

For a current signal of $i = I_m \sin \omega t$,

$$\left| \frac{di}{dt} \right| \approx k\omega I_m \dots\dots\dots (3.1)$$

where, I_m is the peak magnitude of instantaneous inverter current, k is the tolerance constant, and ω is the angular frequency of the current. The threshold value for the rate limiter labeled as ‘Ref rate’ in Fig. 3.4 is based on the peak instantaneous value of rated current, $I_m = I_{m_rated}$. This rate limiter, therefore, does not replicate the current signal at its input if $I_m > I_{m_rated}$. For the study system, the detailed calculation for the threshold level and the rated peak magnitude of current is described in Appendix B by arbitrarily choosing a tolerance constant of 1.06 times of I_{m_rated} . Note that, depending on the requirements of the utility, the value of the tolerance constant can be chosen to be any value above 100% or 1 p.u. of the rated current.

Meanwhile, the threshold value of the other rate limiter is set to a very high value such that it can replicate the input current signal at its output even if the current signal exceeds its rated peak. As a result, by comparing the signals from the two rate limiters the comparator can generate a trigger signal at its output if $I_m > I_{m_rated}$, in other words, when the actual rate of rise of current is more than the permissible rate of rise of current. Note that, prior to the input of the comparator, two absolute value detectors, $|x|$, are used to eliminate the comparison with negative signals.

In the other path, the magnitude detector compares the magnitude of instantaneous current signal with the maximum allowable instantaneous peak current magnitude as shown in section-B of Fig. 3.4.

As explained earlier, the output of these detectors are then passed through OR gate and R-S flip-flop to generate the triggering signal ‘PVIso’. The PVIso signal thus becomes high when either the rate of rise of the current violates the acceptable limit, or when the instantaneous current magnitude exceeds the rated current of the inverter (multiplied with the tolerance constant).

The operation of this fault detector can be further explained with the flowchart given in Fig. 3.5. During the start-up operation of a PV solar farm the fault detector is disabled. A delay of 1 second is provided, after which the fault detector is synchronized with the PV inverter output current. The fault detector then monitors the output current for any abnormal situation in the grid. During normal operation, the slope and the magnitude of

the current are within acceptable threshold limits and the comparator outputs associated with the slope detector or the magnitude detector do not become 'high'. Therefore, the trigger signal 'PVIso' remains low. However, during a fault or any other abnormal condition of the system during which either the current magnitude or slope of current exceeds acceptable limits, a high signal is sent to the input of the RS flip-flop. However, this 'high' triggering signal is transmitted to the output of the R-S flip-flop after a certain time delay. The time delay in the clock signal of this R-S flip flop plays an important role in preventing the generation of undesired trigger signal, as explained earlier. Finally, the output of all triggering signals from all other channels are passed through a digital 'OR' gate to generate the output triggering signal, 'PVIso'. This signal can therefore become high due to the detection of fault with any of the phase current signals.

As soon as the triggering signal 'PVIso' is generated upon detection of fault in the grid, it immediately stops the gating signals to all IGBTs in the inverter through the ANDing operation with the inverter gating signals generated from the inverter controller as shown in Fig. 3.2. As a result, the PV solar inverter stops the power transfer from the PV modules to the grid within a few hundred micro-seconds.

It is noted that once the gating signal is stopped the DC voltage across the capacitor starts to increase due to the incoming PV module current. According to the I-V characteristics of the PV module, the current output gradually decreases with the increase of voltage at the output of the PV module and, eventually, stops at the rated open circuit voltage of the PV module. However, to reduce the DC voltage stress across each IGBT switch, the same triggering signal 'PVIso' is used to operate a solid state DC breaker as shown in Fig. 3.2 (g), to disconnect the PV modules from the inverter.

In addition, this triggering signal 'PVIso' is used to isolate the AC filter capacitor by switching off the back-to-back connected gate turn off (GTO) thyristors, or IGBTs, as demonstrated in Fig. 3.2 (c) to prevent high ringing currents between filter capacitance and inductance [59].

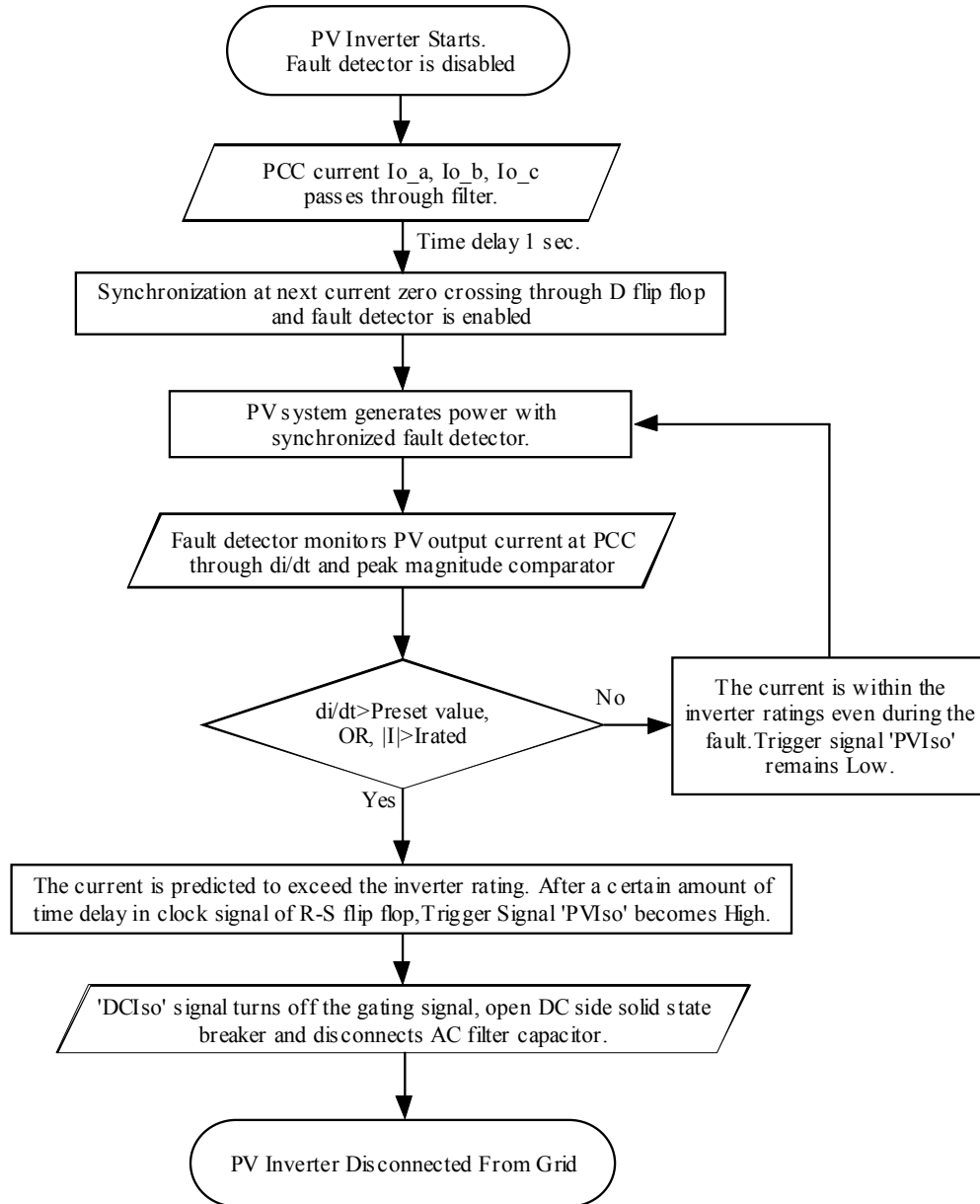


Figure 3.5 Fault detector operation flowchart.

3.3 Case Studies

Fault studies are performed at two locations – at the grid bus and at the PCC for a duration of either 0.1 seconds, or 6 cycles. Both the symmetrical (three phase to ground) and asymmetrical faults cases are investigated with the proposed fault current controller. In each case, two scenarios are considered: fault occurs when the inverter current is not at its peak, and second, when the inverter current is at its peak. This is done in order to demonstrate the effectiveness of the controller. Moreover, a load switching is simulated

to ensure that the controller does not respond in such an event. Finally, the ringing effect of the filter capacitor is demonstrated, as well as the controller operation, to isolate the filter during such a fault event. The simulation results are presented below.

3.3.1 Symmetrical Fault at PCC

Fig. 3.6 depicts the instantaneous current from solar farm without the fault current controller. At the occurrence of fault at $t=5$ seconds, the current exceeds its rated value. The dotted line in the figure represents the rated current of the inverter which is 0.25 kA. It is noted that while simulating the fault, a high frequency switching spike is observed in EMTDC/PSCAD which is due to the mismatch between simulation time step (1 μsec) and the plotting time step (10 μsec). This spike can be eliminated by using the same time step for both simulations and plotting the time step. It is noted that setting a lower simulation time step gives a precise output but taking a large amount of computer memory to plot at the same time step which crashes the simulation most of the time whereas the higher simulation time step causes lack of accuracy. Therefore, the aforementioned settings are considered as acceptable settings to explain the concept by overlooking the high frequency spike prior to the fault for rest of the simulation analysis. It is clearly seen that the fault current achieves a value of 1.5 p.u., which is acceptable to certain utilities.

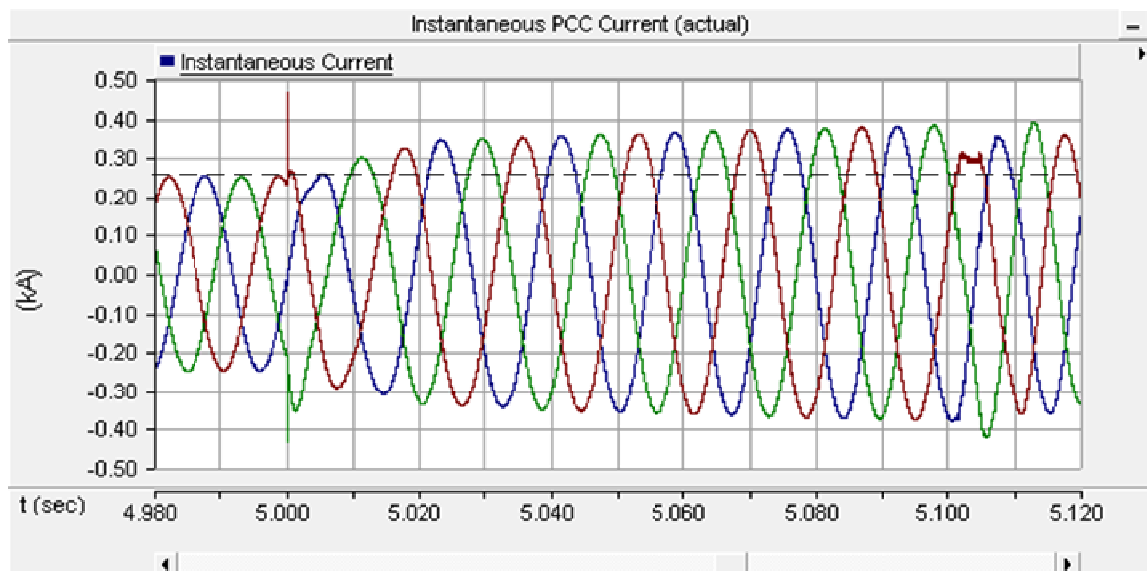


Figure 3.6 PV system operation for fault at $t=5$ sec, at rated power output.

3.3.1.1 PV Solar Farm operating at rated power:

For a symmetrical fault at PCC, Fig. 3.7 shows the instantaneous current waveform when the fault takes place at a non-peak fault instant (at $t=5$ seconds) with the proposed fault controller enabled. Fig. 3.8 shows the instantaneous current waveform when the fault takes place at a peak fault instant at $t=4.996$ seconds with the proposed fault controller enabled.

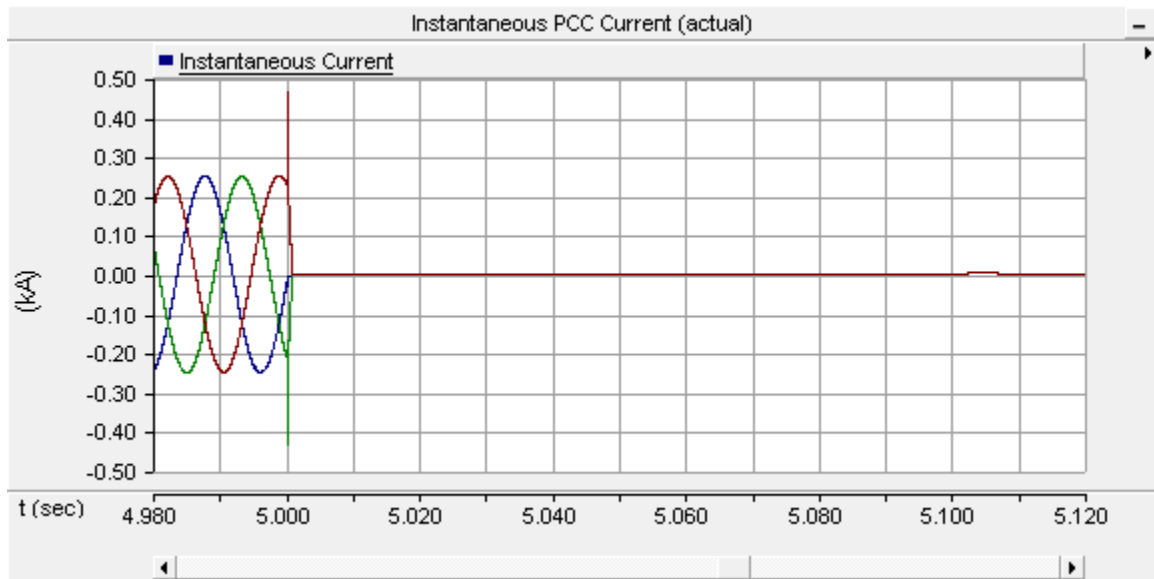


Figure 3.7 Inverter output current at non-peak fault instant.

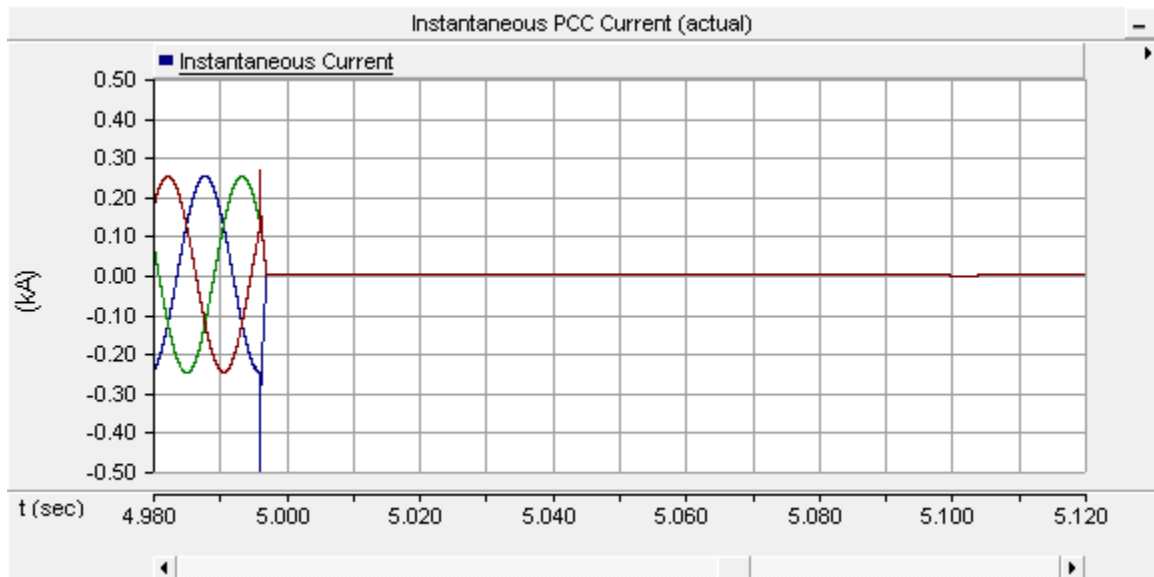


Figure 3.8 Inverter output current at peak fault instant.

In both the cases, while the PV solar farm is operating at rated power the tendency of over current is sensed immediately, and with the use of the proposed controller, a trip signal is issued which stops the gating signals of the inverter. The current output from the inverter stops immediately without exceeding the rated peak current as demonstrated in Fig. 3.7 and Fig. 3.8, respectively

3.3.1.2 PV Solar Farm operation at low power:

For a symmetrical fault at PCC, Fig. 3.9 shows the instantaneous current waveform with the fault detector enabled when the fault takes place at a peak fault instant at $t=4.996$ seconds while the PV solar farm is generating 40% of its rated power. When the PV solar farm is operating at such a low power level, the fault current contribution from the solar farm does not exceed its rated current (0.25 kA) regardless of its fault occurring instants. In this case, the use of the proposed fault current controller does not generate any trip signal. This allows the solar farm to remain online and deliver the current to the grid as demonstrated in Fig. 3.9. The switching spike as seen in the figure at $t=4.996$ seconds is due to a simulation features of EMTDC/PSCAD as discussed in the previous section and is not a performance of the controller.

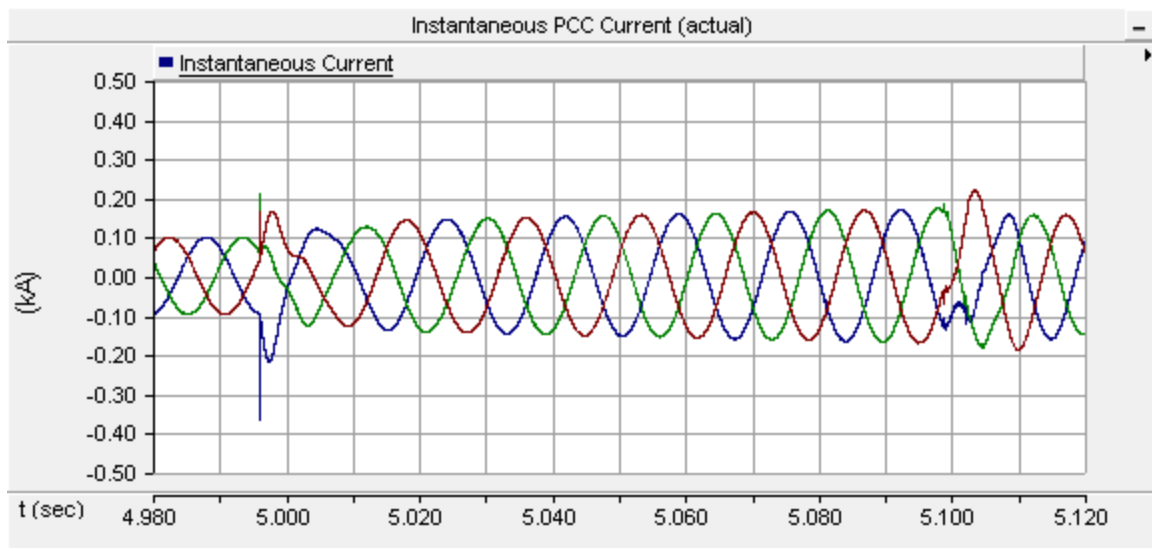


Figure 3.9 Inverter output current waveform with 0.4 pu PV solar farm generation

3.3.2 Symmetrical Fault at Grid Bus

For a symmetrical fault at grid bus, Fig. 3.10 shows the instantaneous current waveform when the fault takes place at a non-peak fault instant at $t=5$ seconds with the proposed fault controller enabled. Whereas Fig. 3.11 shows the instantaneous current waveform when the fault takes place at a peak fault instant at $t=4.996$ seconds with the proposed fault controller enabled.

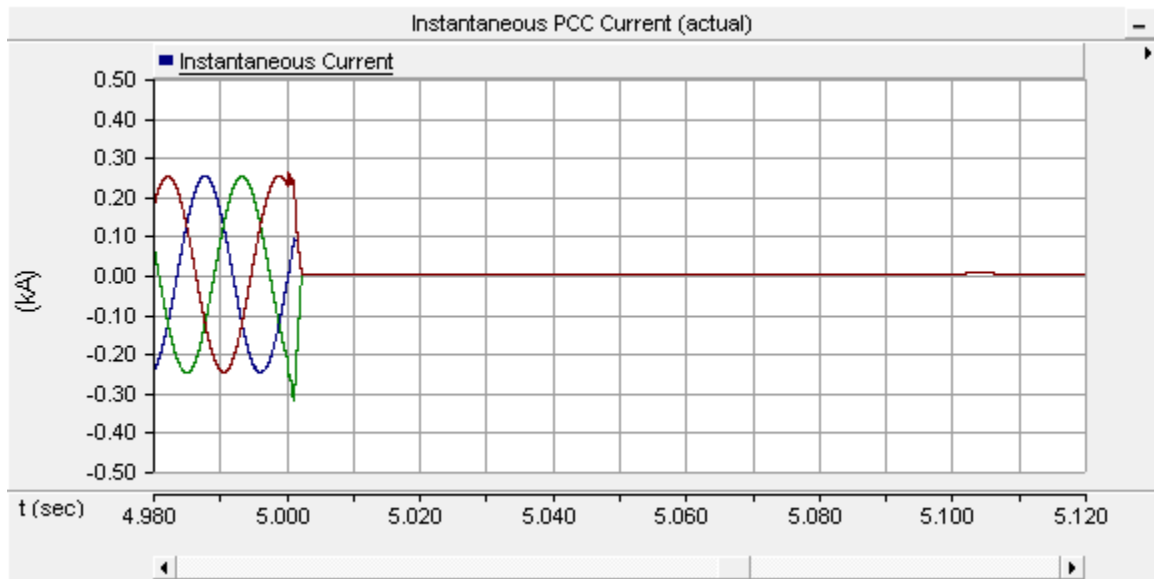


Figure 3.10 Inverter output current at non-peak fault instant

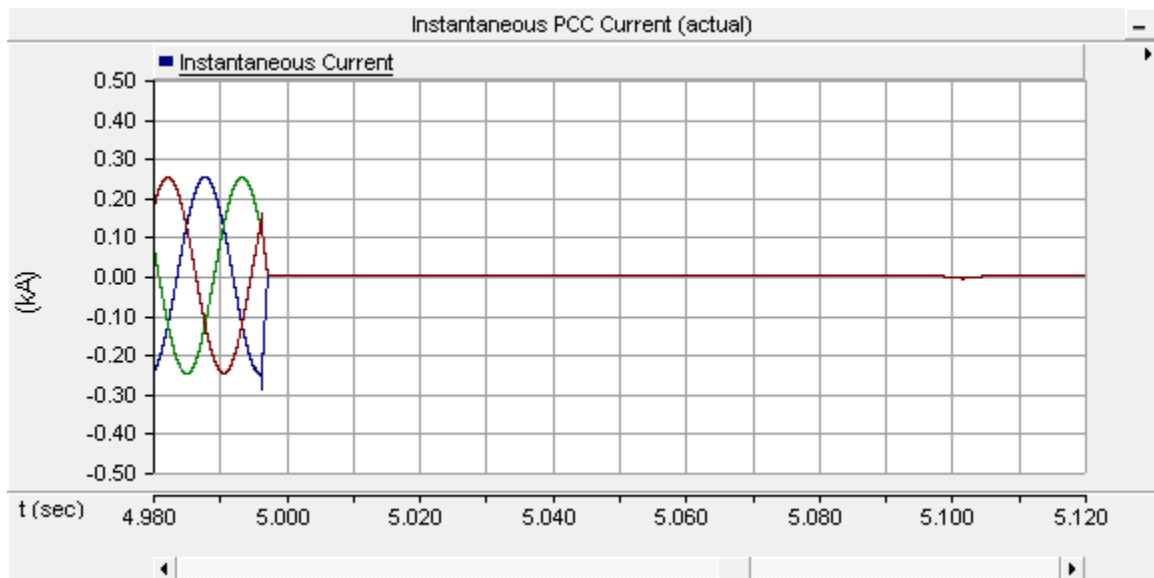


Figure 3.11 Inverter output current at peak fault instant.

In the case of a Grid Bus fault, the rate of rise of current is much slower due to a lower current contribution to the remote fault. As a result, it takes comparatively longer to detect the fault but the fault current controller still responds within 1ms, as demonstrated in Fig. 3.10 and Fig. 3.11. Note that the rated current limit is set arbitrarily to 1.06 times of the rated peak for the study system. As a result of slow response, the inverter output current reaches its peak value as seen in Fig. 3.10 and then the PV solar farm gets disconnected. However, for the peak fault instant as shown in Fig. 3.11 the fault detector disconnects the PV solar farm before it exceeds the peak.

It is noted that when the PV solar farm generates low power, similar to the fault event at the PCC bus, the fault detector does not respond to grid bus fault as well. In these cases the contributed fault current does not exceed its rated limit and generate the identical waveforms as shown in Fig. 3.9.

3.3.3 Asymmetrical Fault at PCC and Grid Bus

Fig. 3.12 depicts the instantaneous current from solar farm during an asymmetrical fault (single line to ground fault) at PCC with the fault controller disabled. At the occurrence of fault at one phase $t=5$ seconds, while the PV solar farm is generating its rated power, the current exceeds its rated value at other two phases.

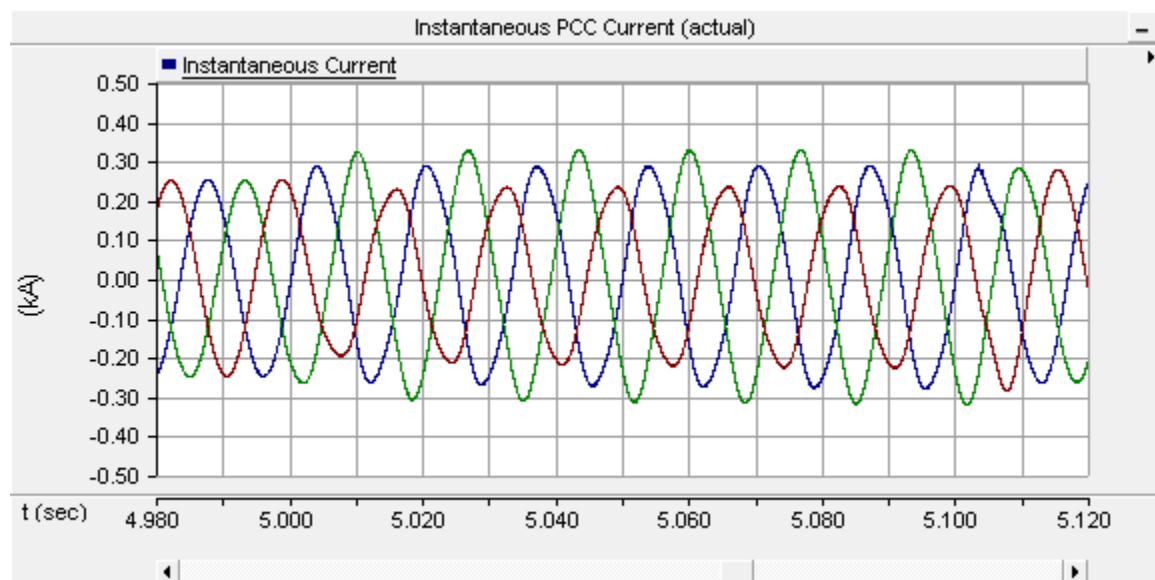


Figure 3.12 Different phase currents of PV inverter for fault at PCC.

Fig. 3.13 depicts the instantaneous current from the solar farm during an asymmetrical fault (single line to ground fault on phase B) at PCC with the fault controller enabled. At the occurrence of a fault on phase B at $t=4.996$ seconds (peak fault instant), while the PV solar farm is generating its rated power, the fault detector generates the trigger signal and disconnects the solar farm.

Fig. 3.14 presents the instantaneous current from the solar farm during an asymmetrical fault (single line to ground fault on phase B) at the Grid bus with the fault controller enabled. It also shows the same performance and disconnects the PV solar farm from the grid for the case of this asymmetrical grid fault event.

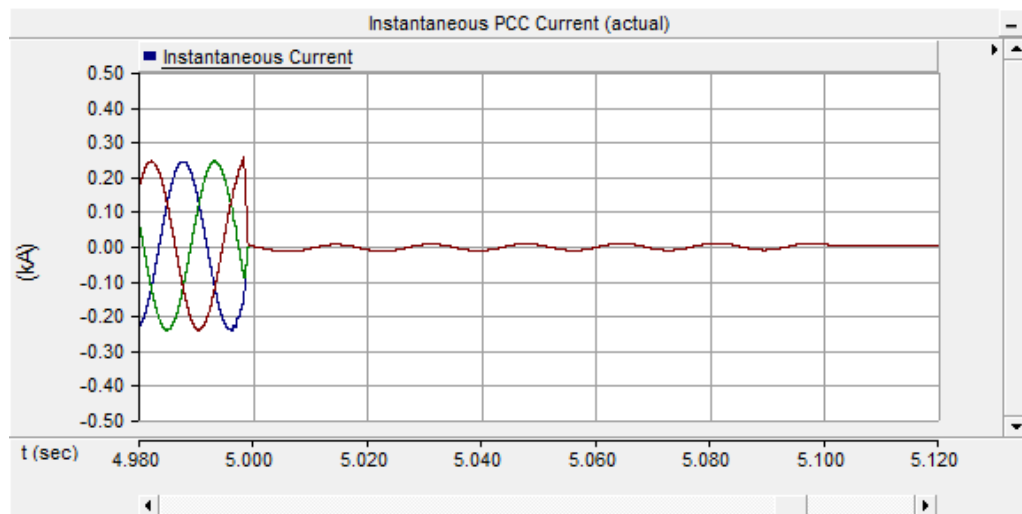


Figure 3.13 Inverter output current for a SLG fault at PCC (peak fault instant).

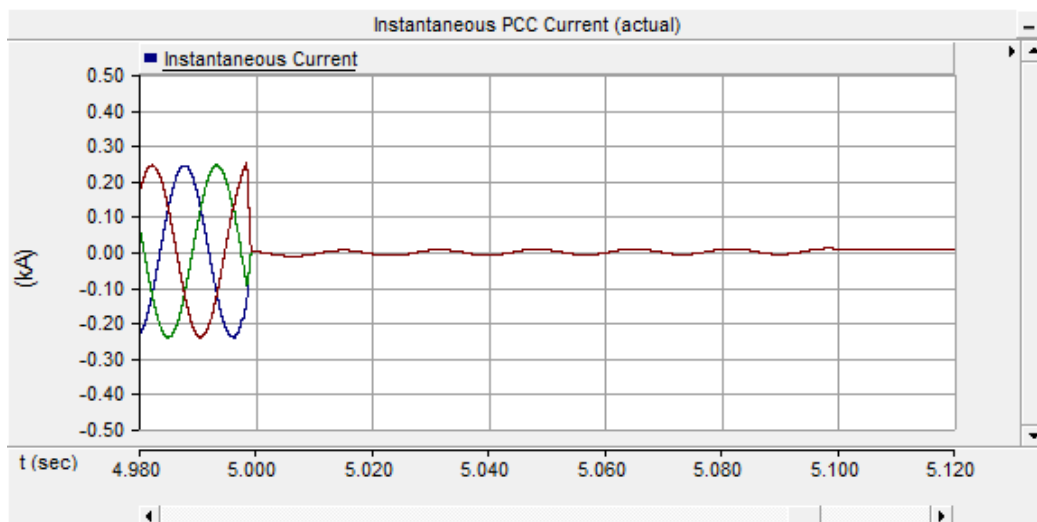
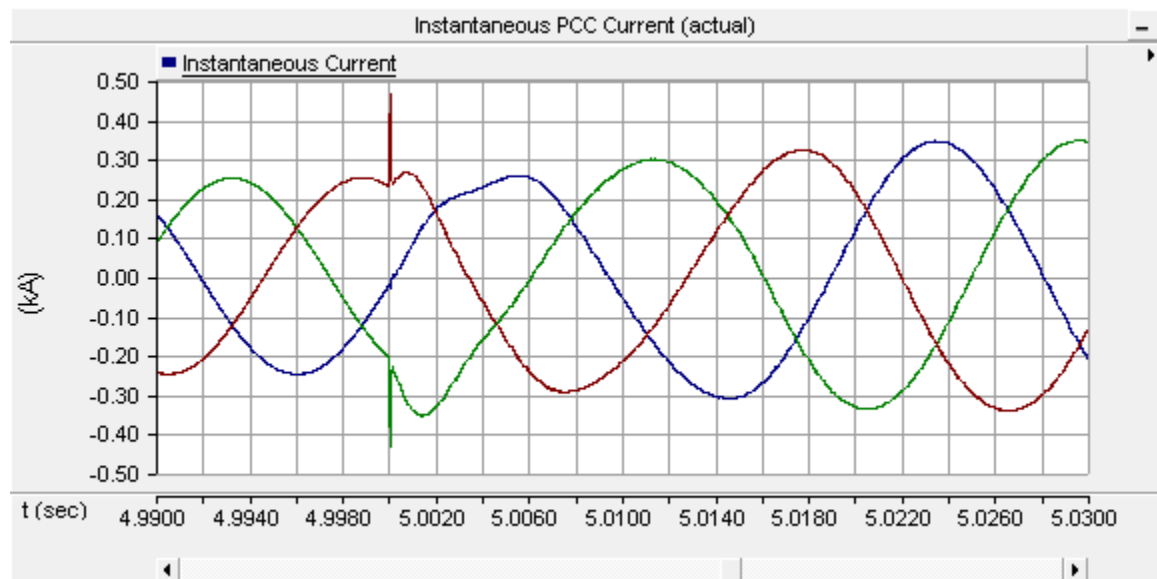


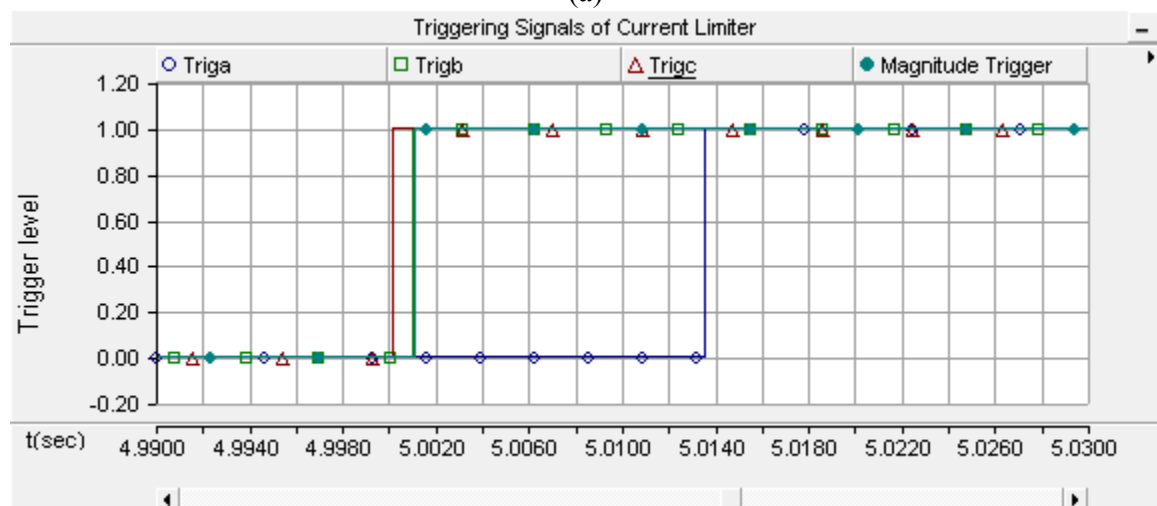
Figure 3.14 Inverter output current for a SLG fault at Grid Bus (peak fault instant).

3.3.4 Performance comparison of slope detector and magnitude detector in the fault controller

To compare the performance of the slope detector and magnitude detector, the PV solar farm is exposed to a fault at the PCC bus. The current wave shapes and the trigger signals generation by monitoring the current signals are demonstrated in Fig. 3.15 for a fault instant at $t=5$ seconds (i.e., at non-peak current instant). It is evident from this figure that the slope detectors on phase b and phase C respond before the magnitude detector. The slope detector of phase a responds last as it has a lower (d/dt) value before its triggering instant.



(a)



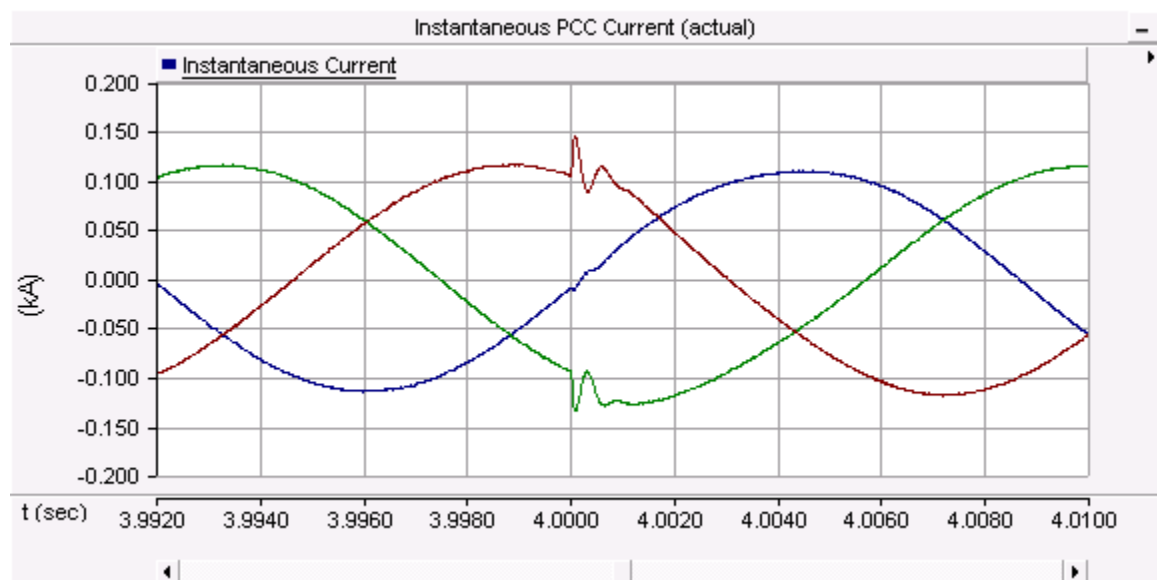
(b)

Figure 3.15 (a) Inverter output current and (b) generation of trip signals.

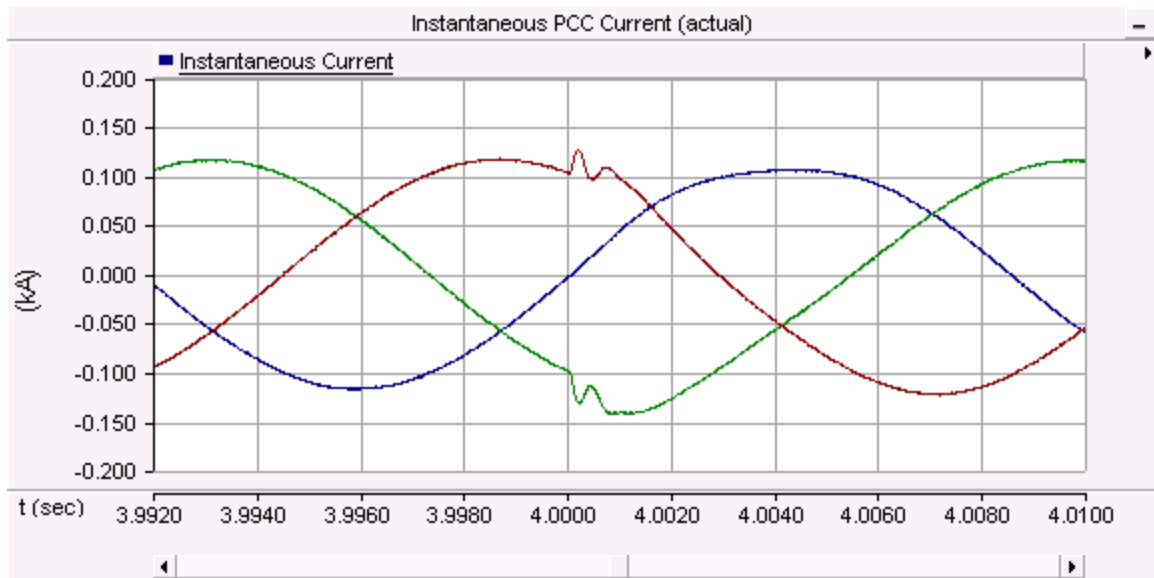
However, when the PV solar farm operates with the proposed controller, the fastest triggering signal (in this case ‘Trigc’) will disconnect the solar farm from the grid and, thus, no over current will be observed. Similar investigation is done for all of the cases described in the earlier sections (3.3.1 to section 3.3.2) and the response of the slope detector is found to be the faster than the magnitude detector. Hence, the magnitude detector technique is used as a secondary detection technique if the primary slope detector technique fails to respond.

3.3.5 Load Switching

Fig. 3.16 illustrates the output current waveforms of the PV solar farm with the fault controller enabled for a fault instance at $t=4$ seconds (non-peak instant) to test the proposed controller for a load switching event. It is observed that the fault detector does not respond to a distributed load switching of approximately 8.9 MVA near the PCC, or a large feeder load switching of 66.7 MVA, as demonstrated in Fig. 3.16 (a) and 3.16 (b) respectively. The PV solar farm is generating 65% of its rated power in this study. During the load switching, the steep change (d/dt) in current is considered as the slope of high frequency spike which does not last long. Therefore, the time delay in the RS flip-flop does not allow the triggering signal output from OR_a (Fig. 3.3) to pass through the RS flip-flop for this transient event and hence the false triggering is avoided at this switching event, as discussed earlier in section 3.2.3.1.



(a)

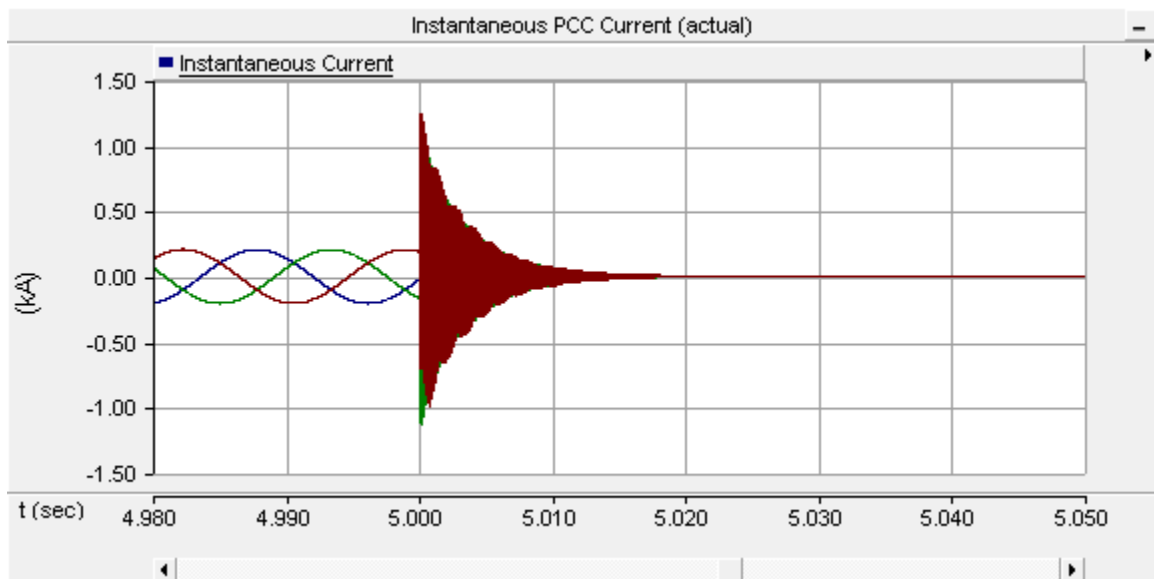


(b)

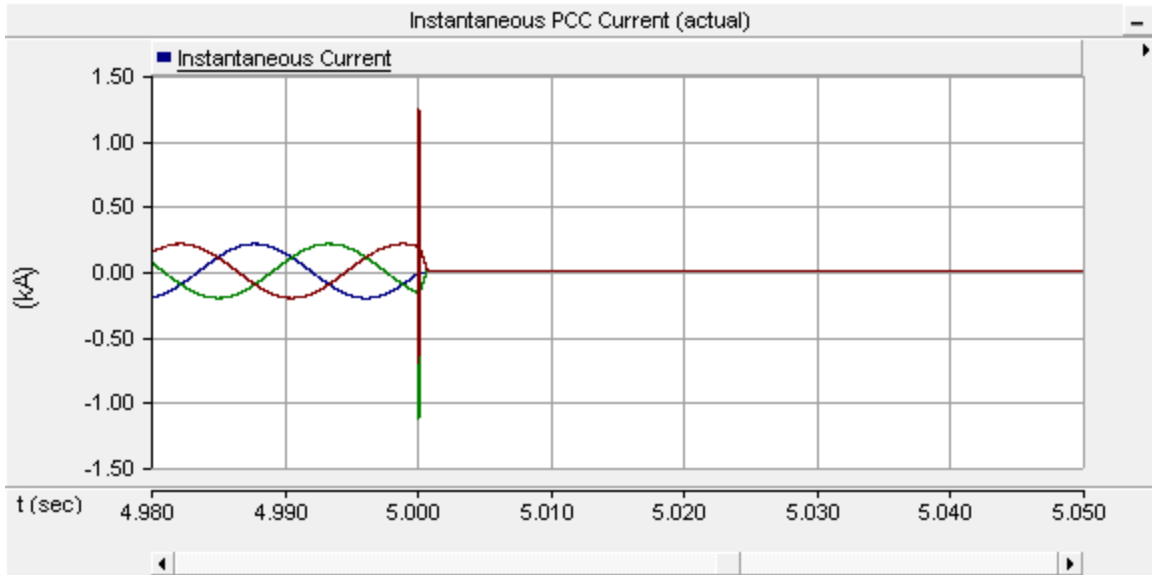
Figure 3.16 PV current with (a) 8.9 MVA and (b) 66.7 MVA load switching.

3.3.6 Filter Capacitor Ringing Effect

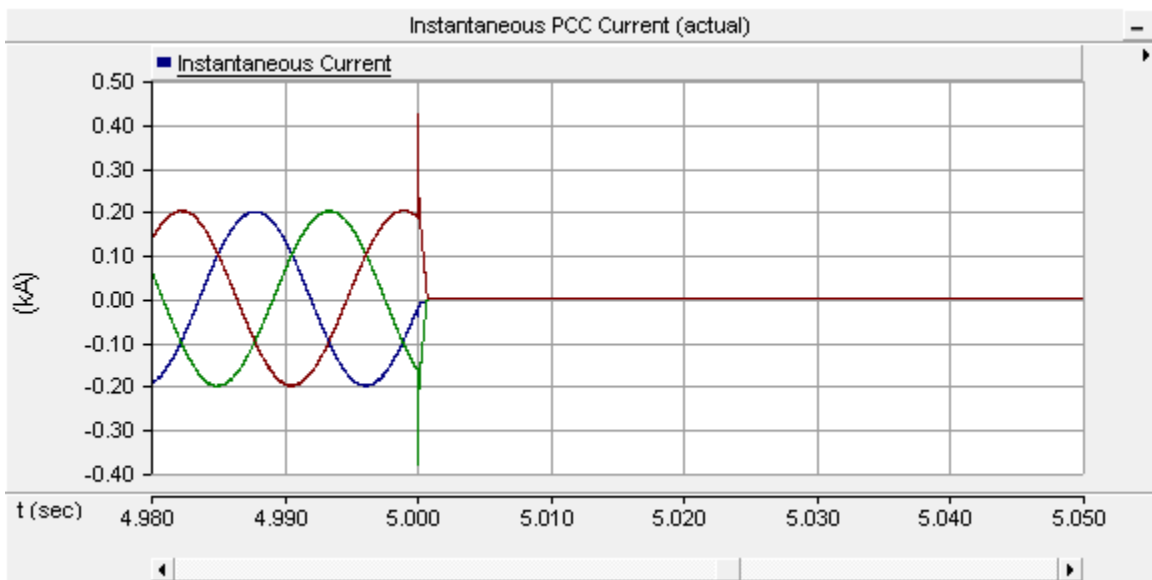
Fig. 3.17 shows the current waveforms at inverter output for a symmetrical fault at $t=5$ seconds.



(a)



(b)



(c)

Figure 3.17 Current at PCC with the proposed controller when (a) filter unit uses smaller damping resistor (b) filter unit disconnects and (c) filter unit uses larger damping resistor.

It is observed that the use of a very small value of damping resistor in the AC filter creates a ringing effect after disconnecting the PV solar inverter upon detection of a fault, as demonstrated in Fig. 3.17 (a). To prevent the ringing effect, the generated triggering signal from the proposed controller 'PVIso' is applied to a set of back-to-back connected

(GTO) thyristor or IGBT switches placed in series with the AC filter capacitors, as shown in Fig. 3.2 (c), to instantly disconnect the filter capacitor from the grid. Thus the ringing effect is eliminated, as demonstrated in Fig. 3.17 (b). The ringing effect may be avoided by using a comparatively larger damping resistor in the AC filter, as demonstrated in Fig. 3.17 (c). In this case, the isolation of the filter capacitor from the AC filter may not be needed to eliminate the ringing effect. However, it should still be isolated as a back-up safety measure.

3.4 Conclusion

In this chapter, a new fast fault detection technique is proposed for PV inverter based DGs. The proposed controller is based on the slope (d/dt) and the magnitude of the PV system output current $|I|$ computation. As soon as it detects the fault it (a) disables firing pulses to inverter, (b) disconnects the PV solar modules from the inverter and, (c) isolates the filter from the PCC. In this new controller, the slope (d/dt) detection technique is used as primary detection strategy whereas the magnitude detection technique is used as a secondary detection strategy. The new proposed controller responds successfully regardless of the type of fault or the location of the fault on the distribution system. It can effectively distinguish between large load switching and fault current.

The performance of this novel fault current controller is demonstrated with EMTDC/PSCAD software on an NRCAN network. As discussed earlier in Chapter 1, the use of traditional technique takes about 7-8 cycles [61] to disconnect a DG with an overcurrent being observed for typically 7-8 cycles. Whereas, the proposed technique does not allow the overcurrent to exceed the peak limit even for the first cycle. Therefore, this new fault detection and management of fault current can create an opportunity to integrate more inverter based DGs into the network. A patent has been filed on this controller design [P.1].

Chapter 4

4 Novel Control of PV Solar System as STATCOM (PV-STATCOM).

4.1 Introduction

A conventional grid connected Photovoltaic PV solar farm utilizes an inverter for converting the DC power output from PV arrays into AC power to be supplied to the grid. As already described in Section 1.5, the STATCOM (a FACTS device) is also based on a voltage sourced converter which functions both as an inverter and rectifier [94]-[96]. A novel control technology was proposed in [57], [117] by which a PV solar farm can be operated as a STATCOM in the night time as well as during day. During the night time the entire inverter capacity of the PV solar farm is utilized as STATCOM, whereas during the day, the inverter capacity remaining after real power generation is utilized for STATCOM operation. Since this STATCOM is based on a PV solar system, it has been given the name PV-STATCOM [166], [167]. Fig. 4.1 demonstrates the operation of a PV solar farm as PV-STATCOM during the night time when the conventional PV solar farm is absolutely idle.

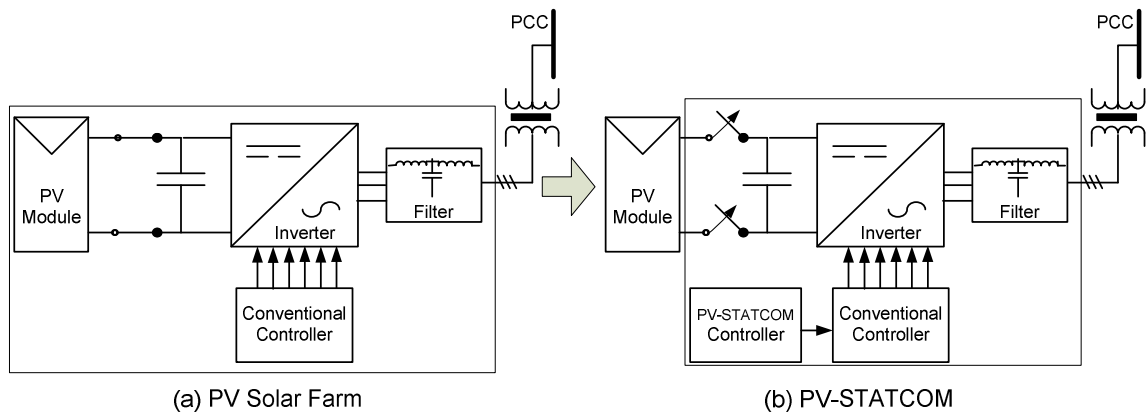


Figure 4.1 PV Solar Farm operation as PV-STATCOM in the night.

The desired STATCOM functionality is implemented by providing an auxiliary PV-STATCOM controller as shown in Fig 4.1. In this thesis, different types of PV-STATCOM controllers have been developed for providing alternative new functions.

4.2 Novel PV-STATCOM Control Concept

While the concept of PV-STATCOM is itself new, two novel types of PV-STATCOM are proposed in this thesis for which a patent has been filed [168],[169]. These are:

- i) PV-STATCOM utilizing “unused” PV solar farm inverter capacity both in night and day, and
- ii) PV-STATCOM utilizing “used” PV solar farm inverter capacity during the day.

These two types of PV-STATCOMs along with the various benefits they offer to power systems are described below:

4.2.1 PV-STATCOM Based on “Un-Used” PV Solar Farm Inverter Capacity

As the PV solar farm remains completely idle during nighttime, the entire capacity of its inverter can be used as STATCOM. However, during daytime the PV solar farm generates real power for the grid either by using the whole inverter capacity (at rated power generation around noon time on sunny days or partial inverter capacity (at a lower level of real power generation during early mornings and late evenings or anytime in a cloudy day). As a result, substantial inverter capacity is left unutilized during the morning, evening, and on cloudy days. Hence, during the daytime the remaining PV inverter capacity can be used to act as STATCOM during daytime without affecting the normal real power generation functionality of the PV solar farm. In other words, there is no real power curtailment due to PV-STATCOM operation and the PV modules do not need to be disconnected from the inverter.

From the rated inverter capacity of ‘ S ’ MVA, the remaining available reactive power ‘ Q ’ for PV-STATCOM operation is obtained as $Q = \sqrt{S^2 - P^2}$, where P is the real power produced by the solar farm. With the data provided by Hydro One from 80MW Sarnia Solar farm in Sarnia, ON, Canada, the real power P and Q capability of the PV solar farm inverter are plotted in Fig. 4.2.

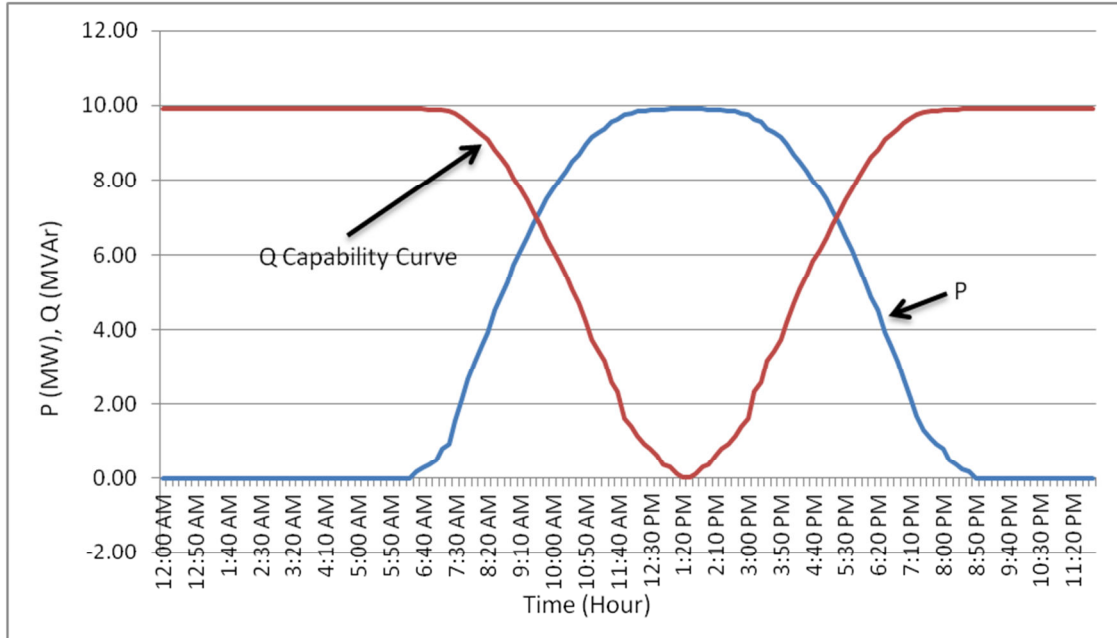


Figure 4.2 Reactive power capability of PV-STATCOM.

This clearly shows that there is a significant amount of unused capacity of a PV solar farm inverter over a 24 hour period, which can be utilized for PV-STATCOM operation.

4.2.2 PV-STATCOM Based on “Used” Solar Farm Inverter Capacity

Another novel control concept of PV-STATCOM examined in this thesis is the disconnection of PV solar farm modules on an emergency demand basis for a temporary period. The PV modules are disconnected completely or partially from the inverter to curtail the PV generation. The newly made available inverter capacity is now utilized as PV-STATCOM to provide dynamic reactive power support for short durations of time during critical events. These are events which could have serious implications on power systems such as critical Induction Motor (IM) failures, or impending blackouts. In Fig. 4.3, for an event of duration t , the shaded area ABCD denotes the curtailment of PV solar farm real power generation, whereas the dotted area AEFD denotes the newly made available ‘ Q ’ support during these events.

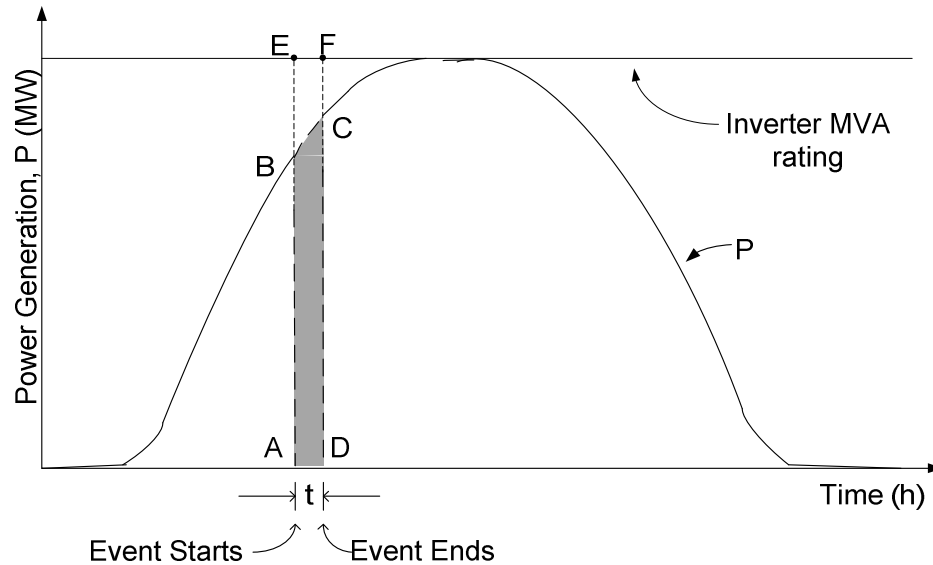


Figure 4.3 PV-STATCOM operation during an event.

4.3 Novel Application of PV-STATCOM Utilizing “Unused” Inverter Capacity.

4.3.1 Line Loss Reduction

In this application an individual PV solar farm or multiple PV solar farms are operated as PV-STATCOMs in a coordinated manner to regulate their PCC voltages at optimal or near-optimal values in order to reduce I^2R heating losses in transmission and distribution networks. The voltage set points at each solar farm are provided through an optimal power flow study. This new application of PV-STATCOM is presented in Chapter 5.

4.3.2 Improvement of Power Transfer Capacity in Transmission Lines

The PV solar farm is operated as a PV-STATCOM for providing controlled reactive power exchange with the transmission system. This results in voltage regulation as well as damping enhancement of electromechanical and inter area oscillations [95],[96]. Both of these functions lead to a much desired increase in transient stability and power transfer capacity across long lines. This novel control aspect is presented in Chapter-7.

In both the above applications, the real power generation capability of the PV solar farm(s) is not affected at all.

4.4 Novel Application of PV-STATCOM Utilizing “Used” Inverter Capacity.

In power systems, there exist critical induction motor loads such as in petrochemical plants, rolling mills, and batch processing plants, where their shutdown, even for a few minutes, could result in a very high loss of revenues, up to millions of dollars. Also during cascading faults, the voltages in the network start sinking, leading to a potential blackout situation.

In both of the above scenarios, there is a strong need for reactive power support at the critical buses.

If PV solar farms are located close to such buses, they can shut down their real power production and operate as PV-STATCOM utilizing their used capacity for a limited duration of time under a pre agreed arrangement with the owners of the critical induction machines or the system operator. This novel control is presented in Chapter-6, for helping the improvement of critical induction motor loads stability.

4.5 Conclusion

PV solar farms remain absolutely unutilized during the night and are only partially utilized during the day. This chapter presents the concepts of a novel use of a PV solar farm inverter as a PV-STATCOM, which can potentially lead to complete utilization of the PV solar farm inverter asset both during night and day. Two sets of novel PV-STATCOM technologies are presented: one based on the “unused” capacity of the solar inverter, and the other based on “used” capacity of the solar inverter. These new applications of PV solar farms can help to improve the performance of power systems. In addition, they can potentially bring new sources of revenue for PV solar farms by providing these benefits, in addition to those earned from the sale of real power.

Chapter 5

5 Reduction of Line Losses Through a Novel Control of PV Solar Farm as PV-STATCOM

5.1 Introduction

Transmission and distribution networks experience I^2R heating losses due to the flow of current I through the resistance R of the lines. In North American systems, the line losses are typically 4-5% of the total power delivered [170]-[172], whereas, in some Asian countries the line losses can be more than 20% [173]. This results in a significant loss of revenue for the system operator.

Line losses are a function of voltages at different buses in a transmission or distribution network. One of the objectives of optimal power flow studies [174] is to determine the voltage set points at different generator buses for optimal power flow by minimizing the losses subject to system operating constraints [174].

This chapter presents a novel patent pending technology whereby PV solar farms operating as PV-STATCOM are utilized for controlling their bus voltages to levels at which line losses can be minimized or substantially reduced. The “optimal” bus voltages can be determined locally by solar farms themselves, or may be computed by the system operator and transmitted to individual PV solar farms. Studies are conducted for both the above scenarios and the resulting decreases in line losses are demonstrated.

The rest of the sections are organized as follows: Section 5.2 formulates an expression for system line loss in a simple two bus network, whereas, Section 5.3 describes the study system and the PV-STATCOM controller. Section 5.4 describes the control strategy of the proposed system. Two case studies are performed for a long feeder in a rural area and presented in Section 5.5 and Section 5.6; one is with a single DG, and the other is with multiple DGs. An economic evaluation of this PV-STATCOM technology is presented in Section 5.7. Finally, the work is concluded in Section 5.8.

5.2 Loss Formulation of a Two Bus Network with a Distributed Generator.

Fig. 5.1 depicts a typical line having resistance R and reactance X . The sending end voltage is $V_S \angle \delta^\circ$ where the receiving voltage is $V_R \angle 0^\circ$. P_S and Q_S denote the sending end real and reactive power flow in the line, and P_R and Q_R denote the net receiving end real and reactive power. A Distributed Generator (DG) is connected at the end of the line where the aggregated load is also connected. The line current is $I \angle \theta^\circ$. The complex power flow \bar{S}_R in the line at the receiving end is expressed as:

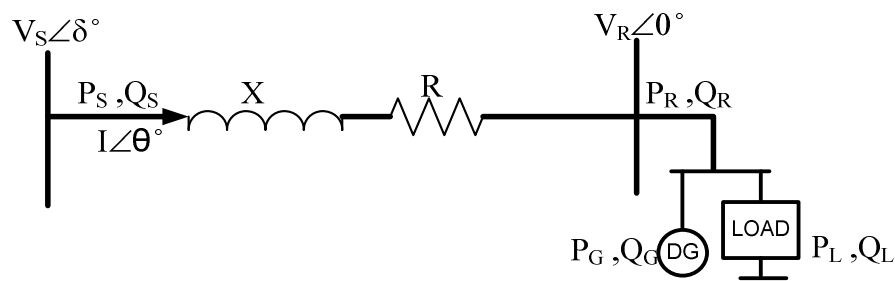


Figure 5.1 A two bus network.

$$\bar{S}_R = P_R + jQ_R = \bar{V}_R \cdot \bar{I}^*, \text{----- (5.1)}$$

$$\text{or, } \bar{S}_R^* = P_R - jQ_R = \bar{V}_R^* \cdot \bar{I} \text{----- (5.2)}$$

The real power loss in the line P_{loss} is given by:

$$P_{Loss} = I^2 \cdot R = R \cdot (P_R^2 + Q_R^2) / V_R^2 \text{----- (5.3)}$$

where,

$$I = \sqrt{\frac{(P_R^2 + Q_R^2)}{V_R^2}}, S_R = \sqrt{P_R^2 + Q_R^2}, \bar{V}_R^* = \bar{V}_R = V_R \angle 0.$$

By neglecting the line charging of the overhead line, the receiving end voltage can be expressed as:

$$V_R \angle 0^\circ = V_S \angle \delta^\circ - \bar{I}(R + jX) \text{----- (5.4)}$$

Substituting I from (5.3) in (5.1) and combining with (5.3), we get:

$$V_R^2 = \frac{V_S^2 - 2.K_1 \pm \sqrt{\{(V_S^2 - 2.K_1)^2 - 4.(K_1^2 + K_2^2)\}}}{2}, \text{----- (5.5)}$$

$$\text{and, } \delta = \tan^{-1} \left(\frac{K_2}{V_R^2 + K_1} \right) \text{----- (5.6)}$$

where, $K_1 = (P_R.R + Q_R.X)$, and, $K_2 = (P_R.X - Q_R.R)$

The receiving end power P_R , Q_R is the net power consumption at the receiving end:

$$P_R = (P_L - P_G), \quad \text{and, } Q_R = (Q_L - Q_G)$$

Therefore, (5.3) becomes:

$$P_{Loss} = I^2.R = R. [(P_L - P_G)^2 + (Q_L - Q_G)^2] / V_R^2 \text{----- (5.7)}$$

Using the positive quantity before the radical in the receiving end voltage expression of (5.5) [175], the loss can be found from (5.7) as follows:

$$P_{Loss} = I^2.R = \frac{2R. [(P_L - P_G)^2 + (Q_L - Q_G)^2]}{V_S^2 - 2.K_1 + \sqrt{\{(V_S^2 - 2.K_1)^2 - 4.(K_1^2 + K_2^2)\}}} \text{----- (5.8)}$$

where, K_1 and K_2 can be rewritten as

$$K_1 = [(P_L - P_G).R + (Q_L - Q_G).X], \quad \text{and, } K_2 = [(P_L - P_G).X - (Q_L - Q_G).R]$$

It is evident that $P_{loss} = f(P_L, Q_L, V_S, R, X, P_G, Q_G)$, where all the quantities are constant for a given network with known DG power generation and loads. Thus by variation of ' Q_G ' the loss can be varied. The receiving end voltage V_R also changes with the variation of ' Q_G ' as seen from (5.5). Therefore, an optimal V_R can be determined for which the loss becomes a minimum.

The derivative of ' P_{loss} ' with respect to ' Q_G ' in (5.8) is equated to zero, which returns an optimal value of ' Q_G '. Inserting this ' Q_G ' into (5.5) gives the optimal set point of the voltages V_R for minimum system loss. Therefore, this optimal V_R is achieved by controlled reactive power exchange with the PV-STATCOM.

The above analysis is for a simplistic network. It is obvious that for a more complex network an Optimal Power Flow (OPF) solution is required which provides the voltage set point for minimum line loss. According to OPF formulation the voltage magnitudes

and the angles at each bus acts as state variables, real and reactive powers acts as the control variables [203].

There are also some internal losses for operating the DGs. For power inverter based DGs like PV solar farms these losses, P_{loss_inv} , are associated with IGBT conduction, switching and snubber losses which can be expressed in terms of a polynomial expression [176]-[178]:

$$P_{loss_inv} = C_S + C_V \cdot S + C_R \cdot S^2 \quad (p.u.) \quad (5.9)$$

where, S is the apparent power output from the DG inverter expressed in p.u., C_S is associated with the standby fixed losses, C_V is associated with voltage dependent losses and C_R is associated with resistive losses for IGBT conduction. The efficiency, η , of the inverter can be expressed as:

$$\eta = \frac{S}{(S + P_{loss_inv})} \quad (5.10)$$

Therefore, for a typical inverter efficiency curve [179] having an efficiency of 98%, by using the curve fitting technique of MATLAB with (5.9) and (5.10), the values of C_S , C_V , and C_R are determined to be 0.2414%, 0.00364% and 0.0002%, respectively.

5.3 System Model

5.3.1 System Description

As network losses are associated with steady state operation of the power system, the study is performed using load flow software PowerWorld Simulator [180]. However, for a better understanding of the control concepts of the PV-STATCOM, the system is simulated in EMTDC/PSCAD and the output is validated with the PowerWorld Simulator output. In PowerWorld Simulator the PV solar farm is modeled as a P-Q bus providing zero reactive power, while acting as conventional PV system. However, when the PV solar farm operates as PV-STATCOM, it is modeled as a P-V bus considering that the PV solar farm is producing power P (based on its maximum power point- MPP) at the optimal voltage V_R to result in minimum loss.

On the other hand, in EMTDC/PSCAD, the conventional PV solar farm along with the Maximum Power Point Tracking (MPPT) feature is modeled as given in Chapter 2.

5.3.2 PV System Control

Fig. 5.2 depicts the detailed diagram for a conventional PV solar farm to act as PV-STATCOM with an auxiliary PV-STATCOM voltage controller, and the optimal power flow (OPF) unit.

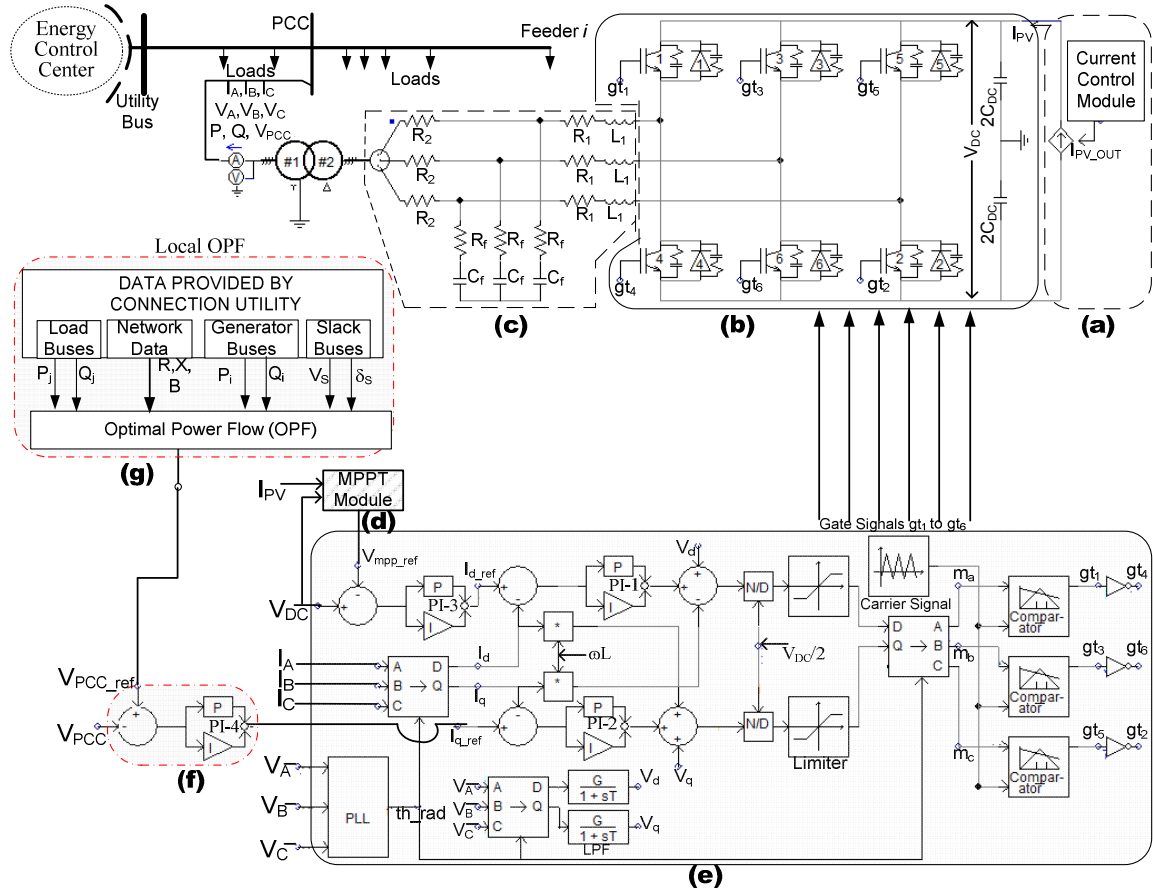


Figure 5.2 Detailed PV-STATCOM configuration in the study system (a) PV array model, (b) IGBT matrix of inverter, (c) L-C-L filter, (d) MPPT module, (e) conventional inverter controller, (f) PCC voltage regulator and (g) Optimal Power Flow unit.

5.3.2.1 Conventional PV System Control

The conventional PV solar farm controller regulates the reactive power output of the inverter such that it can perform unity power factor operation along with the DC link voltage control, as demonstrated in Chapter 2. The d-axis current control loop regulates the DC voltage and the real power transfer through two PI regulators (PI-1 and PI-3), as shown in Fig. 5.2 (e). However, the q-axis current control loop regulates the reactive

power to zero through a single PI controller (PI-2), as shown in Fig. 5.2 (e). The DC link voltage reference is set by the MPPT output as shown in Fig. 5.2 (d) such that, corresponding to MPP voltage, all of the available real power output from the PV modules is transferred to the network through the inverter.

5.3.2.2 PV-STATCOM with PCC Voltage Controller

To operate the PV system as PV-STATCOM and to control the PCC bus voltage, a ‘PCC voltage control module’, as shown in Fig. 5.2 (f), is added to the q-axis current control loop by adding an additional PI controller PI-4 [62],[108]. It regulates the voltage at the Point of Common Coupling (PCC) by comparing the measured voltage signal at PCC, V_{PCC} , with the reference voltage value of PCC, V_{PCC_ref} . The output of this module sets the reference value of ‘ I_q ’ which ultimately controls the reactive power flow from the inverter using the remnant capacity of the inverter after real power generation. The I_d current control loop serves the same purpose of the DC link voltage control as in a conventional PV solar system control. The rest of the controller is the same as the conventional controller. In the proposed novel control, the “optimal” set point voltage of the PCC, V_{PCC_ref} , is determined locally by the DG operator, by running an optimal power flow program as shown in Fig. 5.2 (g). This utilizes system data which includes real power, P_i and reactive power Q_i of all ‘ i ’ generators, loads P_j , Q_j at all ‘ j ’ bus, network resistance R , inductance, X , susceptance, B values, and the slack bus voltage V_s , and angle δ_s .

5.4 Control Strategy for Line Loss Reduction

5.4.1 Single PV System as PV-STATCOM

It is proposed that at the outset, the PV solar farm reaches an agreement with the connecting utility to provide voltage regulation at its PCC for reducing loss in the feeder to which it is connected, and receives revenue for loss reduction. The utility agrees to provide all system data required regarding the generators, loads, and line parameters to the PV solar farm. The PV solar farm performs this optimal load flow at regular intervals and determines a desired voltage reference for the PCC, V_{PCC_ref} . The PV solar farm acts as a PV-STATCOM and with its available inverter capacity (fully in the night and

partially during the day), exchanges (injects or absorbs) controlled reactive power with the network to bring the PCC voltage equal to or as close as possible to V_{PCC_ref} .

5.4.2 Coordinated Control of Multiple PV Systems as PV-STATCOMS

In this case, the utility reaches an agreement with multiple PV solar farms to maintain their PCC voltages at “optimal” levels in a coordinated manner to reduce line losses in the complete utility network and to be financially compensated for providing this service. The control strategy is depicted in Fig. 5.3, where the utility’s Energy Control Center centrally performs an optimal load flow at regular intervals and determines the desired PCC voltage references for each of the participating PV solar farms. The voltage reference set points are communicated to all the participating PV solar farms through bidirectional communication links as shown in Fig. 5.3.

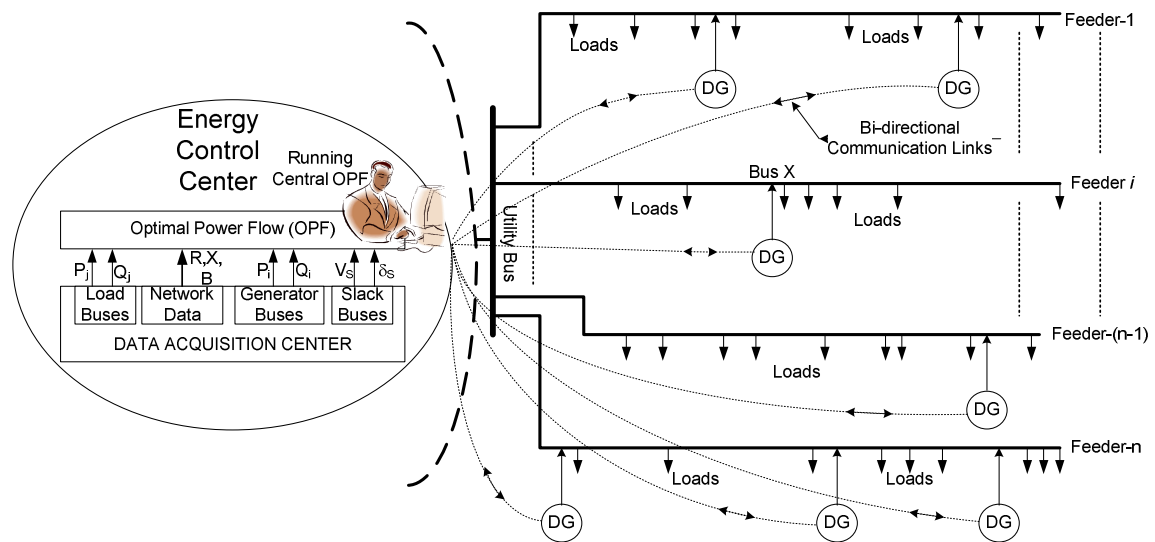


Figure 5.3 Schematic diagram of control co-ordination strategy

5.5 Case Study 1: Radial Feeder with Single PV System

5.5.1 Scenario-1

Fig 5.4 depicts a radial feeder with a length of 48 km connected with a 12 MW PV solar farm at the end of the feeder. A load of 4MW, 2MVA_r is also connected at the end of the feeder. The network loss is studied for this system at different levels of power generation with the proposed function of the PV solar farm as a PV-STATCOM.



Figure 5.4 Scenario 1: PV system connected at feeder end.

The voltage profile for different levels of PV power generation at unity power factor is presented in Fig. 5.5.

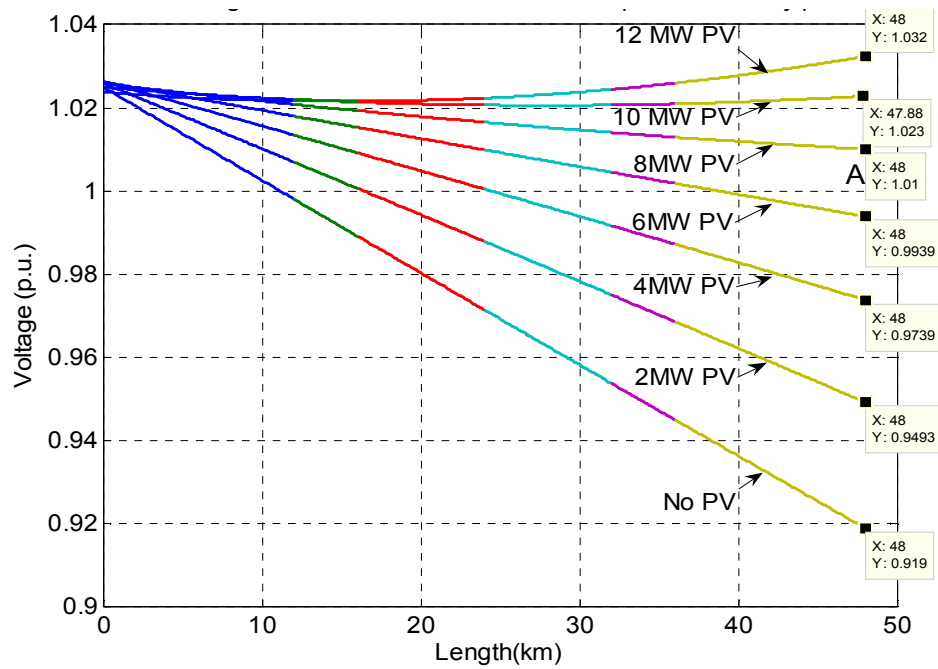


Figure 5.5 Voltage profile with conventional PV solar farm operation.

It is seen that the voltage rises with injection of real power and hence reduces the system losses, which is expected [118]-[125], [130]. The observed magnitude of voltage increase is compared to the voltage rise predicted by (5.5) and (5.6). For instance, in the case of a 12 MW solar farm operating at unity power factor with a load of 4MW and 2MVar, the observed voltage rise at the receiving end is 0.113 pu, while the analytically predicted rise is 0.118 pu. This 4% discrepancy is attributed to line charging effect which is neglected in the analytical prediction.

Fig. 5.6 shows the total losses for different power outputs with varying PCC voltages. These plots are used to determine the “best” value of PCC voltage for minimizing line losses. The PCC voltage is controlled to always remain between 0.94 pu to 1.06 pu, as stipulated by the utility. It is seen that for certain specific PCC voltages, the line losses become very low or the lowest.

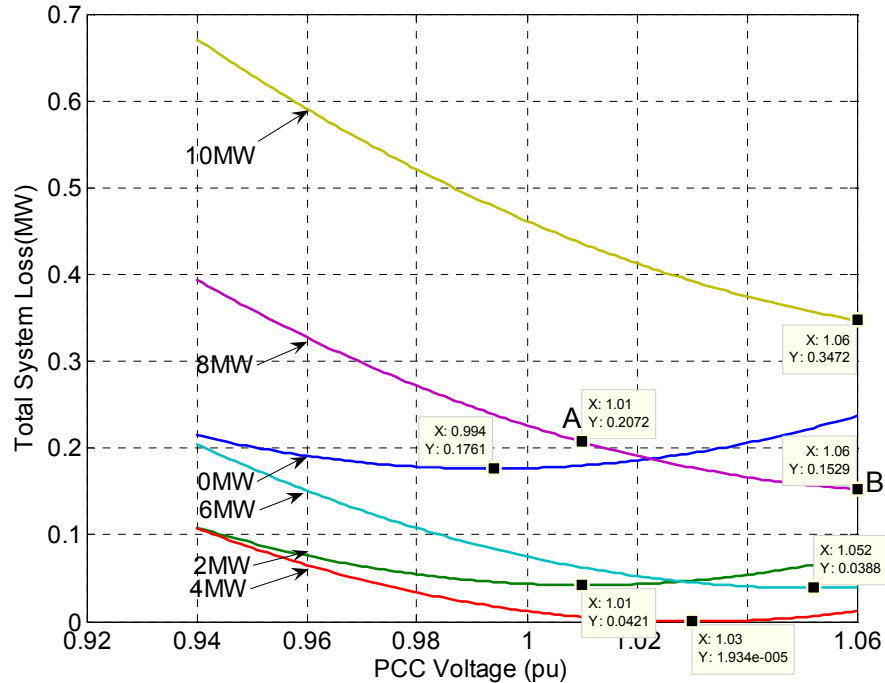


Figure 5.6 Loss profile to identify optimal set point of PCC voltage.

Fig. 5.7 illustrates the feeder voltage profile when the PV solar system is operated as a PV-STATCOM to maintain the PCC voltage at the above obtained PCC voltage set point, V_{set} for different real power outputs from the PV system.

The line losses for each value of real power output from the PV system, when it is operated conventionally and as a PV-STATCOM, are illustrated in Table 5.1. The corresponding PCC voltage set point V_{set} , PV-STATCOM reactive power Q_{PV} , and the STATCOM internal loss computed from (5.9) are compiled in the Table (5.7). It is noted that the STATCOM loss during the night is considerably higher than the daytime operation. This is due to the fact that during the night, the PV-STATCOM does not generate any real power and the whole inverter is used solely as a PV-STATCOM. Therefore, all of the losses in the STATCOM correspond to PV-STATCOM operation

during the night. On the other hand, during the daytime, as the PV system is producing real power, the losses due to the additional reactive power support of PV system as PV-STATCOM are only accounted for as STATCOM loss. Finally, the net loss reduction due to PV-STATCOM operation as compared to that of the conventional PV system operation is presented in Table 5.1. It is seen that the net loss savings are substantial and are in the range of 42-60kW.

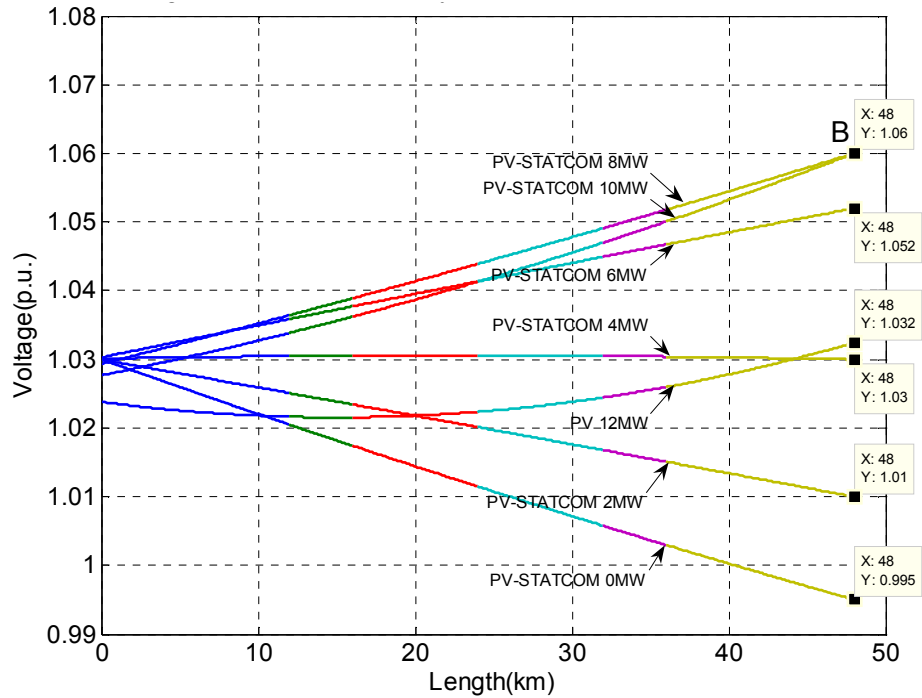


Figure 5.7 Voltage profile with PV-STATCOM operation.

Table 5.1 Line Loss Evaluation for Scenario 1.

PV Active Power Generation (MW)	CONVENTIONAL OPERATION: Line Loss (kW) [x]	PROPOSED PV-STATCOM OPERATION				Net Loss Reduced (kW) [x-y-z]	
		PCC Set Point Voltage V_{setr} (pu)	Reactive Power, Q_{PV} MVar	Line Loss (kW) [y]	STATCOM Loss (kW) [z]		
Night	0	250.7	0.994	2.415	176.1	29	45.6
Day	2	92.1	1.01	2.021	42.1	0.03	49.97
	4	42.1	1.03	1.918	0	0.016	42.084
	6	83.7	1.052	2.026	38.8	0.012	44.89
	8	207	1.06	1.738	152.8	0.0068	54.19
	10	406.5	1.06	1.272	347.3	0.003	59.2
	12	680.4	-	-	-	-	-

5.5.2 Scenario 2

In this scenario, the 12 MW PV solar farm is relocated to the middle of the same feeder, as depicted in Fig 5.8. The load of 4MW, 2MVA_r remains connected at the end of the feeder. The network loss is studied for this system at different levels of power generation, as well with the proposed operation of the PV solar farm as a PV-STATCOM.

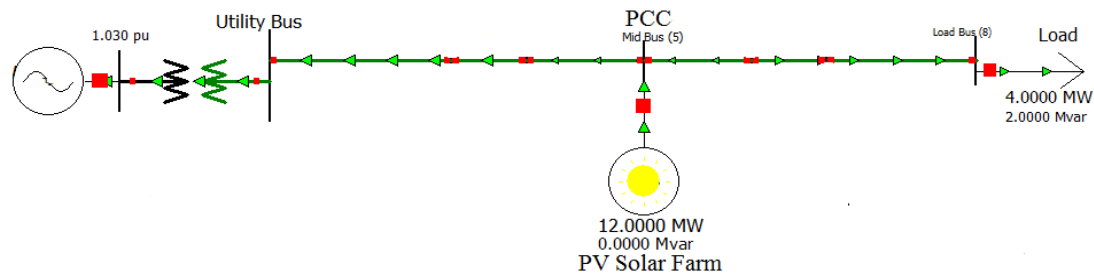


Figure 5.8 Scenario 2: PV system connected in the middle of feeder.

As in Scenario 1, the voltage magnitude at the PCC also increases and satisfies equations (5.5) and (5.6) in Scenario 2. The network losses with the conventional operation of the PV system are compiled in Table 5.2.

Table 5.2 Line Loss Evaluation for Scenario 2.

PV Active Power Generation (MW)	CONVENTIONAL OPERATION: Line Loss (kW) [x]	PROPOSED PV-STATCOM OPERATION				Net Loss Reduced (kW) [x-y-z]	
		PCC Voltage Set Point V_{setv} (pu)	Reactive Power, Q_{PV} MVA _r	Line Loss (kW) [y]	STATCOM Loss (kW) [z]		
Night	0	250.7	1.015	2.766	204.1	29	17.6
Day	2	173.7	1.025	2.612	135.1	0.047	38.55
	4	144.6	1.035	2.534	109.5	0.0268	35.07
	6	159.9	1.045	2.527	124.9	0.0185	34.98
	8	216.9	1.06	2.936	179.1	0.019	37.78
	10	313.7	1.06	2.365	270.4	0.01	43.29
	12	448.7	-	-	-	-	-

With PV-STATCOM, the PCC voltage is maintained between 0.94 pu to 1.06 pu. It is observed from Table 5.2 that there is a net reduction in losses while operating as a PV-STATCOM. However, comparing Table 5.1 and Table 5.2, it is seen that the net loss reduction in Scenario 2 is generally lower than in Scenario 1. This is because the PV

solar system is located at a distance from the load, thus the net current and power flow on the line is relatively higher, causing more losses.

5.6 Case Study 2: Radial Feeder with two PV Systems

5.6.1 Scenario-3

In this scenario, a total of 12 MW PV solar farm (as considered in Case Study 1) is connected in a distributed manner with two 6 MW PV solar farms, as shown in Fig. 5.9. One is connected at the middle of the feeder and the other is connected at the end of the feeder. The same load of 4MW, 2MVAR remains connected at the end of the feeder. The network loss is studied for this system at different levels of power generation as well with the proposed operation of the PV solar farm as a PV-STATCOM.

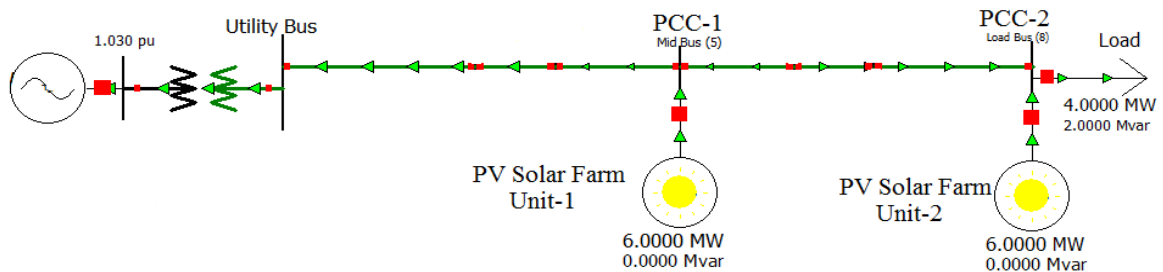


Figure 5.9 Scenario 3: Two PV systems connected at the middle of feeder and at the end of the feeder.

Fig. 5.10 illustrates the voltage profile at different levels of PV power generation at unity power factor for the system of Scenario 3. The rise in voltage at each PCC, due to the injection of real power by the conventional PV solar farm operation, is observed to be in agreement with the modified versions of equations (5.5) and (5.6) for 2 DG systems. The real power generation at two conventional PV systems is varied simultaneously by the same amount (assuming similar solar radiation) and the losses in the network are presented in Table 5.3. In this scenario, with the use of both solar farms as PV-STATCOMs, the PCC voltages are also maintained within 0.94 pu to 1.06 pu. The net loss reduction for a different combination of PCC set point voltages at both PCCs is illustrated in Table 5.3. It is observed that the net loss reduction is higher than in Scenario 1, as presented in Table 5.1. This is due to the relative locations of the load and

generation in the system, and to the amount of additional generated power from the PV system transferred as a reverse power flow to the grid.

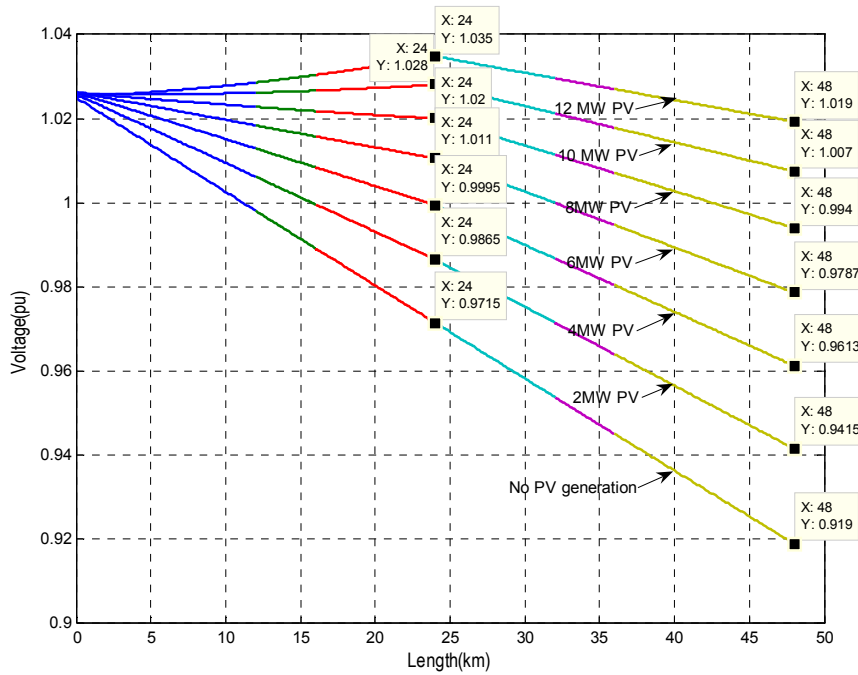


Figure 5.10 Voltage profile with two solar farms for Scenario 3

Table 5.3 Line Loss Evaluation for Scenario 3.

	Total PV Active Power Gen. (MW)	CONVENTIONAL OPERATION: Line Loss (kW) [x]	PROPOSED PV-STATCOM OPERATION					Net Loss Reduce (kW) [x-y-z]	
			PCC-1		PCC-2		Line Loss kW [y]		STATCOM Loss (kW) [z]
			V _{SET1} (pu)	'Q _{PV1} ' (MVar)	V _{SET2} (pu)	'Q _{PV2} ' (MVar)			
Night	0	250.7	1.01	0.3061	0.99	2.1122	175.8	29.05	45.85
Day	2	125.5	1.02	-0.0032	1.005	2.092	69.3	0.0486	56.15
	4	67.1	1.03	-0.0832	1.02	2.0225	20.5	0.031	46.57
	6	67.9	1.04	-0.0844	1.035	1.9788	24.8	0.0217	43.078
	8	122.5	1.05	-0.0128	1.05	1.96	78.4	0.0166	44.08
	10	227.1	1.06	0.5304	1.06	1.5629	178.3	0.01	48.79
	12	379.4	-	-	-	-	-	-	-

5.6.2 Scenario 4

Fig. 5.11 depicts two 6MW solar farms (totaling 12 MW as considered in Scenario 1) connected at 1/3rd and 2/3rd distance from the utility bus. As well, the same load of 4MW, 2MVar is connected at the end of the feeder. The network losses are determined in a

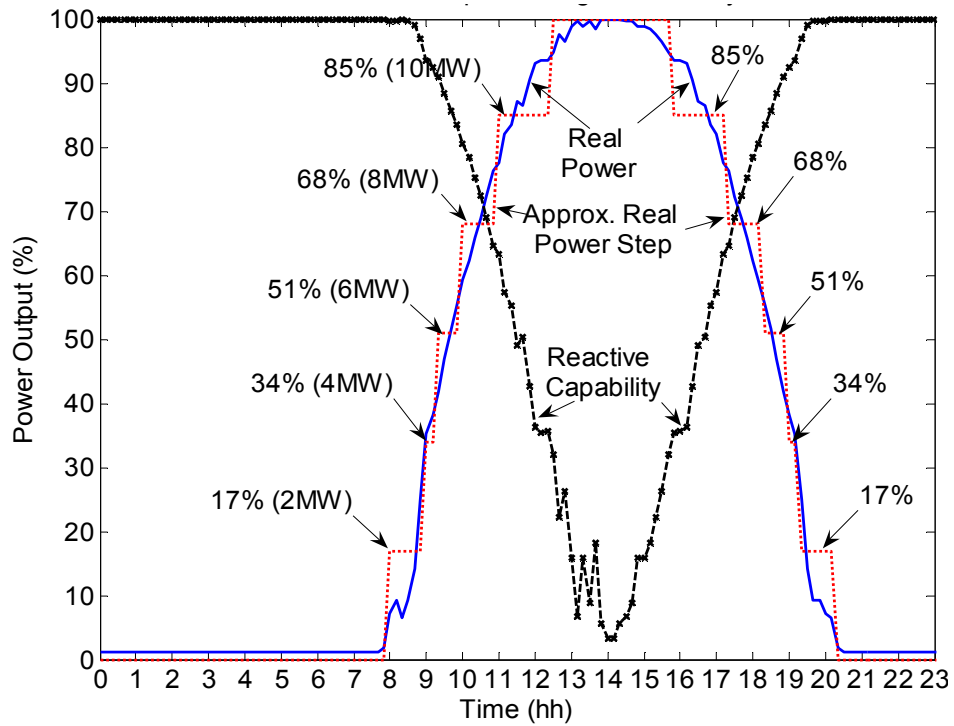
5.7 Economic Evaluation and Discussion

Fig. 5.12 (a) depicts the real power output (solid line) and reactive power capability (bold dotted line) of an actual 12 MW (name withheld due to confidentiality) PV solar farm over one day. For the study system, the PV system is assumed to change its power output in several steps shown by dotted lines representing its average value during different periods of the day. It is considered that the generation remains constant around an average value of generation for a certain period of time and changes to another step of generation for another period of time.

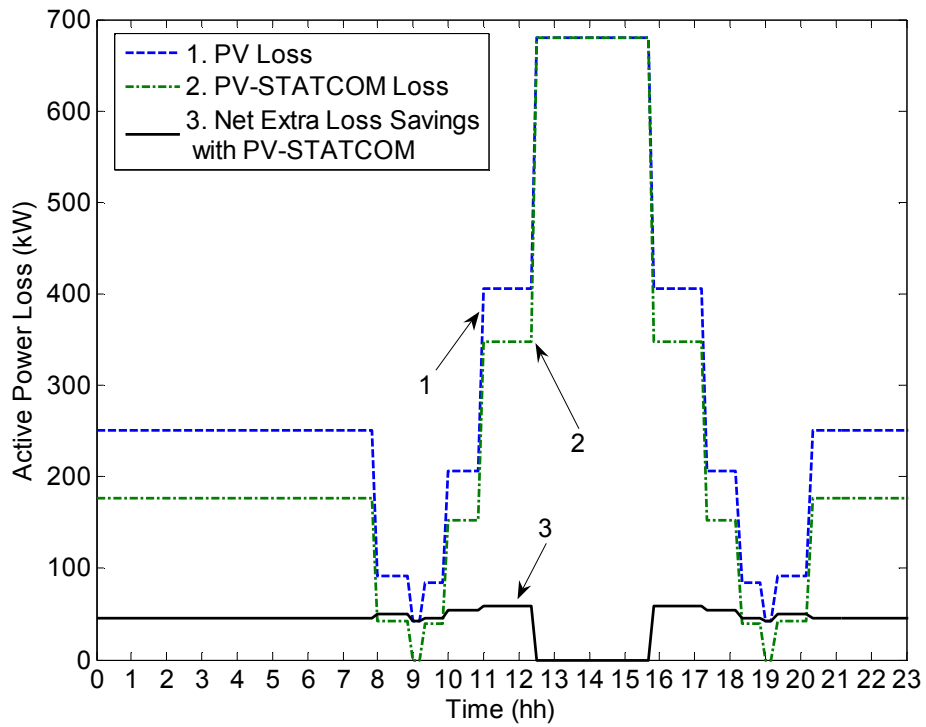
Fig. 5.12 (b) presents the losses and net loss savings with the PV-STATCOM operation for Scenario 1. The total loss reduction is calculated with the use of Table 5.3 for every step change of PV power generation, as given in Fig. 5.12 (a), and plotted over one day in Fig. 5.12 (b). It is noted that during night time when the conventional PV system is not generating any power, the network losses (presented by blue dotted line) are higher than the losses while operating as a PV-STATCOM. Therefore, a net loss reduction is achieved during the night time with the use of a PV-STATCOM. Similarly, during early morning and late evening the PV-STATCOM also reduces line losses.

Similar results of net loss reductions with the use of PV-STATCOMs are obtained for Scenarios 2-4. Fig. 5.12(c) plots the net loss reduction with the use of a PV-STATCOM operation for all scenarios. By comparing these plots, the net energy loss reductions over one day are compiled in Table 5.5. The cost of the energy is calculated at a rate of \$0.06 per kWh. It is evident from Fig. 5.12 (c) that the power loss reduction for Scenario 1 with a single DG at the load bus is much higher than the Scenario 3 with distributed DGs at the mid-bus and load bus during the day. As a result, it leads to higher net energy savings for Scenario 1 as presented in Table 5.5. On the other hand, the energy savings for Scenario 4 with distributed DGs at 1/3rd and 2/3rd locations on the feeder are much higher than in Scenario 2, with single DG at the mid-bus. It is noted that there is always a net loss reduction with the proposed control of a PV-STATCOM, which is dependent upon the location and size of the DGs and loads. The amount of energy savings with the proposed PV-STATCOM for the study system in Scenario 1 is capable of providing

electricity to 30 homes free of cost all year long, assuming a single home consumes 1000kW/h per month [181].



(a)



(b)

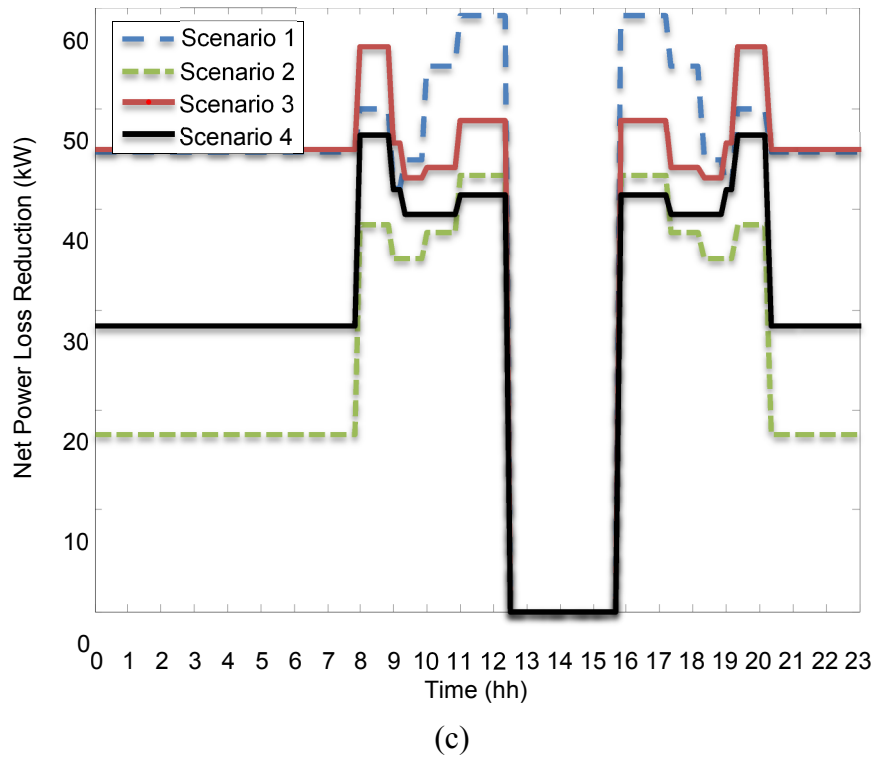


Figure 5.12 (a) PV-STATCOM reactive capability, (b) line loss reduction with PV-STATCOM for scenario 1 and (c) comparison of loss reduction with PV-STATCOMs in different scenarios.

Table 5.5 Summary of Energy Loss Savings and Cost Savings.

Scenarios	Energy Savings (kWh/day)	Energy Consumption of Equivalent Number of Homes	Cost Savings (CAD \$/year)
1	1005.6	30	22,022
2	557.88	16	12,217
3	939.19	28	20,568
4	710.27	21	15,555

5.8 Conclusion

It is known that Distributed Generators (DGs), while conventionally generating real power at unity power factor, improve the network voltage profile based on the generation levels, and hence reduce the line losses [118]-[125], [130]. In this chapter, a novel control of a PV-STATCOM with the use of remnant inverter capacity is demonstrated to reduce line losses even further in a radial system through appropriate voltage control. The

optimal voltage reference is obtained from the network operator running a centralized Optimal Power Flow (OPF) for the whole system, or by the individual owner of the participating DGs. The voltage regulation with the proposed PV-STATCOM technology at these optimal set points gives a net loss reduction even after accounting for the operational losses of the PV-STATCOM. Following are the conclusions for the four scenarios in a radial network.

(i) Comparing Scenarios 1 to 4, it is observed that the PV-STATCOM control is more effective in reducing line losses when connected close to the load.

(ii) Comparing Scenarios 2 and 4, it is noted that more distributed voltage control than a centralized mid-point voltage control by the PV-STATCOM results in higher loss reduction.

Overall, the annual cost of energy savings by such a novel PV-STATCOM control is substantial. For the 12MW PV solar farm based study system, the energy saving is sufficient enough to power 30 homes. It is recommended that a mechanism be evolved to compensate solar farms for providing such loss reduction in utility networks.

In this chapter, optimal load flow studies have not been performed. However, best (near optimal) voltage set points have been determined by a set of systematically conducted load flow studies. The objective here is to demonstrate the novel concept of PV-STATCOM control for loss reduction by appropriately selecting voltage set points. However, the recommendation is to use OPF in large real power networks.

Chapter 6

6 Prevention of Instability of Critical Induction Motor Load with a Novel Control of PV Solar Farm as PV-STATCOM.

6.1 Introduction

Power systems are commonly faced with disturbances, such as faults and outages of equipment (transformers, lines, generators etc.). These disturbances cause voltage fluctuations which can be severe if the power system is weak. Faults in such weak networks can potentially result in shut down of Induction Motor (IM) loads due to voltage instability, lack of reactive power support, etc. In some cases IM loads are critical such as those used in process control, rolling mills, etc. Shutdown of these critical IM loads even for a very short duration as few minutes can result in huge losses to the industrial facility using these IMs [182].

This chapter presents another new application of PV-STATCOM to provide voltage support to a critical voltage sensitive induction motor load connected in the vicinity of a solar farm. The novel fast fault detection technique described in Chapter-3 is integrated with the PV system to sense any fault on the grid. Upon detection of a fault, the PV solar farm inverter transforms into a PV-STATCOM and provides the required voltage regulation. A set of PV solar panels are temporarily disconnected from the DC side of the inverter while the inverter still remains connected with the AC grid. As a result, during day time, the real power generation is partially or fully curtailed as required. The inverter capacity is thus freed up to provide required amount of reactive power support to the grid for a short duration of time during fault and post fault recovery period.

In this chapter, the performance of PV solar system is compared for (i) conventional operation, and (ii) PV-STATCOM operation.

In section 6.2, the system model is described whereas in section 6.3 the performance and detailed simulation study results of the proposed PV-STATCOM are presented. Finally, section 6.4 concludes the chapter.

6.2 System Model

The one line diagram for the study system is presented in Fig. 6.1 which is modeled in an EMTDC/PSCAD environment.

6.2.1 Study System

The same study system described in Chapter 3 is adopted for this study. However, the static load at the end of the feeder is replaced with an Induction Motor (IM) load. The detailed parameters of the source and network are given in Chapter 3. A 7.5MW PV solar farm is connected at the feeder end as given in Chapter 3. The parameters of the solar farm model are given in Appendix-B.

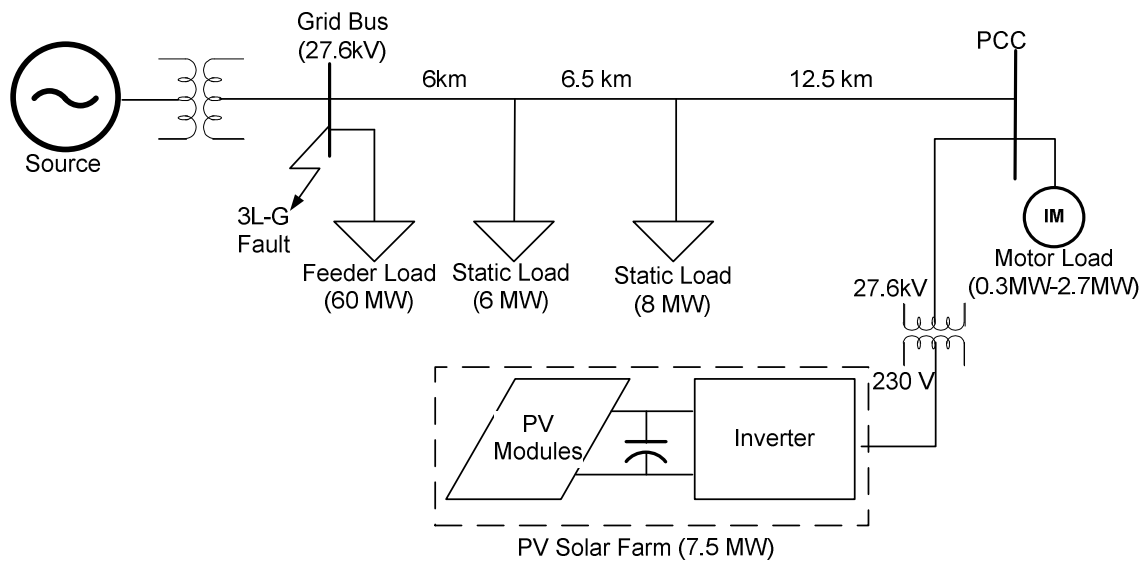


Figure 6.1 One line diagram of study system.

6.2.2 Induction Motor (IM)

A 400 HP (300kW) squirrel cage IM load is modeled in detail. The IM parameters are obtained from the manufacturer's datasheet of American Motors [183] and given in Appendix-C. The obtained parameters are converted to fit into the EMTDC/PSCAD library model [165] by using the conversion expressions given in [184], and calculated in Appendix-C. As the IM is rated for lower voltage, a step down transformer (not shown in the one line diagram) is used to match the IM voltage ratings.

6.2.3 Proposed PV-STATCOM Control

The proposed operation of a PV system as a PV-STATCOM is illustrated in Fig. 6.2, in the form of a generalized block diagram.

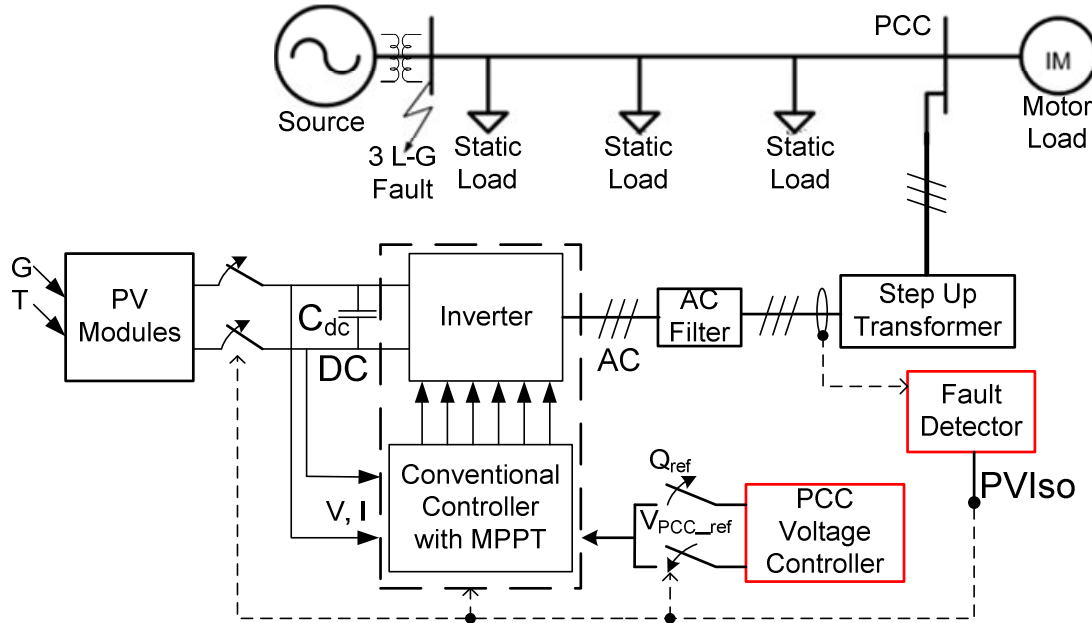


Figure 6.2 Conceptual block diagram of proposed PV-STATCOM system.

In this figure, the inverter IGBT, DC link capacitor, AC filter, MPPT, and the conventional PV inverter controller are the components of a conventional PV solar farm. The PCC voltage controller is incorporated with the conventional PV system to operate it as a PV-STATCOM upon sensing any fault on the network. The fault detector unit comprises the fault detection module and the associated switches to turn off the PV modules and MPPT, and turns on the PCC voltage controller for PV-STATCOM operation.

The simulation model of this system is presented in detail in Fig. 6.3. The current control module representing the PV modules, the inverter IGBT matrix with DC link capacitor, AC filter, MPPT, and the conventional controller are shown in Fig 6.3 (a)-(e), sequentially. The descriptions for modeling these components are provided in Chapter 2. Fig 6.3 (g) presents the PCC voltage control module that was discussed in Chapter 5. Fig. 6.3 (f) depicts the fault detection module, whereas Fig. 6.3 (h) illustrates the DC switches to disconnect the PV modules from the inverter.

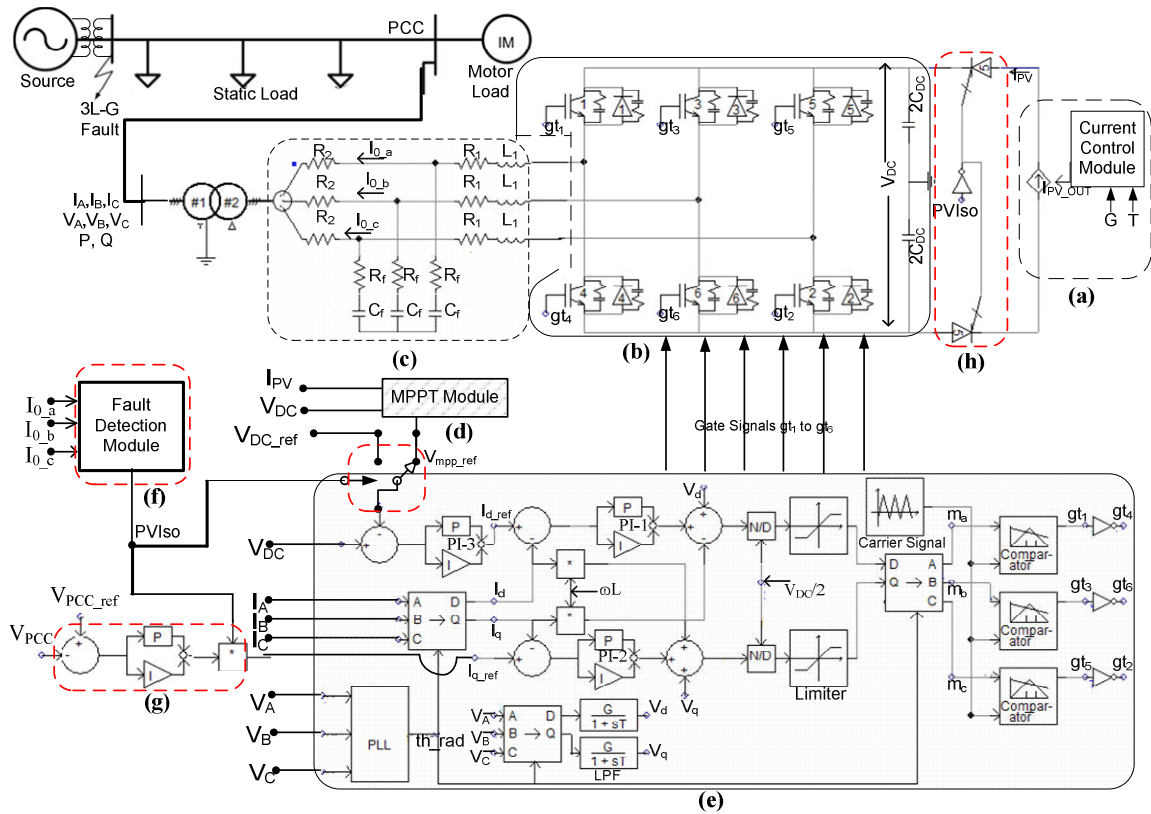


Figure 6.3 Detailed system diagram in EMTDC/PSCAD

The normal operation of a PV solar farm, through conventional controller of the PV inverter, ensures unity power factor at PCC, as described in Chaptre 2. The MPPT technique is implemented with the inverter controller while operating as a conventional PV solar farm. The DC link terminal voltage V_{dc} and PV current I_{pv} are used for MPPT operation as described Chapter 2. It is noted that during normal operation, the fault detection module does not generate any triggering signal.

For the proposed PV-STATCOM operation, the control technique is described as follows:

As soon as any fault is detected the grid connected PV solar farm begins operating as a PV-STATCOM with the help of a fault detection module. The fault detection module shown in Fig. 6.2 (f) monitors the inverter output currents and generates a triggering signal ‘PVIso’ in case of any fault event in the network and does the following:

- (i) Disconnects the PV modules from the inverter and disables the MPPT
- (ii) Enables the PV-STATCOM PCC voltage controller.

As discussed in Chapter 3, the fault detector is capable of detecting any fault within a few hundred microseconds and the power electronics devices (e.g., solid state breakers, IGBTs of the inverter, GTOs, etc.) are capable of responding within a few hundred nanoseconds to several microseconds [185], [63]. The complete operation of the fault detection and switching to PV-STATCOM operation takes a few milliseconds.

Once a fault is detected, the output signal of the fault detector enables the PV-STATCOM voltage controller through a multiplier inside the PCC voltage control module as shown in Fig. 6.3 (g). The voltage control module then begins regulating the voltage at the PCC, as described in Chapter 5. The PCC rms voltage is chosen as the feedback signal; thus, the PCC rms voltage is regulated to the reference value. As a result, the PV inverter completely behaves like a STATCOM with the PCC voltage control mode of operation upon detection of fault in the network.

During the PV-STATCOM operation the DC link voltage is maintained constant to a predefined reference value, V_{DC_ref} . This is chosen arbitrarily around the maximum power point voltage, V_{mpp} at rated power, such that the DC link voltage is more than twice the AC voltage at the inverter output for smooth operation of the inverter [56], [108]. In both the operation modes either as conventional PV solar farm or as PV-STATCOM, the grid synchronization is accomplished through the use of a phase lock loop (PLL) oscillator [108], [165].

6.3 Study Results

The simulation study is performed and an IM response is obtained for the following cases:

Case 1: Conventional PV system becomes disconnected, as per grid code [59], [60],

Case 2: Conventional PV system stays connected with the network during the fault,

Case 3: PV system acts as proposed PV-STATCOM during and after the fault.

In all of these studies a three phase to ground fault, which is considered as a worst case scenario in terms of speed recovery of the motor [186], is applied for 9 cycles at the grid bus. The fault is initiated at $t=5$ seconds and cleared at $t=5.15$ seconds. The maximum size of IM that can be supported by a 7.5 MVA PV-STATCOM is also determined in this

study. Finally, the reconnection of the solar farm after successful recovery of fault is demonstrated.

6.3.1 Case-1: Conventional PV system disconnected during fault:

The grid code [59], [60] requires a conventional PV solar farm to generate power at unity power factor and to disconnect within 6 cycles if there is a fault on the network. System relays are incorporated to disconnect the PV system from the grid. However, in this study, a fast fault detection technique, as discussed in Chapter 3, is integrated to disconnect the PV system. Fig. 6.4 illustrates the IM response at this event. Three phase triggering signals generated by the PV system fault detector are depicted in Fig. 6.4 (a), real and reactive power generation by the PV solar farm are demonstrated in Fig. 6.4 (b), voltages both at the PV solar farm and IM terminal are illustrated in Fig. 6.4 (c), IM speed is shown in Fig. 6.4 (d), and the real and reactive power drawn by the IM are presented in Fig. 6.4 (e).

As soon as the fault is detected, the fault detector generates a triggering signal on phase-a as shown in Fig. 6.4 (a). As discussed in Chapter 3, a triggering signal generated by the fault detector on any one of the three phases can disconnect the PV modules from the inverter and stop DC power generation. It can also stop the gating signal of the PV inverter as discussed in Chapter 3, which, eventually, stops the AC power output at the PV inverter terminal, as evident from Fig. 6.4 (b). A gradual decrease in AC power output is observed; this is due to the inductive effect of the filter and transformer.

During the fault, the voltage at the IM terminal becomes considerably low as illustrated in Fig. 6.4 (c). Therefore, the IM speed decreases and drops to 0.78 pu as seen in Fig. 6.4 (d). After the fault is cleared at $t=5.15$ seconds, the voltage at the IM terminal recovers but the IM speed becomes unstable. By examining the power drawn by the IM as shown in Fig. 6.4 (e), it is observed that both the active and reactive power drawn by the IM reduce substantially during fault. However, the reactive power increases more than its nominal value right after the fault is cleared. This leads to a destabilization of the IM oscillations: around 58 Hz are observed in IM power, which relate to the low stator and rotor resistances of the IM.

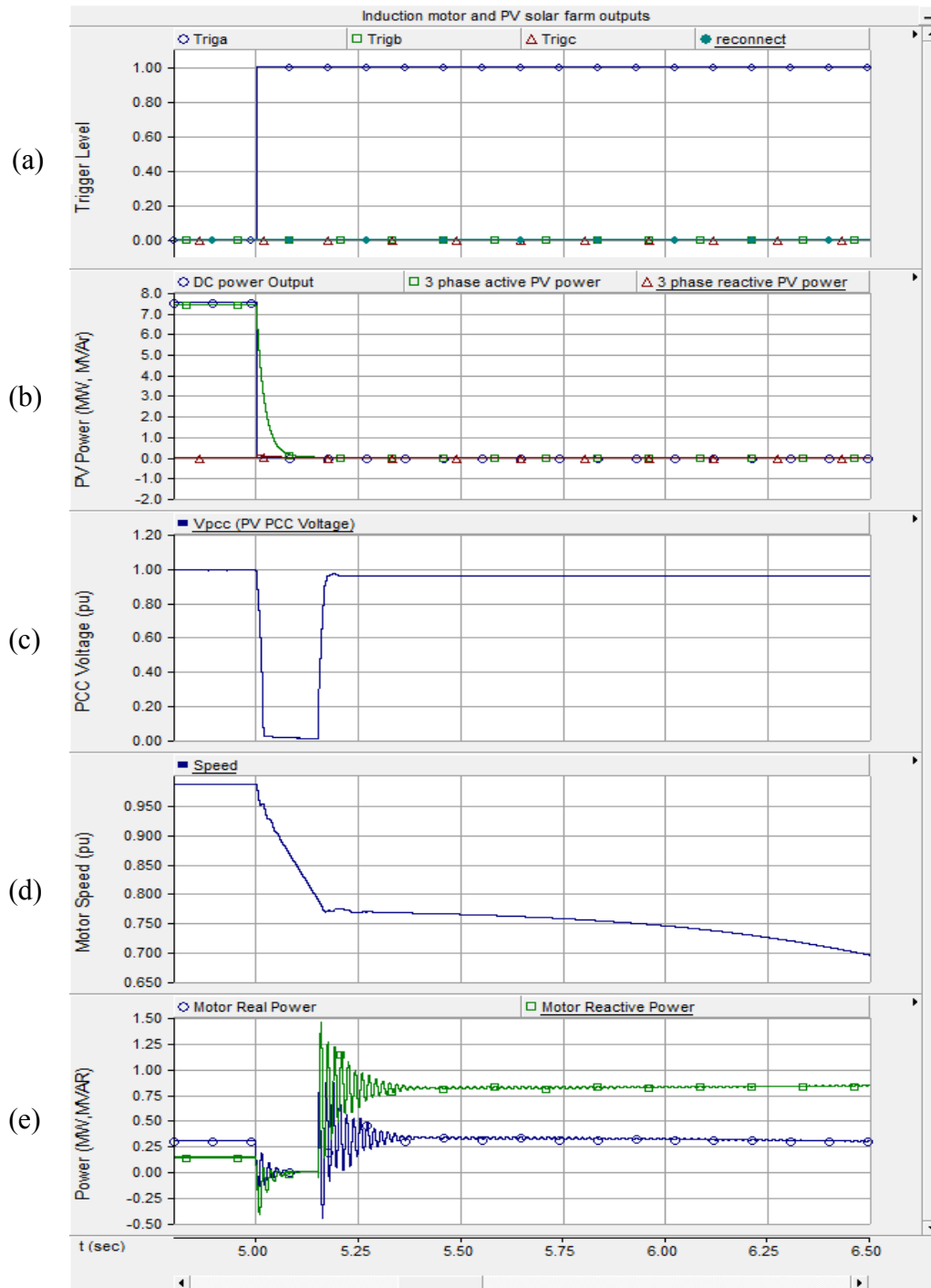


Figure 6.4 Conventional operation of the PV solar farm.

6.3.2 Case 2: Conventional PV system stays connected during fault

In this case, the conventional PV solar farm is allowed to remain connected during and after the fault. Fig. 6.5 illustrates the IM response at this event. The PV system DC link

voltage is depicted in Fig. 6.5 (a), real and reactive power from the PV solar farm are demonstrated in Fig. 6.5 (b), voltage at the IM terminal is illustrated in Fig. 6.5 (c), IM speed is shown in Fig. 6.5 (d), and real and reactive power at the IM terminal are presented in Fig. 6.5 (e).

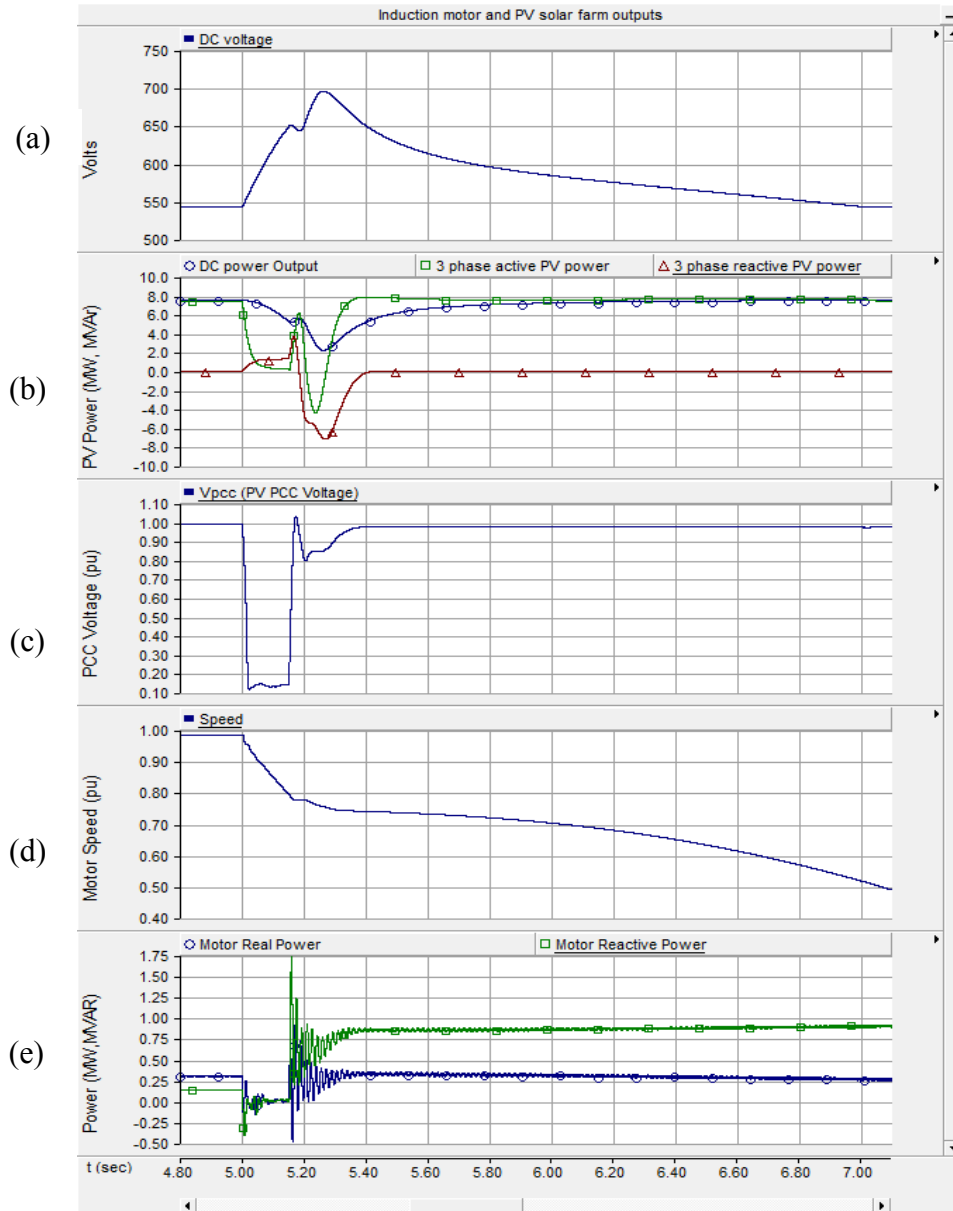


Figure 6.5 Conventional PV solar farm operates during and after the fault.

(i) Period I - During a fault, $t=5$ seconds to $t=5.15$ seconds.

When the fault initiates, the PV solar farm does not disconnect and continues generating real power as shown in Fig. 6.5 (b). The AC power output at the inverter terminal

decreases rapidly during a fault, due to the sudden drop of PCC voltage as shown in Fig. 6.5 (c). On the other hand, the DC power generation from the PV modules decreases relatively slow, as seen in Fig. 6.5 (b), because the PV modules act as a voltage controlled current source, as described in Chapter 2. The balance of real power increases the DC link voltage across the DC link capacitor of the solar farm as shown in Fig. 6.5 (a). During this transient period of fault a small amount of reactive power output from the solar farm inverter is observed in Fig. 6.5 (b), which occurs due to the decoupled power model of the solar farm for steady state condition as described in Chapter 2. In this period, power consumption by the IM reduces, as illustrated in Fig. 6.5 (e). During the fault the IM speed, as shown in Fig. 6.5 (d), also reduces due to the drop in voltage at its terminal, as shown in Fig. 6.5 (c).

(ii) Period II - At post fault clearance, $t=5.15$ seconds to $t= 5.26$ seconds.

The voltage at PCC recovers but takes much longer to stabilize, as seen in Fig. 6.5 (c). As a result, the power output from the PV inverter increases momentarily from $t=5.15$ seconds to $t=5.18$ seconds and then falls again from $t=5.18$ seconds to $t=5.26$ seconds, as seen in Fig. 6.5 (b) following the PCC voltage. The fall in real power to a negative value within this period is due to the inverter switching action which indicates more power consumption by the DC link capacitor. As a result, the voltage across the DC link capacitor increases further which results in lower DC power output from the module, as shown in Fig. 6.5 (b). In this period the IM speed decelerates further, as shown in Fig. 6.5 (d), and the reactive power consumption by IM increases as illustrated in Fig. 6.5 (e).

(iii) Period III - At Post Fault Clearance, after $t= 5.26$ seconds.

The power output from the PV solar farm follows the PCC voltage and settles to steady state at $t=5.37$ seconds. The DC link voltage decreases gradually to follow the MPPT voltage at $t=7$ seconds. The additional time taken after $t=5.37$ seconds to settle the DC link voltage, as shown in Fig. 6.5 (a), is due to the response time of the MPPT controller. During this period, the reactive power output from the PV solar farm, as illustrated in Fig. 6.5 (b), shows a transient behavior also according to the PCC voltage, as shown in Fig. 6.5 (c). The IM speed further deteriorates at this period and does not recover further, as

seen in Fig. 6.5 (d). The demand for motor reactive power also increases, as shown in Fig. 6.5 (e).

6.3.3 Case 3: PV system operation as PV-STATCOM

In this case, the PV solar farm is operated as a PV-STATCOM as soon as the fault is detected in the network. Two scenarios are investigated.

6.3.3.1 Scenario 1: PV solar farm located at induction motor terminals

Fig. 6.6 depicts the IM response when the solar farm acts as a PV-STATCOM and is located at the IM terminal. The PV system DC link voltage is depicted in Fig. 6.6 (a), the real and reactive power from the PV solar farm are demonstrated in Fig. 6.6 (b), voltage at IM terminal is illustrated in Fig. 6.6 (c), IM speed is shown in Fig. 6.6 (d), and the real and reactive power at IM terminal are presented in Fig. 6.6 (e).

(i) Period I - During fault, $t=5$ seconds to $t=5.15$ seconds.

After the fault is initiated, the fault detector detects the fault and transforms the PV solar farm into a PV-STATCOM with a PCC voltage control mode of operation, as discussed earlier in section 6.2.3. As a result, the DC power generated by the PV modules reduces immediately to zero and the active power output of the PV inverter also gradually decreases to zero, as shown in Fig. 6.6 (b). The reactive power output of the PV-STATCOM provides voltage support during this period. The DC link voltage decreases gradually, as seen in Fig. 6.6 (a), due to this reactive power support. The IM terminal voltage also falls to a low value, as shown in Fig. 6.6 (c). The IM speed in Fig. 6.6 (d) and power in Fig. 6.6 (e) drop due to the fall of IM terminal voltage.

(ii) Period II - At post fault clearance, $t= 5.15$ seconds to $t= 5.75$ seconds.

The DC link voltage of the PV solar system shows a transient behavior ($t=5.15$ seconds to $t= 5.5$ seconds) as shown in Fig. 6.6 (a). Although, this transient behavior is due to the combined transient effect of real and reactive power of the inverter, the transient effect of real power is dominant, as observed in Fig. 6.6 (b). It is noted that there is no real power input at the inverter. Therefore, during this transient period when the active power flows

in the reverse direction, from PCC to inverter due to the switching action of the inverter, it increases the DC link voltage. When the active power flows towards the PCC from the inverter, it decreases the DC link voltage. The DC link voltage finally settles to its predefined value of 550Volts at $t= 5.5$ seconds when the real power transient has ended. On the other hand, the PCC voltage recovers much faster, as seen in Fig. 6.6 (c). During the period of $t= 5.15$ seconds to $t= 5.3$ seconds, the PCC voltage follows the transient behavior of the reactive power output of the PV-STATCOM inverter and settles to a predefined value of 1 pu at $t= 5.3$ seconds.

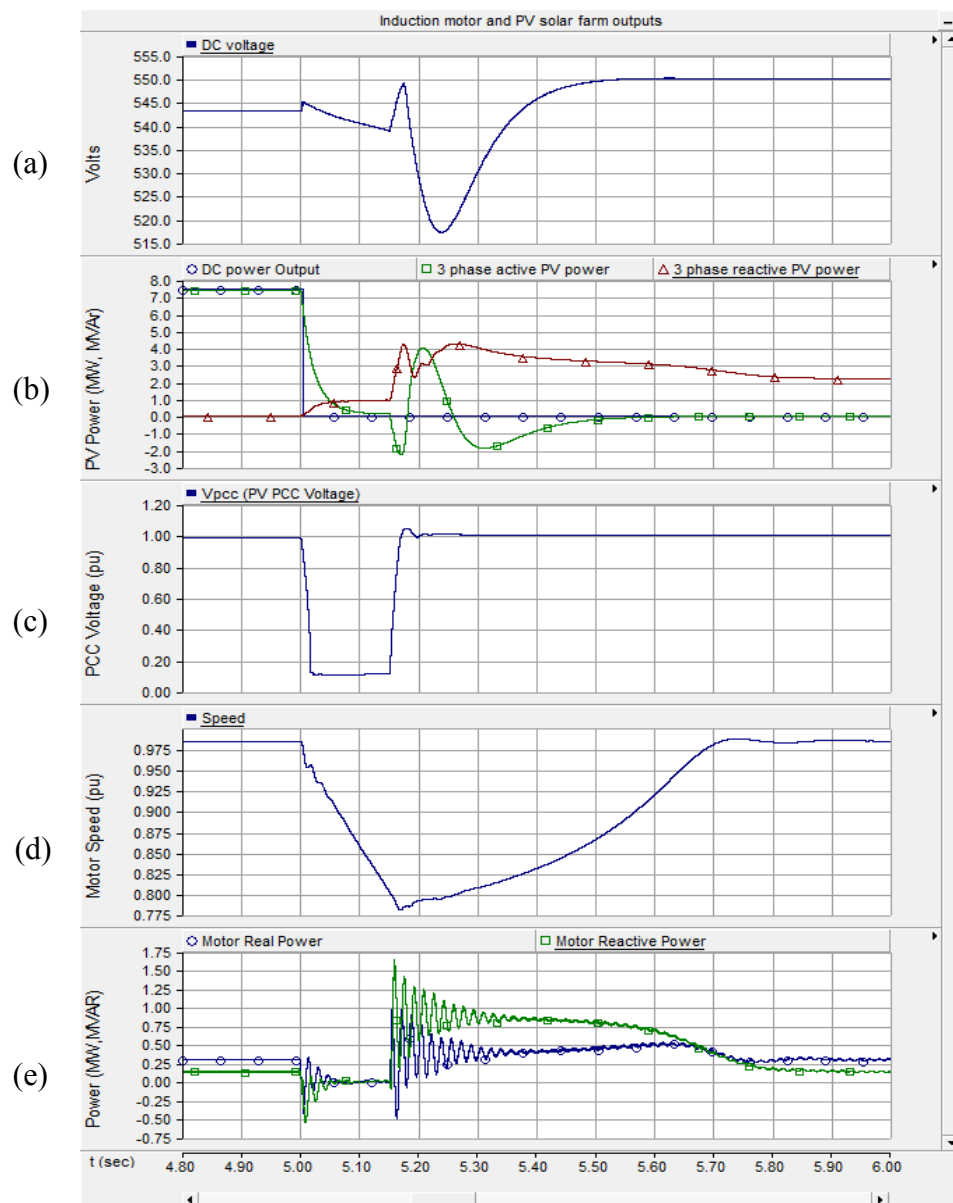


Figure 6.6 PV-STATCOM operation at the motor terminal.

During this period ($t = 5.15$ seconds to $t = 5.75$ seconds), the IM speed rises and settles to its pre-fault level at $t = 7.5$ seconds, as shown in Fig. 6.6 (d). The real and reactive power at the IM terminal shoot up with decreasing oscillation, as discussed earlier, and subsequently start decreasing, as shown in Fig. 6.6 (e). The increased power consumption by the IM during the transient period from $t = 5.15$ seconds to $t = 5.75$ seconds is due to the additional torque to bring back the IM to its pre-fault speed. The reactive power of the IM stabilizes at the pre-fault level, as seen in Fig. 6.6 (e), when the speed is settled at $t = 5.75$ seconds. It is noticed that after $t = 5.3$ seconds, the reactive power consumption by the IM in Fig. 6.6 (e) follows exactly the same behavior as the reactive power output of the PV-STATCOM inverter as shown in Fig. 6.6 (b). Therefore, it is obvious that the PV-STATCOM provides reactive power to meet the reactive power need of the IM until the speed of the IM stabilizes successfully. The PV-STATCOM reactive power then remains constant after $t = 5.75$ seconds to maintain the PCC voltage constant.

6.3.3.2 Scenario 2: PV solar farm located far from motor terminal

To observe the effectiveness of this PV-STATCOM control on IM stability, the PV solar farm is located at a remote location: 19 km away from the IM terminals. Fig. 6.7 depicts the IM response for this scenario. The triggering signals of the fault detector are depicted in Fig. 6.7 (a), the real and reactive power from the PV solar farm are demonstrated in Fig. 6.7 (b), voltage at IM terminal is illustrated in Fig. 6.7 (c), IM speed is shown in Fig. 6.7 (d), and the real and reactive power at IM terminal are presented in Fig. 6.7 (e).

It is evident that even when the PV system is connected 19 km away from the motor terminal, it prevents the IM instability through its PV-STATCOM operation. The behavior of different variables shown in Fig. 6.7 is very similar to those depicted in Fig. 6.6. However, the IM speed recovery takes much longer than previously. This delay is attributed to the line impedances between the motor and the PV solar farm. It is noted that although there are two triggering signals generated by the fault detector from the monitoring of all three phase currents at different time instants, as shown in Fig. 6.7 (a), the first triggering signal which is based on the phase-b current signal, initiates the disconnection of PV modules and starts the PV-STATCOM operation, in this scenario.

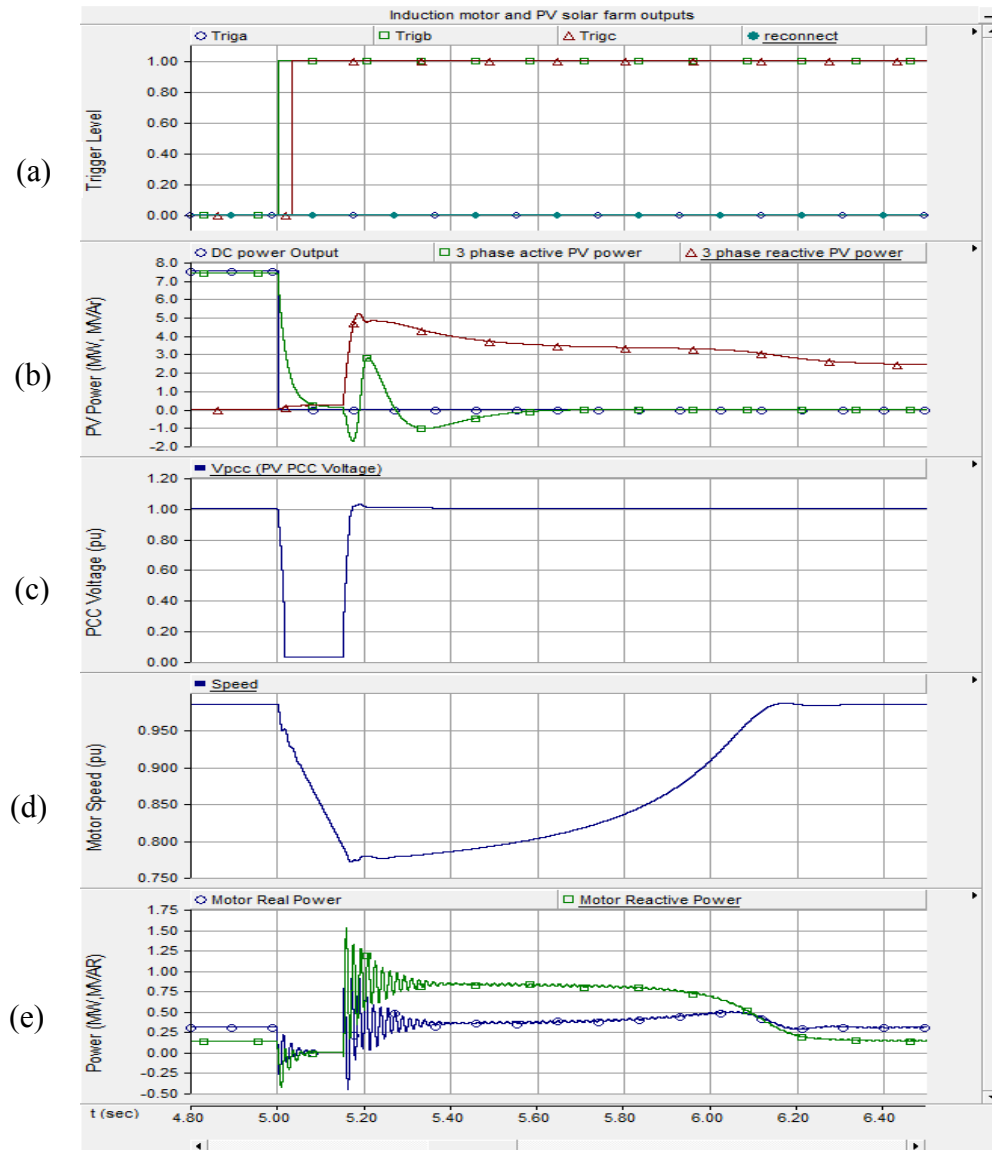


Figure 6.7 PV-STATCOM operation when located 19 km far from motor terminal.

6.3.4 Determination of maximum size of induction motor stabilized with 7.5 MVA PV-STATCOM

This study is performed to determine the largest size of IM load that can be stabilized with the same 7.5 MVA PV-STATCOM. For the same fault and same PV-STATCOM control, the size of the IM load is increased, until it becomes unstable. It is observed through simulation studies that the 7.5 MVA PV-STATCOM can prevent instability of up to 2.7MW IM load connected at the PCC with a PCC voltage set point of 1.0 pu for the study system. On the other hand, when the solar farm PCC is relocated 19 km away from the IM terminal with a voltage set point at PCC of 1.01 pu, it can prevent the

instability of a maximum size of IM load of 0.9 MW. Different PCC set point voltages are selected for different locations of the solar farm in order to attain the same IM terminal voltage of 1.0 pu. It is also noticed from the simulations that the IM speed recovery takes much longer if the motor size is larger. Moreover, relocating the PV solar farm to a farther point from the IM terminal also increases the recovery time due to the network impedance. Therefore, the IM speed recovery time is system dependent and influenced by several factors such as network strength, PV solar farm reactive support capability, and network loading condition.

6.3.5 Reinstatement of a conventional PV solar farm operation following PV-STATCOM operation

In the above study, the PV solar system is converted to a PV-STATCOM as soon as a fault is sensed in the network. However, it is required to revert the PV-STATCOM back to a conventional PV solar farm after successful post fault recovery of the IM.

To determine the time taken for motor recovery by PV-STATCOM operation for this specific study system, a number of cases have been investigated with respect to IM size and location of PV solar farm on the network. It is found that for a maximum size of 2.7 MW IM, with the solar farm located at IM terminal, the time to recover the nominal speed from the fault initiation is *2seconds*. This is the longest recovery time for this study system. Hence, the time to transform the PV-STATCOM back into a PV solar farm after fault is considered as *k times 2seconds* where the factor *k* depends upon various factors such as choice of safety margin, and requires prior investigation based on different loading and network conditions. This is outside the scope of this chapter. However, in this study system this factor is chosen arbitrarily as 1.5.

Fig. 6.8 depicts the IM response for $t= 4.8$ seconds to $t= 7.5$ seconds, when the PV solar farm acts as a PV-STATCOM connected at the terminal of 2.7 MW IM terminal. The DC link voltage of the PV system is depicted in Fig. 6.8 (a), triggering signals are shown in Fig. 6.8 (b), real and reactive power from the PV solar farm are demonstrated in Fig. 6.8 (c), voltage at IM terminal is illustrated in Fig. 6.8 (d), IM speed is shown in Fig. 6.8 (e), and real and reactive power at IM terminal are presented in Fig. 6.8 (f). Meanwhile Fig.

6.9 (a)-(f), depict the same quantities for an extended period of time, from $t=7.5$ seconds to $t=15$ seconds.

(i) Period I - During a fault, $t=5$ seconds to $t=5.15$ seconds.

After the fault is initiated, the fault detector detects the fault and transforms the PV solar farm into a PV-STATCOM. All of the quantities in Fig. 6.8 (a)-(e) show a similar behavior, as shown in Fig. 6.6.

(ii) Period II - At post fault clearance, $t=5.15$ seconds to $t=7.5$ seconds.

All of the quantities shown in Fig. 6.8 (a)-(f) show similar behavior to those shown in Fig. 6.6. In this case, as the size of IM is large, the demand of reactive power by the IM is high, shown in Fig. 6.8 (f). Therefore, during the transient period of $t=5.15$ seconds to $t=7.0$ seconds, the whole PV-STATCOM capacity is used for reactive power support, as shown in Fig. 6.8 (c), to stabilize such a large size of IM. Although the PCC voltage recovers right after the post fault clearance, it is not able to maintain its predefined set value as shown in Fig. 6.8 (d). The PCC voltage achieves its predefined set value of 1.0 pu after the IM speed recovers successfully at $t=7.0$ seconds, as illustrated in Fig. 6.8 (e).

(iii) Period III - At post fault clearance, $t=7.5$ seconds to $t=15$ seconds.

As shown in Fig. 6.9 (b), the reconnect signal triggers at $t=8$ seconds and resets all other trigger signals from the fault detector. As a result, the PV-STATCOM reverts into a conventional PV solar farm which starts generating rated DC power as shown in Fig. 6.9 (c). This DC power initially increases the DC link voltage from $t=8$ seconds to $t=8.5$ seconds, as shown in Fig. 6.9 (a). During this transient period the input and output power of the inverter reach their equilibrium position, i.e., all of the input DC power transfers to the output of the inverter, as shown in Fig. 6.9 (c). After $t=8.5$ seconds, the DC link voltage starts to decrease towards the MPPT voltage which gradually increases the real power output and finally settles at $t=14.5$ seconds. On the other hand, the reactive power output from the PV solar farm decreases to zero to ensure unity power factor operation after $t=8$ seconds. The PCC voltage is no longer regulated and follows the pre-fault network voltage, as shown in Fig. 6.9 (d). As a result of the reinstatement, a small transient is observed in motor speed at $t=8$ seconds, as illustrated in Fig. 6.9 (e), and IM power as shown in Fig. 6.9 (f), due to the change in PCC voltage.

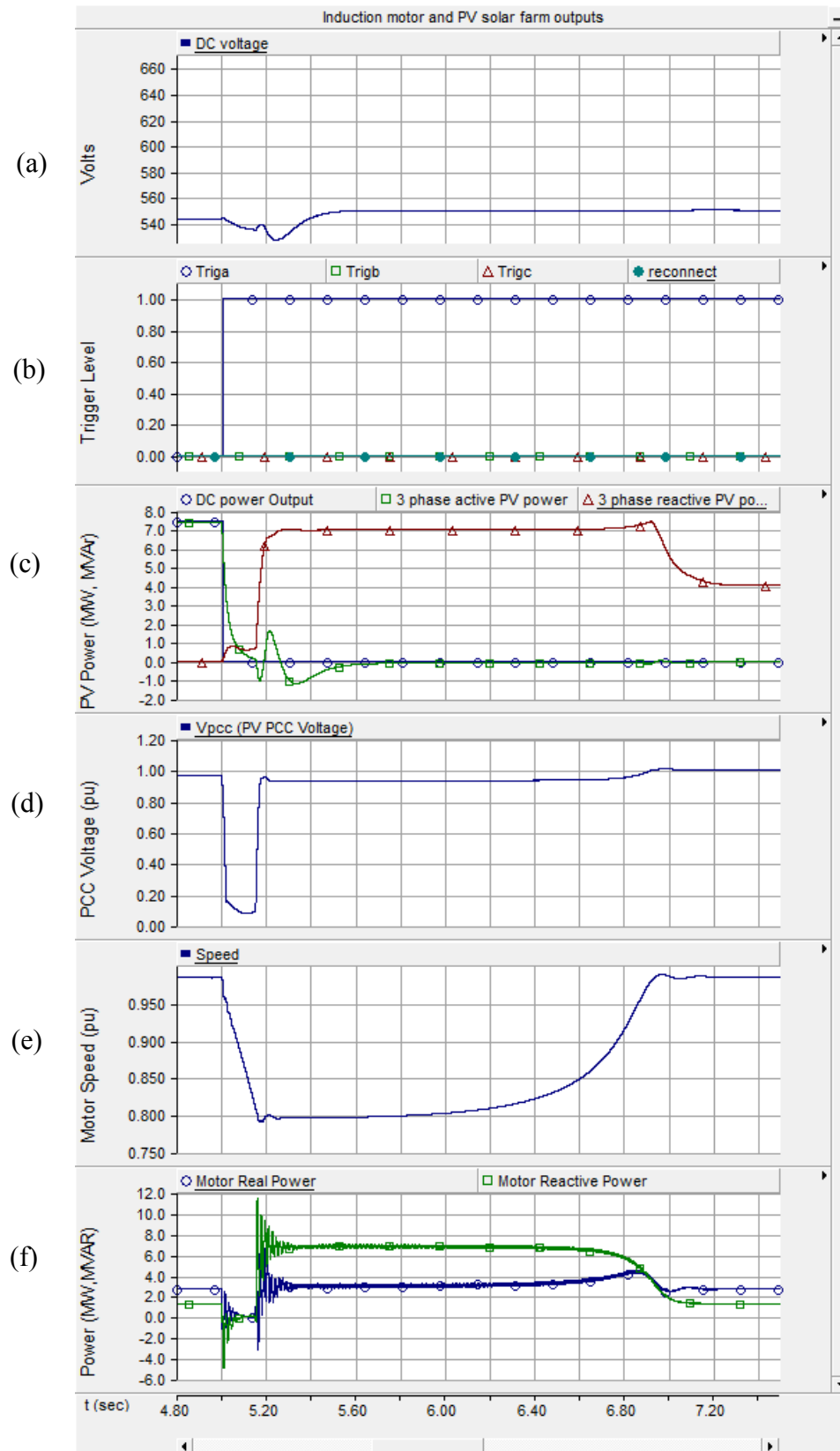


Figure 6.8 PV solar farm operating as PV-STATCOM.

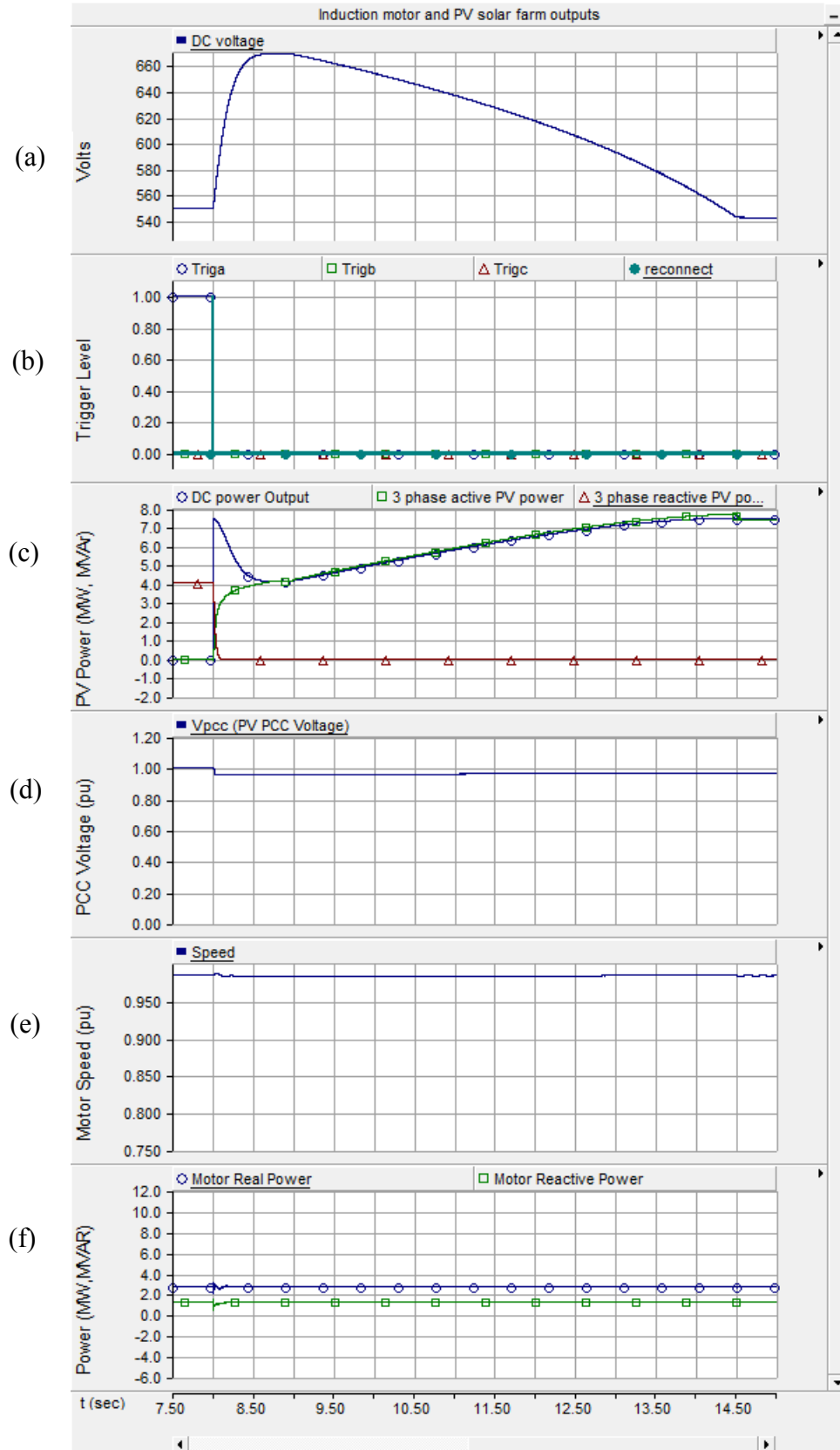


Figure 6.9 PV solar farm reinstated following the PV-STATCOM operation.

6.4 Conclusion

In this chapter, a new application of a PV solar farm as a PV-STATCOM is presented for preventing instability of a critical induction motor load. The performance of the PV-STATCOM is compared to a conventional PV solar farm operation to determine whether it stays connected or is disconnected during the fault. The induction motor (IM) becomes destabilized due to the fault and the conventional operation of PV solar farm does not alleviate the situation. For the specific study system it is seen that a 7.5 MW solar farm acting as PV-STATCOM can stabilize (i) an induction motor (IM) load of 2.7 MW if connected at motor terminals, and (ii) an induction motor (IM) load of 0.9 MW, if connected 19 km away from motor terminals. The PV solar farm is transformed into a PV-STATCOM only when there is a need or prior agreement to provide dynamic voltage support to stabilize a critical induction motor load. Once the motor is stabilized, the PV-STATCOM transforms into a conventional PV solar farm and starts generating real power as usual. The operation of a PV-STATCOM utilizes the entire or partial PV inverter capacity depending upon the dynamic reactive power demand of the induction motor for its recovery. The effectiveness of the proposed PV-STATCOM operation is dependent on the size and location of the PV solar farm and the system strength. It is recommended that the solar farm be suitably remunerated for providing this service to the customer owning the large induction motor during a critical period.

Chapter 7

7 Improvement of Power Transfer Limit Over a Long Transmission Line with a Novel Control of PV Solar Farm as PV-STATCOM.

7.1 Introduction

This chapter presents a new application of a grid connected PV solar farm inverter as a PV-STATCOM, during both night and day for increasing transient stability and consequently, the power transmission limit of long transmission line. It utilizes the entire solar farm inverter capacity during the night and the remainder inverter capacity after real power generation during the day; both of which remain unused in conventional solar farm operation. Similar STATCOM control functionality can also be implemented in inverter based wind turbine generators during no-wind or partial wind scenarios for improving the transient stability of the system. Studies are performed for two variants of a Single Machine Infinite Bus (SMIB) system. One SMIB system uses only a single PV solar farm as PV-STATCOM connected at the midpoint; whereas, the second system uses a combination of a PV-STATCOM and another PV-STATCOM or an inverter based wind Distributed Generator (DG) with similar STATCOM functionality. Three-phase fault studies are conducted using the electromagnetic transient software EMTDC/PSCAD, and the improvement in stable power transmission limit is investigated for different combinations of STATCOM controllers on the solar and wind farm inverters, during both night and day.

Section 7.2 describes the study systems. The results for various fault studies are presented in section 7.3. Performances of different proposed controls both during daytime and nighttime are presented. The implications of this new PV-STATCOM technology and the conclusions are presented in Section 7.4 and Section 7.5, respectively.

7.2 System Model

The single line diagrams of two study systems - Study System 1 and Study System 2 are depicted in Fig. 7.1 and Fig. 7.2, respectively. Both systems are Single Machine Infinite

Bus (SMIB) systems in which a large equivalent synchronous generator (1110 MVA) operating at 22kV system supplies power to the infinite bus over a 200 km, 400 kV transmission line. An 1110 MVA, 22/400kV transformer having leakage reactance of 8.66% is coupled with the generator. This line length is typical of a long line carrying bulk power in Ontario. In Study System 1, a 100 MW PV solar farm (DG) as a STATCOM (PV-STATCOM) is connected at the midpoint of the transmission line.

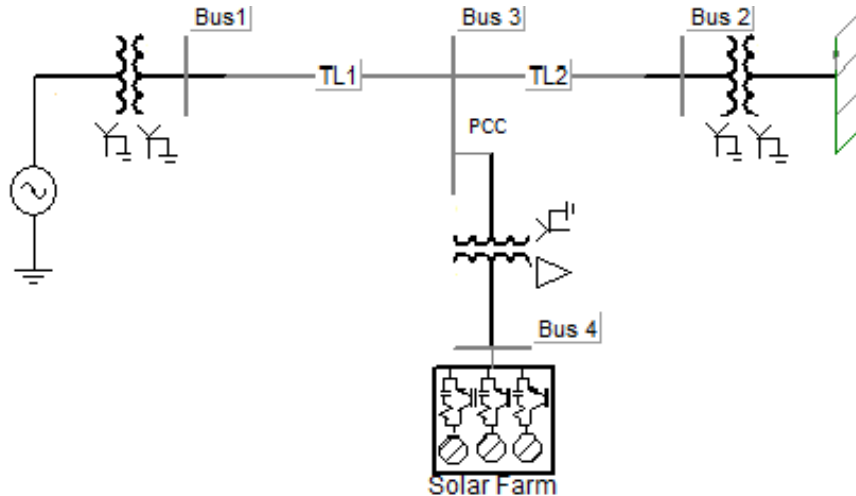


Figure 7.1 One line diagram of Study System 1.

In Study System 2, two 100 MVA inverter based Distributed Generators (DGs) are connected at $1/3^{\text{rd}}$ (bus 5) and $2/3^{\text{rd}}$ (bus 6) of the line length from the synchronous generator. The DG connected at bus 6 is a PV-STATCOM and the other DG at bus 5 is either a PV-STATCOM or a wind farm with STATCOM functionality. In this case, the wind farm employs Permanent Magnet Synchronous Generator (PMSG) based wind turbine generators with a full AC-DC-AC converter. It is understood that both the solar DG and wind DG employ several inverters. However, for this analysis, each DG is considered to have a single equivalent inverter with the rating equal to the total rating of solar DG or wind DG, respectively. The wind DG and solar DG are considered to be of the same rating, hence they can be interchanged in terms of location, depending upon the studies being performed. Fig. 7.3 presents the detailed diagrams of various subsystems of the two equivalent DGs. All of the system parameters [95], [113] are given in Appendix-D.

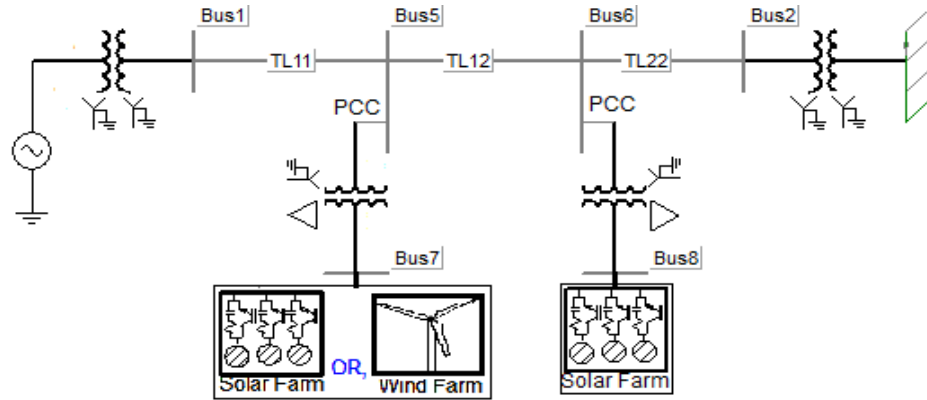


Figure 7.2 One line diagram of Study System-2.

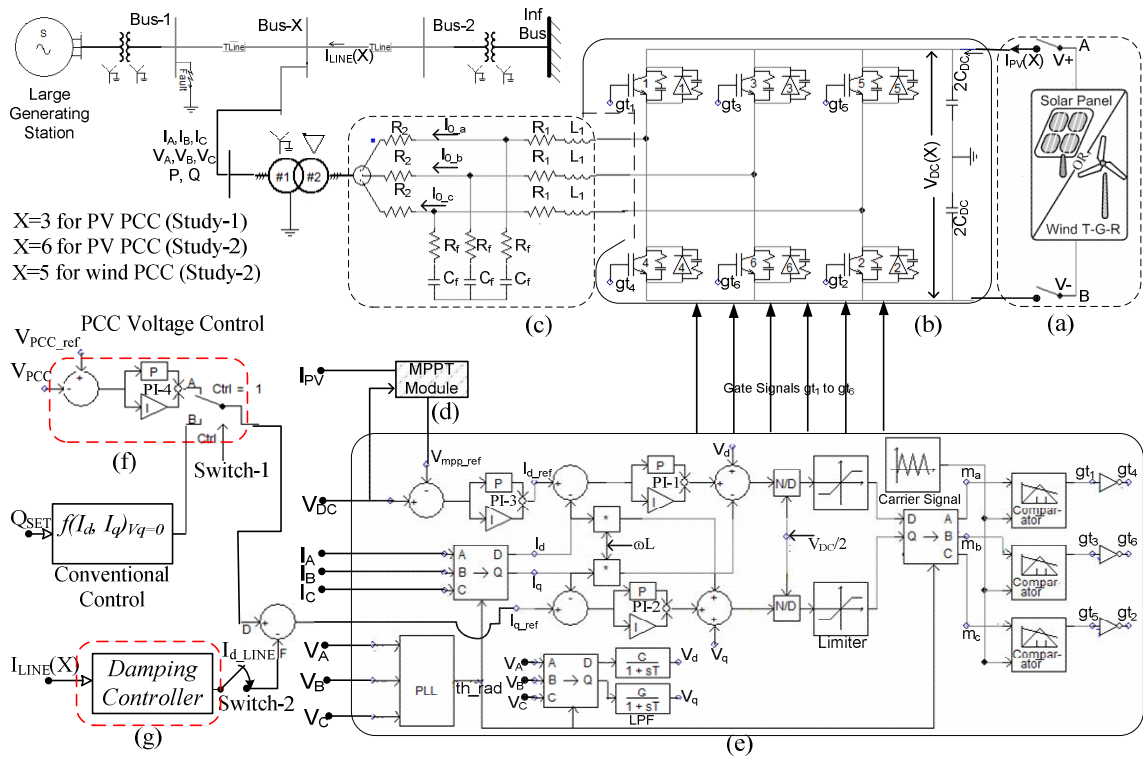


Figure 7.3 Detailed DG control diagram of study systems

7.2.1 Generator and Line Models

The synchronous generator is represented by a detailed sixth order model and a DC1A type exciter [113]. The associated parameter values are given in Appendix-D. The transmission line segments TL1, TL2, TL11, TL12, and TL22 shown in Fig. 7.1 and Fig. 7.2 are represented by lumped pi-circuits. The positive and zero sequence R, X, B values of the line are given in Appendix-D. The saturation is neglected in both sending and receiving end transformers.

7.2.2 Distributed Generator Models

The PV solar DG, as shown in Fig. 7.3, is modeled as an equivalent voltage sourced inverter along with a voltage controlled DC current source which follows the I-V characteristics of Photovoltaic (PV) panels, as described in Chapter 2. The wind DG is similarly modeled as an equivalent voltage sourced inverter. In the solar DG, the DC power is provided by the solar panels, whereas in the wind DG, the DC power comes from thyristor controlled rectifiers connected to the output of PMSG wind turbines, denoted here as ‘wind T-G-R’ and shown in Fig. 7.4. A maximum power point tracking (MPPT) system (as implemented in Chapter 2) is also incorporated with the inverter controller to operate the solar DGs at its maximum power point at all times. The wind DG is also assumed to be operating at its maximum power point. The proposed STATCOM control utilizes only the inverter capacity left after the maximum power point operation of both the solar DG and wind DG.

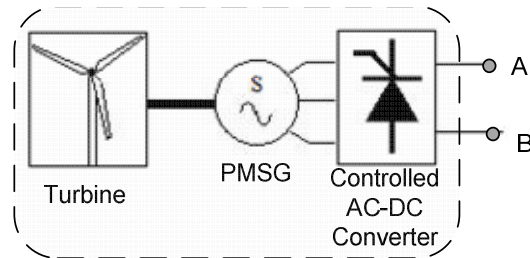


Figure 7.4 Gearless Wind Turbine-Generator-Rectifier (Wind T-G-R) Model

The DC power produced by each DG is fed into the DC bus of the corresponding inverter, as illustrated in Fig. 7.3. The magnitude of real power injection from the DGs to the grid depends upon the level of solar insolation, temperature, wind availability, etc. For PV-STATCOM operation during the night, the solar panels are disconnected from the inverter and a small amount of real power is drawn from the grid to charge the DC capacitor. The DC capacitor size is selected appropriately to reduce the DC side ripple. The inverter uses the Sinusoidal Pulse Width Modulation (SPWM) technique to transfer the DC power to the AC grid as described in Chapter 2. An L-C-L filter is also connected at the AC side of the inverter to mitigate harmonics generated by each DG inverters.

7.2.3 Control System

7.2.3.1 Conventional Reactive Power Control

The conventional reactive power control only regulates the reactive power output of the inverter such that it can perform unity power factor operation along with the DC link voltage control [24]. The switching signals for the inverter switching are generated through two current control loops in a d-q-0 co-ordinate system as described in Chapter 2. The inverter operates in conventional controller mode only, provided that ‘Switch-2’ is in the ‘OFF’ position. In this controller, Q_{ref} is proportional to I_q , which sets the reference I_{q_ref} for the quadrature current control loop. Therefore, setting the value of $Q_{ref} = 0$ ensures unity power factor operation of the solar farm.

7.2.3.2 PCC Voltage Control:

In the *PCC voltage control* mode of operation, the PCC voltage is controlled through reactive power exchange between the DG inverter and the grid. In this control mode of operation, the conventional ‘ Q ’ control channel is replaced by the PCC voltage controller in Fig. 7.3 (f), simply by switching the ‘Switch-1’ to position ‘A’. Hence, the measured signal, V_{PCC} , at the PCC is compared with the preset reference value V_{PCC_ref} and is passed through the PI regulator, PI-4, to generate I_{q_ref} . The rest of the controller settings remain unchanged. The quadrature axis current control loop is used to regulate the PCC voltage; whereas, the direct axis current control loop is used for DC voltage control as well as for the supply of DG power to the grid. The amount of reactive power flow from the inverter to the grid depends on set point voltage at PCC. The parameters of the PCC voltage controller are tuned by systematic hit and trial method to achieve the fastest step response, least settling time, and a maximum overshoot of 10-15%. The procedures of the hit and trial method for selecting the parameters for all four PI controllers are described in Appendix-D.

7.2.3.3 Damping Control:

A novel auxiliary *damping control* mode is added to the PV control system, shown in Fig. 7.3 (g). This output is compared with I_{q_ref} . The transfer function of this damping controller can be expressed along the general expression given in [187] as follows:

$$F_D = G \cdot \frac{sT_w}{1 + sT_w} \cdot G_1 \cdot \frac{1 + sT_1}{1 + sT_2} \dots\dots\dots (7.1)$$

The transfer function is comprised of a gain, a washout stage, and a 1st order lead-lag block. This controller is utilized to damp the rotor mode oscillations of the synchronous generator and to thereby improve system transient stability; it is activated by toggling the ‘Switch-2’ to the ‘ON’ position. The principle of this damping controller is to modulate the voltage at the PCC with the auxiliary damping signal. An auxiliary line current signal $I_{LINE}(X)$ is chosen as the input of the damping controller. The direct axis component $I_{d_LINE}(X)$, of $I_{LINE}(X)$ reflects the active power oscillation in the system. As the PCC voltage is mainly controlled by the q-axis component, the output of the auxiliary controller $I_{d_LINE}(X)$ is given to the q-axis control loop through a low pass filter or washout block and a lead-lag compensator with proper gain. The purpose of the low pass filter or the washout block is to make the system observable for rotor mode oscillation up to 2Hz. The lead lag compensator is developed along the concepts presented in [95], [187], [188], and the parameter values are selected with systematic hit and trial method using EMTDC/PSCAD simulation, based on the procedure explained in [187]. The detailed procedure of systematic hit and trial method to determine the damping controller parameters and the parameter values are given in Appendix-D.

It is emphasized that these controller parameters are not optimal and better parameters could be obtained by following more rigorous control-design techniques: [96],[188]-[190]. Since the objective of this chapter is only to demonstrate a novel concept showing that a solar DG can be used for damping rotor mode oscillations while operating as a STATCOM, a rigorous damping controller design has not been undertaken. This damping controller can operate in conjunction with either the conventional reactive power control mode or with the PCC voltage control mode by toggling the ‘Switch-1’ to position ‘B’ or ‘A’, respectively. In this controller, although line current magnitude signal is used as the control signal, other local or remote signals which reflect the rotor mode oscillations of the generator [95] may also be utilized.

7.3 System Studies

Transient stability studies are carried out using EMTDC/PSCAD simulation software for

both the study systems during night and day, by applying a 3-Line to Ground (3LG) fault at bus 1 for 5 cycles. It is recommended that the damping ratio should be at 5% and the time frame of interest for rotor mode oscillation of approximately 1 Hz should be considered as 10 seconds followed by the disturbance [174], [190]. In other words, for a 5% damping ratio of the rotor mode having oscillation frequency of 1 Hz, the post-fault clearance settling time of the oscillations (to arrive at and maintain within 5% of its steady state value) is almost 10 seconds. The peak overshoot of PCC voltage is considered to stay within 1.1pu of nominal voltage. This maximum stable generator power limit for the system is determined for different modes of operation of the solar DG in Study System 1 and those of the solar DG and the solar/winds DGs in Study System 2.

7.3.1 Case Study 1: Power Transfer Limits in Study System 1

7.3.1.1 Conventional Reactive Power Control with the Novel Damping Control

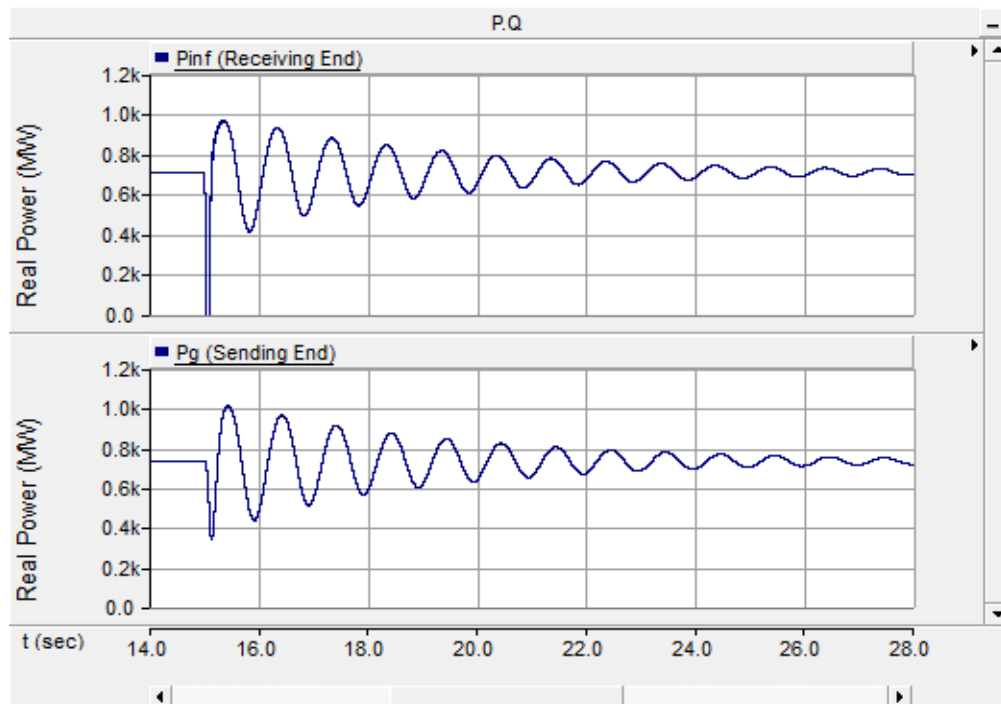
In this study, the solar DG is assumed to operate with its conventional reactive power controller through which the reactive power output from the solar DG is maintained at zero in steady state, and the DG operates at near unity power factor. For the nighttime operation of the solar DG, the DC sources (solar arrays) are disconnected and the solar DG inverter is connected to the grid using appropriate controllers, as described below. Power transmission limits are now determined for the following four cases. The stable power transmission limits obtained from fault studies and the corresponding load flow results are presented in Table 7.1, where –ve Q represents the inductive power drawn from network, and +ve Q represents capacitive power injected into the network.

i) Solar DG operation during the night with conventional reactive power controller:

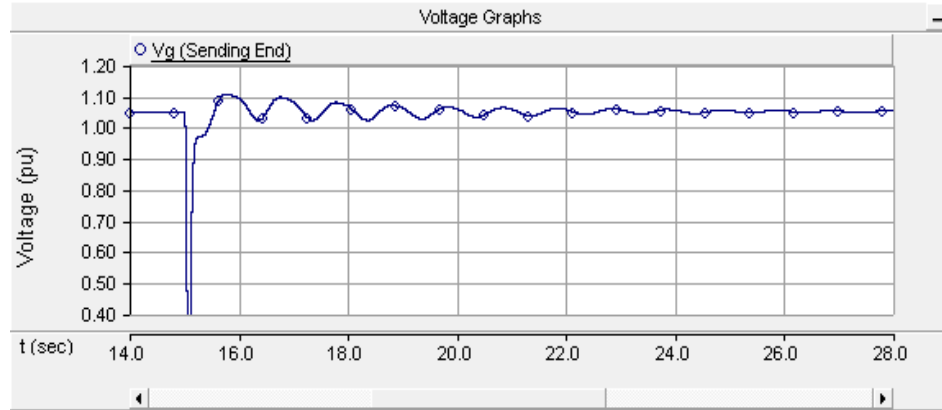
The maximum stable power output from the generator P_g is 731 MW when the solar DG is simply sitting idle during the night and is disconnected from the network. This power flow level is chosen to be the base value against which the improvements in power flow with different proposed controllers are compared and illustrated later in Table 7.3. The real power from generator P_g and that entering into the infinite bus P_{inf} for this fault study are shown in Fig. 7.5 (a). The sending end voltage at the generator is shown in Fig 7.5 (b), showing a voltage overshoot of 1.1pu.

Table 7.1 Power Flows and Voltages for Study System I for Solar DG with Conventional Reactive Power Control and Proposed Damping Control both during Nighttime and Daytime ($V_g=1.05$ pu)

Simulation Description		Generator Bus (Sending End)			PCC/Middle Bus (3)				Infinite Bus (Receiving End)	
		P_g MW	Q_g MVar	θ_g deg	V_{PCC} pu	θ_{PCC} deg	P_{solar} MW	Q_{solar} MVar	P_{inf} MW	Q_{inf} MVar
Nighttime	Conventional operation of solar DG	731	139	26.92	1.010	13.75	0	0	-708	82
	Solar DG with damping Controller	850	196	37.71	1.000	16.21	-0.2	0.08	-819	153
Daytime	Conventional Operation of Solar DG	730	140	27.25	1.010	14.1	19.0	-0.50	-725	89
		719	144	28.48	1.008	15.43	91.0	-0.20	-786	115
	Solar DG with Damping Controller	851	200	32.21	1.000	16.65	19.0	-0.06	-839	164
		861	216	34.15	0.994	18.36	91.0	-0.20	-917	208



(a)

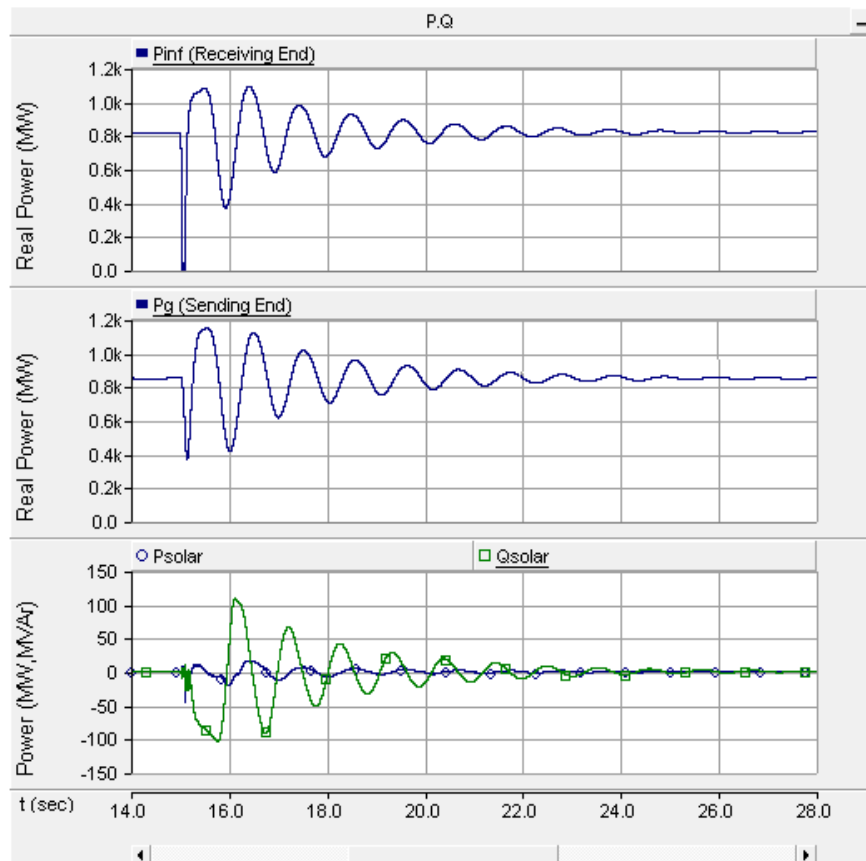


(b)

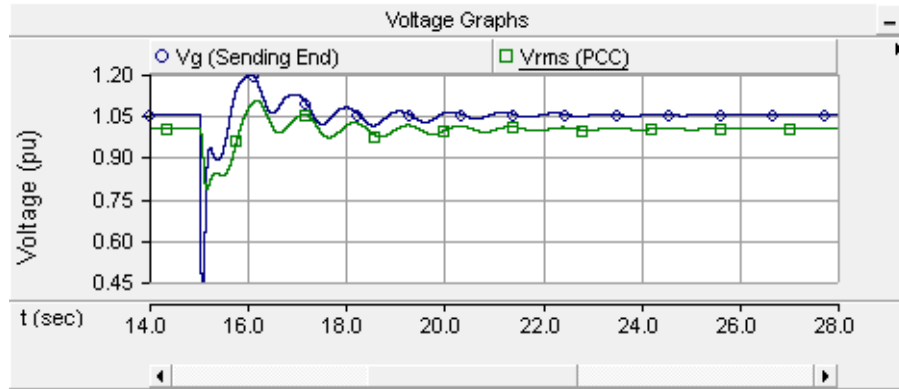
Figure 7.5 (a) Maximum nighttime power transfer (731 MW) from a generator when a solar DG remains idle (b) Voltage at generator terminal.

ii) *Solar DG operation during night with a damping controller:*

The quantities P_g , P_{inf} , P_{solar} , and Q_{solar} are illustrated in Fig. 7.6 (a). The damping controller utilizes the full rating of the DG inverter at night to provide controlled reactive power Q_{solar} and effectively damps the generator rotor mode oscillations. The voltages at generator bus V_g and at PCC bus $V_{rms}(PCC)$ are depicted in Fig. 7.6 (b).



(a)



(b)

Figure 7.6 (a) Maximum nighttime power transfer (850 MW) from a generator with a solar DG using a damping controller, (b) Voltages at generator terminal and PCC.

A very small amount of negative power flow from the solar farm P_{solar} is observed during nighttime. This reflects the losses in the inverter IGBT switches, transformer, and filter resistances caused by the flow of real current from the grid into the solar farm inverter to charge the DC link capacitor and maintain its voltage constant while operating the PV inverter as STATCOM with the damping controller (or even with voltage controller). During nighttime, the reference DC Link voltage V_{mpp_ref} is chosen around the typical daytime rated maximum power point (MPP) voltage to ensure V_{DC} remains more than twice that of V_{ac} for smooth inverter operation [108], [56].

The oscillation observed in the PV power is essentially due to the oscillation in the PCC voltage that is significantly low and continues as long as the voltage oscillation occurs at the PCC. In nighttime, during the negative half cycle of the oscillations, the active power is consumed by the DC link capacitor of the PV inverter resulting in the rise in DC link voltage as seen in Fig. 7.6. Meanwhile, during the positive half cycle of the oscillations, the DC link capacitor of the PV inverter supplies real power, resulting in the fall of DC link voltage across the capacitor. Due to this rise (charging) and fall (discharging) at the oscillation frequency, the DC link capacitor voltage also becomes oscillatory which reflects the oscillation of real power output of the PV inverter.

iii) Solar DG operation during day with conventional reactive power controller:

Fig. 7.7 illustrates the quantities P_g , P_{inf} , P_{solar} , and Q_{solar} when the conventional solar farm generates a high level of power of 91MW. In this case the maximum power transfer

from the generator is 719MW. Hence it is evident that the conventional control of a PV solar DG does not alter the stable transmission limit in any appreciable manner.

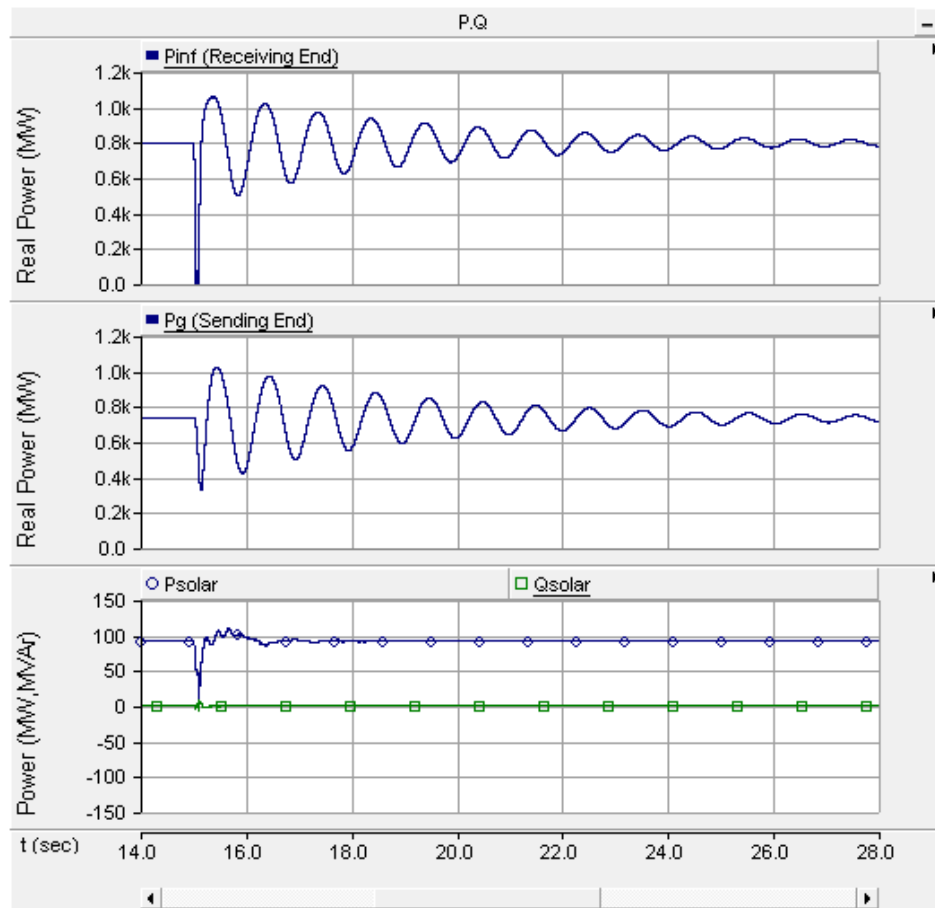


Figure 7.7 Maximum daytime power transfer (719 MW) from generator with solar DG generating 91 MW real power.

iv) Solar DG operation during day with damping controller:

The quantities P_g , P_{inf} , P_{solar} , and Q_{solar} are shown for the case with a damping controller in Fig. 7.8. The available inverter capacity after real power generation of 91 MW is, $Q = \sqrt{S^2 - P^2} = 41.5$ MVar, which is utilized for damping the oscillations during this lower power generation period.

It is noticed from Table 7.1 that the maximum power transfer during the night (850 MW) is actually less than the maximum power transfer during the day (861 MW). This is because of an additional constraint that while increasing the power transfer, the overshoot in PCC voltage should not exceed 1.1pu. If the power transfer is allowed until its

damping ratio limit of 5% is reached, regardless of voltage overshoot, the maximum nighttime power transfer is observed to be 964MW; whereas, the maximum daytime power transfer is expectedly seen to be lower at 940MW (plots not shown).

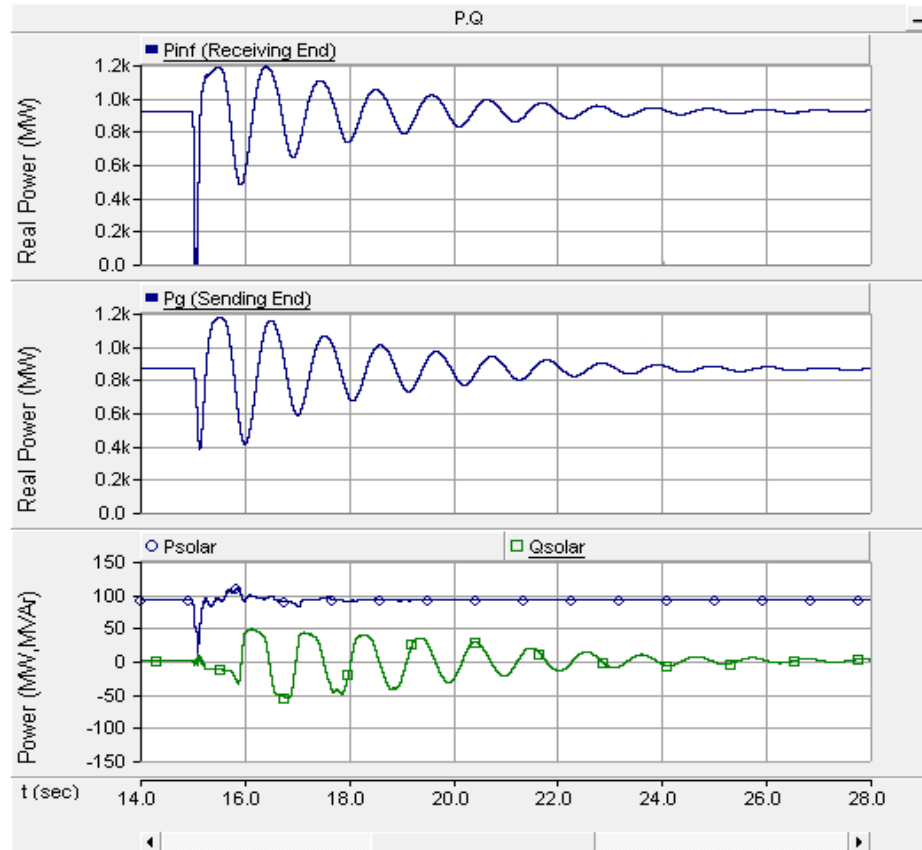


Figure 7.8 Maximum daytime power transfer (861 MW) from generator with solar DG generating 91 MW real power and using the damping controller.

7.3.1.2 PCC Voltage Control with the Novel Damping Control

Transient stability studies are now carried out to investigate the impact of a new control strategy involving PCC voltage control together with damping control. The results are shown in Table 7.2 for the following four cases:

i) Solar DG operation during night with voltage controller

The increase in power transfer limit is dependent upon the choice of reference values for PCC voltage V_{pcc} . In the best scenario, when V_{pcc} is regulated to 1.01pu, the maximum power output from the generator increases to 833 MW, as compared to 731 MW when the solar DG operates with conventional reactive power control.

Table 7.2 Power Flows and Voltages for Study System I for Solar DG with Proposed PCC Voltage Control and Damping Control, both during Nighttime and Daytime.

Simulation Description		Generator Bus (Sending End)			PCC/Middle Bus (3)				Infinite Bus (Receiving End)	
		P_g MW	Q_g MVar	Θ_g deg	V_{PCC} pu	θ_{PCC} deg	P_{solar} MW	Q_{solar} MVar	P_{inf} MW	Q_{inf} MVar
Nighttime	Solar DG with voltage Controller	789	222	29.75	0.988	15.25	-1.5	-95.8	-761	170
		824	222	30.95	0.990	15.86	-0.8	-66.0	-793	175
		830	191	30.96	1.000	15.83	-0.3	-9.5	-801	146
		833	160	30.87	1.010	15.74	-0.5	46.8	-803	116
		803	116	29.33	1.022	14.91	-1.5	99.0	-775	68
	Solar DG with both voltage and damping Controller	855	197	31.91	1.000	16.31	-0.3	4.0	-824	154
		899	174	33.22	1.010	16.92	-1.2	85.0	-866	133
Daytime	Solar DG with voltage controller	781	216	29.81	0.990	15.49	19.0	-90.0	-773	171
		815	188	30.79	1.000	15.92	19.0	-13.7	-804	147
		782	116	29.00	1.021	14.93	19.0	86.0	-775	72
		726	172	28.73	0.990	15.60	91.0	-43.0	-792	143
		719	170	28.61	1.000	15.53	91.0	-44.0	-786	140
	Solar DG with both voltage and damping Controller	823	190	31.09	1.000	16.08	19.0	-9.0	-813	150
		755	184	29.95	1.000	16.22	91.0	-41.0	-817	159

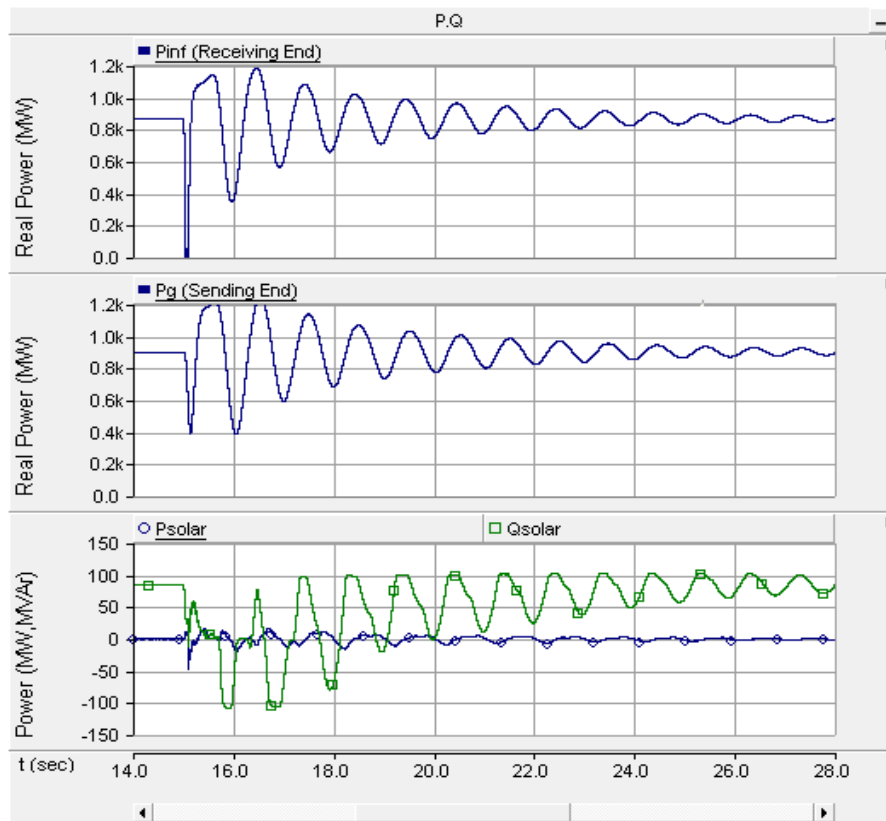
ii) Solar DG operation during day with voltage controller

If the solar farm is operated with the proposed voltage control while producing a relatively high amount of real power of 91 MW, the maximum generator power output can be increased to be 726 MW, as shown in Table 7.2. The net increase in the power transfer limit is 7 MW (726 MW - 719 MW) compared to the results for the corresponding case from Table 7.1. For a low amount of real solar power output of 19 MW, the voltage controller increases the generator power output to 815 MW. A substantial increase of 85 MW (815 MW – 730 MW) is observed in the generator power limit as compared to the result with conventional reactive power controller, shown in Table 7.1. As seen from Table 7.2, the power transfer increases for both high (91 MW) and low (19 MW) power outputs from the solar farm are seen to be highly sensitive to the PCC bus voltage set point. It is also noted that with lower availability of reactive power

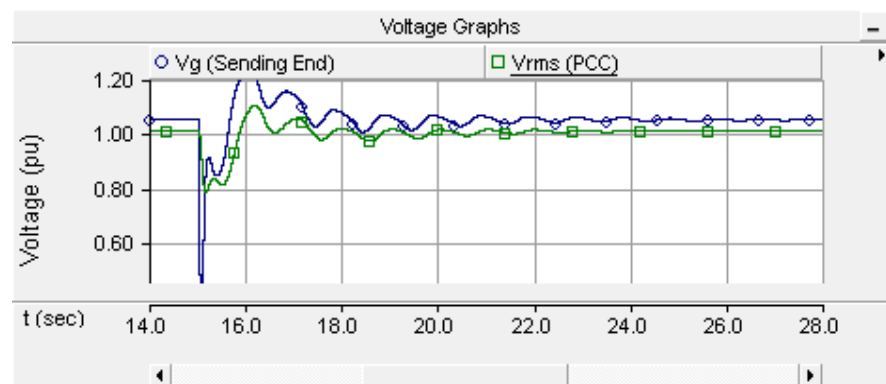
capacity after real power production, the ability to change the bus voltage is limited, leading to a lower increase in power transmission capacity.

iii) Solar DG operation during the night with both voltage and damping controllers

The generator power and infinite bus power are depicted in Fig. 7.9 (a), and corresponding voltages are shown in Fig. 7.9 (b).



(a)



(b)

Figure 7.9 (a) Maximum nighttime power transfer (899 MW) from generator while the solar DG uses damping controller with voltage control and (b) Voltages at generator terminal and solar DG PCC (1.01pu).

Although rotor mode oscillations settle faster, the power transfer cannot be improved beyond 899 MW due to high overshoot in voltages.

iv) Solar DG operation during day with both voltage and damping controller.

A further increase in power transfer is observed when both voltage control and damping control are employed, as compared to case (ii), when only a voltage controller is utilized.

For Study System 1, the net increases in power transfer capability as achieved with different PV-STATCOM controls, in comparison with that obtained from conventional reactive power control of the solar DG, are summarized in Table 7.3.

Table 7.3 Increase in Stable Power Transfer Limit (MW) for Study System 1 with Different PV-STATCOM Controls.

PV-STATCOM Control	Nighttime Power Limit Gain (MW)	Daytime Power Limit Gain (MW)	
		Solar DG Power output 19MW	Solar DG Power output 91MW
Voltage control	102	85	7
Damping Control	119	121	142
Voltage control with damping control	168	93	36

The maximum increase in power transfer limit during the night is achieved with a combination of voltage control and damping control; whereas, the same during the day is accomplished with damping control alone. This is because during the night, the entire MVA rating of the solar DG inverter is available for reactive power exchange, and can be utilized for achieving the appropriate voltage profile at PCC conducive for increasing the power transfer, and for increasing the damping of oscillations.

During daytime, firstly, the generation of real power from the solar DG tends to increase the voltage at PCC and secondly, the net reactive power availability is also reduced, especially with large solar real power outputs. Therefore, it becomes difficult with limited reactive power to accomplish the appropriate voltage profile at PCC for maximum power transfer as well as to impart adequate damping to the oscillations. However, if only damping control is exercised during daytime, power transfer limits appear to improve with higher real power outputs from the solar DG. This is because real power generation

increases the PCC voltage which can be potentially helpful in increasing the power transfer capacity.

Since damping control is found to be more effective during daytime, the same is explored further for the following studies.

7.3.2 Case Study 2: Power Transfer Limits in Study System 2

In this study, the proposed damping control strategy is compared with the conventional reactive power control strategy for Study System 2, shown in Fig. 7.2. A three phase to ground fault of 5 cycles is applied to generator bus at $t = 8$ seconds. The power transfer limits for different cases are illustrated in Table 7.4.

Table 7.4 Power Flows and Voltages for Study System 2 for both Solar DG and Wind DG with Conventional Reactive Power Control and Proposed Damping Control both during Nighttime and Daytime ($V_g = 1.05$ pu)

System Description	Generator Bus			Wind DG Bus (5)			Solar DG Bus (6)			Infinite Bus		
	P_g MW	Q_g MVAR	Θ_g deg	V_{wnd} pu	P_{wnd} MW	Q_{wnd} MVAR	V_{sol} pu	P_{sol} MW	Q_{sol} MVAR	P_{inf} MW	Q_{inf} MVAR	
Nighttime ($P_{solar}=0$)	Conventional Control	Case-1: None of the DGs generate real power										
		731	139	26.92	1.019	0	0	1.004	0	0	-708	82
		Case-2: Only wind DG generates real power but both DGs operate at unity pf.										
	With damping controller	716	146	28.6	1.017	95	-0.3	1.01	0	0	-785	119
		729	141	27.4	1.018	20	-0.1	1.003	0	0	-726	92
		Case-3: None of the DG generate real power but both DG operate with damping control										
Daytime ($P_{solar}\neq 0$)	Conventional Control	960	260	36.2	0.998	-0.7	0.07	0.982	-0.2	0.01	-918	229
		Case-4: Only wind DG generates real power but both DGs operate with damping control										
		936	270	37.86	0.995	95	0.4	0.976	-0.3	0.03	-987	275
Daytime ($P_{solar}\neq 0$)	Conventional Control	948	258	36.34	0.998	20	-0.01	0.981	-0.7	0.01	-927	234
		Case-5: Both DGs generate real power										
		700	149	29.67	1.016	95	-0.4	1.000	95	-0.4	-865	148
	With damping controller	726	142	27.55	1.019	20	-0.05	1.004	20	-0.05	-743	96
		Case-6: Only solar DG generates real power										
		719	140	27.9	1.017	0	0	1.002	95	-0.3	-790	111
Daytime ($P_{solar}\neq 0$)	With damping controller	730	139	27.17	1.018	0	0	1.003	20	-0.1	-727	89
		Case-7: Both DGs generate real power and operate on damping control.										
		930	277	39.23	0.99	95	-0.4	0.972	95	-0.5	-1023	321
		923	245	35.66	1.0	20	-0.3	0.983	20	-0.3	-924	224
Daytime ($P_{solar}\neq 0$)	With damping controller	Case-8: Only solar DG generates real power but both DGs operate on damping control.										
		938	257	37.01	0.998	-0.5	0.1	0.98	95	-0.3	-991	259
		944	253	35.97	0.999	-0.3	-0.1	0.982	20	-0.2	-925	228

7.3.2.1 Nighttime:

i) *Case 1 - None of the DGs generate real power*

The maximum power transfer limit is 731 MW, as reported in Table 7.1.

ii) *Case 2 - Only the wind DG generates real power. Both DGs operate with conventional reactive power control*

The power transfer limit decreases slightly with increasing wind power output.

iii) *Case 3 - None of the DGs generate real power but both DGs operate with damping control*

The different variables: generator power P_g , infinite bus power P_{inf} , real power of wind DG P_{wind} , reactive power of the wind DG Q_{wind} , real power of the solar DG P_{solar} , and the reactive power of the solar DG Q_{solar} are illustrated in Figure 7.10.

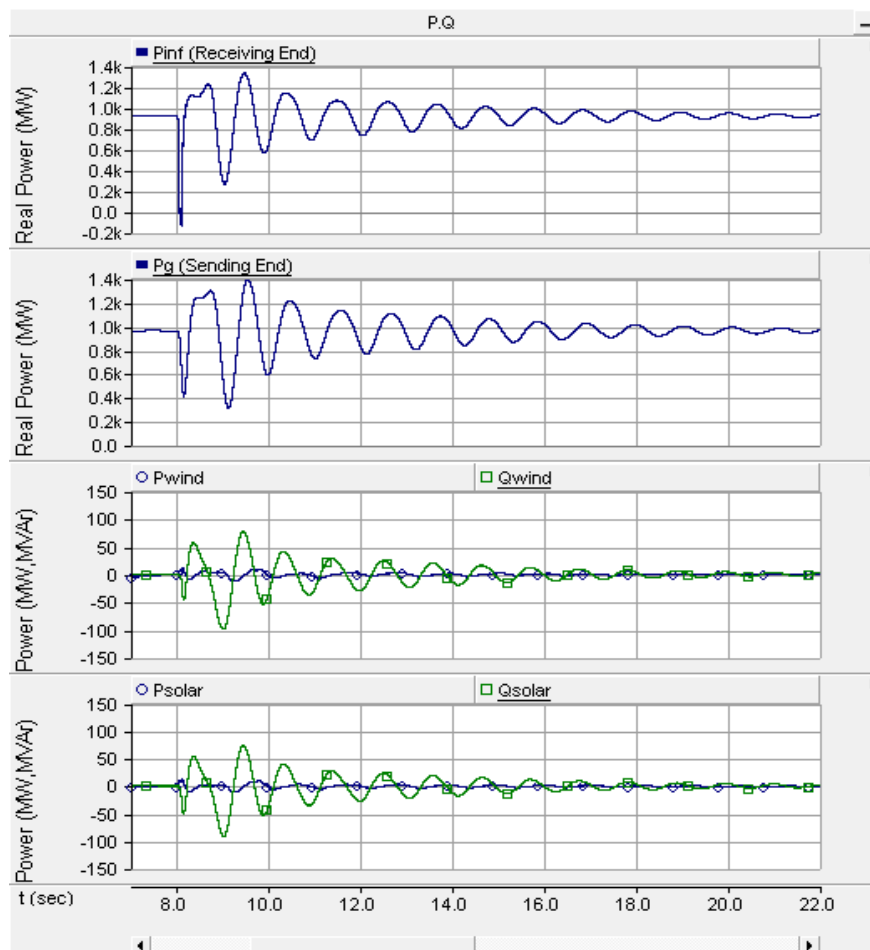


Figure 7.10 Maximum nighttime power transfer from generator with both DGs using damping controller but with no real power generation.

Even though the entire ratings (100 MVar) of the wind DG and solar DG inverters are not completely utilized for damping control, the power transfer limit increases significantly to 960 MW.

iv) Case 4 - Only wind DG generates real power but both DGs operate on damping control.

There is only a marginal improvement in the power limit with decreasing power output from the wind DG.

7.3.2.2 Daytime:

i) Case 5 - Both DGs generate real power

The power transfer limit from the generator decreases as the power output from both DGs increase.

ii) Case 6 - Only solar DG generates power

The power transfer limit from the generator decreases as the power output from the solar DG increases. However, no substantial changes in power limits are observed as compared to the case when both DGs generate power (Case 5).

iii) Case 7 - Both DGs generate real power and operate on damping control:

This case is illustrated by different variables P_g , P_{inf} , P_{wind} , Q_{wind} , P_{solar} , and Q_{solar} in Fig. 7.11. The power limit does not change significantly with increasing power output from DGs.

iv) Case 8 - Only the solar DG generates real power but both of the DGs operate on damping control:

The power limit does not appear to change significantly with increasing power output from the solar DG.

For Study System 2, the net increases in power transfer limits accomplished with the proposed novel damping control for different real power outputs from both DGs as compared to those attained with the conventional operation of both DGs, are depicted in Table 7.5.

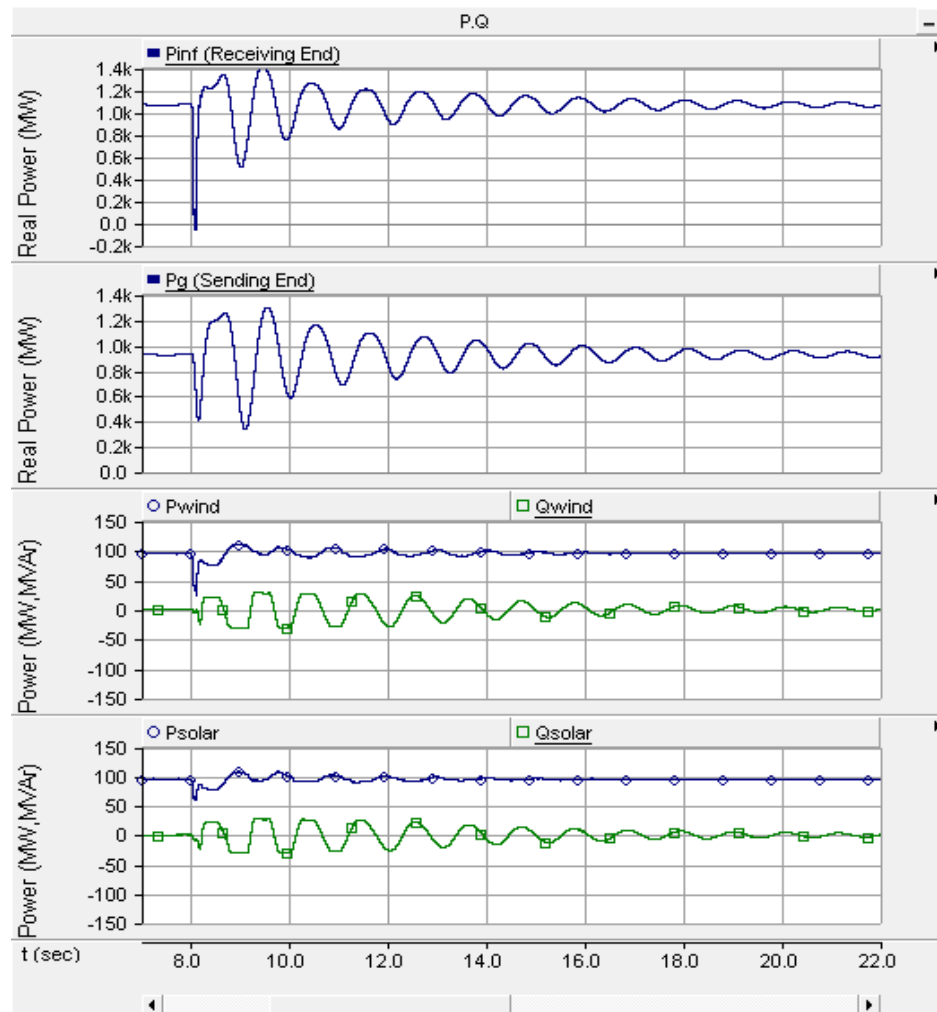


Figure 7.11 Maximum daytime power transfer from generator where both DGs generate 95MW each while using a damping controller.

Table 7.5 Increase in Power Transfer Limits for Study System 2 with Different DG Power Outputs.

DG Real Power Outputs (MW)	Increase of Power Transfer Limits (MW)
Nighttime	
$P_{\text{solar}}=0; P_{\text{wind}}=0$	229
$P_{\text{solar}}=0; P_{\text{wind}}=20$	219
$P_{\text{solar}}=0; P_{\text{wind}}=95$	220
Daytime	
$P_{\text{solar}}=20; P_{\text{wind}}=20$	197
$P_{\text{solar}}=95; P_{\text{wind}}=95$	230
$P_{\text{solar}}=20; P_{\text{wind}}=0$	214
$P_{\text{solar}}=95; P_{\text{wind}}=0$	219

It is seen that with the proposed damping control on the two DGs (of rating 100 MW each) during the night increases the power transfer limits substantially, by about 220 MW. This is expected as, during the night, the entire inverter MVA rating of both the DGs is available for damping control. The improvement is slightly less when the wind DG produces a high level of real power. This is also expected as the reactive power availability decreases with the wind DG real power output.

During daytime, the proposed damping control on both of the DGs also increases the power transfer limits substantially. A greater increase is seen for high real power generation by either one or both the DGs. This is because high real power output can potentially improve the voltage profile at the PCC, which can assist in increasing the power transfer capacity.

7.4 Implementation of PV-STATCOM on Large Scale Solar System

The PV-STATCOM technology will be showcased, for the first time, on two 10 kW solar systems in the networks of two electrical distribution utilities in Ontario, Canada, in late Fall 2012. These utilities are Bluewater Power in Sarnia, and London Hydro in London. The 10 kW solar systems will be utilized for voltage regulation and power factor correction in addition to generating real power. Several detailed testing and validation studies are required to be completed before the PVSTATCOMs will be allowed to connect to the wires of the two utilities. These include: (i) PV-STATCOM controller testing with EMTDC/PSCAD simulation studies [166], [191], (ii) controller validation using Real Time Digital Simulation (RTDS) [192], and finally, a full scale 10 kW lab demonstration of the PV-STATCOM performance in accomplishing the above desired objectives [192]. In the lab, some of the tests that would be performed to meet the requirements of IEEE standards 519 [69] and 1547 [59], in addition to others, are:

- Power Efficiency
- Current Harmonics
- Power Losses
- AC/DC Disconnection tests
- Response to Abnormal Utility Conditions

- Response to Short Circuit at PV System AC Terminals

The path for implementing PV-STATCOM technology in large real scale solar power systems is much more complex than that for the 10 kW systems. Major issues have to be examined and addressed. With respect to inverter technologies, adapting the PV-STATCOM concept to different configurations of inverters – 6 pulse, multi pulse, multilevel, etc., and control coordination amongst multiple inverters in a PV solar plant, with each operating in PV-STATCOM mode, need to be addressed. Grid connection issues, such as protection and control, voltage rise and harmonics, short circuit current limitations, and disconnection during faults or staying connected with Low Voltage Ride Through (LVRT) Capabilities, need to be examined. Retrofitting PV inverters in large solar plants with PV-STATCOM technology will have to deal with warranty issues of inverters, in addition to revalidation of the solar system performance with the new PV-STATCOM retrofit. Another aspect that must be considered is conformance to grid connectivity standards, such as, IEEE 1547 and its planned updates.

7.5 Conclusion

STATCOM and other FACTS controllers have been extensively used in power systems for enhancing the power transfer limits. However, this is the first time that a study is being presented for a large PV solar farm (typically 100 MW) to be employed as a STATCOM during the night to increase the power transmission limits [193]. This chapter proposes a new application of a PV solar DG as a STATCOM utilizing a novel voltage and damping control for improving the transient stability and, consequently, the stable power transfer limit in a transmission system. This new control of a PV solar DG as STATCOM is termed PV-STATCOM.

Similar control can also be implemented on inverter based wind turbine generators. The effectiveness of the proposed controls is demonstrated on two study systems in which a large equivalent generator supplies power over a long transmission line. In Study System 1, a single 100 MW PV solar DG is connected in the middle of transmission line. In Study System 2, two 100 MW DGs are used – one solar/wind and another PV solar, located at $1/3^{\text{rd}}$ and $2/3^{\text{rd}}$ of line length, respectively. Three-phase fault studies using

EMTDC/PSCAD software are conducted to obtain the stable power transfer limits for different DG controls.

Three different types of STATCOM controls are demonstrated for both the PV solar DG and inverter based wind DG. These are pure voltage control, pure damping control, and a combination of voltage control and damping control. The following conclusions are made:

Solar farms are presently idle during the night. The proposed novel control brings a paradigm change in the operation of PV solar farms, whereby they can be operated during the night as STATCOMs, for providing significant improvements in the power transfer limits of the transmission system.

In Study System 1, the maximum increase in power transfer limit (up to 168 MW) during the night is achieved with a combination of voltage control and damping control. The level of power transfer increase with voltage control is dependent on the choice of bus voltage reference. During the daytime, the PV-STATCOM can also improve the power transfer limit substantially (up to 142 MW) with the proposed damping control even when the solar DG is generating a high amount of real power. Damping control is seen to be more effective than a combination of voltage control and damping control.

In Study System 2, during the night, when both the 100 MW solar DG and 100 MW wind DG are operated as STATCOMs with the proposed damping control (with no voltage controller), the transmission capacity is increased substantially (up to 229 MW) if none are producing real power. During both nighttime and daytime, the proposed damping control on both the DGs also increases the power transfer limits substantially (of about 200 MW), even when one or both of the DGs are generating high real power. The power transfer limit enhancements will understandably vary for different transmission systems, sizes, and locations of the PV solar and wind DGs.

It is understood that solar DGs, while performing as PV-STATCOMs, will be utilizing almost the full inverter capacity, which may lead to increased inverter losses. However, the economic benefits to the transmission system in the form of increased stability limit

are very significant. This study, thus, makes a strong case for relaxing the present grid codes to allow selected inverter based renewable generators (solar and wind) to exercise damping control, thereby increasing much needed power transmission capability. Such novel controls on PV solar DGs (and inverter based wind DGs) will potentially reduce the need for investments in additional expensive devices such as series/ shunt capacitors and FACTS. The PV-STATCOM operation opens up a new opportunity for PV solar DGs to earn revenues during both the night and day, in addition to revenue from the sale of real power during the day. This will of course require appropriate agreements between the regulators, network utilities, solar farm developers, and inverter manufacturers.

Chapter 8

8 Harmonic Analysis of Distribution Network with Large Scale PV Solar Farm.

8.1 Introduction

In this chapter, a harmonics impact study is presented for a distribution network which connects the largest solar farm in Canada. This study is performed utilizing detailed network data, a central Geographical Information System (GIS) database, and Supervisory Control And Data Acquisition (SCADA) infrastructure made available by the utility service provider, Bluewater Power Corporation (BWP), Sarnia. The network is modeled in detail by using EMTDC/PSCAD software which is validated through CYME software based load flow study and SCADA measurements. The validated network model is used for network resonance study and analysis of harmonics injection by the 80 MW solar farms for different network conditions. The objective is to investigate if such a large solar farm can cause any harmonic distortion issues in the network of Bluewater Power.

Section 8.2 provides the general system description for the real distribution network connecting to the large scale solar farm. Section 8.3 describes the general overview of various sources of data acquisition system for the real network. In Section 8.4, the system modeling both in CYME [194] and EMTDC/PSCAD [165] are discussed. Section 8.5 presents the load flow validation results for the modeled network with SCADA measurements. Section 8.6 describes the frequency scan results for the network during different scenarios based on EMTDC/PSCAD simulations. Section 8.7 presents the impact of harmonic currents injected by the large scale solar farm on the network. Section 8.8 presents a discussion of the results and finally, the conclusions from this work.

8.2 System Description

8.2.1 Sarnia Solar Farm

The total size of the Sarnia solar farm is 80MW, which makes this solar, farm the largest in Canada [195]. The entire solar farm is interfaced with the Bluewater Power (BWP)

distribution network operating at 27.6 kV voltage level and is connected on four feeders with an equal generation of 20 MW on each feeder. These four feeders are 96M23, 96M27, 96M28 and 18M14. The first three are connected at the downstream of the Modeland substation and the fourth is connected at the downstream of the St. Andrews Substation. This thesis deals with the solar farms on feeder 18M14 only.

8.2.2 St. Andrews Substation and Feeder Capacitors

The St. Andrews substation is supplied from the 115 kV network of Hydro One Inc. through two 50/66.6/83.3 MVA, 110/28.4kV tap changer substation transformers having percentage impedances of 12.4% (ONS)¹/16.5% (ONP)²/20.7% (OFP)³. However, this impedance can vary with the change in transformer tap at any side of the transformer. At the secondary of the substation transformers the nominal voltage is 27.6 kV. The operating voltage varies between 28 kV to 29kV throughout the day and night depending upon the tap settings of the substation transformers and the loading condition of the feeder. There are two sets of feeder capacitors or station capacitors installed on this substation with a capacity of 20MVA_r each, for voltage support. In this chapter, one of the feeders from the St. Andrews substation, 18M14, is modeled for various case studies.

8.2.3 Feeder 18M14 and Major Loads

The feeder 18M14 is connected with 'Q' bus at the St. Andrews substation. This feeder basically feeds two large industrial customers. The largest customer consumes approximately 10-11 MW; whereas, the second large customer consumes approximately 2 MW. A set of power factor correction capacitors of 1.2 MVA_r in size is installed on the second large customer's premises. A small number of residential and commercial customers are also connected with this feeder. However, the load profile is almost flat all day and night, at around 13-14 MW. The total number of distribution transformers connected with 27.6kV system on this feeder is 54; feeding all of the customers on this

¹ ONS stands for Oil-immersed, Natural-cooling, Self-circulation.

² ONP stands for Oil-immersed, Natural-cooling, Pumped-circulation.

³ OFP stands for Oil-immersed, Fan-cooling, Pumped-circulation.

feeder. Almost all of the distribution lines are overhead except two small segments of three phase underground cable. The length of the feeder supplying the farthest distribution transformer is approximately 7.8 km. There are two 10MW solar farms on this feeder; Sarnia Solar 2 and Sarnia Solar 5. Both are installed at a distance of approximately 6.2 km from the substation. As a result, occasionally this feeder can have a total generation of 20 MW, which is partially fed back to the substation.

8.3 Network Data Acquisition Systems

For this research, data corresponding to each of the feeder, solar farms, and substations are obtained from different authentic sources such as, Supervisory Control and Data Acquisition System (SCADA) installed at BWP office, Geographical Information System (GIS), central customer data storage vault etc. All of the data for different network elements are given in Appendix-E.

8.3.1 SCADA System

The SCADA system grabs the online data from the field wherever the monitoring equipment or sensors are placed on the network. In the BWP network, the sensors or monitoring equipment are placed mostly at the substation feeder level, solar farms or at some other specific points on the network. Historic data can also be obtained from SCADA archives. The SCADA monitoring system is capable of showing graphically the online power flow, voltages, currents, power factors, and status of switches, etc. The snapshots for monitored quantities in each substation are attached in Appendix E.

8.3.2 GIS System

GIS stores specific technical parameters of the electrical network laid on a geographical map with all geographical data. Therefore, the location of loads, line lengths, cable specification, transformer specifications, etc. can be obtained from GIS. Thus, it graphically depicts the overall network structure. The GIS networks of the concerned feeders and the location of the substation and solar farms are presented in Appendix E.

8.4 System Model

In modeling the system for feeder 18M14, two software are used; CYME [194] and EMTDC/PSCAD [165]. In BWP, the CYMEDist module from CYME software is used to construct the network model from GIS and SCADA information, and performs steady state load flow studies. As CYMEDist does not have any network frequency scanning capability, the network is modeled in EMTDC/PSCAD, which is capable of performing the frequency scan of the network. The CYMEDist model is basically used to calculate network parameters and validate the network model of EMTDC/PSCAD through steady state load flow.

8.4.1 Grid/Source Model and Capacitor Banks Model

The St. Andrews substation is modeled as Grid or Source from the given short circuit data behind two parallel transformers. It is noted that the St. Andrews substation includes two station capacitors, which are also included in the source model.

8.4.1.1 CYME Model

In CYME, the St. Andrews substation is modeled as an ideal voltage source behind an impedance, according to the short source circuit data available from BWP on the downstream (LV side) of the substation transformer for feeder 18M14. Based on the 3-phase fault MVA and X/R ratio at the downstream of the transformer, CYMEDist is used to calculate the equivalent source parameters, which includes substation transformer impedances. It is noted that the transformer configuration is delta-wye grounded with delta winding at HT side. In CYME, incorporating the equivalent impedances inside the source does not show any voltage drop effects as the CYME source model always presents a constant voltage at the terminal of the sources. To address this problem, the equivalent source impedance is calculated first with the CYME source model by using given short circuit data and X/R ratio. Finally, the calculated impedance is modeled by connecting a 1:1 delta-wye grounded transformer as equivalent source impedance. Therefore, an ideal source connected behind the transformer shows the source voltage drop effect. However, the zero sequence impedances calculated with CYME source parameters are included as grounding impedance at the wye side windings of the modeled

transformer. The snapshots for the CYME software modeling are illustrated in Appendix-E.

8.4.1.2 EMTDC/PSCAD Model

In EMTDC/PSCAD software, the St. Andrews substation is modeled as an ideal voltage source behind the short circuit impedances as given in Appendix-E. It is noted that, in EMTDC/PSCAD, incorporating the source impedance in the source itself is able to show the voltage drop effect due to the source impedances at its terminal. The substation transformers are modeled in detail with their percentage impedance given in Appendix-E.

8.4.2 Feeder Model

8.4.2.1 CYME Model

In modeling 18M14, each overhead line and cable is modeled based on the data from GIS, BWP material list documents for underground cables and overhead line conductors, conductor manufacturer's datasheet, visual inspection at the sites, and discussion with BWP linesman and technical personnel. Based on the information gathered from these sources for the cables, conductors, and overhead lines, the parameter values for R, X and B are modeled in CYME. The values of R are found in the conductor manufacturer's datasheet; whereas, the value of X and B are calculated by using the conductor and its spacing as defined in the dialog box of 'conductor' and 'single circuit spacing' under 'equipment' menu in CYMEDist [194]. In a similar fashion the cable parameters are also calculated by using CYME and the manufacturer's datasheet by defining the conductor structures [194]. The corresponding lengths and sizes of the cables and overhead line conductors used in the network are taken, specifically, from an existing ArcGIS database. The snapshot for the CYME software modeling is illustrated in Appendix-E.

8.4.2.2 EMTDC/PSCAD Model

In EMTDC/PSCAD, the overhead line and underground cables are modeled as nominal PI section which is a multiphase coupled equivalent PI circuit representation [165]. It is recommended that overhead line segments lower than 150/h miles and underground cables lower than 90/h miles should be modeled as multiphase coupled equivalent circuits

[143], [196], [197] where ‘h’ represents the harmonic number. Therefore, in this study for a harmonic of maximum 30th order, the threshold length for modeling as a nominal PI section for overhead line segment is calculated as 5 miles, and the underground cable segment is calculated as 3 miles. In the feeder modeling, none of the overhead line segment or cable segment exceeds this threshold value, thus, modeling as a nominal PI section satisfies the recommended guideline. In modeling this nominal PI section in EMTDC/PSCAD, the line length and positive and zero sequence parameters are used. These parameters are obtained from the CYME feeder model as illustrated in Appendix-E.

8.4.3 Loads and Load Capacitor Models

8.4.3.1 CYME Model

The solar farm is connected with the 27.6kV system. The low voltage network of the concerned feeders does not include any long cables or capacitors, hence the modeling of low voltage networks with the load transformers is avoided [196]. For the feeder 18M14, each distribution transformer at the 27.6kV level is considered as a passive spot load and is modeled as a constant power load at a fundamental frequency [143], [149]. Since the details of each individual load are not available, the loads are distributed based on the total connected capacity of distribution transformers obtained from ArcGIS database and the total loading information of the feeder as obtained from historical data of SCADA. For large customers, wherever the load data is available from metering units, they are modeled as constant power or fixed spot load based on historic data.

8.4.3.2 EMTDC/PSCAD Model

As in the CYME load model, all of the spot loads are modeled in EMTDC/PSCAD as fixed P,Q loads by choosing both dP/dV and dQ/dV indexes as zero. Since the feeder 18M14 is the most critical feeder at the St. Andrews substation, the remaining feeders on this substation are modeled as aggregated fixed loads [143].

8.4.4 PV System Model

In modeling the PV system both for harmonics and load flow analysis, each 10 MW PV system is modeled as a single aggregated source, both in CYME and EMTDC/PSCAD, as follows:

8.4.4.1 CYME Model

The PV system injects only real power at unity power factor and is coupled electronically with PCC. Hence, it is modeled as an electronically coupled generator given in the CYME library.

8.4.4.2 EMTDC/PSCAD Model

In EMTDC/PSCAD, the modeling of the inverter based PV solar farm is simplified by modeling the solar farm as an equivalent P-Q bus for load flow validation purposes only. However, for a detailed harmonics analysis, the inverter based DGs are represented as current sources with multiple harmonic current sources injecting into the network [198]. The network is considered to be balanced and the ambient harmonics from prior investigations are found to be less than 5%, which validates the modeling of the PV system by harmonics current sources [143], [149]. The line impedance between the PCCs of two 10 MW PV systems is negligible, and hence, does not create any significant phase differences between the harmonic current sources of same order of two 10MW units [143], [149], [197]. Moreover, modeling corresponding harmonics with the same phase angle adds them arithmetically; which is the worst-case scenario for multiple sources [149]. Modeling the ambient harmonics due to the harmonics current drawn by the loads [198] is outside the scope of this work. It is, therefore, assumed that the phase angles of the ambient PV harmonics do not influence the harmonic distortion study [143], [149]. However, the phase angle of the fundamental current from the solar farm is adjusted according to the voltage at the PCC through load flow study [143], [149] for unity power factor operation. Further, the phase angles of the harmonics are adjusted relative to the fundamental current component. All of the harmonic current sources up to the 25th order are modeled for the analysis as recommended in [149]. As the harmonics of interest are less than the 30th order, the modeling of transformers connected to the PV solar farm is

avoided [196]. The current source model of each 10MW PV solar farm unit in EMTDC/PSCAD is attached in Appendix E with proper phase sequence for each harmonic source.

8.5 Steady State Load Flow Validation of System Model

A load flow study is performed to validate the network model in EMTDC/PSCAD with CYME and real time data from SCADA. Although, EMTDC/PSCAD is electromagnetic transient simulation software, the load flow results can be validated with its steady state simulation output. The validation is performed in terms of voltages at different points on the feeder with corresponding power flow. The voltage at the source modeled in CYME representing the substation is chosen such that it matches the substation bus voltage.

Table 8.1 and Table 8.2 present the voltages and power flow from load flow for feeder 18M14. It is seen that the bus voltages from the CYME model data closely match with the SCADA measurements. The power generation mismatch between the CYME results and SCADA is also less than 4%. This validates the CYME model of the feeder 18M14.

Table 8.1 Daytime Data on 18M14 (time stamp-25/05/2011 at 12:22PM)

Measurement Location	SCADA	CYME	EMTDC/PSCAD	Deviations (%) SCADA vs. CYME	Deviations (%) CYME vs. EMTDC/PSCAD
Voltage (kV)					
St. Andrews Substation ('Q' Bus)	28.615 (Avg.)	28.618	28.618	0.01	0
Sarnia Solar 2 (SS2)	28.579	28.53	28.538	0.171	0.028
Sarnia Solar 5 (SS5)	28.579 (16.5 L-N)	28.529 (16.47 L-N)	28.537	0.171	0.028
Load end Capacitor	-	28.486	28.486	-	0
Largest load end	-	28.321	28.24	-	0.01
Real Power (MW)					
St. Andrews Substation (Feeder relay 18M14)	6.821	6.825	682	0.058	0.073
Sarnia Solar 2 (SS2)	3.023	3.136	3.023	3.74	3.6
Sarnia Solar 5 (SS5)	3.252	3.136	3.25	3.57	3.63
Reactive Power (MVar)					
St. Andrews Substation (Feeder relay 18M14)	2.694	2.688	2.69	0.222	0.074

Table 8.2 Nighttime Data on 18M14 (time stamp-7/10/2011 at 12:05 am)

Measurement Location	SCADA	CYME	EMTDC/P SCAD	Deviations (%) SCADA vs. CYME	Deviations (%) CYME vs. PSCAD
Voltage (kV)					
St. Andrews Substation ('Q' Bus)	28.911 (Avg.)	28.914	28.916	0.01	0.007
Sarnia Solar 2 (SS2)	28.694	28.618	28.633	0.265	0.05
Sarnia Solar 5 (SS5)	28.752	28.618	28.633	0.466	0.052
Load end Capacitor	-	28.651	28.66	-	0.031
Largest load end	-	28.469	28.449	-	0.07
Real Power (MW)					
St. Andrews Substation (Feeder relay 18M14)	14.44	14.44	14.46	0	0.138
Sarnia Solar 2 (SS2)	0	0	0	-	-
Sarnia Solar 5 (SS5)	0	0	0	-	-
Reactive Power (MVar)					
St. Andrews Substation (Feeder relay 18M14)	4.417	4.42	4.42	0.068	0

It is further seen that both bus voltage and the power flow obtained from the EMTDC/PSCAD model are in close correlation (less than 4%). Therefore, it is demonstrated that the EMTDC/PSCAD model represents the network of feeder 18M14 with high accuracy. The validated EMTDC/PSCAD model of the feeder 18M14 is now used for harmonic studies.

8.6 Network Impedance and Resonance

Every electrical system has resonance at certain frequency(s) due to the presence of inductive and capacitive elements in the network. Resonance condition of a network varies depending on different operating scenarios such as loading conditions, short circuit levels (SCL), capacitor switching schemes, and line outages, etc. However, if for any aforementioned condition(s), the network resonance frequency aligns with the harmonics injected by PV system or any other harmonic generating loads, excessive voltage and current harmonic distortions may occur, which can potentially lead to malfunction or damage of a customer's or utility's protective devices and equipment.

To analyze the network resonances in the 18M14 feeder, a frequency scan technique is adopted by using the EMTDC/PSCAD software. The frequency scan calculates the network Thevenin equivalent impedances seen from a certain point of interest on the network at different frequencies. By plotting the impedance magnitude versus frequency obtained from this frequency scan, the network resonance frequency can be identified as that at which the impedance exhibits a peak. If one of the harmonic frequencies injected by a harmonic source on the network matches with this resonance frequency, the corresponding harmonic voltage may become amplified based on corresponding impedance magnitudes [147], [148]. The MATLAB software is used to plot the data exported from the EMTDC/PSCAD frequency scan simulation in the feeder network for various network conditions.

On the feeder 18M14, as there are two large station capacitor banks of 20MVAR each, and a load capacitor bank of 1.2 MVAR, a wide range of studies is conducted in EMTDC/PSCAD. The frequency scan study is performed at several locations on the feeder: at the substation, at the solar farm, at the load capacitor bank, and at a large customer end consuming about 80% loads on the feeder 18M14. The following cases are studied at these locations:

Case-I: Base case

Case-II: Variation in Short Circuit Level (SCL) of source

Case-III: Loss of substation transformer.

Case-IV: Loss of large distribution line segment with largest customer on the feeder.

All of these cases are studied with respect to the total station capacitors providing 20 MVAR and 40 MVAR reactive supports to the substation.

8.6.1 Case-I: Base Case

Fig. 8.1 shows the frequency scan at different locations for the case when there is no capacitor bank connected with the feeder. Therefore no impedance peak is observed.

Fig. 8.2 illustrates the frequency scan for the case when the load capacitor of 1.2 MVAR is connected to the feeder. In this case, the resonance peak occurs between the 11th harmonic and the 23rd harmonic at different locations. Fig. 8.3 and Fig. 8.4 depict the frequency scans for the cases when 20 MVAR and 40 MVAR feeder capacitors are

connected, respectively. In these cases, the resonance peaks shift further towards higher frequency regions and at the same time another resonance peak occurs in the low frequency region, between the 2nd and 5th harmonics, as illustrated in Fig. 8.3. Usually, the load capacitor (1.2 MVAR) and one station capacitor (20MVAR) remain connected to the feeder; this is considered to be a base case scenario. Fig. 8.3, thus, represents the network impedances for the base case scenario.

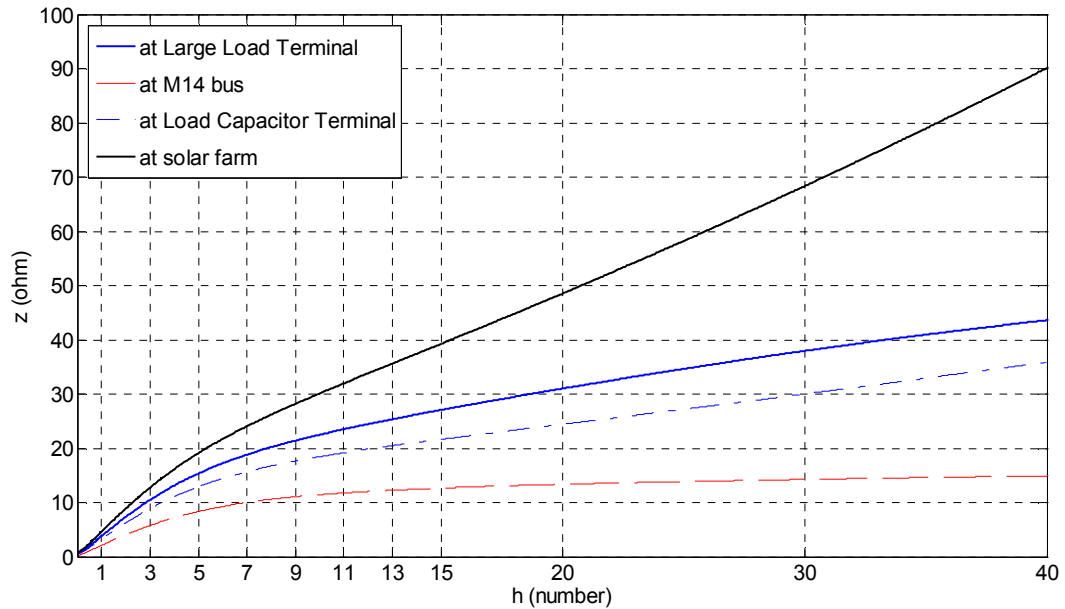


Figure 8.1 Network Impedance vs. Harmonic Frequencies plot when no capacitor is on 18M14.

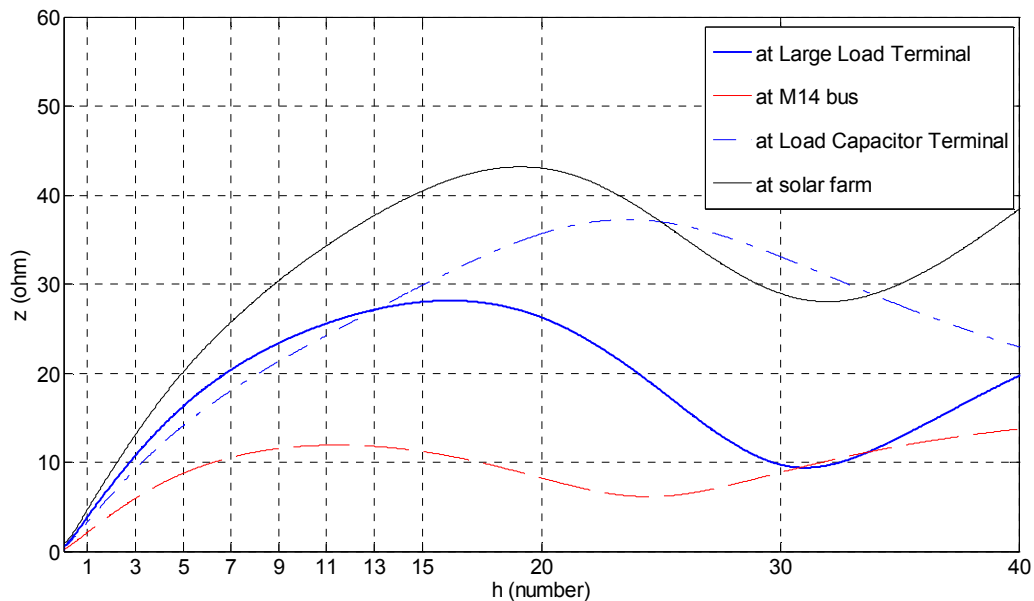


Figure 8.2 Network Impedances vs. Harmonic Frequencies plot when only load capacitor is on 18M14.

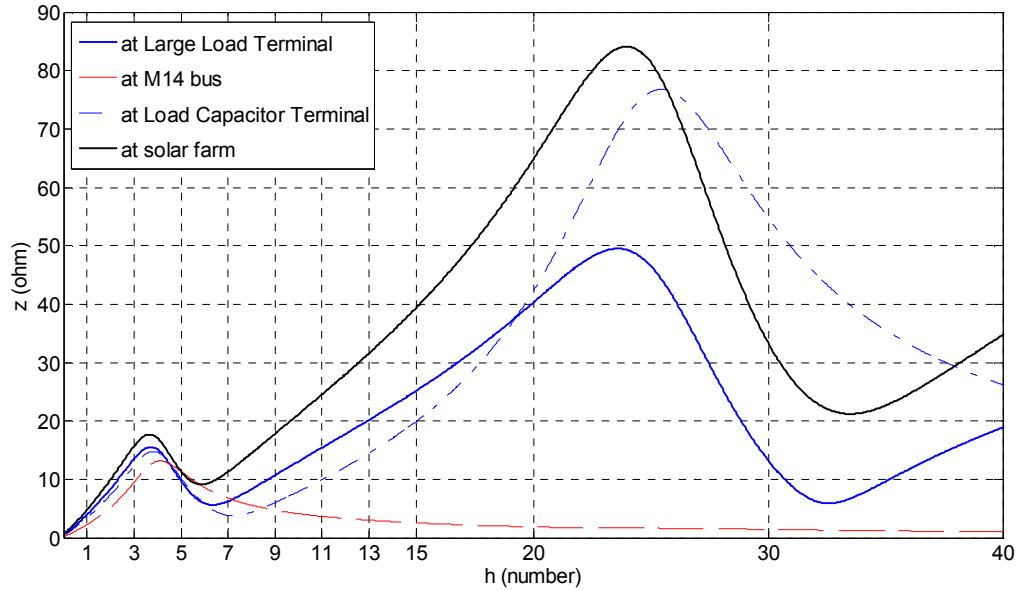


Figure 8.3 Network Impedance vs. Harmonic Frequencies plot when load capacitor and 20 MVar station capacitors are on 18M14.

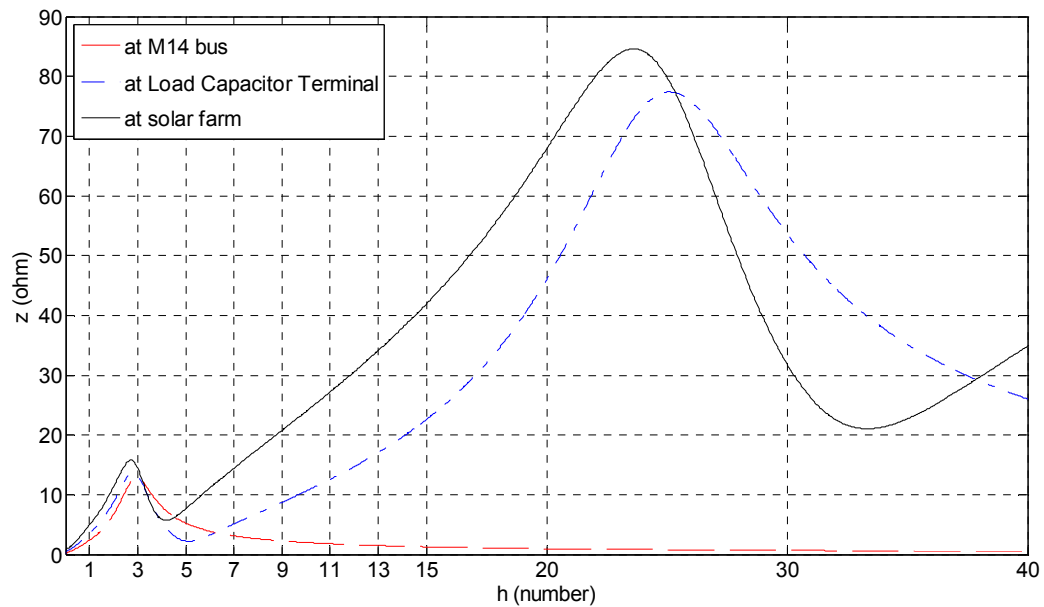


Figure 8.4 Network Impedance vs. harmonic frequencies plot when load capacitor and 40 MVar station capacitors are on 18M14.

8.6.2 Case-II: Variation of SCL of Source

The SCL of the source is altered by varying the short circuit impedance of the source that is connected between the source and the high voltage (HV) side of the transformer. The network resonance peak is observed by connecting 20 MVar and 40 MVar substation

capacitors. Fig. 8.5 and Fig. 8.6 represent the frequency scan plot for 1/3rd SCL and 10 SCL of source, respectively, with 20MVAR reactive support at the substation. It is observed that with the decrease of SCL of source, the low frequency peak shifts further towards the lower frequency region as shown in Fig. 8.5, which coincides with third harmonic frequency for 1/3rd SCL. However, with the increase of SCL of source the low frequency peak shifts toward the high frequency region as presented in Fig. 8.6 for 10 SCL. Fig. 8.7 and Fig. 8.8 represent the frequency scan plots for 4 SCL and 10 SCL of source, respectively, with 40MVAR reactive support at the substation. It is observed from Fig. 8.7 that for 4 SCL the low frequency peak coincides with the third harmonic frequency. However, it is evident from these figures that after the 3rd harmonics alignment they never coincide with any other higher order odd harmonics regardless of the value of SCL. In fact, at higher SCL, the source impedance at the HV side of the transformer becomes relatively lower than the transformer impedance. As a result, the transformer impedance itself dominates the peak resonance which becomes almost constant after a certain network resonance frequency. The high frequency peak due to load capacitor remains almost unaffected due to this variation and is therefore not shown.

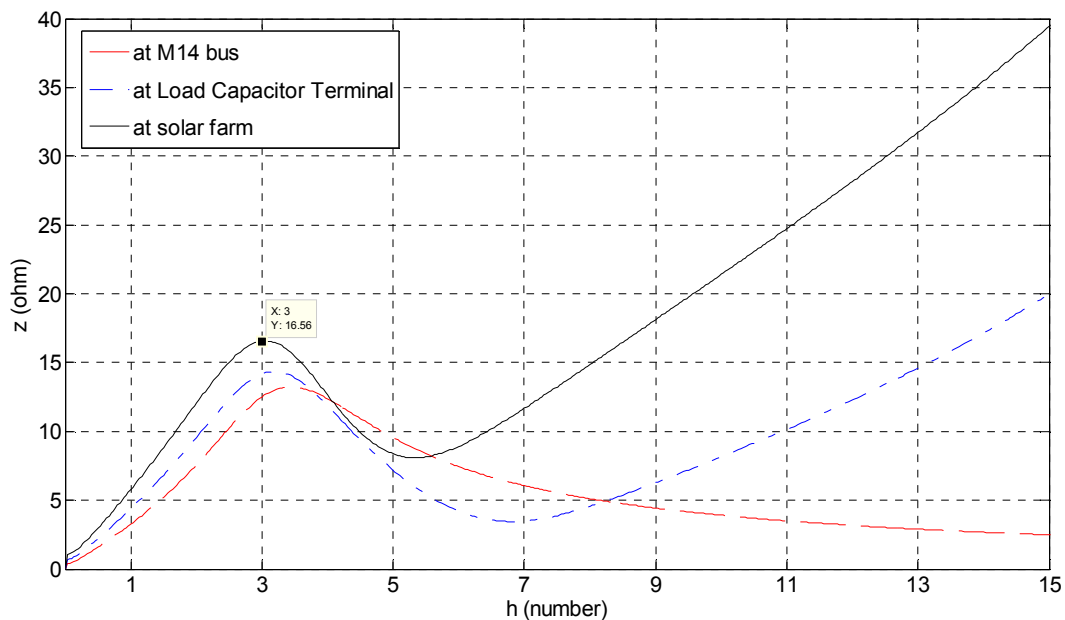


Figure 8.5 Network Impedances vs. Harmonic Frequencies plot when load capacitor and 20 MVAR station capacitors are on 18M14 with 1/3rd SCL of the source.

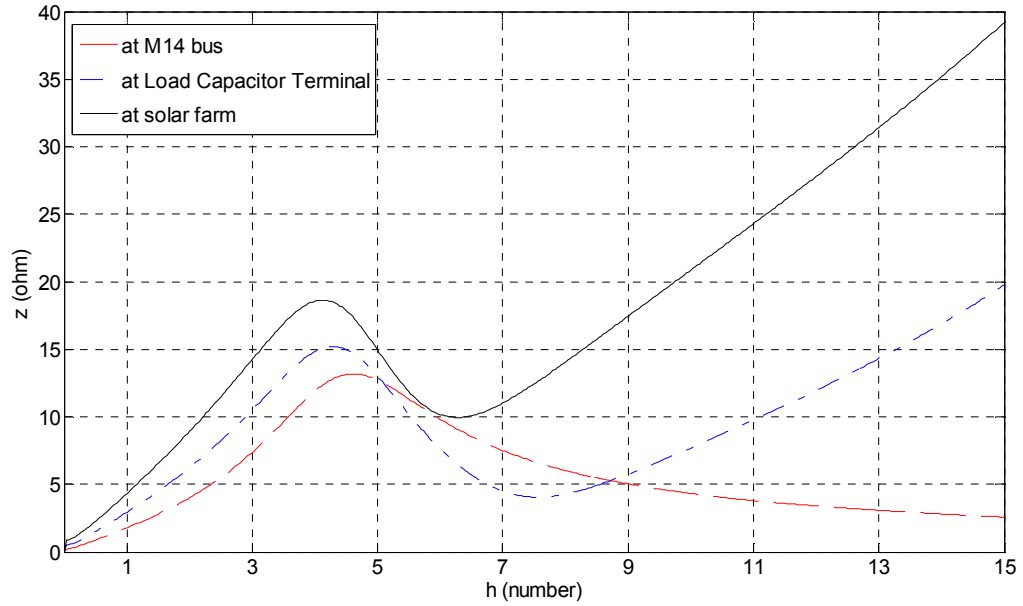


Figure 8.6 Network Impedances vs. Harmonic Frequencies plot when load capacitor and 20 MVar station capacitors are on 18M14 with 10 SCL of the source.

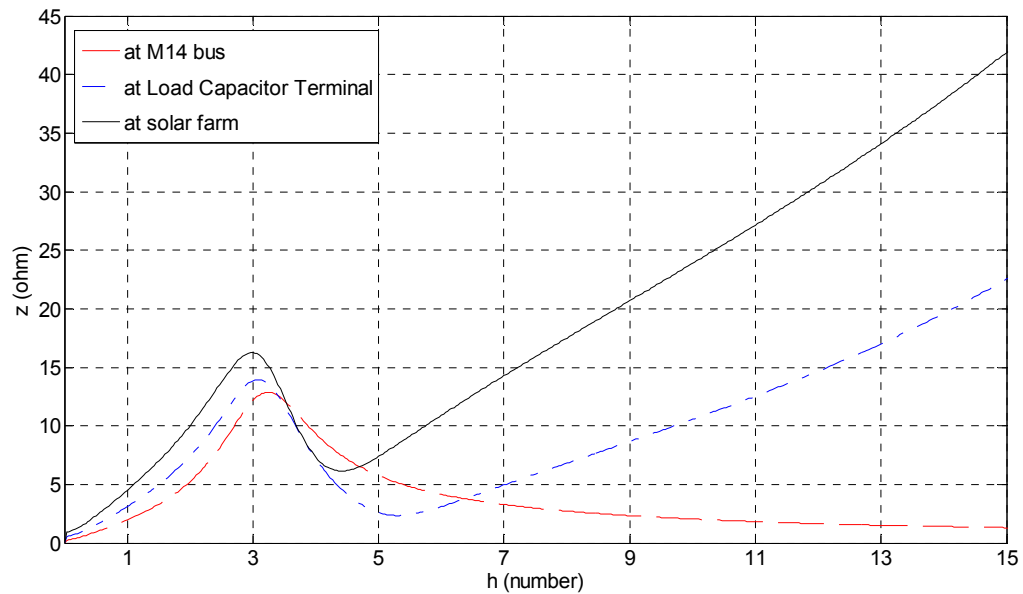


Figure 8.7 Network Impedances vs. Harmonic Frequencies plot when load capacitor and 40 MVar station capacitors are on 18M14 with 4 SCL of the source.

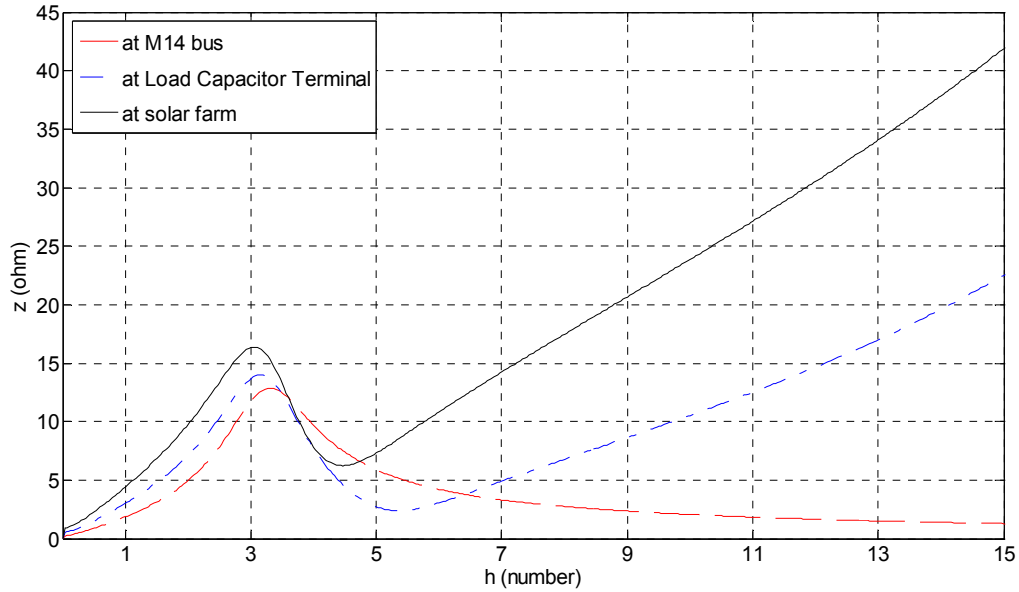


Figure 8.8 Network Impedances vs. Harmonic Frequencies plot when load capacitor and 40 MVar station capacitors are on 18M14 with 10 SCL of the source.

8.6.3 Case-III: Loss of Substation Transformer

Fig. 8.9 and Fig. 8.10 illustrate the cases with the loss of one substation transformer when 20 MVar and 40 MVar feeder capacitors are connected, respectively. This case is also equivalent to the low short circuit level at the LV side.

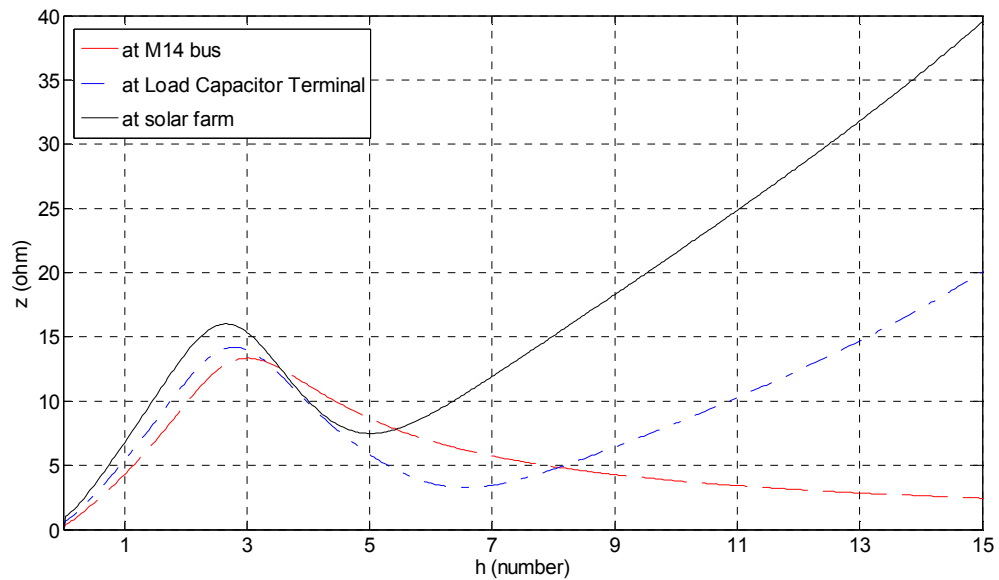


Figure 8.9 Network Impedance vs. Harmonic Frequencies plot when load capacitor and 20 MVar station capacitors are on 18M14 with the loss of one transformer.

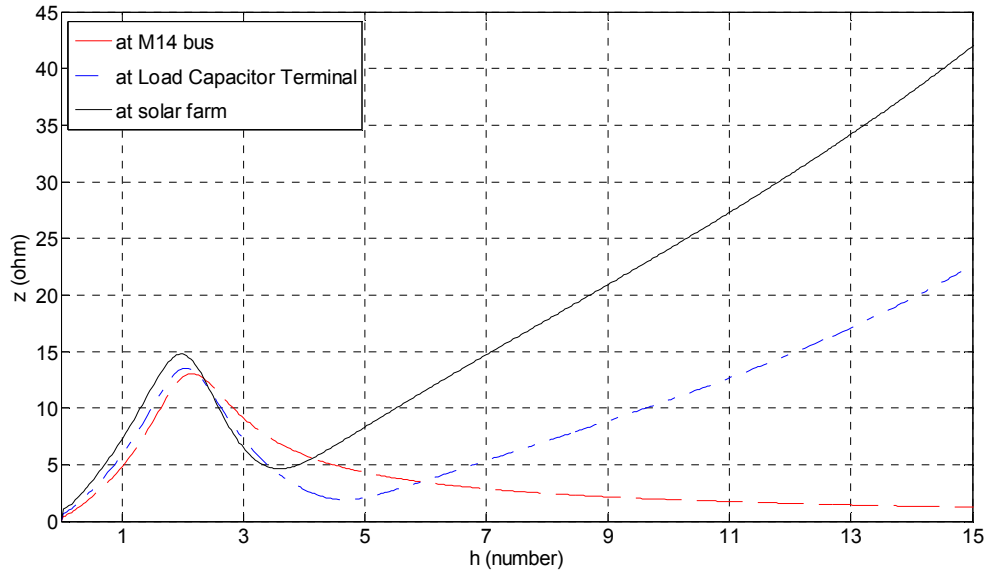


Figure 8.10 Network Impedance vs. Harmonic Frequencies plot when load capacitor and 40 MVAR station capacitors are on 18M14 with the loss of one transformer.

In these cases, the peaks in the low frequency region move towards the lower frequency region around the 2nd harmonic resonance with relatively higher peak magnitudes. However, the second peak resonance, due to customer capacitor, remains almost unaffected with regards to peak magnitude and the frequency and, hence, it is not shown here.

8.6.4 Case-IV: Loss of Large Distribution Line Segment with Large Customer Load

Fig. 8.11 and Fig. 8.12 illustrate the frequency response due to outage of the distribution line segment having a large customer load, while keeping 20MVAR and 40MVAR feeder capacitors connected, respectively. As a result, the low frequency resonance peak moves toward the 5th harmonics by a small amount, and the magnitude of the peak increases due to the loss of large load. The change in magnitude is much more significant for the case of high frequency resonant peaks which more than doubles, compared to those shown in Fig. 8.3 and Fig. 8.4 for 20MVAR and 40MVAR reactive support, respectively. It is thus seen that the large loads decrease the magnitude of impedance peak.

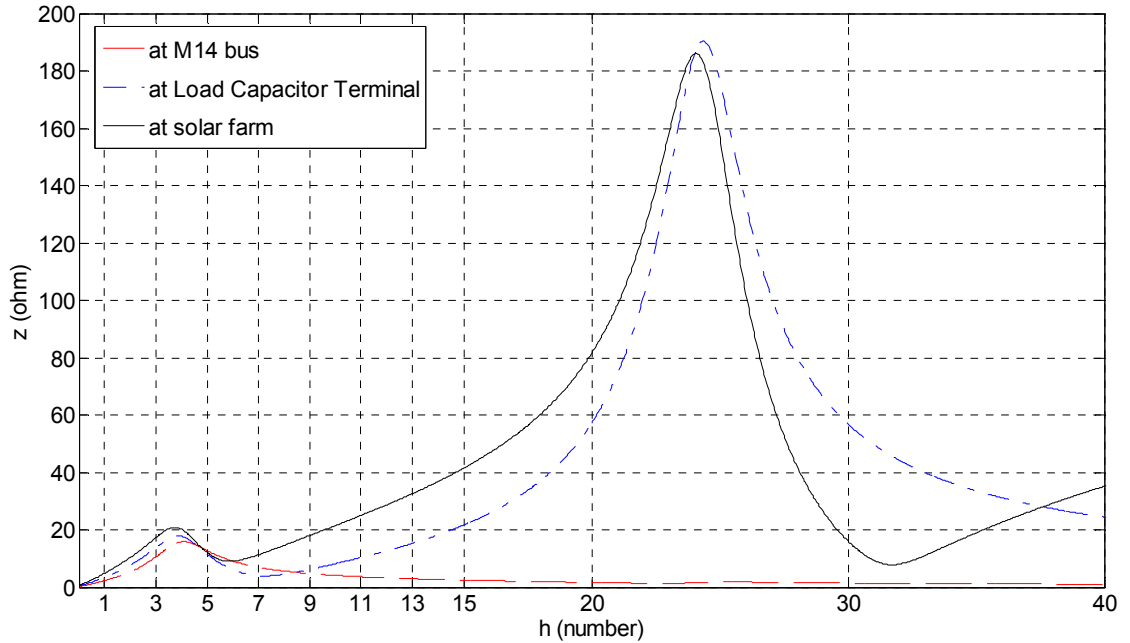


Figure 8.11 Network Impedance vs. Harmonic Frequencies plot when load capacitor and 20 MVar station capacitors are on 18M14 with the loss of largest load on the feeder.

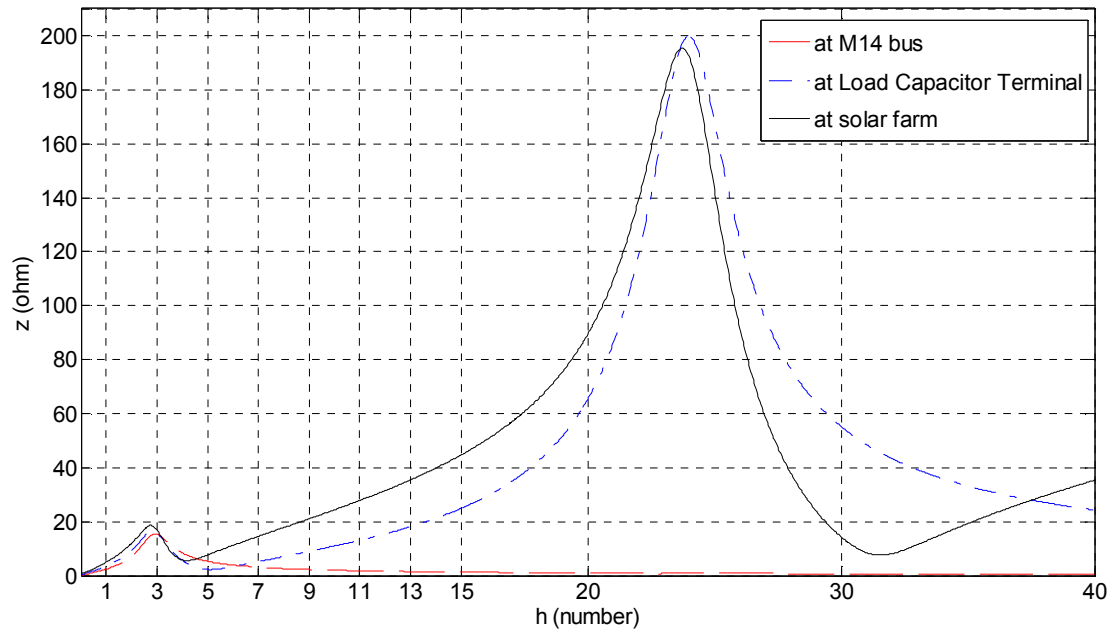


Figure 8.12 Network Impedance vs. Harmonic Frequencies plot when load capacitor and 40 MVar station capacitors are on 18M14 with the loss of largest load on the feeder.

8.7 Impact of PV Solar Farm Harmonics Injection on Network Impedance

The harmonic currents generated by the PV system are injected into the network. This results in harmonics voltages due to the network impedances. These harmonics voltages may be amplified due to network resonances at certain frequencies, as discussed earlier. These harmonic voltages appears across each linear and non-linear loads which may distort both voltage and currents on the network leading to potential malfunction or damage to protective and other equipment. Therefore, the injection of harmonics from the PV system needs to be investigated with respect to network impedance and network resonance. This is also as recommended by IEEE standard 519.

A wide range of harmonics, voltage, and power data from two 10 MW PV solar systems are recorded for the month of June, 2012 by Hydro One Inc. At the same time, the corresponding harmonics, voltage, and power data are also recorded at the St. Andrews substation, by Hydro One Inc. From the data analysis of these two 10MW systems, it is observed that both of them generate identical harmonic currents. The calculated Total Demand Distortion (TDD) for the output harmonics current and the Total Harmonic Distortion (THD) of voltage measured from each 10 MW PV system satisfies the IEEE standard 519, and remains within the specified limits for a wide range of power generation. From the analysis of harmonics data, the 5th, 7th, 11th and 13th current harmonics are found to be relatively dominant. However, as the network conditions and system short circuit levels change continuously, the harmonic distortions are investigated for different short circuit levels and network resonance conditions for different levels of harmonics injection from the solar farms.

8.7.1 Selection of Worst Network Condition by Varying SCL

The conditions for which the network resonance coincides with one or more of the harmonics injected by the solar farm are investigated first. It is observed from the frequency scan in Fig. 8.5 and Fig. 8.7 that the network resonance coincides with the third harmonic for the condition of 1/3rd SCL for 20 MVAR capacitor connection, and 4SCL with 40 MVAR feeder capacitor connection. These are taken to be the worst

network conditions. The harmonics data set from the solar farm is then chosen for the time instant at which it injects the largest third harmonic current into the network.

Fig. 8.13 presents the different harmonic currents injected by each 10 MW solar farm when the third harmonic current injection is highest.

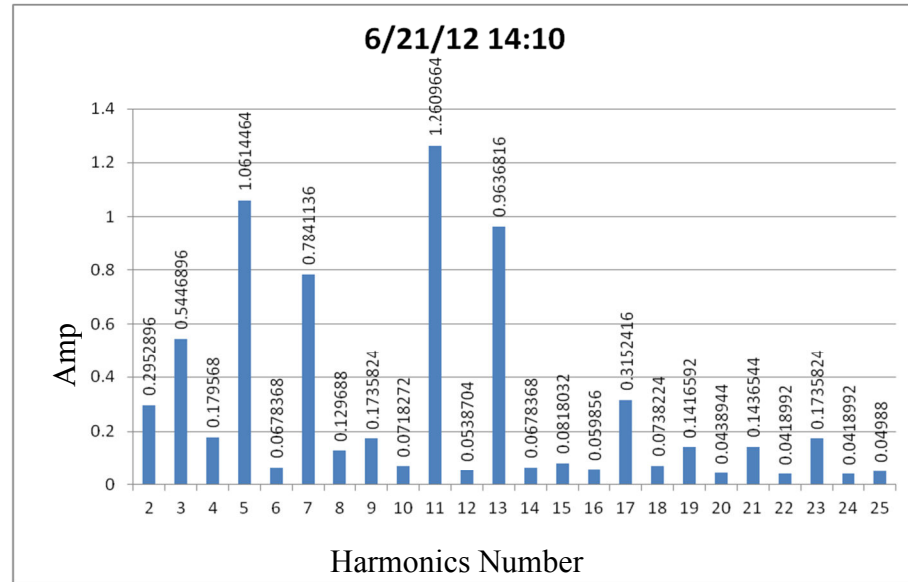


Figure 8.13 Harmonics Dataset for High Third Harmonics Injection

Table 8.3, Table 8.4 and Table 8.5 represent the simulated power, voltage, TDD, THD, voltage harmonic distortion, and some selected individual voltage harmonic quantities for the base case, 1/3rd SCL with 20 MVar feeder capacitor case and for the 4SCL with a 40 MVar feeder capacitor case, respectively. The quantities are tabulated for the St. Andrews substation and each of the 10 MW solar systems: Sarnia Solar SS2 and Sarnia Solar SS5.

Table 8.3 Power, Voltage and Harmonics for Base Case Scenario of Fig. 8.3

Quantities	St. Andrew SS	Sarnia Solar farm SS2	Sarnia Solar farm SS5
Power, P+jQ (MVA)	-6.561+j5.141	10+j0.2831	10.02+j0.2771
Fundamental Phase Voltage, Vf (kV)	16.6277	16.738	16.735
Fundamental Current, If (Amp)	167.88	199.52	199.84
Current TDD (%)	-	1.063	1.063
Voltage THD (%)	0.2053	0.66	0.653
HONI Measured Voltage THD (%)	0.875	1.264	1.274
Voltage Harmonic Distortion (kV)	0.03415	0.1104	0.1092
3 rd harmonic voltage (kV)	0.0137	0.02056	0.0204
5 th harmonic voltage (kV)	0.02485	0.0235	0.02336
7 th harmonic voltage (kV)	0.01132	0.01715	0.01687
11 th harmonic voltage (kV)	0.011	0.06	0.05067

Table 8.4 Power, Voltage and Harmonics for the Network Impedance of Fig. 8.5

Quantities	St. Andrew SS	Sarnia Solar farm SS2	Sarnia Solar farm SS5
Power, P+jQ (MVA)	-6.397+j6.239	9.927-j0.2483	9.941-j0.2551
Fundamental Phase Voltage, Vf (kV)	16.554	16.61	16.608
Fundamental Current, If (Amp)	180.64	199.52	199.84
Current TDD (%)	-	1.063	1.063
Voltage THD (%)	0.185	0.66	0.653
Voltage Harmonic Distortion (kV)	0.03065	0.1097	0.1085
3 rd harmonic voltage (kV)	0.0137	0.02056	0.0204
5 th harmonic voltage (kV)	0.0206	0.017	0.0169
7 th harmonic voltage (kV)	0.01	0.0178	0.01754
11 th harmonic voltage (kV)	0.0105	0.061	0.0602

Table 8.5 Power, Voltage and Harmonics for the Network Impedance of Fig. 8.7

Quantities	St. Andrew SS	Sarnia Solar farm SS2	Sarnia Solar farm SS5
Power, P+jQ (MVA)	-6.931+j4.736	10.19+j0.4582	10.2+j0.4525
Fundamental Phase Voltage, Vf (kV)	16.926	17.057	17.054
Fundamental Current, If (Amp)	166.23	199.52	199.84
Current TDD (%)	-	1.063	1.063
Voltage THD (%)	0.1085	0.6874	0.6805
Voltage Harmonic Distortion (kV)	0.018376	0.117259	0.116056
3 rd harmonic voltage (kV)	0.00816	0.018	0.0177
5 th harmonic voltage (kV)	0.0129	0.015	0.0147
7 th harmonic voltage (kV)	0.0056	0.02178	0.0215
11 th harmonic voltage (kV)	0.0056	0.0671	0.0664

The following observations are made regarding harmonics from these tables:

1. From Table 8.3, it is observed that there is a mismatch between the measured quantity and the simulated quantity of THD which is due to the presence of network harmonics. In the simulation model the ambient harmonics are not considered.
2. In comparison with Table 8.3, the 3rd harmonic voltage at the solar farm is almost the same as the base cases, as shown in Table 8.4 and Table 8.5, which tabulate the peak resonance cases at the 3rd harmonic frequencies. This is due to the same impedance magnitudes at third harmonics for all cases.
3. The fifth harmonics voltage in both Table 8.4 and Table 8.5 are lower compared to Table 8.3. From the frequency scan in Fig. 8.5 and Fig. 8.7, it is observed that the 5th harmonic impedance falls in the valley region. Therefore, the magnitude of voltage harmonics for 5th order is lower.
4. The seventh and eleventh harmonics voltage in Table 8.5 is much lower compared to Table 8.3 and Table 8.4 which is mainly due to the lower impedance magnitudes at those certain frequencies.

5. As compared to base case given in Table 8.3, the voltage THDs as seen from Table 8.4 and Table 8.5 are lower than the base case at the bus of the St. Andrews substation. This is because of the relatively lower net harmonic voltages V_{HD} due to the lower 5th harmonic voltages. Hence, Table 8.4 could be the worst case for third harmonics voltage, but not the worst-case scenario in terms of V_{THD} or overall harmonics voltages. It is noted that the harmonics current injection by the solar farms always remains the same regardless of network condition.

From the above observations, it is evident that the 3rd harmonic resonance at the 18M14 network does not make the worst situation for voltage distortion.

The frequency scan plots in an earlier section are re-examined and it is noted that the network with no capacitors results in high 5th, 7th, 11th, and 13th harmonic impedances (much higher than 3rd) as seen in Fig. 8.1. It is also observed that there is a high injection of 5th, 7th, 11th, and 13th harmonics. Therefore, the network condition in Fig. 8.1 is chosen as the next base case system for the study of harmonics amplification (in a non-resonant case). Table 8.6 represents the simulated power, voltage, TDD, THD, voltage harmonic distortion, and some selected individual voltage harmonic quantities for the case when there are no capacitors connected to the feeder.

Table 8.6 Power, Voltage and Harmonics for the Network Impedance of Fig. 8.1

Quantities	St. Andrew SS	Sarnia Solar farm SS2	Sarnia Solar farm SS5
Power, P+jQ (MVA)	-6.568+j6.469	10.01+j0.2542	10.02+j0.2482
Fundamental Phase Voltage, Vf (kV)	16.66	16.74	16.737
Fundamental Current, If (Amp)	166.23	199.52	199.84
Current TDD (%)	-	1.063	1.063
Voltage THD (%)	0.3	0.827	0.82
Voltage Harmonic Distortion (kV)	0.0499	0.13848	0.13726
3 rd harmonic voltage (kV)	0.0122	0.0313	0.03106
5 th harmonic voltage (kV)	0.01946	0.0413	0.041
7 th harmonic voltage (kV)	0.01674	0.03786	0.0376
11 th harmonic voltage (kV)	0.03055	0.0795	0.0788

From this table it is observed that the voltage THD and the voltage harmonic distortion is higher compared to all of the earlier cases presented in Table 8.3, Table 8.4 and Table 8.5. Note that, as there is no valley in the plot of corresponding frequency scan presented in Fig. 8.1, all of the harmonics voltages over third harmonics are higher than the

previous cases. Therefore, the network condition, without any capacitors is considered to be the worst network condition for the successive studies.

8.7.2 Harmonics Distortion Due to Worst Network Condition

Fig. 8.14 presents the power output from the solar farm during a sunny day with measured harmonics, current THD, and the calculated TDD.

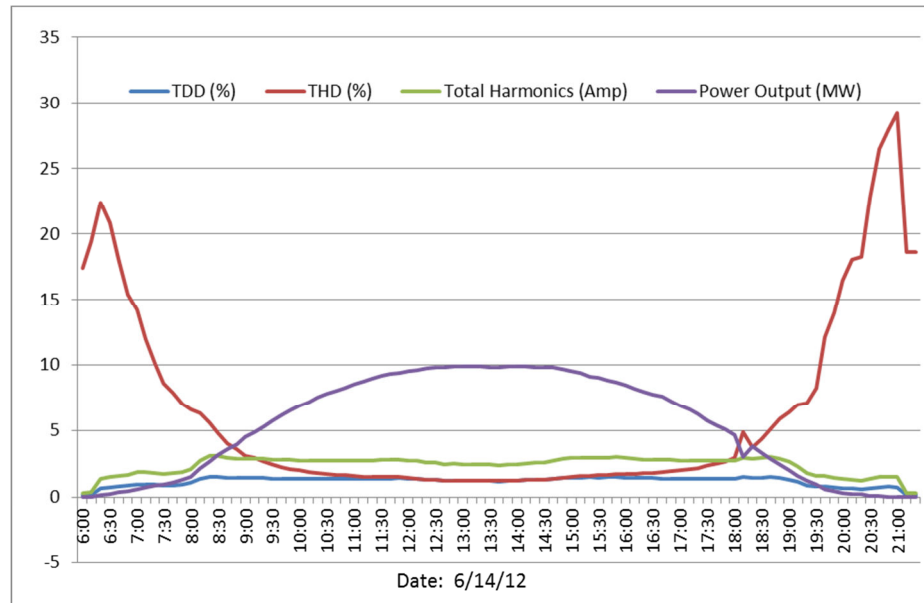


Figure 8.14 10 MW Solar Farm Output for a Sunny Day

Three arbitrary harmonic datasets are chosen: evening time, noon time, and the moment of the highest harmonic injection in that day, which are depicted in Fig. 8.15, Fig. 8.16 and Fig. 8.17, respectively. The corresponding simulation results are presented in Table 8.7, Table 8.8 and Table 8.9 for the evening, noon, and the high harmonics injection time, respectively. Note that the simulation results are obtained for worst network condition in Fig. 8.1.

It is observed from Fig. 8.14, Fig. 8.15, Fig. 8.16, and Fig. 8.17 that the pattern of harmonics is similar at different times, but the magnitude of harmonics varies with the power output level of the solar farm. Comparing Table 8.7, Table 8.8 and Table 8.9, the voltage THD as well as the voltage harmonics are seen to be higher for the case of high harmonic injection from the solar farm, as seen in Table 8.9.

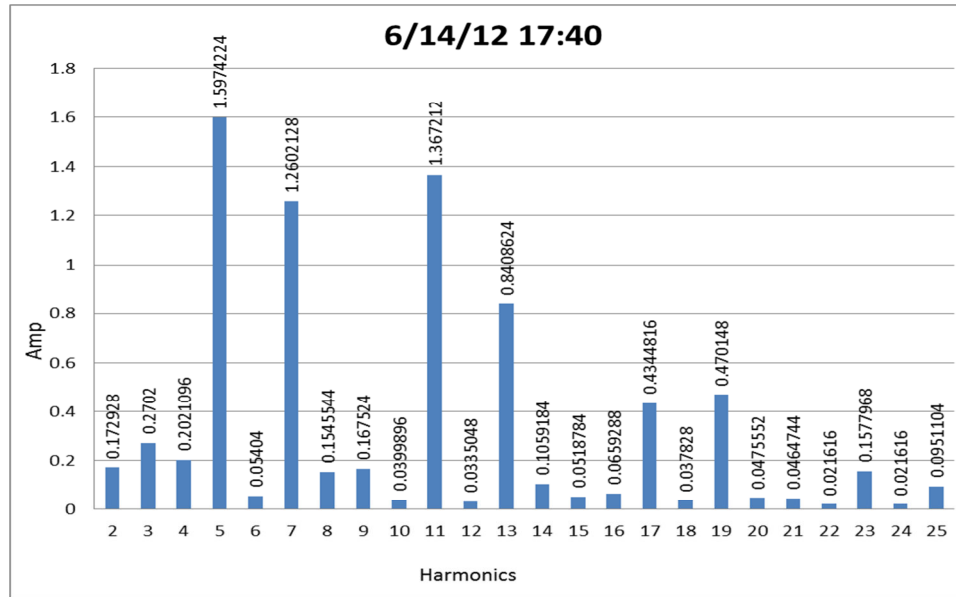


Figure 8.15 Harmonics Dataset in the Evening of a Sunny Day

Table 8.7 Power, Voltage, Harmonics Distortion during the Evening of a Sunny Day

Quantities	St. Andrew SS	Sarnia Solar farm SS2	Sarnia Solar farm SS5
Power, P+jQ (MVA)	2.639+j6.789	5.33-j0.1482	5.33-j0.1501
Fundamental Phase Voltage, Vf (kV)	16.532	16.463	16.461
Fundamental Current, If (Amp)	145.56	108.08	108.08
Current TDD (%)	-	1.3	1.3
Voltage THD (%)	0.356	0.927	0.919
Voltage Harmonic Distortion (kV)	0.0589	0.15263	0.15136

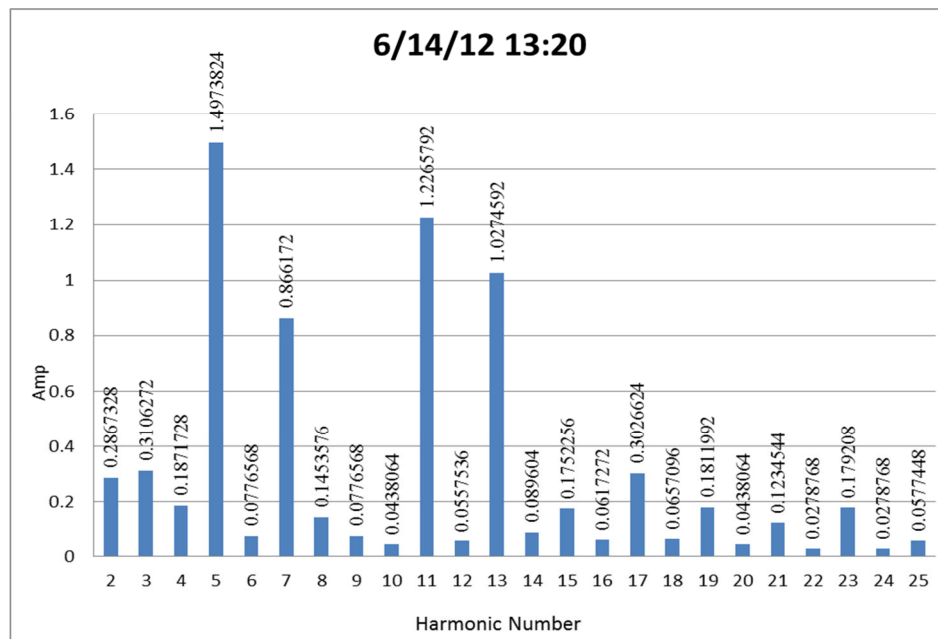


Figure 8.16 Harmonics Dataset around noon on a Sunny Day

Table 8.8 Power, Voltage, and Harmonics Distortion at noon on a Sunny Day.

Quantities	St. Andrew SS	Sarnia Solar farm SS2	Sarnia Solar farm SS5
Power, P+jQ (MVA)	-6.508+j6.471	9.983+j0.2518	9.981+j0.2455
Fundamental Phase Voltage, Vf (kV)	16.66	16.738	16.736
Fundamental Current, If (Amp)	184.46	199.12	199.12
Current TDD (%)	-	1.175	1.175
Voltage THD (%)	0.32	0.864	0.857
Voltage Harmonic Distortion (kV)	0.05345	0.14467	0.14342

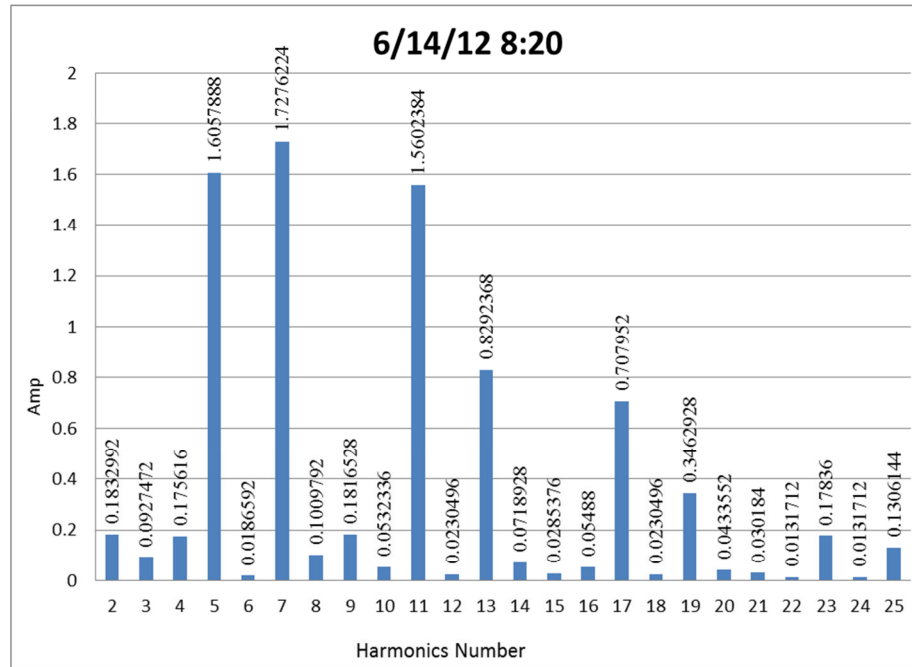


Figure 8.17 High Harmonics Dataset on a Sunny Day

Table 8.9 Power, Voltage, and Harmonics Distortion for High Harmonics Injection on a Sunny Day.

Quantities	St. Andrew SS	Sarnia Solar farm SS2	Sarnia Solar farm SS5
Power, P+jQ (MVA)	7.852+j6.756	2.712-j0.1716	2.712-0.1721
Fundamental Phase Voltage, Vf (kV)	16.65	16.513	16.512
Fundamental Current, If (Amp)	205.75	54.88	54.88
Current TDD (%)	-	1.474	1.474
Voltage THD (%)	0.4085	1.0457	1.0372
Voltage Harmonic Distortion (kV)	0.06801	0.17269	0.17127

Further investigation is made for a cloudy day. Fig. 8.18 presents the power output from the solar farm during a cloudy day with measured harmonics, current THD, and the calculated TDD. Like the sunny day case, three arbitrary harmonic datasets are chosen: evening, noon, and the moment of highest harmonic injection in the day, which are

depicted in Fig. 8.19, Fig. 8.20 and Fig. 8.21, respectively. The corresponding harmonics simulation results are presented in Table 8.10, Table 8.11 and Table 8.12 for the evening, noon, and the high harmonics injection time, respectively. The same worst case network is used for this simulation study as well.

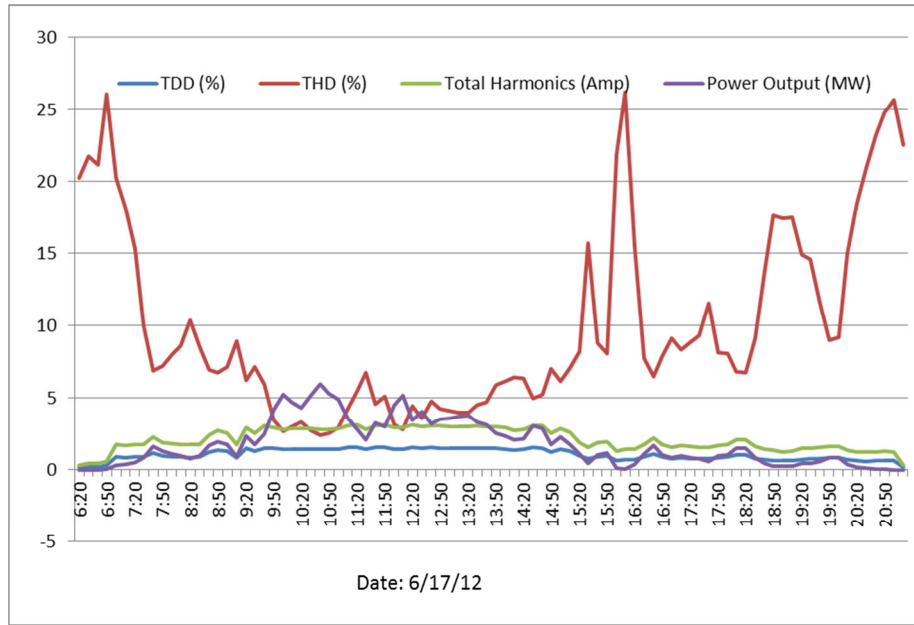


Figure 8.18 10 MW Solar Farm Output for a Cloudy Day

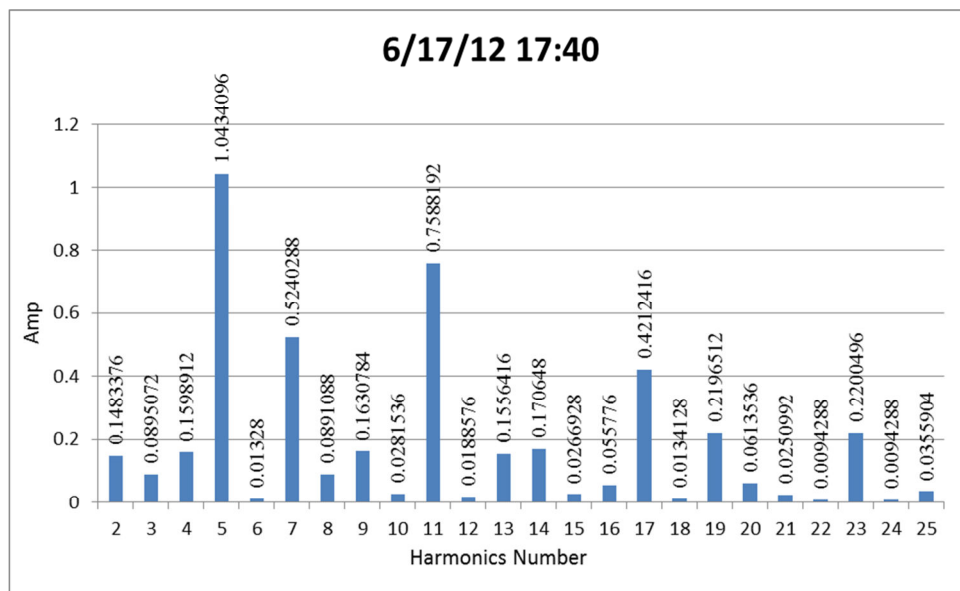


Figure 8.19 Harmonics Dataset during the Evening on a Cloudy Day

Table 8.10 Power, Voltage, Harmonics Distortion during the Evening on Cloudy Day

Quantities	St. Andrew SS	Sarnia Solar farm SS2	Sarnia Solar farm SS5
Power, P+jQ (MVA)	11.97+j6.582	0.6519-j0.05674	0.6519-j0.05681
Fundamental Phase Voltage, Vf (kV)	16.599	16.416	16.416
Fundamental Current, If (Amp)	272.777	13.28	13.28
Current TDD (%)	-	0.736	0.736
Voltage THD (%)	0.208	0.524	0.518
Voltage Harmonic Distortion (kV)	0.0346	0.086	0.085

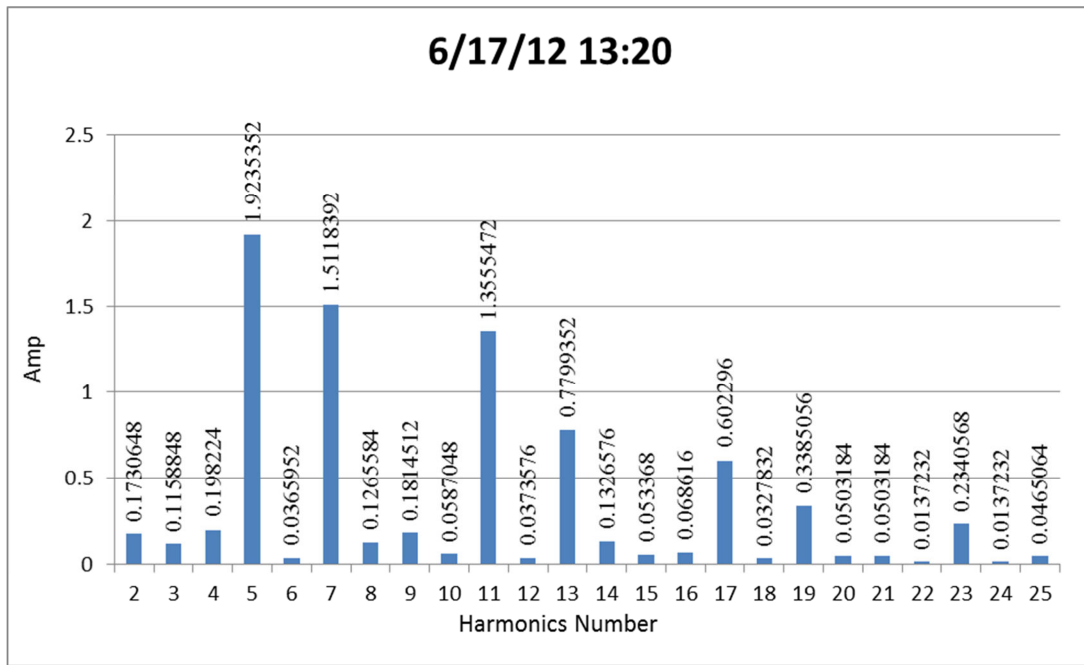


Figure 8.20 Harmonics Dataset around noon on a Cloudy Day

Table 8.11 Power, Voltage, and Harmonics Distortion at noon on a Cloudy Day

Quantities	St. Andrew SS	Sarnia Solar farm SS2	Sarnia Solar farm SS5
Power, P+jQ (MVA)	5.785+j6.751	3.739-j0.1689	3.738-j0.1699
Fundamental Phase Voltage, Vf (kV)	16.491	16.379	16.378
Fundamental Current, If (Amp)	178.31	76.24	76.24
Current TDD (%)	-	1.446	1.446
Voltage THD (%)	0.391	0.983	0.977
Voltage Harmonic Distortion (kV)	0.0646	0.161	0.16

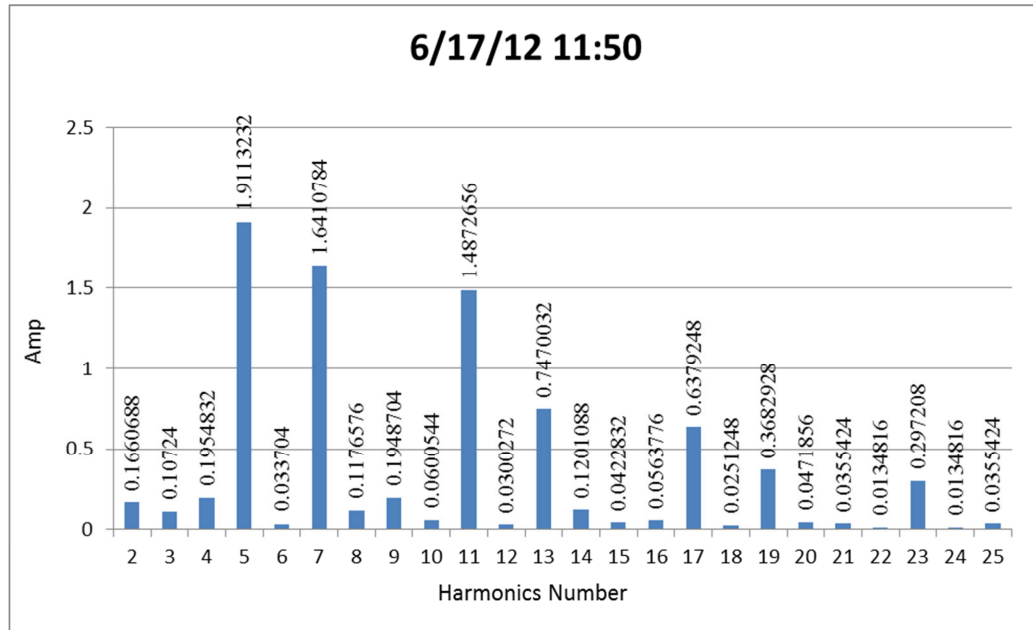


Figure 8.21 High Harmonics Dataset on a Cloudy Day

Table 8.12 Power, Voltage, and Harmonics Distortion for High Harmonics Current Injection on a Cloudy Day

Quantities	St. Andrew SS	Sarnia Solar farm SS2	Sarnia Solar farm SS5
Power, P+jQ (MVA)	7.175+j6.753	3.031-j0.18	3.031-j0.1807
Fundamental Phase Voltage, Vf (kV)	16.66	16.53	16.53
Fundamental Current, If (Amp)	195.8	61.28	61.28
Current TDD (%)	-	1.506	1.506
Voltage THD (%)	0.4063	1.028	1.022
Voltage Harmonic Distortion (kV)	0.0677	0.17	0.169

From Fig. 8.18, Fig. 8.19, Fig. 8.20 and Fig. 8.21 it is seen that the harmonics data pattern is similar at different times. However, similar to the sunny day case, the magnitude of harmonics varies with the power output level of the solar farm. Comparing Table 8.10, Table 8.11 and Table 8.12, it is seen that the voltage THD becomes higher for the case of high harmonic injection from the solar farm for the worst condition of network, as in Table 8.9.

However, on both the sunny and cloudy days, the above studies show that the maximum voltage harmonics distortion occurs for the case of maximum harmonic injection level from the solar farm on that particular day.

Fig. 8.22 presents the harmonics spectrum for highest harmonics injection by the solar farm over the period of one month. Table 8.13, Table 8.14, and Table 8.15 present the simulation results at 1SCL, 1/3rd SCL, and 4SCL of the source on the selected network condition of Fig 8.1, respectively. The voltage distortions along with the power and voltage quantities for this highest level of harmonics injection by the solar farm are compiled in these tables.

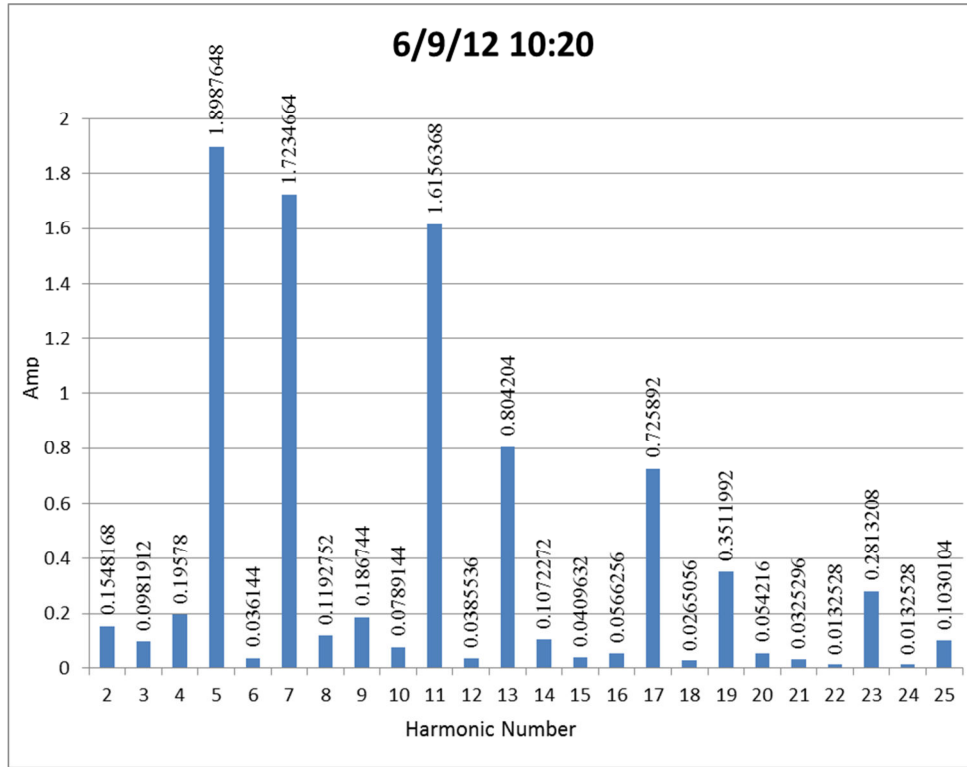


Figure 8.22 Harmonics Spectrum for Highest Harmonics Current Injection Over the Whole Period.

Table 8.13 Simulated Power, Voltage, and Harmonics Corresponds to Highest Harmonics Injection by the Solar Farm at 1SCL

Quantities	St. Andrew SS	Sarnia Solar farm SS2	Sarnia Solar farm SS5
Power, P+jQ (MVA)	7.305+j6.77	2.98-j0.1796	2.98-j0.1802
Fundamental Phase Voltage, Vf (kV)	16.657	16.5266	16.526
Fundamental Current, If (Amp)	197.824	60.24	60.24
Current TDD (%)	-	1.567	1.567
Voltage THD (%)	0.429	1.094	1.085
Voltage Harmonic Distortion (kV)	0.0715	0.18084	0.17936

Table 8.14 Simulated Power, Voltage, and Harmonics Corresponds to Highest Harmonics Injection by the Solar Farm at 1/3rd SCL

Quantities	St. Andrew SS	Sarnia Solar farm SS2	Sarnia Solar farm SS5
Power, P+jQ (MVA)	7.297+j6.572	2.981-j0.08409	2.981-j0.08469
Fundamental Phase Voltage, Vf (kV)	15.662	15.498	15.497
Fundamental Current, If (Amp)	222.693	60.24	60.24
Current TDD (%)	-	1.567	1.567
Voltage THD (%)	0.4867	1.129	1.119
Voltage Harmonic Distortion (kV)	0.076	0.175	0.173

Table 8.15 Simulated Power, Voltage, and Harmonics Corresponds to Highest Harmonics Injection by the Solar Farm at 4SCL

Quantities	St. Andrew SS	Sarnia Solar farm SS2	Sarnia Solar farm SS5
Power, P+jQ (MVA)	7.297+j6.572	2.981-j0.08409	2.981-j0.08469
Fundamental Phase Voltage, Vf (kV)	16.637	16.515	16.515
Fundamental Current, If (Amp)	195.45	60.24	60.24
Current TDD (%)	-	1.567	1.567
Voltage THD (%)	0.395	1.097	1.087
Voltage Harmonic Distortion (kV)	0.066	0.181	0.1796

By comparing Table 8.13, Table 8.14 and Table 8.15, it is demonstrated that the distortion in voltage increases with the decrease in short circuit level of the source on the selected worst network condition (with the frequency response presented in Fig. 8.1).

8.8 Conclusion

In this chapter, a detailed harmonics impact study is performed for a 20 MW solar farm on the distribution network of Bluewater Power. The network is modeled with actual network data. Load flow studies are conducted to validate the network model built in CYME and EMTDC/PSCAD with actual SCADA measurements with PV systems. Network resonance studies for different network conditions are performed for the feeder 18M14, which connects the large-scale solar farms by using EMTDC/PSCAD. The measured harmonic data obtained from the solar farm is analyzed and utilized to demonstrate the impact on the network harmonic distortion for different short circuit levels.

The following conclusions are made:

1. Network resonances are caused by capacitors on the feeder.

2. The large substation capacitor (20 MVAR or 40 MVAR) causes resonance around the 3rd harmonics.
3. The load capacitor 1.2 MVAR causes network resonance around the 25th harmonics.
4. Presence of load on the feeder reduces the magnitude of network resonant impedances.
5. The solar farm typically injects high 5th, 7th, 11th, and 13th harmonics.
6. A small number of ambient harmonics are observed in the network.
7. Network resonance at 3rd harmonics does not cause any substantial increase in voltage THD on the feeders.
8. The highest voltage distortion is observed for the case with no capacitor connected, and with high harmonics injection from the solar farm. Even in this case the voltage THD is seen to be 1.13%, which is much lower than the 5% level specified by the IEEE standard 519.
9. Thus, based on the studies conducted, it is inferred that the large solar farm of 20 MW may not cause any substantial voltage distortion on the feeder 18M14 during steady state operating conditions.

This study has been conducted with a huge set of data provided by Bluewater Power Corp., Hydro One Inc., and with the cooperation of Enbridge Inc. and First Solar, who are all sincerely acknowledged.

Chapter 9

9 Conclusion

9.1 Introduction

This thesis presents four novel applications of PV solar farms for providing various benefits to electric power systems in addition to generating real power from solar insolation. A conventional grid connected Photovoltaic (PV) solar farm utilizes an inverter for converting the DC power output from PV arrays into AC power to be supplied to the grid. During the night, the entire PV solar system remains completely idle and is also only partially utilized during the day, especially in the early morning and late evening hours. This thesis presents new technologies for a complete utilization of the inverter of a PV solar system, both during day and night time. These technologies transform the PV solar system inverter into a Static Synchronous Compensator (STATCOM) which is a major device in the family of Flexible AC Transmission Systems (FACTS). This novel technology is termed as PV-STATCOM.

A STATCOM is a dynamic reactive power compensator which provides very rapid voltage regulation and damping at the point of connection with the grid. It is known in power systems operation that a capacitor increases voltage and an inductor decreases voltage at the terminal when it is controlled. The STATCOM functions as a variable inductor (consuming reactive power) and as a variable capacitor (injecting reactive power), and thus, performs very rapid voltage control. In a similar manner, the PV system transformed into a PV-STATCOM performs voltage control or damping control by using the entire PV inverter capacity during the night, and the remaining capacity of the PV inverter after real power generation during the day.

In this thesis, novel control of PV-STATCOMs is proposed to perform loss reduction in a distribution network, to prevent the instability of a critical induction motor load, and to increase the power transfer limit of a long transmission line. These new applications of PV solar farms can help to improve the performance of power systems significantly. They can also potentially bring new sources of revenue for PV solar farms by providing

these benefits, in addition to those earned from the sale of real power. Moreover, a new technique for short circuit current management is presented for conventional PV solar farms that will potentially solve the problem which has caused several solar farms to be denied connectivity in Ontario. This thesis also presents a generalized PV solar system model in the EMTDC/PSCAD software environment. Another major study performed in this thesis is the harmonics impact of the largest PV solar farm in Canada, in the distribution utility network of Bluewater Power (BWP), located in Sarnia, Ontario.

9.2 Modeling of a Conventional PV Solar Farm

A detailed modeling of the complete grid connected PV solar system requires the electrical rating of PV solar panels, which is mainly dependent on the manufacturing materials and their physical properties. Many times, manufacturers do not disclose detailed physical properties of the PV module, except for some electrical quantities such as open circuit voltage (V_{oc}), Short Circuit Current (I_{sc}), Maximum Power Point voltage (V_{mpp}) Maximum Power Point Current (I_{mpp}), and maximum Power (P_{mpp}). However, to model the PV system comprehensively, it is required to determine other physical parameters, such as series resistance of PV cell (R_s), shunt resistance of PV cell (R_{sh}), and diode ideality factor (n) from generalized data. The use of a DC-DC converter based Maximum Power Point Tracking (MPPT) system at the output of a PV module causes additional losses and hence, reduces the overall efficiency. On the other hand, the converter-less MPPT system is much more efficient. However, modeling of a converter-less MPPT system with the help of an iteration technique increases the complexity of the model and potentially increases the simulation time.

Therefore in Chapter 2, a complete generalized model of a grid connected PV solar system in EMTDC/PSCAD is presented with the necessary mathematical relationships. A 100 kW PV module is modeled by using only the quantities provided in manufacturer's datasheet. The proposed technique determines all of the PV module parameters without any explicit repetitive iteration. This model also includes a converter-less MPPT controller to generate the maximum power output at any level of solar irradiation and temperature, thus reducing overall losses. The simulation results for the PV modules are validated for two levels of solar insolation and temperature for a commercial PV system,

with respect to the manufacturer's datasheet values of voltage, current, and power. Simulation studies are performed using commercial grade electromagnetic transient simulation software EMTDC/PSCAD.

The study demonstrates that this model: (i) maintains unity power factor at any level of power, (ii) ensures maximum power point tracking at any level of solar insolation and temperature and, (iii) maintains acceptable ranges of harmonics. This generalized EMTDC/PSCAD model can be adapted for any other PV module and system operating conditions.

9.3 New Fault Detection and Management Technique for PV Solar System

Several PV solar systems have been denied connections in Ontario due to their potential short circuit current contributions. Inverter based Distributed Generators (DGs) like PV solar systems typically contribute 1.2 pu to 1.8 pu fault current, which is not acceptable to utility companies due to the need for very expensive protective breaker upgrades. Therefore, to alleviate the short circuit current contribution, it is necessary to limit the current before it exceeds its rated peak values.

In Chapter 3, a new fast fault detection technique is proposed for PV inverter based DGs. The proposed controller is based on the detection of a rate of rise, or slope (d/dt), of the PV inverter output current and the peak magnitude of current. In this new controller, the slope (d/dt) detection technique is used as the primary detection strategy, whereas, the magnitude detection technique is used as a secondary detection strategy. As soon as the proposed fault detector detects the fault, it (a) disables firing pulses to the inverter, (b) disconnects the PV solar modules from the inverter and, (c) isolates the filter from the PCC. A typical network of Ontario, Canada, obtained from Natural Resource Canada (NRCan) is used as the study system, which is comprised of 25km radial feeder with approximately a 103 MW load. A 7.5 MW PV system which incorporates the proposed fault detector is connected at the end of the feeder. To demonstrate the effectiveness of the proposed fault detector, both symmetrical (3-phase to ground) and asymmetrical (single line to ground) fault studies are conducted for 9 cycles. The faults are initiated

both at the point of common coupling of the PV system, and at the beginning of the feeder. Simulation results are also presented for peak and non-peak fault instances of instantaneous output current of the PV system inverter. EMTDC/PSCAD software simulations are used to demonstrate the performance.

The simulation study shows that the new proposed fault current controller responds and disconnects the PV solar farm within one millisecond, regardless of the type of fault or the location of the fault on the distribution system. The controller can also effectively distinguish between large load switching and fault current.

A patent has been filed on this short circuit current management system [P.1].

9.4 Novel Control of PV Solar Farm as PV-STATCOM

Chapter 4 presents the concepts of a novel use of a PV solar farm inverter as a PV-STATCOM, which can potentially lead to complete utilization of the PV solar farm inverter asset during both night and day. Two sets of novel PV-STATCOM technologies are presented: one based on the “unused” capacity of the solar inverter, and the other based on “used” capacity of the solar inverter. The entire solar farm inverter capacity during the night, S MVA, and the remainder inverter capacity $\sqrt{(S^2 - P^2)}$ after real power ‘ P ’ MW generation during the day, remain unused in conventional solar farm operation. These are referred to as the “unused” capacity of the inverter. In the proposed new control, during an emergency need in the daytime, the real power generation of a PV solar farm is curtailed to create new capacity for reactive power support by the PV-STATCOM. This additional new capacity created through real power curtailment is referred as the “used” capacity of the solar inverter.

9.4.1 Utilization of Unused Capacity of a PV Inverter

In this strategy, two applications of PV-STATCOM are demonstrated by utilizing the “unused” capacity of the inverter.

9.4.1.1 Reduction in Line Losses

In power systems, power is supplied to the loads over a network by both conventional generators and DGs. The flow of current ' I ', in the lines causes ' I^2R ' heating losses due to line resistance ' R '. These losses are a function of bus voltages and also increase as the square of the current. Injection of real power from a DG or PV solar farm into the network typically increases bus voltage and can indirectly reduce the system losses to some extent.

However, Chapter 5 presents a new control of a PV system as a PV-STATCOM, to reduce the line losses even further through coordinated voltage control. In the proposed control, the optimal voltage set point may be provided to all participating solar farms by the network operator running a central Optimal Power Flow (OPF) for the entire system, or by the individual owner of the participating DGs. In this study, a radial feeder having an aggregated load of 4 MW, 2MVAr connected at the end of the feeder is used. By using a 12 MVA PV solar system as a PV-STATCOM connected either at a single bus or at two distributed buses on the feeder, four different scenarios are studied. The best voltage set points are determined by a set of systematically conducted load flow studies in PowerWorld Simulator.

It is demonstrated that with the above voltage regulation by a PV-STATCOM, a substantial net loss reduction is achieved even after accounting for the operational losses of the PV-STATCOM. From the comparison of all four scenarios, it is observed that the PV-STATCOM control is more effective in reducing line losses when connected close to the load. Further, a distributed voltage control as compared to a centralized mid-point voltage control by PV-STATCOM results in higher loss reduction. Overall, the annual cost of energy savings by such a novel PV-STATCOM control is substantial. For the 12MW PV solar farm based study system the energy saving is sufficient enough to power 30 homes annually.

This study is one of the first applications of the filed patent [PR.1].

9.4.1.2 Power Transfer Limit Improvement of a Long Transmission Line

Transmission grids worldwide are presently facing a major challenge in integrating large-scale renewable systems (wind farms and solar farms) due to their limited power transmission capacity. The power transfer over a transmission line is constrained by several limits such as: thermal limit, steady state stability limit, transient stability limit, and damping limit. To increase the transmission capacity of existing lines, series compensation and various Flexible AC Transmission System (FACTS) devices are utilized. In an extreme situation, new lines may need to be constructed at a very high expense.

Chapter 7 presents three different types of PV-STATCOM controls. These are (i) pure voltage control, (ii) pure damping control, and (iii) a combination of voltage control and damping control. Studies are performed for two variants of a Single Machine Infinite Bus (SMIB) system. One SMIB system uses only a single PV solar farm of 100MW as a PV-STATCOM, connected at the midpoint, whereas the other system uses a combination of a PV-STATCOM and another PV-STATCOM, or an inverter based wind Distributed Generator (DG) with similar STATCOM functionality, of 100 MW each. Three-phase fault studies are conducted and the improvement in stable power transmission limit is investigated using the electromagnetic transient software EMTDC/PSCAD both during night and day.

It is demonstrated that for the study system with a single 100 MW PV solar farm, the PV-STATCOM can increase the power transfer capacity by 168 MW during the night with the use of voltage control, along with the damping control technique. This control further increases the power transfer by 142 MW during the day with the use of damping control, even at a high PV power generation of 91MW (91%). During the day, damping control is seen to be more effective than a combination of voltage control and damping control.

In another case study with multiple DGs acting as PV-STATCOMs, the power transfer limits is increased up to 229 MW during the night through damping control, when none of the DGs generate any real power. During the day, the maximum limit of power

transfer achieved with the PV-STATCOM is 230 MW when both the DGs are generating a high amount of real power, typically around 95 MW each. Thus, with the proposed novel control of a PV-STATCOM, a substantial amount of power transfer improvement is achieved.

A PCT patent application has been filed on this work and corresponding full patents are filed in five different countries USA, Canada, Europe, China and India [P.2], [P.3].

9.4.2 Utilization of Used Capacity of a PV Inverter for Prevention of Induction Motor Instability

Power systems are commonly faced with disturbances, such as, faults and outages of equipment (transformers, lines, generators, etc.). These disturbances cause voltage fluctuations which can be severe if the power system is weak. Faults in such weak networks can potentially result in the shut down of Induction Motor (IM) loads due to voltage instability. In some cases, IM loads are very critical, such as those used in process control, rolling mills, etc. Shutdown of these critical IM loads even for a very short time can result in huge losses (in the order of million dollars) to the industrial facility using these IMs.

Chapter 6 presents another new application of a PV-STATCOM to provide voltage support to a critical voltage sensitive IM load connected in the vicinity of a solar farm. In this strategy, the solar farm is controlled to temporarily stop its normal operation of power generation and instead to operate as a PV-STATCOM utilizing the whole or partial inverter capacity to support the grid for a very short amount of time. The novel fast fault detection technique proposed earlier in Section 9.3, is integrated with the PV system to sense any fault on the grid. Upon detection of a fault, the PV solar farm inverter transforms into a PV-STATCOM and provides the required voltage support. A set of PV solar panels are temporarily disconnected from the DC side of the inverter while the inverter remains connected with the AC grid. As a result, during the day, the real power generation is partially or fully curtailed, as needed. The inverter capacity is thus freed up to provide the needed amount of reactive power support to the grid for a short duration of time during fault and post fault period. A real NRCan network is

adopted for this study. One of the static loads is replaced with an industrial IM load at the end of the feeder. The performance of the PV-STATCOM operation is compared for (i) conventional PV operation and (ii) PV-STATCOM operation. The PV solar farm is transformed into a PV-STATCOM only when there is a need or prior agreement to provide dynamic voltage support to stabilize a critical induction motor load. Therefore, once the motor is stabilized, the PV-STATCOM transforms into a conventional PV solar farm and begins generating real power as usual. These simulation studies are conducted using EMTDC/PSCAD software.

It is demonstrated that the induction motor (IM) becomes destabilized due to a three-phase fault and the conventional operation of the PV solar farm does not alleviate the situation. For the study system it is shown that a 7.5 MW solar farm acting as a PV-STATCOM can stabilize (i) an induction motor (IM) load of 2.7 MW, if connected at motor terminals, and (ii) an induction motor (IM) load of 0.9 MW, even if it is connected 19 km away from the motor terminals. However, the effectiveness of the proposed PV-STATCOM operation is dependent on the size and location of the PV solar farm and the system strength.

This is the first study conducted for the filed patent [PR.2].

9.5 Harmonic Impact Study of a Large Scale PV Solar Farm in a Distribution Network

IEEE 519 Standard recommends that a utility should perform a harmonic analysis whenever significant number or certain sizes of DGs (that produce harmonics) are connected in their network.

In Chapter 8, a harmonics impact study is presented for the distribution network of Bluewater Power (BWP), Sarnia which connects the largest solar farm in Canada, of 80 MW. This study is performed utilizing detailed network data, central Geographic Information System (GIS) database, and Supervisory Control And Data Acquisition (SCADA) infrastructure, made available by BWP. The network is modeled in detail by using EMTDC/PSCAD software. The network model is validated through CYME

software based load flow studies and SCADA measurements. The validated model for the feeder 18M14 is used for performing a network resonance study by EMTDC/PSCAD for different network conditions. This feeder connects 20 MW solar farms. Hydro One (HONI) contributed to this study by installing meters to measure the harmonics injection by the 20 MW solar farms. From the analysis of solar farm data provided by HONI, (which is confidential) it is observed that the solar farm typically injects high 5th, 7th, 11th, and 13th harmonics. A small amount of ambient harmonics is also observed in the network. The impact of these harmonics on the Bluewater Power distribution network is investigated for different Short Circuit Levels (SCL).

It is concluded that network resonances (resulting in high network impedance) are caused by capacitors on the feeder. However, the magnitude of the resonance peak is not substantial. The large substation capacitors of 20 MVAR or 40 MVAR cause resonance around the 3rd harmonic, whereas, the load capacitor of 1.2 MVAR causes network resonance around the 25th harmonic. The network resonance at the 3rd harmonic does not cause any substantial increase in voltage THD on the feeders. The highest voltage distortion is observed for the case with no capacitor connected and with high harmonic injections from the solar farm. Even in this case the voltage THD is seen to be 1.13%, which is much lower than the 5% level specified by the IEEE standard 519. Thus, based on the studies conducted, it is inferred that the large solar farm may not cause any substantial voltage distortion on the feeder 18M14 during steady state operating conditions.

This study has been conducted with a large set of data provided by Bluewater Power Corp. and Hydro One Inc. This study was also made possible by the cooperation of Enbridge Inc. and First Solar who are all sincerely acknowledged.

It is noted that the PV system model used in Chapter 2 to Chapter 7 does not provide any representation of harmonics. Therefore, with the determination of harmonic injections for a real solar farm as demonstrated in Chapter 8, the model of the PV solar farm utilized in Chapter 2 to Chapter 7 can be updated to include harmonic current sources to make the PV system model more comprehensive and realistic for future studies.

9.6 Contribution and Significance of this Thesis

This thesis presents several novel patent pending controls of PV solar farms which can bring significant benefits to power systems. Following are the main contributions of this thesis:

1. A generalized electromagnetic transient model for a grid connected PV solar farm is developed, and which can generate all required parameters by using the standard datasheets of any PV module. This model is validated for different temperatures and solar insolation. A converter-less MPPT technique is also implemented, which can track maximum power effectively at any level of solar radiation and temperature.
2. A new short circuit current management technique is developed for inverter based DGs for the first time which can sense the network fault and isolate the inverter within one millisecond. The technique thus enables the inverter based DGs to trip before the instantaneous output current reaches its rated peak. This technique will help to integrate more inverter based DGs to the network. *A patent is filed on this work [P.1].*
3. A novel control of a PV solar farm as a PV-STATCOM utilizing the ‘used’ capacity to prevent critical Induction Motor (IM) load instability is demonstrated for the first time. This controller uses the above fast fault detection technique to transform the PV system into a PV-STATCOM upon sensing any fault by disconnecting the PV module for a short period of time. The controller subsequently reverts the PV-STATCOM into a conventional PV solar farm after successful recovery of the IM load. Although generation is curtailed for a short period of time, a significant gain is achieved in the form of avoidance of instability of critical IM. *This is the first study conducted for the filed patent [PR.2].*
4. A new coordinated control strategy for a PV solar farm as a PV-STATCOM is proposed to reduce the network I^2R heating losses through the use of the PV inverter’s remnant capacity at any level of PV power generation. The saved energy is

- significant and can power several homes annually. ***This work is the first time application of a filed patent [PR.1].***
5. A novel control of a PV solar farm as a PV-STATCOM to enhance the transient stability and thereby the power transfer limit of a long transmission line is proposed. A significant improvement in power transfer limit is achieved both during the night and day with the use of proposed voltage control and damping control technique. This benefit is accomplished by utilizing the PV inverter remnant capacity after real power generation. ***Two patents are filed on this work [P.2], [P.3].***
 6. The impact of harmonics due to the largest solar farm in Canada, on a real distribution network is studied. Such a study has now been conducted for the first time in literature.

In conclusion, this thesis makes a strong case for relaxing the present grid codes to allow selected inverter based renewable generators (solar and wind) to exercise these novel controls, thereby increasing much needed power transmission capability, reducing distribution losses, preventing instability of critical IMs, etc. Such novel controls on PV solar Distributed Generator (DGs) (and inverter based wind DGs) will potentially reduce the need for investments in additional expensive devices such as series/shunt capacitors and FACTS devices. The PV-STATCOM operation also creates a new opportunity for PV solar DGs to earn revenues during the night, and also during the day, in addition to the revenue from the sale of real power. This will of course require appropriate agreements between the regulators, network utilities, solar farm developers, and inverter manufacturers.

9.7 Future Work

The following tasks are proposed as future work emanating from this thesis:

1. The developed electromagnetic transients model of a PV solar farm needs to be validated with respect to small scale PV systems (<10kW) and as well as the large scale PV systems (>10MW).

2. Detailed EMTDC/PSCAD studies need to be conducted on actual power systems in Ontario for demonstrating the benefit of the proposed novel PV-STATCOM control technologies.
3. Real Time Digital Simulation (RTDS) studies need to be performed for development of a PV-STATCOM for
 - (a) Fault detection and short circuit current management
 - (b) Line loss reduction
 - (c) Prevention of induction motor load instability
 - (d) Improvement of transmission capacity
4. Harmonics studies need to be conducted, including ambient harmonics, for both steady state and transient scenarios.

Patents and Publications from this Thesis:

A. Patents:

[P.1] Rajiv Varma and **Shah Arifur Rahman**, “Fault Detection and Short Circuit Current Management Technique for Inverter Based Distributed Generators (DG)”, US Provisional Patent Application No. 61/706,387 Filed on September 27, 2012.

[P.2] Rajiv K. Varma and **Shah Arifur Rahman**, “Novel Control of Inverter based DGs as FACTS (DGFACTS) for Enhancing Grid Power Transmission Limits, US Provisional Patent application No. 61/309,612 filed 2nd March 2010.

[P.3] Rajiv K. Varma, Vinod Khadkikar and **Shah Arifur Rahman**, "Utilization of Distributed Generator Inverters as STATCOM" PCT Patent application PCT/CA2010/001419 (for worldwide coverage) filed on 15 September, 2010

- a. Chinese National Phase Entry Application: 201080038759.9
- b. US National Phase Entry Application: 13/391,699
- c. India National Phase Entry Application: 1641/DELNP/2012
- d. Europe Regional Phase Entry Application: 10816511.9
- e. Canada National Phase Entry Application: 2,768,101

B. Patents Referred:

[PR.1] Rajiv K. Varma, “Use of Distributed Generator (DG) Inverters as STATCOMS for Decreasing Line Losses”, US Provisional Patent Application No. 61/681,335, Filed August 9, 2012.

[PR.2] Rajiv Varma and Vinay Sharma, “Enhanced Utilization Of Real Power Generating Capacity Of Distributed Generator (DG) Inverters as STATCOM – (DG-STATCOM)”, US Provisional Patent Application No. 61/641,245, Filed May 1, 2012.

C. Journals:

[J.1] Rajiv K. Varma, **Shah Arifur Rahman** and Tim Vanderheide, “New Control of PV Solar Farm as STATCOM (PV-STATCOM) for Increasing Grid Power Transmission Limits During Night and Day,” Submitted to IEEE Transaction on Power Delivery, Manuscript ID: TPWRD-01030-2011.R2. (2nd revision submitted).

D. Conferences:

[C.1] Rajiv K. Varma, **Shah Arifur Rahman** and Ravi Seethapathy, “Novel Control of Grid Connected Photovoltaic (PV) Solar Farm for Improving Transient Stability and Transmission Limits Both During Night and Day,” in *Proc. 21st World Energy Congress*, Montreal, September, 2010.

[C.2] **Shah A. Rahman**, and R.K. Varma, “PSCAD/EMTDC Model of a 3-Phase Grid Connected Photovoltaic Solar System,” in *Proc. 2011 43rd North American Power Symposium, Boston, U.S.A.*, pp. 1-5.

[C.3] Rajiv K. Varma, **Shah Arifur Rahman**, Vinay Sharma, Tim Vanderheide, “Novel Control of a PV Solar System as STATCOM (PV-STATCOM) for Preventing Instability of Induction Motor Load,” in *Proc. IEEE CCECE 2012 conference*, April 30-May 2, 2012, Montreal, Quebec.

[C.4] Rajiv K. Varma, **Shah Arifur Rahman** and A.C. Mahendra, “Novel Nighttime Application of PV Solar Farms as STATCOM (PV-STATCOM),” in *Proc. 2012 IEEE PES GM 2012*, San Diego, CA, U.S.A. pp. 1-8.

[C.5] Rajiv. K. Varma, **Shah Arifur Rahman** and Wayne H. Litzemberger, “Bibliography of FACTS: 2008 Part I IEEE Working Group Report,” in *Proc. IEEE 2010, Power and Energy Society General Meeting*, Minneapolis, MN, U.S.A. pp. 1-7.

[C.6] **Shah Arifur Rahman**, Rajiv. K. Varma and Wayne H. Litzemberger, “Bibliography of FACTS: 2008 Part II IEEE Working Group Report,” in *Proc. IEEE 2010, Power and Energy Society General Meeting*, Minneapolis, MN, U.S.A. pp. 1-8.

[C.7] Rajiv. K. Varma, **Shah Arifur Rahman** and Wayne H. Litzemberger, “Bibliography of FACTS: 2008 Part III IEEE Working Group Report,” in *Proc. IEEE 2010, Power and Energy Society General Meeting*, Minneapolis, MN, U.S.A. pp. 1-7.

[C.8] **Shah Arifur Rahman**, Rajiv. K. Varma, and Wayne H. Litzemberger, “Bibliography of FACTS Applications for Grid Integration of Wind and PV Solar

Power Systems: 1995-2010, IEEE Working Group Report", in *Proc. of IEEE PES General Meeting*, Detroit, MI, U.S.A. 2011.

[C.9] Shah Arifur Rahman, Rajiv. K. Varma, Wayne H. Litzenberger and Jon Berge "Bibliography of FACTS 2011: Part I; IEEE Working Group Report," in *Proc. 2012 IEEE PES GM 2012*, San Diego, CA, U.S.A. pp. 1-6.

References or Bibliography

- [1] Invest in Canada, "Solar Energy," [Online]: <http://investincanada.gc.ca/eng/industry-sectors/renewableenergy/solar-energy.aspx>, Date: 13.06.2012.
- [2] Rajiv K. Varma, Graham Sanderson and Ken Walsh, "Global PV Incentive Policies and Recommendations for Utilities", in *Proc. 2011 IEEE Canadian Conference on Electrical and Computer Engineering*, Niagara Falls, Canada, May 2011.
- [3] Photovoltaic Incentive Programs & Country Profiles from Yole Development. [Online]. Available: http://globalsolartechnology.com/index.php?option=com_content&task=view&id=3519&Itemid=9.
- [4] FIT and microFIT program, Ontario Power Authority, [Online]: <http://fit.powerauthority.on.ca/>, Date: 13.06.2012.
- [5] Incentives/Policies for Renewables & Efficiency, US Department of Energy, [Online]: http://www.dsireusa.org/incentives/incentive.cfm?Incentive_Code=NY10F, Date: 13.06.2012.
- [6] "Europe Solar PV Markets and Strategies: 2011-2025," IHS Emerging energy research, [Online]: <http://www.emerging-energy.com/uploadDocs/EuropeSolarPVMarketsandStrategies2011.pdf>, Sep. 2011.
- [7] S. Liu and R. A. Dougal, "Dynamic multiphysics model for solar array", *IEEE Trans. on Energy Conversion*, vol.17, no.2, pp.285-294, 2002.
- [8] J. A. Gow, C. D. Manning "Development of a photovoltaic array model for use in power electronics simulation studies," *IET Proceedings on Electric Power Applications*, vol. 146, no. 2, pp. 193-200, March 1999.
- [9] Weidong Xiao, William G. Dunford and Antoine Capel,"A Novel Modeling Method for Photovoltaic Cells", in *Proc. 2004 35th IEEE Power Electronics Specialist Conf.*, pp. 1950-1956.
- [10] Michael Jensen, Russell Louie, Mehdi Etezadi-Amoli and M. Sami Fadali, "Model and Simulation of a 75kW PV Solar Array," *Presented at Transmission and distribution conference and exposition, New Orleans, Louisiana, U.S.A.* 2010.
- [11] Mateus F. Schonardie and Denizar C. Martins,"Three-Phase Grid-Connected Photovoltaic System With Active And Reactive Power Control Using $dq0$ Transformation," in *Proc. 2008 Power Electronics Specialists Conf.*, pp. 1202-1207.
- [12] Walker, G. R. "Evaluating MPPT Converter Topologies Using a MATLAB PV Model", *Journal of Electrical & Electronics Engineering, Australia*, 2001, vol. 21, issue. 1, pp. 49-55.
- [13] F.M. Gonzalez-Longatt, "Model of Photovoltaic Module in Matlab™," *II CIBELEC*, Puerto La Cruz, Venezuela, Dec. 2005.
- [14] M.G. Villalva, J.R. Gazoli and E.R. Filho,"Comprehensive Approach to Modeling and Simulation of Photovoltaic Arrays," *IEEE Trans. On Power Electronics*, vol. 24, no. 5, pp. 1198-1208, 2009.
- [15] D. Sera, R. Teodorescu and P. Rodriguez,"PV panel model based on datasheet values," in *Proc. 2007 IEEE International Symposium on Industrial Electronics*, pp. 2392-2396.
- [16] M.G. Villalva, J.R. Gazoli and E.R. Filho, "Modeling and Circuit-Based Simulation of Photovoltaic Arrays," in *Proc. 2009 IEEE Brazilian Power Electronics Conference*, pp. 1244-1254.
- [17] C. Chang, J. Zhu and H. Tsai, "Model-Based Performance Diagnosis for PV Systems," in *Proc. 2010 SICE Annual Conference*, pp. 2139-2145.
- [18] National Instruments Tutorial, "Photovoltaic Cell I-V Characterization Theory and LabVIEW Analysis Code-Part II," Available [Online]: <http://www.ni.com/white-paper/7230/en>, Date: 09.07.2012.
- [19] B. Wang, T. Huang, B. Jiang, X. Dong and Z. Bo, "Dynamic modeling and transient fault analysis of feeder in distribution system with MW PV substation," in *Proc. 2010 45th International Universities Power Engineering Conference*, pp. 1-5
- [20] R. Gupta, G. Gupta, D. Kastwar, A. Hussain and H. Ranjan, "Modeling and Design of MPPT Controller for a PV Module using PSCAD/EMTDC," in *Proc. IEEE PES 2010 Innovative Smart Grid Technologies Conference Europe*, pp. 1-6.
- [21] J. Xue, Z. Yin, B. Wu and J. Peng, "Design of PV Array Model Based On EMTDC/PSCAD," in *Proc. IEEE 2009 Asia-Pacific Power and Energy Engineering Conference*, pp. 1-5.
- [22] Ryan C. Campbell, "A Circuit-based Photovoltaic Array Model for Power System Studies", [Online]. [Online]:

- http://www.ee.washington.edu/research/sesame/publication/Conference/2007/Campbell_PWL_PV_Model_NAPS2007.pdf, date: 17.07.2010.
- [23] Natthaphob Nimpitiwan, "Inverter-Based Photovoltaic distributed Generations: Modeling and Dynamic Simulations," in *Proc. 2010 IEEE Region 10 Conference*, pp. 7-12.
- [24] Seul-Ki Kim, Jin-Hong Jeon, Chang-Hee Cho, Eung-Sang Kim and Jong-Bo Ahn "Modeling and simulation of a grid-connected PV generation system for electromagnetic transient analysis," *Solar Energy*, vol. 83, pp. 664–678, 2009.
- [25] Hongbin Wu and Xiaofeng Tao, "Three Phase Photovoltaic Grid-connected Generation Technology with MPPT Function and Voltage Control," in *Proc. 2009 International Conference on Power Electronics and Drive Systems*, pp. 1295-1300.
- [26] Thanh Phu Nguyen "Solar Panel Maximum Power Point Tracker," [Thesis] The University of Queensland, 2001.
- [27] G. M. S. Azevedo, M. C. Cavalcanti, K. C. Oliveira, F. A. S. Neves and Z. D. Lins "Evaluation of Maximum Power Point Tracking Methods for Grid Connected Photovoltaic Systems," in *Proc. IEEE 2008 Power Electronics Specialist Conference*, pp. 1456-1462.
- [28] Bangyin Liu, Shanxu Duan, Fei Liu, and Pengwei Xu "Analysis and Improvement of Maximum Power Point Tracking Algorithm Based on Incremental Conductance Method for Photovoltaic Array," in *Proc. 2007 Power Electronics and Drive Systems*, pp. 637-641.
- [29] Chihchiang Hua and Chihming Shen, "Study of Maximum Power Tracking Techniques and Control of DC/DC Converters for Photovoltaic Power System," in *Proc. 1998 29th Annual IEEE Power Electronics Specialists Conference*, vol. 1, pp. 86-93.
- [30] D. P. Hohm and M. E. Ropp "Comparative Study of Maximum Power Point Tracking Algorithms," *Prog. Photovolt: Res. Appl.* 2003; 11:47–62 (DOI: 10.1002/pip.459).
- [31] Ioulia T. Papaioannou, Minas C. Alexiadis, Charis S. Demoulias, Dimitris P. Labridis, and Petros S. Dokopoulos "Modeling and Field Measurements of Photovoltaic Units Connected to LV Grid. Study of Penetration Scenarios," *IEEE Trans. On Power Delivery*, vol. 26, no. 2, pp. 979-987, April 2011.
- [32] H. Oldenkamp, I. J. de Jong, "AC modules: past, present and future", in *Proc. of workshop installing the solar solution*, January 1998, UK.
- [33] M. Meinhardt, G. Cramer, "Past, present and future of grid connected photovoltaic- and hybrid-power-systems," in *Proc. IEEE power engineering society summer meeting*, vol. 2, pp. 1283-1288, 2000.
- [34] M. Meinhardt, D. Wimmer, "Multi-string-converter. The next step in evolution of string-converter technology," *EPE proc. of the 9th European power electronics and applications conference (EPE'01)*, CDROM, 2001.
- [35] Søren Bækthøj Kjær "Design and Control of an Inverter for Photovoltaic Applications," Ph.D. Thesis, Aalborg University, DENMARK, 2005.
- [36] B. Lindgren, "Topology for decentralised solar energy inverters with a low voltage ac-bus," in *Proc. EPE'99 Conf.*, 1999.
- [37] S. B. Kjaer and F. Blaabjerg, "A novel single-stage inverter for the AC-module with reduced low-frequency ripple penetration," in *Proc. EPE'03 Conf.*, 2003.
- [38] T. Shimizu, O. Hashimoto, and G. Kimura, "A novel high-performance utility-interactive photovoltaic inverter system," *IEEE Trans. Power Electron.*, vol. 18, pp. 704–711, Mar. 2003.
- [39] T. Shimizu, M. Hiraata, T. Kamezawa, and H. Watanabe, "Generation control circuit for photovoltaic modules," *IEEE Trans. Power Electron.*, vol. 16, pp. 293–300, May 2001.
- [40] M. Calais, V. G. Agelidis, L. J. Borle, and M. S. Dymond, "A transformerless five level cascaded inverter based single-phase photovoltaic system," in *Proc. PESC'00 Conf.*, vol. 1, 2000, pp. 224–229.
- [41] M. Calais and V. G. Agelidis, "Multilevel converters for single-phase grid connected photovoltaic systems—aAn overview," in *Proc. ISIE'98Conf.*, vol. 1, 1998, pp. 224–229.
- [42] T. Shimizu, K. Wada, and N. Nakamura, "A flyback-type single-phase utility interactive inverter with low-frequency ripple current reduction on the dc input for an ac photovoltaic module system," in *Proc. PESC'02Conf.*, vol. 3, 2002, pp. 1483–1488.
- [43] S. B. Kjaer and F. Blaabjerg, "Design optimization of a single-phase inverter for photovoltaic applications," in *Proc. PESC'03 Conf.*, vol. 3, 2003, pp. 1183–1190.
- [44] S. Saha and V. P. Sundarsingh, "Novel grid-connected photovoltaic inverter," *Proc. Inst. Elect. Eng.*, vol. 143, no. 2, pp. 219–224, Mar. 1996.

- [45] F. Blaabjerg, Z. Chen, S. B. Kjær, *Power electronics as efficient interface indispersed power generation systems*, IEEE trans. on power electronics, vol. 19, no. 5, pp. 1184-1194, September 2004.
- [46] NKF electronics, The Netherlands, www.nkf.nl
- [47] A. Lohner, T. Meyer, A. Nagel, "A new panel-integratable inverter concept for grid-connected photovoltaic systems", in *proc. IEEE ISIE '96*, vol. 2, pp. 827-831, June 1996, Poland.
- [48] G. Kern, *SunSineTM 300: Manufacture of an AC photovoltaic module*, Ascension Technology, Inc., 1998.
- [49] S.B. Kjær, J.K. Pedersen, F. Blaabjerg, *Power inverter topologies for photovoltaic modules – a review*, IEEE proc. of the 37th annual industry application conference (IAS'02), vol. 2, pp. 782-788, 2002.
- [50] H. Haeberlin, "Evolution of inverters for grid connected PV-systems from 1989 to2000," in *proc. of the 17th European photovoltaic solar energy conference*, 2001.
- [51] S.W.H. de Haan, H. Oldenkamp, C.F.A Frumau, W. Bonin, "Development of a 100W resonant inverter for ac-modules," in *Proc. of the 12th European photovoltaic solarenergy conference*, 1994.
- [52] AN 3095 Application note, "grid-connected PV system, based on the STM32x," [Online]: http://www.st.com/internet/com/TECHNICAL_RESOURCES/TECHNICAL_LITERATURE/APPLICATION_NOTE/CD00253868.pdf, date: 13.06.2012.
- [53] Xantrex GT 500E Operation Manual, [Online] Available : [http://www.global-download.schneider-electric.com/85257689000007EE/all/CEF7144F2C909C7A8525775C0051365C/\\$File/gt500e-630e-operation_manual.pdf](http://www.global-download.schneider-electric.com/85257689000007EE/all/CEF7144F2C909C7A8525775C0051365C/$File/gt500e-630e-operation_manual.pdf), Date : 12/12/2011.
- [54] R. West, "Advanced, High-Reliability, System-Integrated 500-kW PV Inverter Development," Final Subcontract Report, NREL/SR-520-43839, Xantrex Technology Inc. California.
- [55] J. Keller and B. Kroposki, "Understanding Fault Characteristics of Inverter-Based Distributed Energy Resources," *Technical Report, NREL/TP-550-46698*, Jan'2009.
- [56] N. Mohan, W. P. Robbin, and T. Undeland, *Power Electronics: Converters, Applications, and Design*, 2nd ed. New York: Wiley, 1995.
- [57] Rajiv K. Varma, Vinod Khadkikar, and Ravi Seethapathy, "Nighttime application of PV solar farm as STATCOM to regulate grid voltage," *IEEE Trans. on Energy Conversion (Letters)*, vol. 24, no. 4. Dec. 2009.
- [58] Sunny Boy 6000u flyer, available [online]: http://www.sunwize.com/documents/sma_6000.pdf, date: July 11, 2012.
- [59] IEEE Standard for Interconnecting Distributed Resources With Electric Power Systems, IEEE Std. IEEE-1547, 2003.
- [60] Inverters, Converters, Controllers and Interconnection System Equipment for Use with Distributed Energy Resources, UL 1741, November 7, 2005.
- [61] Hydro One Networks Inc, Distributed Generation Technical Interconnection Requirements; Interconnection at Voltages 50kV and Below, Hydro One, Toronto, DT-10-015, rev. 2, June 2011.
- [62] Z. Ye, R. Walling, L. Garces, R. Zhou, L. Li and T. Wang, "Study and Development of Anti-Islanding Control for Grid-Connected Inverters," General Electric Global Research center, Niskayuna, New York, NREL/SR-560-36243, May 2004.
- [63] Bochuan Liu and Byeong-Mun Song, "Modeling and Analysis of an LCL Filter for Grid-Connected Inverters in Wind Power Generation Systems," in *Proc. 2011 IEEE Power and Energy Society General Meeting*, pp. 1-6.
- [64] M. Liserre, F. Blaabjerg and S. Hansen, "Design and Control of an LCL-Filter-Based Three-Phase Active Rectifier", *IEEE Transaction on Industry Applications*, 2005, vol. 41, no. 5. Pp.1281-1291.
- [65] Chatterjee, K., Fernandes, B.G., Dubey, G.K., "An instantaneous Reactive Volt-Ampere Compensator and Harmonic Suppressor System", *IEEE Transactions on Power Electronics*, 1999, vol. 14, issue 2, pp. 381-392.
- [66] Pekik Argo Dahono, Yukihiko Sato and Teruo Kataoka, "Analysis and Minimization of Ripple Components of Input Current and Voltage of PWM Inverters," *IEEE Transaction on Industry Application*, vol. 32, no. 4, pp. 945-950, 1996.
- [67] P.G.Barbosa, L.G.B. Rolim, E.H. Watanabe and R. Hanitsch, 'Control Strategy for Grid Connected DC-AC Converters with Load Power Factor Correction,' in *Proc. IEE 1998 Generation, Transmission and Distribution*, vol. 145, no. 5, pp. 487-491.

- [68] Y. Chen, H. Wu, Y. Chen, K. Lee and S. Shyu, "The AC Line Current Regulation Strategy for the Grid-Connected PV System," *IEEE Transaction in Power Electronics*, vol. 25, no. 1, pp. 209-218, 2010.
- [69] IEEE Recommended Practices and Requirements for Harmonic Control in Electrical Power Systems, IEEE Std. 519-1992, Jun. 2004.
- [70] Chen Y. and Liu F. "Design and Control for Three-phase Grid-connected Photovoltaic Inverter with LCL Filter", *Int. Conf. on Circuits and Systems*, 2009, pp. 1-4.
- [71] Parikshith. B.C and Vinod J., "Higher Order Output Filter Design for Grid Connected Power Converters", *Presented at Fifteenth National Power Systems Conference (NPSC)*, Bombay, India, Dec. 2008, pp. 614-619.
- [72] Ralph E. Fehr, *Industrial power distribution*, Prentice Hall Inc, 2001.
- [73] E.J. Currence, J.E.Plizga, H. Nelson, "Harmonic Resonance at Medium Sized Industrial Plant", *IEEE Industry Applications Society Annual Meeting 1994*, vol. 31, no.4, pp. 682-690, 1995.
- [74] Pouyan Saifi, "Network Resonance and Temporary Overvoltages in Distributed Generation Systems," M.E.Sc. thesis, University of Western Ontario, 2009.
- [75] Installation and operational Manual, Commercial, Grid-Tied Photovoltaic Inverter, Solectria Renewables, 2010.
- [76] "Operation and Maintenance manual for 10kW Grid-Tied photovoltaic Inverter," Trace Technologies, Trace Technologies, 1999.
- [77] E. Baran Mesut and Ismail El-Markaby, "Fault Analysis on Distribution Feeders With Distributed Generators," in *IEEE Transaction on Power Systems*, vol. 20. no.4, pp. 1757-1764, 2005.
- [78] R. Dugan, R. Zavadil and D. Van Holde, "Interconnection Guidelines for Distributed Generation," [Online]: http://grouper.ieee.org/groups/scc21/pdfs/ESourceDG_InterconnectionAppGuide.pdf, Date: 26/02/2012.
- [79] "The Contribution to Distribution Network Fault Levels From the Connection of Distributed Generation," Contract No: DG/CG/00027/00/00, URN No:05/636, KEMA Limited, [Online] http://webarchive.nationalarchives.gov.uk/20100919181607/http://www.ensg.gov.uk/assets/14_06_20_05_dgcg0000200.pdf, Date: 12/12/2011.
- [80] "The Contribution to Distribution Network Fault Levels From the Connection of Distributed Generation," Contract No: DG/CG/00027/00/00, URN No:05/636, KEMA Limited, [Online]: http://webarchive.nationalarchives.gov.uk/20100919181607/http://www.ensg.gov.uk/assets/14_06_20_05_dgcg0000200.pdf, Date: 12/12/2011.
- [81] S. Phuttapatimok, A. Sangswang, M. Seapan, D. Chenvidhya and K. Kirtikara, "Evaluation of Fault Contribution in the Presence of PV Grid-Connected Systems," in *Proc. 2008 33rd IEEE Photovoltaic Specialists Conference*, pp. 1-5.
- [82] J. Fuerth, "Distribution Generation Connection Impact Assessments," [Online]: http://www.appro.org/docs/HONIconnectionsJan2009/John_Fuerth_%20-APPPrO_presentation_Jan_22_2009.pdf, Date: 12/12/2011.
- [83] A. Ellis, "Bulk-Level Models for Solar Grid Interconnection and Planning," [Online]: http://www.nrel.gov/eis/pdfs/uwig_solar_wkshp_ellis.pdf, Date: 12/12/2011.
- [84] H. Kobayashiet al., "Utility Interconnection Techniques for Dispersed Residential Photovoltaic Systems," in *Proc. 1993 4th Annual Conference of Power & Energy Society*.
- [85] H. Kobayashi and K. Takigawa, "A New Protective Method for Grid Connected Dispersed PV Systems to Detect Short Circuit Fault in Distribution Line," *Solar Energy Materials and Solar Cells*, vol. 47, pp. 117-123, 1997.
- [86] C. Hou and X. Hu, "A study of Voltage Detection Based Fault Judgement Method in Micro-grid with Inverter Interfaced Power Source," in *Proc. The International Conference on Electrical Engineering*, 2009, pp. 1-5.
- [87] M.S. Gustavo, A.S. N. Francisco, C. C. Marcelo, R. L. Leonardo and B. Fabricio, "Fault Detection System for Distributed Generation Converters," in *Proc. 2011 Brazilian Power Electronics Conference*, pp. 320-327.
- [88] C. Scauder, "Transient Modeling for Inverter Based Distributed Generation," *Satcon Technology Corporation*, March 2, 2010.
- [89] H. Al-Nasseri, M. A. Redfern and R. O'Gorman, "Protecting Micro-grid Systems Containing Solid-State Converter Generation," in *Proc. 2005 International Conference on Future Power Systems*, pp.1-5.

- [90] X. Liu, A. Thirumalai and G. G. Karady, "Design and Development of an Ultrafast Pilot Protection," in *Proc. 2011 IEEE/PES Power System Conference and Exposition*, pp. 1-7.
- [91] A. Y. Wu and Y. Yin, "Fault Current Limiter Applications in Medium- and High-Voltage Power Distribution Systems," in *IEEE Transaction on Industry Applications*, vol. 34, no. 1, pp. 236-242, 1998.
- [92] M. Öhrström, "Fast fault detection for peak current limitation based on few samples," in *Proc. of 17th Int. Conf. Electricity Distribution*, Barcelona, Spain, May 12–15, 2003.
- [93] FACTS Terms & Definitions Task Force of the FACTS Working Group of the DC and FACTS Subcommittee, "Proposed terms and definitions for flexible AC transmission system (FACTS)," *IEEE trans. On Power Delivery*, vol. 12, no. 4, pp. 1848-1853, 1997.
- [94] N. G. Hingorani and L. Gyugyi, *Understanding FACTS*, IEEE Press, 1996.
- [95] R. M. Mathur and R. K. Varma, *Thyristor-Based FACTS Controllers for Electrical Transmission Systems*, New York: Wiley-IEEE Press, 2002.
- [96] K.R. Padiyar, "FACTS Controllers in Power Transmission and Distribution," New Age International (P) Limited, New Delhi.
- [97] P. Kundur, "Power System Stability and Control", McGraw-Hill, Inc. 1994.
- [98] H. Toodeji, S.H. Fathi and N. Farokhnia, "Using Current-Based MPPT Method in New Integrated System of PV Module and STATCOM," in *Proc. 2010 5th IEEE Conference on Industrial Electronics and Application*, pp. 1028-1033.
- [99] K. K. Sen, "SSSC—Static Synchronous Series Compensator: Theory, Modeling, and Applications," *IEEE Transactions on Power Delivery*, vol. 13, no. 1, pp. 241–246, 1998.
- [100] L. Gyugyi, C. D. Schauder, and K. K. Sen, "Static Synchronous Series Compensator: A Solid-State Approach to the Series Compensation of Transmission Lines," *IEEE Transactions on Power Delivery*, Vol. 12, No. 1, January 1997.
- [101] L. Gyugyi, C. D. Schauder, S. L. Williams, T. R. Reitman, D. R. Torgerson, and A. Edris, "The Unified Power Flow Controller: A New Approach to Power Transmission Control," *IEEE Transactions on Power Delivery*, vol. 10, no. 2, 1995.
- [102] C. D. Schauder, L. Gyugyi, M. R. Lund, D. M. Hamai, T. R. Reitman, D. R. Torgerson, and A. Edris, "Operation of the Unified Power Flow Controller (UPFC) Under Practical Constraints," *IEEE Transactions on Power Delivery*, vol. 13, no. 2, 1998.
- [103] M. H. Rashid, *Power Electronics Handbook*, 2nd ed., Burlington, U.S.A., Elsevier, 2007
- [104] Hou Rui Cao Taibin and Qian Bifu, "Design of Sliding Mode Controller for STATCOM with LCL Filter," in *IEEE Proc. 2010 International Conference on Computer, Mechatronics, Control and Electronic Engineering (CMCE)*, pp. 80-83.
- [105] Guopeng Zhao, Jinjun Liu and Minxiao Han, "Design of Input Filters Considering the Stability of STATCOM Systems," *Journal of Power Electronics*, vol. 11, no. 6, pp. 904-913, 2011.
- [106] Bijaya Pokharel "Modeling, Control and Analysis of a Doubly Fed Induction Generator Based Wind Turbine System with Voltage Regulation," M.Sc. Thesis, Tennessee Technological University, U.S.A, 2011.
- [107] K. C. Kalaitzakis and G. J. Vachtsevanos, "On the Control and Stability of Grid Connected Photovoltaic Sources," *IEEE Transactions on Energy Conversion*, vol. EC-2, No. 4, pp. 556-562, December 1987.
- [108] A. Yazdani and R. Iravani, "Voltage-Sourced Converters in Power Systems-Modeling, Control and Applications," IEEE Press, John Wiley & Sons Inc. Publications.
- [109] Hong Shen, Hai Wei Li, Bin Huang, Jing Li, "Study on Integration and Transmission of Large Scale Wind Power in JiuQuan Area Gansu Province China," in *Proc. 2009 CIGRE/IEEE PES Joint Symposium on Integration of Wide-Scale Renewable Resources into the Power Delivery System*, pp. 1-8.
- [110] Ying Xiao, Y.H. Song, Chen-Ching Liu, Y.Z. Sun, "Available transfer capability enhancement using FACTS devices," *IEEE Transactions on Power Systems*, vol.18, no.1, pp. 305-312, Feb 2003.
- [111] X.P. Zhang, L. Yao, K. Godfrey, C. Sasse, "Increasing the transfer of wind power on transmission network through coordinated FACTS control," *CIGRE 2006, C6-308, Paris*.
- [112] "Ercot CREZ Transmission optimization study," www.ercot.com, 15 April 2008.
- [113] K.R. Padiyar and R.K. Varma, "Damping Torque Analysis of Static Var System Controllers", *IEEE Transactions on Power Systems*, Vol. 6, No. 2, pp. 458-465, May 1991.

- [114] N. Mithulananthan, C.A. Canizares, J. Reeve and G. J. Rogers, "Comparison of PSS, SVC, and STATCOM Controllers for Damping Power System Oscillations," *IEEE Transaction on Power Systems*, vol. 18, no.2, pp. 786-792, 2003.
- [115] A.S.P. Kanojia and B. Dr. V. K. Chandrakar, "Damping of Power System Oscillations by Using coordinated Tuning of POD and PSS with STATCOM," *World Academy of Science, Engineering and Technology*, vol. 50, pp. 1067-1072, 2009
- [116] R. Majumdar, B.C. Pal, C. Dufour and P. Korba, "Design and Real-time Implementation of Robust FACTS Controller for Damping Inter-Area Oscillation," *IEEE Transaction on Power Systems*, vol. 21, no. 2, pp. 809-816, 2006.
- [117] Rajiv K. Varma and Vinod Khadkikar, "Utilization of Solar Farm Inverter As STATCOM" US Provisional Patent application filed 15 Sept. 2009.
- [118] A. Lakshmi Devi and B. Subramanyam, "Optimal DG Unit Placement for Loss Reduction in Radial Distribution System-A Case Study," *ARPN Journal of Engineering and Applied Sciences*, pp. 57-61, 2006.
- [119] S. Kumar Injeti and Navuri P. Kumar, "Optimal Planning of Distributed Generation for Improved Voltage Stability and Loss Reduction," *International Journal of Computer Applications*, vol. 15, no. 1, pp. 40-46, 2011.
- [120] M. P. Lalitha, N. S. Reddy and V. C. V. Reddy, "Optimal DG Placement for Maximum Loss Reduction in Radial Distribution System Using ABC Algorithm," *International Journal of Reviews in Computing*, pp. 44-52.
- [121] N. Acharya, P. Mahat and N. Mithulananthan, "An analytical Approach for DG Allocation in Primary Distribution Network," *Electrical Power and Energy Systems, Elsevier*, vol. 28, pp. 669-678, 2006.
- [122] D. Q. Hung, N. Mithulananthan and R. C. Bansal, "Analytical Expression for DG Allocation in Primary Distribution Networks," *IEEE Transaction on Energy Conversion*, vol. 25, no.3, pp. 814-820, 2010.
- [123] D. Q. Hung and N. Mithulananthan, " Multiple Distributed Generator Placement in Primary Distribution Networks for Loss Reduction," *IEEE Transaction on Industrial Electronics, IEEE Early Access 2011* no. 99.
- [124] Priyanka Paliwal and N.P. Patidar, " Distributed Generator Placement for Loss Reduction and Improvement in Reliability," in *Proc. of World Academy of Science, Engineering and Technology 2010*, pp. 809-813.
- [125] T. Griffin, K. Tomsovic and D. Secret A. Law, "Placement of Dispersed Generations Systems for Reduced Losses," in *Proceedings of the 33rd Hawaii International Conference on System Sciences, 2000*, pp. 1-9.
- [126] Stuart van Zyl and CT Gaunt, " A Generalized Method for Evaluating Voltage Rise in DG-Equipped Networks," CIGRE SC-C6 (COLL 2005), topic D-3.
- [127] A.Kazemi, and M.Sadeghi, "Distributed Generation Allocation for Loss Reduction and Voltage Improvement," in *Proc. 2009 IEEE Power and Energy Engineering Conference*, pp. 1-6.
- [128] Aristides E. Kiprakis and A. Robin Wallace, "Hybrid Control of Distributed Generators Connected Weak Rural Networks to Mitigate Voltage Variation," in *Proc.2003 17th International Conference on Electricity Distribution*, pp. 1-5.
- [129] C. L. Masters, " Voltage Rise the Big Issue When Connecting Embedded Generation to Long 11 kV Overhead Lines," *Power Engineering Journal, Embeded Generation*, pp. 5-12, 2002.
- [130] Naoto Kakimoto, Qin-Yun Piao, and Hiroo Ito, "Voltage Control of Photovoltaic Generator in Combination With Series Reactor," *IEEE Transaction on Sustainable Energy*, vol. 2, no. 4, pp. 374-382, 2011.
- [131] T. Hoff and D.S. Shugar, "The Value of Grid-Support Photovoltaics in Reducing Distribution System Losses," *IEEE Transaction on Energy Conversion*, vol. 10, no. 3, pp. 569-576, 1995.
- [132] Yahya Kabiri Renani, , H. Askarian Abyaneh, S. H. H. Sadeghi, H. Hashemi Dezaki and H. Nafisi, A. Talebi, "Effect of the PV/FC Hybrid Power Generation System on Total Line Loss in Distribution Network," in *Proc. 2010 IEEE International Conference on Power and Energy*, pp. 89-94.
- [133] Konstantin Turitsyn, Petr S`ulc, Scott Backhaus, and Michael Chertkov, "Options for Control of Reactive Power by Distributed Photovoltaic Generators," *IEEE Journal 2011 Proceeding of the IEEE* , vol. 99, no. 6, pp. 1063 – 1073.

- [134] Masoud Farivary, Russell Nealy, Christopher Clarke and Steven Low, "Optimal Inverter VAR Control in Distribution Systems with High PV Penetration," [Online]: <http://arxiv.org/pdf/1112.5594.pdf>, submitted on 23rd Dec' 2011, date: Feb. 12, 2012 on eprint: arXiv:1112.5594.
- [135] C. Schuder, "Distribution Grid Codes for High Penetration DER," [Online]: http://www.4thintegrationconference.com/downloads/Distribution%20Grid%20Codes%20Tutorial_SatCon_Schauder.pdf, Date: 12/12/2011.
- [136] A. Beekmann, J. Marques, E. Quitmann, and S. Wachtel, "Wind energy converters with FACTS Capabilities for optimized integration of wind power into transmission and distribution systems", *CIGRE 2009, Calgary, Canada*.
- [137] N. W. Miller and K. Clark, "Advanced Controls Enables Wind Plants to Provide Ancillary Services," in *Proc. 2010 IEEE PES General Meeting*, pp. 1-6.
- [138] R.A. Walling and K. Clark, "Grid Support Functions implemented in Utility-Scale PV Systems," in *Proc. IEEE PES 2010, T&D Conference and Exposition*, pp. 1-5.
- [139] G. C. Pyo, H. W. Kang and S. I. Moon, "A New Operation Method for Grid-Connected PV System Considering Voltage Regulation in Distribution System," in *Proc. IEEE 2008, Power and Energy Society General Meeting - Conversion and Delivery of Electrical Energy in the 21st Century*, pp. 1-7.
- [140] F.L. Albuquerque, A.J. Moraes, G.C. Guimaraes, S.M.R. Sanhueza and A.R. Vaz, "Photovoltaic solar system connected to the electric power grid operating as active power generator and reactive power compensator," *Solar Energy*, vol. 84, no. 7, pp. 1310-1317, July 2010.
- [141] Huajun Yu, Junmin Pan and An Xiang "A multi-function grid-connected PV system with reactive power compensation for the grid," *Solar Energy*, vol. 79, pp. 101–106, 2005.
- [142] F. Delfino, G. B. Denegri, M. Invernizzi, R. Procopio and G. Ronda, "A P_Q Capability Chart Approach to Characterize Grid Connected PV-Units," in *Proc. 2009 CIGRE/IEEE PES Joint Symposium on Integration of Wide-Scale Renewable Resources Into the Power Delivery System*, pp. 1-8.
- [143] Task Force on Harmonics Modeling and Simulation, "Modeling And Simulation of the Propagation of Harmonics in Electric Power Networks-Part I: Concepts, Models and Simulation Techniques," *IEEE Transactions on Power Delivery*, Vol. 11, No. 1, pp. 452-465, January 1996.
- [144] Arrillaga, J., Bradley, D.A., Bodger, P.S., "Power System Harmonics," John Wiley and Sons, New York, 1985.
- [145] P. J. M. Heskes and J. H. R. Enslin, "Power Quality Behaviour of Different Photovoltaic Inverter Topologies," [Online]: <http://www.ecn.nl/docs/library/report/2003/rx03056.pdf>, Date: 12/12/2011.
- [146] M.Ghezelayagh and V.J.Gosbell, " Harmonic modeling of distorting loads on distribution feeders and in a large power system," in *Proc. 2000 International Conference on Advances in Power System Control, Operation and Management* , vol. 1, pp. 96-100.
- [147] W. Xu, "Status and future directions of power system harmonic analysis," in *Proc. 2003 IEEE Power Engineering Society General Meeting*, pp. 4 vol. 2666, 13-17 July 2003.
- [148] D. Mueller, "Case studies of harmonic problems, analysis, and solutions on transmission systems," in *Proc. 2007 IEEE International Conference on Electrical Power Quality and Utilization*, pp.1-6, 9-11 Oct. 2007.
- [149] Task Force on Harmonics Modeling and Simulation, "Modeling And Simulation of the Propagation of Harmonics in Electric Power Networks-Part II: Sample System and Examples," *IEEE Transactions on Power Delivery*, Vol. 11, No. 1, pp. 466-474, January 1996.
- [150] Chris Halliday, Frank Iannelli and Robert Barr, "Distribution Network Capacitor Resonance – A Case Study," [Online]: <http://www.elect.com.au/Attachments/Distribution%20Network%20Capacitor%20Resonance%20%20A%20Case%20Study.pdf>, Date: 12/12/2011.
- [151] A. Khodabakhshian, R. Hooshmand and G. Isazadeh, "Harmonic Resonance and Over-Voltage Assessment During Switching of High Voltage Shunt Capacitors in E.R.E.C. Network," in *Proc. 2009 Canadian Conference on Electrical and Computer Engineering*, pp. 926-930.
- [152] M. Contreras, H. Calleja and V. Cardenas, "Study of Harmonic Propagation in Ring Bus Distribution System," in *Proc. 2005 IEEE Power Electronics Specialists Conference*, pp.1901-1907, 16-16 June 2005.

- [153] Christine D. Crites, Rajiv K. Varma, Vinay Sharma and Bill Milroy, "Characterization of Harmonics in a Utility Feeder with PV Distributed Generation," in *Proc. 2012 IEEE Electrical Power and Energy Conference*, pp. 1-6.
- [154] FS series 2 PV Module Datasheet, Document ID: PD-S-401-02-NA Jun 2010, [Online]: http://www.firstsolar.com/Downloads/pdf/Datasheet_s2_NA.pdf. (12.04.2011)
- [155] Figueres, E.; Garcera, G.; Sandia, J.; Gonzalez-Espin, F.J., "Modelling and control of a 100kW photovoltaic inverter with an LCL grid filter for distributed power systems", in *Proc. 2007 European Conference on Power Electronics and Applications*, pp. 1-10.
- [156] Solar Cells, [Online]: <http://www.pvresources.com/Introduction/SolarCells.aspx>., Date: 13 July, 2012.
- [157] J. Poortmans and V. Arkhaipov, *Thin Film Solar Cells Fabrication, Characterization and Applications*, John Wiley & Sons, Inc., 2006.
- [158] L. Fraas and L. Partain, *Solar Cells and Their Applications*, 2nd Edition, John Wiley & Sons, Inc., 2010.
- [159] H. Bayhan and A.S. Kavasoglu, "Exact Analytical Solution of the Diode Ideality Factor of a pn Junction Device Using Lambert W-function Model," in *2007 Turk J Phys*, pp. 7-10.
- [160] S. Bowden and A. Rohatgi, "Rapid and Accurate Determination of Series Resistance and Fill Factor Losses in Industrial Silicon Solar Cells," Georgia Institute of Technology, [Online]: <http://smartech.gatech.edu/jspui/bitstream/1853/26165/1/Munich-Bowden2.pdf>, date: 14/07/2012.
- [161] K.H. Hussein, I. Muta, T. Hoshino and M. Osakada "Maximum photovoltaic power tracking: an algorithm for rapidly changing atmospheric conditions", *IEE Proc.-Generation, Transmission and Distribution*, vol. 142, no. 1, pp. 59-64, January 1995.
- [162] Dave Turcotte and Farid Katiraei, "Fault Contribution of Grid-Connected Inverters," in *Proc. 2009 IEEE Electrical Power Conference*, pp. 1-5.
- [163] BICC brand product Catalogue, "Energy Wire and Cable for Power Generation, Transmission and Distribuion," General Cable, Nov' 2011
- [164] B.C. Parikshith and J. Vinod, "Higher Order Output Filter Design for Grid Connected Power Converters", *Presented at Fifteenth National Power Systems Conference (NPSC)*, Bombay, India, Dec. 2008, pp. 614-619.
- [165] *EMTDC/PSCAD User Manual*, HVDC Research Center, Manitoba, 2003.
- [166] Rajiv. K. Varma, Byomakesh Das, Iurie Axente, and Tim Vanderheide, "Optimal 24-hr Utilization of a PV Solar System as STATCOM (PV-STATCOM) in a Distribution Network", in *Proc. 2011 IEEE PES General Meeting*, Detroit, U.S.A. pp. 1-8.
- [167] Rajiv K. Varma, Shah Arifur Rahman, Vinay Sharma, Tim Vanderheide, "Novel Control of a PV Solar System as STATCOM (PV-STATCOM) for Preventing Instability of Induction Motor Load," Presented at CCECE 2012, April 30-May 2, Montreal, Quebec.
- [168] Rajiv K. Varma and Shah Arifur Rahman, "Novel Control of Inverter based DGs as FACTS (DGFACTS) for Enhancing Grid Power Transmission Limits, US Provisional Patent application No. 61/309,612 filed 2nd March 2010.
- [169] Rajiv K. Varma, Vinod Khadkikar and Shah Arifur Rahman, "Utilization of Distributed Generator Inverters as STATCOM" PCT Patent application PCT/CA2010/001419 dated 15 September, 2010.
- [170] "2012 Loss Factor," Alberta Electric System Operator (AESO), [Online]: http://www.aeso.ca/downloads/Final_Alberta_Loss_Factors_for_2012.pdf, Date: 14.07.2012.
- [171] Curt Harting, "AC Transmission Line Losses," Stanford University, [Online]: <http://large.stanford.edu/courses/2010/ph240/harting1/>, Date: 14.07.2012.
- [172] "State Electricity Profiles 2010," U.S. Energy Information Administration, DOE/EIA-0348(01)/2, Released: January 27, 2012, [Online]: <http://www.eia.gov/electricity/state/pdf/sep2010.pdf>, Date: 14.07.2012.
- [173] "Reducing Technical and Non-Technical Losses in the Power Sector," Background paper for the World Bank Group Energy Sector Strategy, Available [Online]: http://siteresources.worldbank.org/EXTESC/Resources/Background_paper_Reducing_losses_in_the_power_sector.pdf, Date: 14.07.2012.
- [174] Leonard L. Grigsby, *Electric Power Engineering Handbook* (2nd ed), CRC Press 2007, Ch-7,9.
- [175] M. K. Pal, "Power System Stability," Lecture Notes, Available: [online] <http://www.mkpalconsulting.com/files/stabilitybook.pdf>, date: Feb, 12' 2012, pp. 1-13.

- [176] O. Perpiñan, E. Lorenzo and M.A. Castro “On the calculation of energy produced by a PV grid-connected system,” [online]: http://procomun.files.wordpress.com/2010/02/articulomomentospip_rev1.pdf, date: 16, Feb 2012.
- [177] M. Jantsch, H. Schmidt y J. Schmid. Results on the concerted action on power conditioning and control, *11th European photovoltaic Solar Energy Conference*, Montreux_ pp. 1589-1592, 1992.
- [178] Luque and Steven Hegedus, Handbook of photovoltaic science and engineering, John Wiley and Sons Ltd. 2003, pp. 965.
- [179] “Emerson Solar Utility Scale PV Inverter Systems,” *SPV Product Guide: 145kVA-1590kVA*, [online]: <http://www.emersonpvsolutions.com/>, date: 20/02/2012.
- [180] PowerWorld Corporation, <http://www.powerworld.com/products/simulator.asp>
- [181] “Save the Watt Wednesday”, CNW Canada Newswire, [online], <http://www.newswire.ca/en/story/278939/save-the-watt-wednesday>, date: Feb, 12’ 2012.
- [182] “The Cost of Power Disturbances to Industrial & Digital Companies” White Paper, Electric Power Research Institute, 2001. [Online]: <http://www.onpower.com/pdf/EPRICostOfPowerProblems.pdf>, date: 23rd Aug, 2012.
- [183] J. Pedra, “On the Determination of Induction Motor Parameters from Manufacturer Data for Electromagnetic Transient Programs,” *IEEE Transaction on Power Systems*, vol. 23, no. 4, pp. 1709-1718, Nov 2008.
- [184] J. Pedra, I. Candela and L. Sainz, “Modelling of Squirrel-Cage Induction Motors for Electromagnetic Transient Programs,” *IET Electric Power Applications*, vol. 3, no. 2, pp. 111-122, 2009.
- [185] M. Kempkes, I. Roth and M. Gaudreau, “Solid-State Circuit Breakers for Medium Voltage DC Power,” in *Proc. IEEE 2011 Electric Ship Technologies Symposium*, pp. 254-257.
- [186] H. Hosseinian, H. A. Abyaneh, F. Shahnia, H. Hatami and S. Galvani, “Induction Motor Behavior at Sudden Interruptions and Voltage Sag,” in *Proc. 2008 International Conference on Electrical Engineering*, pp. 1-7.
- [187] Ran Peng, Rajiv K. Varma and Jin Jiang, “New Static Var Compensator (SVC) based damping control using remote generator speed signal”, *Int. J. Energy Technology and Policy*, vol. 4, nos. 3/4, 2006.
- [188] H. F. Wang, "Phillips-Heffron model of power systems installed with STATCOM and applications," *IEE Proc. Generation, Transmission, Distribution*, vol. 146, no. 5 Sep. 1999.
- [189] Leonard L. Grigsby, *Electric Power Engineering Handbook* (2nd ed), CRC Press 2007..
- [190] CIGRE Task Force 38.02.16, “Impact of Interactions among Power System Controls”, *CIGRE Technical Brochure 166*, Paris, France, August 2000.
- [191] Rajiv. K. Varma, Shriram. S. Rangarajan, Iurie Axente, and Vinay Sharma, "Novel application of a PV Solar Plant as STATCOM during Night and Day in a Distribution Utility Network", Paper Presented in Panel Session on "FACTS/Power Electronics Installations" *2011 IEEE PES Power Systems Conference & Expo*, Phoenix, Arizona, USA.
- [192] Rajiv K. Varma, Ehsan Siavashi, Byomakesh Das, Vinay Sharma "Novel application of a PV Solar Plant as STATCOM during Night and Day in a Distribution Utility Network – Part 2", Paper Presented in Panel Session on "FACTS/Power Electronics Installations" *2012 IEEE T&D Conference*, Orlando, USA.
- [193] Shah Arifur Rahman, Rajiv. K. Varma, and Wayne H. Litzemberger, "Bibliography of FACTS Applications for Grid Integration of Wind and PV Solar Power Systems: 1995-2010, IEEE Working Group Report", in *Proc. of IEEE PES General Meeting*, Detroit, 2011.
- [194] CYME International (Quebec, Canada), <http://www.cyme.com/>.
- [195] Large-Scale Photovoltaic Power Plants Ranking 1-50, [Online]: <http://www.pvresources.com/PVPowerPlants/Top50.aspx>
- [196] Task Force on Harmonics Modeling and Simulation, IEEE Power Engineering Society T & D Committee , “Impact of Aggregate Linear Load Modeling on Harmonic Analysis: A Comparison of Common Practice and Analytical Models,” *IEEE Trans. On Power Delivery*, vol. 18, no. 2, pp. 625-630, 2003.
- [197] S. J. Ranade and W. Xu, “An Overview of Harmonics Modeling and Simulation,” [Online]: http://www.calvin.edu/~pribeiro/IEEE/ieee_cd/chapters/pdffiles/c1pdf.pdf, Date: 29.08.2012.

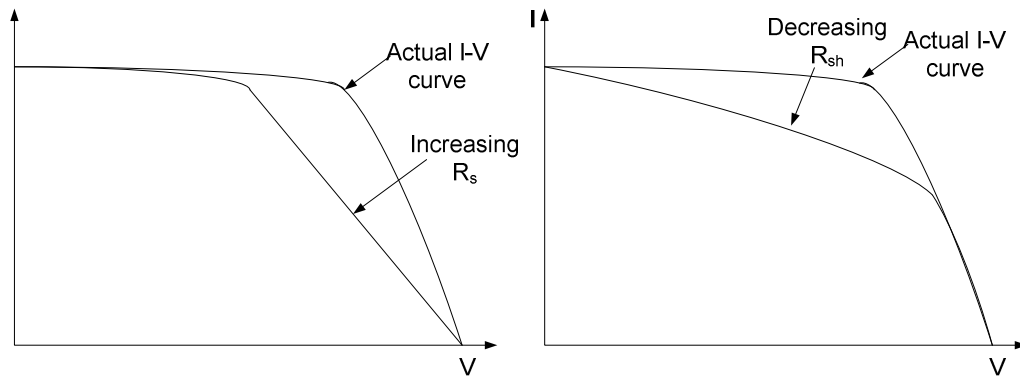
- [198] Constantine Hatziaioniu, “ Step by Step Example of A Simple Harmonic Study (based on a two bus system),” [Online]: <http://www.cpdee.ufmg.br/~selenios/Qualidade/Estudo%20de%20casos.pdf>, Date: 29.08.2012.
- [199] Rajiv. K. Varma, Shah Arifur Rahman and Wayne H. Litzenberger, “Bibliography of FACTS: 2008 Part I IEEE Working Group Report,” in *Proc. IEEE 2010, Power and Energy Society General Meeting*, pp. 1-7.
- [200] Shah Arifur Rahman, Rajiv. K. Varma and Wayne H. Litzenberger, “Bibliography of FACTS: 2008 Part II IEEE Working Group Report,” in *Proc. IEEE 2010, Power and Energy Society General Meeting*, pp. 1-8.
- [201] Rajiv. K. Varma, Shah Arifur Rahman and Wayne H. Litzenberger, “Bibliography of FACTS: 2008 Part III IEEE Working Group Report,” in *Proc. IEEE 2010, Power and Energy Society General Meeting*, pp. 1-7.
- [202] Shah Arifur Rahman, Rajiv. K. Varma, Wayne H. Litzenberger and Jon Berge “Bibliography of FACTS 2011: Part I; IEEE Working Group Report,” Accepted to present on IEEE PES GM 2012, S.A. California, U.S.A.
- [203] J. Carpentier, “Optimal power flows,” *Int. J. Elect. Power Energy Syst.*, vol. 1, no. 1, pp. 3–15, 1979.

Appendices

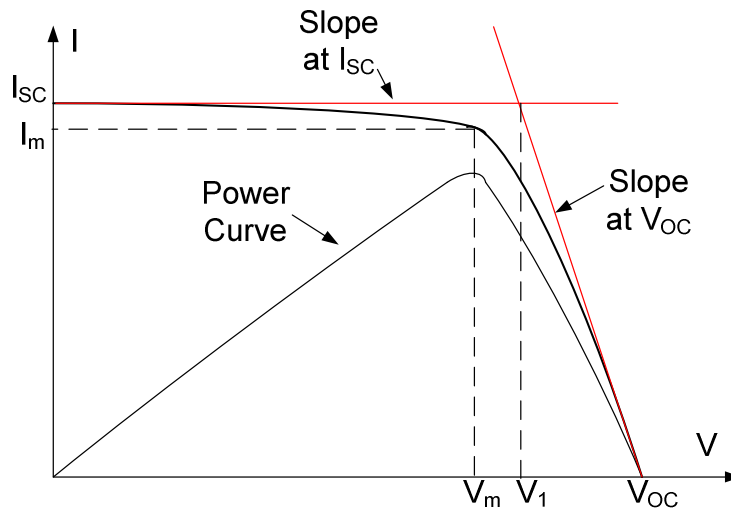
Appendix A: 100kW PV inverter modeling mathematical expression and calculation

A.1 I-V characteristic curve of PV and the approximate value of R_s and R_{sh} :

The following figure shows the effect of the diverged value of R_s and R_{sh} from actual value on an I-V characteristic curve [18].



The following figure shows the slope at V_{OC} which determines the approximate value of R_s , and the the slope of I_{SC} which determines the approximate value of R_{sh} [18].



Therefore, $R_{s_slope} = (V_{oc} - V_1) / I_{sc}$. If we consider, $R_{s_approx} = (V_{oc} - V_m) / I_{sc}$, then $R_{s_approx} > R_{s_slope}$.

A.2 Space Phasor and Park's Transformation

In EMTDC/PSCAD, to transform the three phase signal in to rotary d-q form it uses Park's transformation blocks which can be established in following way:

In space phasor form, by definition, for a phase sequence of a-b-c,

$$\begin{aligned} f_{abc} &= f_a + f_b \cdot e^{-j2\pi/3} + f_c \cdot e^{j2\pi/3} \\ &= f_a + f_b \cdot \left(\cos \frac{2\pi}{3} - j \sin \frac{2\pi}{3} \right) + f_c \cdot \left(\cos \frac{2\pi}{3} + j \sin \frac{2\pi}{3} \right) \dots (a) \end{aligned}$$

Or,

$$\begin{aligned} f_{abc} &= f_a + f_b \cdot \left(-\frac{1}{2} - j \frac{\sqrt{3}}{2} \right) + f_c \cdot \left(-\frac{1}{2} + j \frac{\sqrt{3}}{2} \right) \\ &= \left(f_a - \frac{1}{2} f_b - \frac{1}{2} f_c \right) + j \left(-\frac{\sqrt{3}}{2} f_b + \frac{\sqrt{3}}{2} f_c \right) = f_\alpha + j f_\beta \end{aligned}$$

In matrix form,

$$\begin{bmatrix} f_\alpha \\ f_\beta \end{bmatrix} = \begin{bmatrix} 1 & -\frac{1}{2} & -\frac{1}{2} \\ 0 & -\frac{\sqrt{3}}{2} & \frac{\sqrt{3}}{2} \end{bmatrix} \cdot \begin{bmatrix} f_a \\ f_b \\ f_c \end{bmatrix}$$

With respect to rotating frame at a synchronous speed of ω , multiplying (a) with $e^{-j\omega t}$, (by definition) we get

$$f_r = f_{abc} \cdot e^{-j\omega t}$$

$$f_r = f_a \cdot e^{-j\omega t} + f_b \cdot \left(\cos \frac{2\pi}{3} - j \sin \frac{2\pi}{3} \right) \cdot e^{-j\omega t} + f_c \cdot \left(\cos \frac{2\pi}{3} + j \sin \frac{2\pi}{3} \right) \cdot e^{-j\omega t}$$

Or,

$$f_r = f_a \cdot e^{-j\omega t} + f_b \cdot \left(\cos \frac{2\pi}{3} - j \sin \frac{2\pi}{3} \right) \cdot e^{-j\omega t} + f_c \cdot \left(\cos \frac{2\pi}{3} + j \sin \frac{2\pi}{3} \right) \cdot e^{-j\omega t}$$

$$\begin{aligned} \text{Or, } f_r &= f_a \cdot (\cos \omega t - j \sin \omega t) + f_b \cdot \left(\cos \frac{2\pi}{3} - j \sin \frac{2\pi}{3} \right) \cdot (\cos \omega t - j \sin \omega t) \\ &\quad + f_c \cdot \left(\cos \frac{2\pi}{3} + j \sin \frac{2\pi}{3} \right) \cdot (\cos \omega t - j \sin \omega t) \end{aligned}$$

$$\begin{aligned} \text{Or, } f_r &= f_a \cdot (\cos \omega t - j \sin \omega t) \\ &\quad + f_b \cdot \left(\cos \frac{2\pi}{3} \cdot \cos \omega t - \sin \frac{2\pi}{3} \cdot \sin \omega t \right) - j f_b \cdot \left(\sin \frac{2\pi}{3} \cdot \cos \omega t \right. \\ &\quad \left. + \cos \frac{2\pi}{3} \cdot \sin \omega t \right) \\ &\quad + f_c \cdot \left(\cos \frac{2\pi}{3} \cdot \cos \omega t + \sin \frac{2\pi}{3} \cdot \sin \omega t \right) - j f_c \cdot \left(-\sin \frac{2\pi}{3} \cdot \cos \omega t \right. \\ &\quad \left. + \cos \frac{2\pi}{3} \cdot \sin \omega t \right) \end{aligned}$$

$$\begin{aligned} \text{Or, } f_r &= f_a \cdot (\cos \omega t - j \sin \omega t) + f_b \cdot \cos \left(\omega t + \frac{2\pi}{3} \right) - j f_b \cdot \sin \left(\omega t + \frac{2\pi}{3} \right) \\ &\quad + f_c \cdot \cos \left(\omega t - \frac{2\pi}{3} \right) - j f_c \cdot \sin \left(\omega t - \frac{2\pi}{3} \right) \end{aligned}$$

$$\begin{aligned} \text{Or, } f_r &= [f_a \cdot \cos \omega t \\ &\quad + f_b \cdot \cos \left(\omega t + \frac{2\pi}{3} \right) + f_c \cdot \cos \left(\omega t - \frac{2\pi}{3} \right)] - j [f_a \cdot \sin \omega t + f_b \cdot \sin \left(\omega t \right. \\ &\quad \left. + \frac{2\pi}{3} \right) + f_c \cdot \sin \left(\omega t - \frac{2\pi}{3} \right)] = f_d + j f_q \end{aligned}$$

In matrix form:

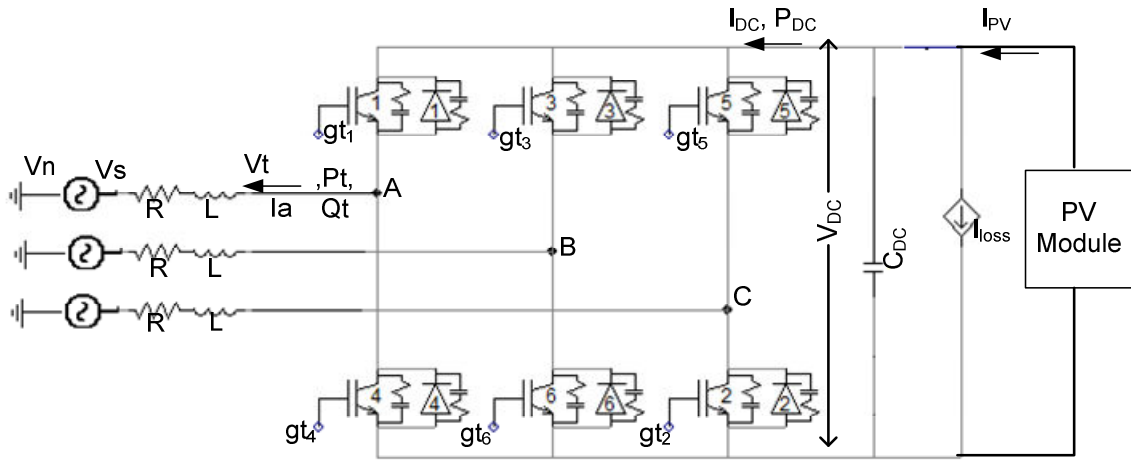
$$\begin{bmatrix} f_d \\ f_q \end{bmatrix} = \begin{bmatrix} \cos \omega t & \cos \left(\omega t + \frac{2\pi}{3} \right) & \cos \left(\omega t - \frac{2\pi}{3} \right) \\ -\sin \omega t & -\sin \left(\omega t + \frac{2\pi}{3} \right) & -\sin \left(\omega t - \frac{2\pi}{3} \right) \end{bmatrix} \cdot \begin{bmatrix} f_a \\ f_b \\ f_c \end{bmatrix}$$

For a-c-b, phase sequence, the transformation is,

$$\begin{bmatrix} f_d \\ f_q \end{bmatrix} = \begin{bmatrix} \cos \omega t & \cos \left(\omega t - \frac{2\pi}{3} \right) & \cos \left(\omega t + \frac{2\pi}{3} \right) \\ -\sin \omega t & -\sin \left(\omega t - \frac{2\pi}{3} \right) & -\sin \left(\omega t + \frac{2\pi}{3} \right) \end{bmatrix} \cdot \begin{bmatrix} f_a \\ f_b \\ f_c \end{bmatrix}$$

A.3 Mathematical expressions for the PV inverter controller

In developing the mathematical expression of the controller, first we have to determine the plant transfer function such that the circuit based components such as Plant and VSC can be represented in terms of functional block diagram for analysis purposes only. To obtain the plant transfer function in the system, given in Fig. 2.2, the PCC is considered to have shifted right after the filter parameters of L_1 and R_1 . Therefore the simplified system becomes as follows:



Here, R includes the IGBT on resistance, i.e., $R=R_1+r_{on}$ and the loss component of current in DC side is presented as I_{loss} . Therefore, the IGBT or the VSC can be considered as ideal which confirms that $P_{DC}=P_t$, $V_t=mV_{DC}/2$ and the DC side loss is $P_{loss}=V_{DC}.I_{loss}$.

The AC side dynamic equations can be written as:

$$L \frac{di_a}{dt} = -Ri_a + V_{t_a} - V_{s_a} - V_n \dots \dots \dots (i)$$

$$L \frac{di_b}{dt} = -Ri_b + V_{t_b} - V_{s_b} - V_n \dots \dots \dots (ii)$$

$$L \frac{di_c}{dt} = -Ri_c + V_{t_c} - V_{s_c} - V_n \dots \dots \dots (iii)$$

The space phasor form is expressed, by definition, $f_{abc} = f_a \cdot e^{j0} + f_b \cdot e^{j4\pi/3} + f_c \cdot e^{j2\pi/3}$ for a phase sequence of a-b-c [108].

Therefore, to express equations (i), (ii) and (iii) in space phasor form, multiply (i) with e^{j0} , (ii) with $e^{j4\pi/3}$ and (iii) with $e^{j2\pi/3}$ we get:

$$L \frac{di_a}{dt} \cdot e^{j0} = -Ri_a \cdot e^{j0} + V_{t_a} \cdot e^{j0} - V_{s_a} \cdot e^{j0} - V_n \cdot e^{j0} \dots \dots \dots (iv)$$

$$L \frac{di_b}{dt} \cdot e^{j4\pi/3} = -Ri_b \cdot e^{j4\pi/3} + V_{t_b} \cdot e^{j4\pi/3} - V_{s_b} \cdot e^{j4\pi/3} - V_n \cdot e^{j4\pi/3} \dots \dots \dots (v)$$

$$L \frac{di_c}{dt} \cdot e^{j2\pi/3} = -Ri_c \cdot e^{j2\pi/3} + V_{t_c} \cdot e^{j2\pi/3} - V_{s_c} \cdot e^{j2\pi/3} - V_n \cdot e^{j2\pi/3} \dots \dots \dots (vi)$$

Now, (iv)+(v)+(vi), we get:

$$\begin{aligned} L \frac{di_a}{dt} \cdot e^{j0} + L \frac{di_b}{dt} \cdot e^{j4\pi/3} + L \frac{di_c}{dt} \cdot e^{j2\pi/3} \\ = -Ri_a \cdot e^{j0} - Ri_b \cdot e^{j4\pi/3} - Ri_c \cdot e^{j2\pi/3} + V_{t_a} \cdot e^{j0} + V_{t_b} \cdot e^{j4\pi/3} + V_{t_c} \cdot e^{j2\pi/3} \\ - V_{s_a} \cdot e^{j0} - V_{s_b} \cdot e^{j4\pi/3} - V_{s_c} \cdot e^{j2\pi/3} - V_n \cdot e^{j0} - V_n \cdot e^{j4\pi/3} - V_n \cdot e^{j2\pi/3} \end{aligned}$$

Or,

$$\begin{aligned} L \frac{d}{dt} \left(i_a \cdot e^{j0} + i_b \cdot e^{j4\pi/3} + i_c \cdot e^{j2\pi/3} \right) \\ = -R(i_a \cdot e^{j0} + i_b \cdot e^{j4\pi/3} + i_c \cdot e^{j2\pi/3}) + (V_{t_a} \cdot e^{j0} + V_{t_b} \cdot e^{j4\pi/3} + V_{t_c} \cdot e^{j2\pi/3}) \\ - (V_{s_a} \cdot e^{j0} + V_{s_b} \cdot e^{j4\pi/3} + V_{s_c} \cdot e^{j2\pi/3}) - V_n(e^{j0} + e^{j4\pi/3} + e^{j2\pi/3}) \end{aligned}$$

Or,

$$L \frac{di_{abc}}{dt} = -Ri_{abc} + V_{t_{abc}} - V_{s_{abc}} - V_n(e^{j0} + e^{j4\pi/3} + e^{j2\pi/3}) \dots \dots \dots (vii)$$

$$\text{But, } e^{j0} + e^{j4\pi/3} + e^{j2\pi/3} = (\cos 0 + j \sin 0) + (\cos \frac{4\pi}{3} + j \sin \frac{4\pi}{3}) + (\cos \frac{2\pi}{3} + j \sin \frac{2\pi}{3})$$

$$= 1 + 0 - \frac{1}{2} - j \sin \frac{2\pi}{3} - \frac{1}{2} + j \sin \frac{2\pi}{3} = 0;$$

Therefore, the equation (vii) in space phasor form can be expressed as:

$$L \frac{di_{abc}}{dt} = -Ri_{abc} + V_{t_{abc}} - V_{s_{abc}} \dots \dots \dots (viii)$$

With the transformation of $f_{dq} = (f_d + jf_q) = f_{\alpha\beta} \cdot e^{-j\omega t} = f_{abc} \cdot e^{-j\omega t}$, in a d-q co-ordinate system [108], the equation (viii) can be written as:

$$L \frac{d(i_{dq} \cdot e^{j\omega t})}{dt} = -R(i_{dq} \cdot e^{j\omega t}) + V_{tdq} \cdot e^{j\omega t} - V_{sdq} \cdot e^{j\omega t}$$

Or,

$$L \cdot e^{j\omega t} \frac{di_{dq}}{dt} + L \cdot i_{dq} \cdot (j\omega) \cdot e^{j\omega t} = -R(i_{dq} \cdot e^{j\omega t}) + V_{tdq} \cdot e^{j\omega t} - V_{sdq} \cdot e^{j\omega t}$$

Or,

$$L \cdot \frac{di_{dq}}{dt} = -R \cdot i_{dq} - L \cdot i_{dq} \cdot j\omega + V_{tdq} - V_{sdq}$$

Or,

$$L \frac{d(i_d + ji_q)}{dt} = -R(i_d + ji_q) - jL\omega(i_d + ji_q) + (V_{td} + jV_{tq}) - (V_{sd} + jV_{sq})$$

Or,

$$L \frac{di_d}{dt} + jL \frac{di_q}{dt} = (-Ri_d + L\omega i_q + V_{td} - V_{sd}) + j(-Ri_q - L\omega i_d + V_{tq} - V_{sq}) \dots \dots \dots (a)$$

Equating real and imaginary parts, we get:

$$L \frac{di_d}{dt} = -Ri_d + L\omega i_q + V_{td} - V_{sd} \dots \dots \dots (b)$$

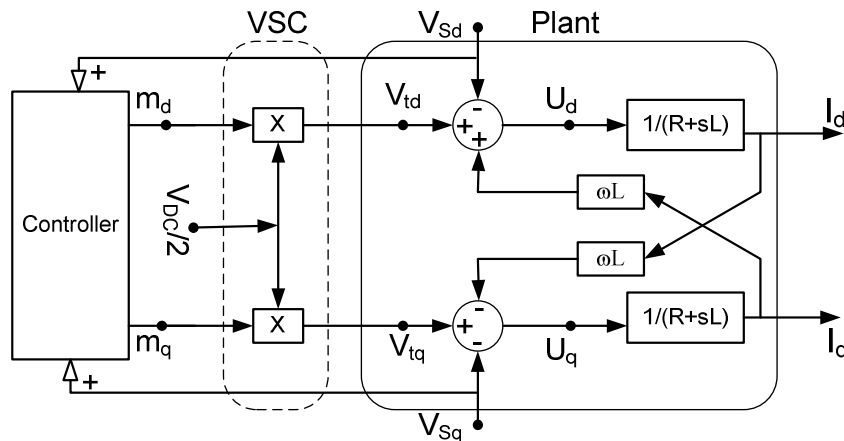
$$L \frac{di_q}{dt} = -Ri_q - L\omega i_d + V_{tq} - V_{sq} \dots \dots \dots (c)$$

In Laplace domain the expressions becomes as follows:

$$LsI_d = -RI_d + L\omega I_q + V_{td} - V_{sd} \dots \dots \dots (d)$$

$$LsI_q = -RI_q - L\omega I_d + V_{tq} - V_{sq} \dots \dots \dots (e)$$

Therefore, the plant can be expressed as shown in following figure:



Here, the plant input is V_{td} and V_{tq} , and the plant output is I_d, I_q by considering V_{sd}, V_{sq} as the disturbance inputs. The coupling factor, $L\omega$ couples the quantity of I_d and I_q . The disturbance input and the coupling factor can be eliminated by compensating through the controller where it acts as a disturbance input with opposite sign to the controller [108]. Therefore, the core plant transfer function becomes as follows:

$$G_p = \frac{I_d}{U_d} = \frac{I_q}{U_q} = \frac{1}{R + sL} \dots\dots\dots (f)$$

$$\text{Where, } U_d = V_{td} - V_{sd} + L\omega I_q \dots\dots\dots (g)$$

$$\text{and, } U_q = V_{tq} - V_{sq} - L\omega I_d \dots\dots\dots (h)$$

The VSC only performs the transformation as expressed [108]:

$$V_{td} = m_d \cdot \frac{V_{DC}}{2}, \text{ and } V_{tq} = m_q \cdot \frac{V_{DC}}{2} \dots\dots\dots (j)$$

It is obvious that the output of the controller is m_d and m_q .

In order to develop the controller part, if we go backward from the modulating signals by adding a suffix on all of the quantities in terms of controller ‘c’, it can be established from (g), (h) and (j), that the output modulating signals from the controller, m_d and m_q , can be expressed as follows:

$$m_d = \frac{V_{td}^c}{V_{dc}/2}, \quad \text{and,} \quad m_q = \frac{V_{tq}^c}{V_{dc}/2} \dots\dots\dots (k)$$

$$V_{td}^c = U_d^c + V_{sd}^c - L\omega I_q \dots\dots\dots (l)$$

$$V_{tq}^c = U_q^c + V_{sq}^c + L\omega I_d \dots\dots\dots (m)$$

As the feedback signal is taken from the system, then:

$$V_{sd}^c = V_{sd}; \quad V_{sq}^c = V_{sq};$$

Moreover, the feedback signal is not a clean sinusoidal signal which requires a feed forward filter, G_{ff} [108].

It is noted that the compensator output of the controller U_d^c and U_q^c should be such that it can control the output of the plant. Therefore, a feedback compensator is chosen to

monitor and compare the output with the reference signal and generates the desired compensator outputs which can be expressed as follows:

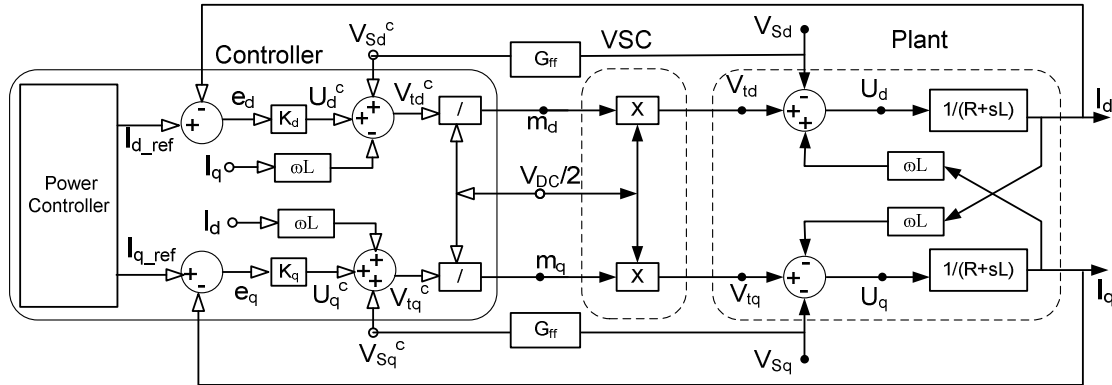
$$U_d^c = (I_{d_ref} - I_d) \cdot K_d \dots\dots\dots (n)$$

$$\text{and, } U_q^c = (I_{q_ref} - I_q) \cdot K_q \dots\dots\dots (p)$$

Where, compensator gain K_d and K_q could be a proportional integral gain as follows:

$$K_d = k_{pd} + \frac{k_{id}}{s}, \quad \text{and, } K_q = k_{pq} + \frac{k_{iq}}{s} \dots\dots\dots (q)$$

However, using expressions, (k) to (q), the controller model can be represented by the following figure:



Note that the VSC and Plant represent the inverter circuit and the power system, respectively. While implementing the controller output m_d and m_q , it must be converted into ABC frame to obtain the three phase modulating signals, which is eventually compared with high frequency carrier signal and generates the gating signals. On the other hand, the monitoring signal I_d , I_q as well as the feedback signal V_{sd} and V_{sq} from the power system are the converted into three phase current signals from the ABC frame. During this conversion processes, a phased locked loop (PLL) oscillator is used to synchronize the input and output signals.

In the expressions (b) and (c), $V_{sd}=V_d \cos(\omega+\theta_0)$ and $V_{sq}=V_q \sin(\omega t+\theta_0)$. If the PLL output is $\theta = \omega t+\theta_0$, at steady state synchronization, then $V_{sd}=V_d$ and $V_{sq}=0$ which means that the voltage vector is aligned with the direct axis component V_{sd} . This eliminates the need for feedback signal V_{sq} . Use of built in PLL in EMTDC/PSCAD, an offset angle of 1.57 rad gives the $\theta = \omega t+\theta_0$ such that $V_{sq}=0$.

However, in a d-q co-ordinate system, the three phase real and reactive power expression can be found as follows [108]:

$$P(t) = \frac{3}{2} [V_{sd}(t) \cdot i_d + V_{sq}(t) \cdot i_q] \dots\dots\dots (r)$$

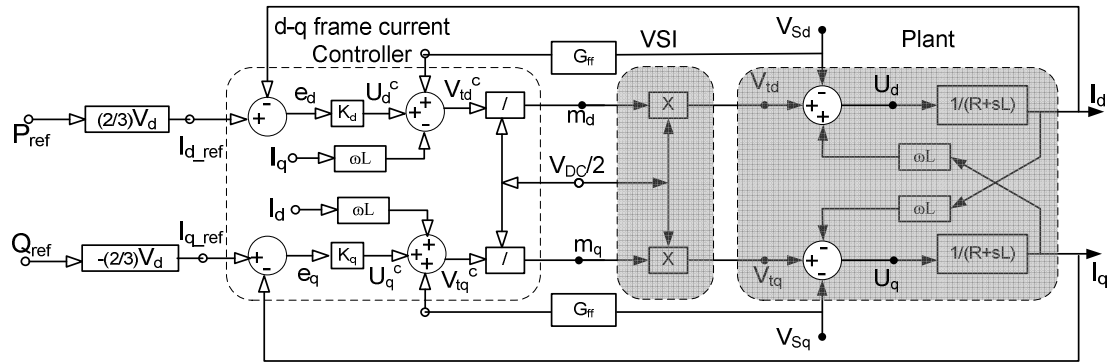
$$Q(t) = \frac{3}{2} [-V_{sd}(t) \cdot i_q + V_{sq}(t) \cdot i_d] \dots\dots\dots (s)$$

At steady state synchronization, when the PLL is setting the voltage vector aligned with the direct axis component, both the real and reactive power can easily be decoupled and the expressions can be simplified as presented in Laplace domain:

$$Pt = \frac{3}{2} V_d \cdot I_d \dots\dots\dots (t)$$

$$Qt = -\frac{3}{2} V_d \cdot I_q \dots\dots\dots (u)$$

Therefore, while implementing with the controller, in the expression (t) and (u), for a reference value of power P_{ref} and Q_{ref} , the I_d becomes I_{dref} and I_q becomes I_{qref} . Hence, the modified controller which controls power only can be represented by the following figure:



In a grid connected PV system, the real power is not controlled directly with the inverter controller as the power generation is governed by the solar radiation and ambient temperature. Moreover, on the DC side of the inverter, the DC link capacitor maintains the constant DC voltage to get the maximum power output from the PV and needs compensation to overcome the loss. Therefore, the DC link voltage of a PV solar farm inverter needs to be controlled such that the inverter can inject the balance of generated

PV power to the grid and can maintain a constant DC link voltage. Usually, the DC link voltage is controlled either by using the DC-DC converter or a converter-less controller. This thesis is dealing with the converter-less DC controller. However, using a converter-less technique, once the DC link voltage is controlled, the power output of the inverter will be governed automatically by injecting the balance of generated PV solar farm power to the inverter output. Hence, the DC link voltage controller replaces the active power control loop. To develop the DC link voltage controller, the dynamics of the DC side at the PV inverter can be expressed as follows by incorporating the losses [106]:

$$C_{DC} \frac{\partial V_{DC}}{\partial t} = i_{PV} - i_{loss} - i_{DC} \dots \dots \dots (v)$$

In Laplace form by expressing in d-q co-ordinate [108], [106]:

$$sV_{DC}C_{DC} = I_{PV} - I_{loss} - I_{DC} = -\frac{3}{4}(m_d I_d + m_q I_q) \dots \dots \dots (w)$$

In this expression, in the steady state, the DC voltage is only compensated through real power component or the direct axis component. Hence the expression in (w) can be rewritten as given in (x):

$$sV_{DC}C_{DC} = -\frac{3}{4}(m_d I_d) \dots \dots \dots (x)$$

Equation (x) yields that the compensator for the DC link voltage controller can also be modeled as proportional integral controller as follows [106]:

$$I_{d_ref} = -\frac{4sC_{DC}}{3m_d} V_{dc_ref} = -K_{DC}(V_{DC} - V_{DC_ref}) \dots \dots \dots (y)$$

Where, the DC compensator gain, K_{DC} , can be modeled as a proportional integral controller.

Hence,
$$K_{DC} = k_{pDC} + \frac{k_{iDC}}{s} \dots \dots \dots (z)$$

Therefore, the controller is implemented in the direct axis current control loops as follows:

selected in a systematic hit and trial manner with an objective to obtain a minimum settling time, a quick rise time, and a peak overshoot less than 10% in V_{DC} . It is noted, that the VDC also depends upon PI-2 controller parameters and as such, a fine tuning is also required, while tuning PI-3.

A.5 Base value and the parameter calculation for inverter controller [108]

At the HT side of the transformer:

$$V_{base} = V_{ph_{peak}} = 0.4kV \times \frac{\sqrt{2}}{\sqrt{3}} = 0.3266kV; P_{base} = 100kW$$

$$I_{base} = \frac{2}{3} \times \frac{P_{base}}{V_{base}} = 0.204kA$$

At the LT side of the transformer:

$$V_{baseLT} = V_{ph_{peakLT}} = 0.23kV \times \frac{\sqrt{2}}{\sqrt{3}} = 0.188kV; P_{base} = 100kW$$

$$I_{baseLT} = \frac{2}{3} \times \frac{P_{base}}{V_{baseLT}} = 0.3546kA$$

$$Z_{baseLT} = \frac{V_{baseLT}}{I_{baseLT}} = \frac{0.188}{0.3546} = 0.53\Omega, \quad \text{and,}$$

$$\omega_{base} = \omega_n = 2\pi f = 314 \text{ rad/sec for } f = 50\text{Hz.}$$

$$\text{Hence, } L_{baseLT} = \frac{Z_{baseLT}}{\omega_{base}} = 1.687 \text{ mH.}$$

The leakage reactance of the 0.1 MVA, 0.23/0.4kV, 3-phase transformer is 1.8%.

Hence, to find out the leakage inductance, the following calculation is done:

$$I_{fl} = \frac{0.1MVA}{\sqrt{3} \times 0.4kV} = 0.144kA, \quad \text{and, } V_m = 0.4kV \times 0.018 = 7.2 \text{ Volts}$$

$$\text{Hence, } Z_T = \frac{7.2V}{144A} = 0.05 \Omega \text{ at } 0.4kV \text{ side of the transformer.}$$

$$\text{Or, } Z_T = 0.05 \frac{0.1MVA}{(0.4kV)^2} = 0.03125 \text{ pu with the transformer base value.}$$

Alternately, this can be determined simply by $\%Z \times \sqrt{3} = 0.018 \times \sqrt{3} = 0.0312 \text{ pu}$

when the %Z is given for a single three phase transformer.

Note that if this transformer would be comprised of three single phase transformer and the %Z is given for each transformer, then the leakage reactance in pu of the three phase transformer would be equal to the %Z i.e., $Z(pu) = \%Z$.

However, the transformer leakage reactance can be found based on inverter base value:

$$Z_T = 0.0312 \times 0.53 = 0.016536 \Omega, \text{ therefore, } L_T = 52.636 \mu H = L_2$$

$$\text{Then, } L = L_1 + L_2 = 500 + 52.636 = 552.636 \mu H = 0.3276 pu.$$

$$\omega = \frac{\omega_n}{\omega_{base}} = 1pu, \quad \text{hence,} \quad \omega L = 0.3276 pu.$$

The base value of the DC side is based on the base value at LT side of the transformer as the LT side is the inverter output side.

$$\text{Hence, } V_{dcbase} = 2 \times V_{baseLT} = 2 \times 0.188kV = 0.376kV., \text{ as,} \quad V_{ph} = m \frac{V_{dc}}{2}$$

The k_p and $T_i=1/k_i$ of PI controllers, are found by hit and trial method as follows:

PI-1: $k_p=1$, $T_i=0.05$; PI-2: $k_p=1$, $T_i=0.0015$; PI-3: $k_p=1$, $T_i=0.2$

The source inductance is $30\mu H$.

The LPF filter parameters for the d-q components are $G=1.0433$ and $\tau=0.1$ seconds.

A.6 PV module parameters: (all are at STC)

Table: Polycrystalline PV Module parameters from LDK-230P-235P-20 datasheet.

(www.ldksolar.com)

Item Description	Symbols	230P-20	235P-20
Nominal Power ($\pm 5\%$)	P_{MPP} (W)	230	235
Voltage at P_{MPP}	V_{ms} (V)	29.9	30.0
Current at P_{MPP}	I_{ms} (A)	7.68	7.84
Open Circuit Voltage	V_{OC} (Volt)	36.8	36.8
Short circuit current	I_{SC} (Amp)	8.34	8.35
Temperature co-efficient of P_{MPP}	K_p ($\%/^{\circ}C$)	-0.47	
Temperature Co-efficient of V_{OC} High temp > 25 $^{\circ}C$	K_v ($\%/^{\circ}C$)	-0.34	
Temperature Co-efficient of V_{OC} Low temp (-40 $^{\circ}C$ to + 25 $^{\circ}C$)	K_v ($\%/^{\circ}C$)	-	
Temperature Co-efficient of I_{SC}	K_i ($\%/^{\circ}C$)	0.06	
Cell Type	Polycrystalline silicon cell 6X10.		

Table: Mono-crystalline PV Module parameters from HELIENE 72^M datasheet.

(www.heliene.ca)

Item Description	Symbols	310Wp	305Wp
Nominal Power ($\pm 5\%$)	P_{MPP} (W)	310	305
Voltage at P_{MPP}	V_{ms} (V)	36.77	36.65
Current at P_{MPP}	I_{ms} (A)	8.43	8.32
Open Circuit Voltage	V_{OC} (Volt)	45.4	45.1
Short circuit current	I_{SC} (Amp)	8.9	8.86
Temperature co-efficient of P_{MPP}	K_p (%/°C)	-0.44	
Temperature Co-efficient of V_{OC} High temp > 25°C	K_v (%/°C)	-0.34	
Temperature Co-efficient of V_{OC} Low temp (-40°C to + 25°C)	K_v (%/°C)	-	
Temperature Co-efficient of I_{SC}	K_i (%/°C)	0.07	
Cell Type	Mono-crystalline silicon cell 72.		

Appendix B: 7.5 MW PV solar system model parameters, fault detector parameters and calculation

B.1 PV module parameters:

Item Description	Symbols	Datasheet value
Nominal Power ($\pm 5\%$)	P_{MPP} (W)	72.6
Voltage at P_{MPP}	V_{ms} (V)	67.9
Current at P_{MPP}	I_{ms} (A)	1.07
Open Circuit Voltage	V_{OC} (Volt)	90.0
Short circuit current	I_{SC} (Amp)	1.19
Temperature co-efficient of P_{MPP}	K_p (%/°C)	-0.25
Temperature Co-efficient of V_{OC} High temp > 25°C	K_v (%/°C)	-0.25
Temperature Co-efficient of V_{OC} Low temp (-40°C to + 25°C)	K_v (%/°C)	-0.2
Temperature Co-efficient of I_{SC}	K_i (%/°C)	0.045
Cell Type	CdS/CdTe with 116 active cells.	

* At STC, AM=1.5, T=25°C and G=1000 watt/m² and all ratings $\pm 10\%$, unless specified otherwise.

No. of series modules= 8 and no. of parallel modules= 12905.

The rating of the coupling transformer of the PV solar farm is 27.6/0.23 kV, 7.5 MVA with a nominal percentage of positive sequence leakage reactance of 5.7%.

The distribution network is all overhead and is constructed with ACSR 336.4 kcmil conductors. The positive sequence resistance is 0.0682E-3 ohm/m, positive sequence inductive reactance 0.3636E-3 ohm/m, positive sequence capacitive reactance 251.395 Mohm*m, zero sequence resistance 0.1643E-3 ohm/m, zero sequence inductive reactance 1.1062E-3 ohm/m and zero sequence capacitive reactance 559.252 Mohm*m [163].

B.2 Base value and the parameter calculation [108]

At HT side of the transformer:

$$V_{base} = V_{ph_{peak}} = 27.6kV \times \frac{\sqrt{2}}{\sqrt{3}} = 22.5353kV; P_{base} = 7.5MW$$

$$I_{base} = \frac{2}{3} \times \frac{P_{base}}{V_{base}} = 0.222kA$$

At LT side of the transformer:

$$V_{baseLT} = V_{ph_{peakLT}} = 0.23kV \times \frac{\sqrt{2}}{\sqrt{3}} = 0.1878kV; P_{base} = 7.5MW$$

$$I_{baseLT} = \frac{2}{3} \times \frac{P_{base}}{V_{baseLT}} = 26.624kA$$

$$Z_{baseLT} = \frac{V_{baseLT}}{I_{baseLT}} = \frac{0.1878}{26.624} = 7.054 m\Omega, \quad \text{and,}$$

$$\omega_{base} = \omega_n = 2 \cdot \pi \cdot f = 377 \text{ rad/sec for } f = 60\text{Hz.}$$

$$\text{Hence, } L_{baseLT} = \frac{Z_{baseLT}}{\omega_{base}} = 18.71 \mu H.$$

The leakage reactance of the 7.5 MVA, 0.23/27.6 kV, 3-phase transformer is 5.7%.

$$\text{Hence, } Z_T = \%Z \times \sqrt{3} = 0.057 \times \sqrt{3} = 0.1 pu$$

when the %Z is given for a single three phase transformer.

However, the transformer leakage reactance can be found based on inverter base value,

$$Z_T = 0.1 \times 7.054 m\Omega = 0.7054m\Omega, \text{ therefore, } L_T = 1.87 \mu H = L_2$$

$$\text{Then, } L = L_1 + L_2 = 8\mu H + 1.87\mu H = 9.87 \mu H = 0.5276 pu.$$

$$\omega = \frac{\omega_n}{\omega_{base}} = 1pu, \quad \text{hence, } \omega L = 0.5276 pu.$$

The base value of the DC side is based on the base value at LT side of the transformer as the LT side is the inverter output side.

$$\text{Hence, } V_{dcbase} = 2 \times V_{baseLT} = 2 \times 0.188kV = 0.3756kV., \text{ as, } V_{ph} = m \frac{V_{dc}}{2}$$

The k_p and $T_i=1/k_i$ of PI controllers, are found by hit and trial method as follows:

$$\text{PI-1: } k_p=1, T_i=0.01; \text{ PI-2: } k_p=2, T_i=0.0015; \text{ PI-3: } k_p=10, T_i=0.015$$

The LPF filter parameters for the d-q components are $G=1.0433$ and $\tau=0.1$ seconds.

The filter parameter for I_{o_a} , I_{o_b} and I_{o_c} feedback current is $G=1.5$ and $\tau=0.003$ seconds.

The threshold value for the rate limiter is 10038[1/s], and the R-S flip-flop delay time is 0.1[μs].

B.3 Parameter calculation for the fault detector

For a 7.5 MW PV solar farm connected with the LT side of the coupling transformer having a voltage level of 230 volts, the peak magnitude of the current is calculated as follows:

$$\hat{I} = \frac{\sqrt{2}}{\sqrt{3}} \cdot \frac{P_{3\phi}}{V_{L-L}} = 26.625 \text{ kA}$$

By considering a peak margin of 1.06pu, the value of the rated peak current is considered as 28.2kA. Hence,

$$\left| \frac{di}{dt} \right| \approx \omega I_{m_{rated}} = 10038 \text{ amps per sec.}$$

Appendix C: Induction motor parameters and calculation

C.1 Induction motor parameters [183]

Table : Double-Cage Model Parameters of American Motors**

Item Description	Symbols	Value
Stator resistance	r_s	0.0071
First cage rotor resistance	r_1	0.0140
Second cage rotor resistance	r_2	0.1025
Unsaturated magnetizing reactance	x_m	3.5189
Unsaturated stator reactance	x_s	0.0956
Unsaturated second cage reactance	x_2	0.0956
Unsaturated first cage reactance	x_1	0.0970
Inertia constant	H	0.47sec

**All units are in P.U unless specified otherwise.

The induction motor is rated at 460 volts, 60Hz, 3 phase, 4 pole, 400 HP.

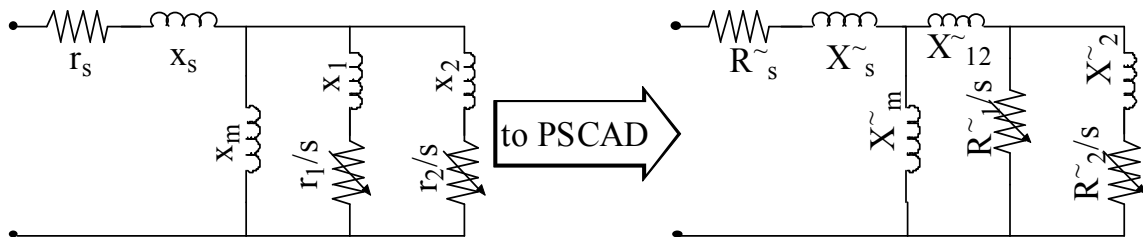
The step down transformer with the induction motor load is rated for 27.6/0.46 kV, 0.5 MVA with a nominal percentage of positive sequence leakage reactance of 5.7%.

The 25 km long network is comprised of ACSR336.4 kcmil overhead lines. The positive sequence R, XL, Xc values are 0.0682E-3 [ohm/m], 0.3636E-3 [ohm/m] and 251.395 [Mohm*m], respectively, whereas the zero sequence R, XL, and Xc are 0.1643E-3 [ohm/m], 1.1062E-3 [ohm/m] and 559.252 [Mohm*m] respectively.

C.2 Conversion formula of induction motor parameters for EMTDC/PSCAD input [184]:

$$L_{12} = \frac{A}{D}; R_1^{\sim} = \frac{B - L_{12}^{\sim}}{D}; R_2^{\sim} = \frac{CR_1^{\sim}}{R_1^{\sim} - C}; R_s^{\sim} = r_s; X_s^{\sim} = X_2^{\sim} = x_s = x_2; X_m^{\sim} = x_m$$

$$\text{where, } A = \frac{L_1 \cdot L_2}{r_1 + r_2}; B = \frac{L_1 \cdot r_2 + L_2 \cdot r_1}{r_1 + r_2}; C = \frac{r_1 \cdot r_2}{r_1 + r_2}; D = \frac{L_1 + L_2}{r_1 + r_2};$$



$$\text{Hence, } X_{12}^{\sim} = 0.048 \text{ pu}; R_1^{\sim} = 0.0295 \text{ pu}; R_2^{\sim} = 0.021 \text{ pu}; R_s^{\sim} = 0.0071 \text{ pu};$$

$$X_s^{\sim} = X_2^{\sim} = 0.0956 \text{ pu}; X_m^{\sim} = 3.5189 \text{ pu} \text{ Mechanical damping} = 0$$

$$\text{and } J = 0.9 \text{ MWS/MVA}$$

Appendix D: SMIB system parameters and 100 MW solar farm parameter calculation.

D.1 SMIB system [95]

Machine parameter (on its own base): $S_n = 1110$ MVA; $V_n = 22$ kV; $f = 60$ Hz; $pf = 0.9$; $R_a = 0.0036$ pu; $x_l = 0.21$ pu; $R_0 = 0$; $x_0 = 0.195$ pu; $T'd_0 = 6.66$ s; $T'q_0 = 0.44$ s; $T''d_0 = 0.032$ s; $T''q_0 = 0.057$ s; $x_d = 1.933$ pu; $x_q = 1.743$ pu; $x'd = 0.467$ pu; $x'q = 1.144$ pu; $x'd' = 0.312$ pu; $x'q' = 0.312$ pu; $H = 3.22$ s; $D = 0$

Transmission line parameter: Resistance (R) = 0.055 Ω / phase/ mi, Reactance (X_L) = 0.62 Ω / phase/ mi, Susceptance (B_C) = 7.11×10^{-6} S / phase/ mi

D.2 100 MW solar farm calculations.

At the HT side of the transformer:

$$V_{base} = V_{ph_{peak}} = 400kV \times \frac{\sqrt{2}}{\sqrt{3}} = 326.6kV; P_{base} = 100MW$$

$$I_{base} = \frac{2}{3} \times \frac{P_{base}}{V_{base}} = 0.204kA$$

At the LT side of the transformer:

$$V_{baseLT} = V_{ph_{peakLT}} = 0.208kV \times \frac{\sqrt{2}}{\sqrt{3}} = 0.17kV; P_{base} = 100MW$$

$$I_{baseLT} = \frac{2}{3} \times \frac{P_{base}}{V_{baseLT}} = 392.157kA$$

$$Z_{baseLT} = \frac{V_{baseLT}}{I_{baseLT}} = \frac{0.17}{392.157} = 0.4335\Omega, \quad \text{and,}$$

$$\omega_{base} = \omega_n = 2 \cdot \pi \cdot f = 377 \text{ rad/sec for } f = 60\text{Hz.}$$

$$\text{Hence, } L_{baseLT} = \frac{Z_{baseLT}}{\omega_{base}} = 1.1499 \times 10^{-6} \text{ H.}$$

The leakage reactance of the 100 MVA, 0.208/400 kV, 3-phase transformer is 5%.

Hence, $\%Z \times \sqrt{3} = 0.05 \times \sqrt{3} = 0.0866$ pu = 0.03754 m Ω or, $L_T = 0.0995$ μH

Then, $L = L_1 + L_T = (500 + 99.5) \times 10^{-9} = 0.5995$ $\mu\text{H} = 0.5217$ pu.

$$\omega = \frac{\omega_n}{\omega_{base}} = 1pu, \quad \text{hence,} \quad \omega L = 0.5217 pu.$$

The base value of the DC side is based on the base value at LT side of the transformer as the LT side is the inverter output side.

$$\text{Hence, } V_{dcbase} = 2 \times V_{baseLT} = 2 \times 0.17kV = 0.34kV. \quad f_{sw} = 5 kHz$$

The k_p and $T_i=1/k_i$ of PI controllers, are found by hit and trial method as follows:

Parameters	Solar Farm/Wind Farm			
	PI-1	PI-2	PI-3	PI-4
K_p	1	1	2	10
T_i	0.0015	0.1	0.2	0.0015

The damping parameter can be found as follows:

DGs	Damping Controller Parameters			
	Tw	G	T1	T2
Solar farm*(study system-1)	0.1	1.2	1	0.37
Solar farm (study sytem-2)	0.1	1.25	1	0.37

*For the wind farm model in Study Sytem 2, the same damping parameters are used.

D.3 Hit and trial procedure for tuning PIs and Auxiliary controller parameters

PI controller tuning: PI-1, PI-2 and PI-3 controller parameter tuning procedure is given in Appendix-A. However, the PI controller, PI-4, is used in the voltage control operation of the PV-STATCOM. A step input is given in the V_{PCC_ref} input signal and the voltage at the PCC is observed. The Proportional and Integral gains are tuned in a systematic hit and trial manner with the objective to obtain a minimum settling time, a quick rise time, and a peak overshoot lof ess than 10% in the PCC bus voltage. It is noted that a fine tuning is required in PI-1, while tuning PI-4 as the PCC voltage response is also dependent upon PI-1.

Auxiliary controller tuning: at first the generator operating power level is selected for performing the damping control design studies. This power level is considered equal to the transient stability limit of the system with the solar farm being disconnected at night. At this operating power level, if a three phase fault occurs at Bus 1, the generator power

oscillations decay with a damping ratio of 5%. The solar farm is now connected and operated in the PV-STATCOM mode. The parameters of the damping controller FD are selected as follows. The washout time constant, T_w , is chosen to allow the electromechanical oscillations in the range of 2 Hz to pass through. The gain G , and time constants T_1 and T_2 are sequentially tuned to get the fastest settling time of oscillation at that particular generation level of transient stability limit following the fault through repetitive simulation. Thus, the best combinations of the parameters are obtained with systematic hit and trial. Once the parameters for the damping controller are chosen for this generator operating power level, the output of the synchronous generator is now increased in a stepwise manner and fault studies are accomplished for the rest of the cases by using same damping controller parameters to determine the improvement of transient stability limit with the damping controller during both night and day.

D.4 Calculation of damping ratio

The damping ratio can be expressed as the rate of decay of the amplitude of oscillation [174], [190]. Hence, for an oscillatory mode having an eigenvalue of $(\sigma + j\omega)$, the damping ratio is $\xi = \frac{-\sigma}{\sqrt{\sigma^2 + \omega^2}}$, where, $\sigma = 1/\tau$. The time constant τ is defined as the time taken to decay the oscillation to 37% from the first peak immediately after the disturbances, i.e., decay, $D = 1/e^{\sigma t}$, at $t = \tau$, $D = 1/e^1 = 0.37$. Hence, for an oscillation frequency of 0.95Hz, with a damping ratio of 5%, as considered in this study, the value of $\sigma=0.2988$, or, the time constant is =3.178 seconds. Therefore, for an observation of a 10 second time frame immediately after the disturbances [174], for an acceptable damping ratio of 5%, [190] the decay, $D = 1/e^{\sigma t}$, at $t = 10 \text{ sec}$, $D = 1/e^{2.988} = 0.05$, or 5%.

Appendix E: Substation data, SCADA, CYME modeling and GIS snapshots for the feeder networks

E.1 Substation data (Source: BWP Personnel)

E.1.1 Short Circuit Data at substation relay of the feeder

Substation Name	Bus Name	Three Phase Fault MVA	Single Phase Fault MVA	Three Phase X/R ratio	Single Phase X/R ratio
St. Andrews	Q Bus	600.0	159	27.44	26.18

E.1.2. Substation data in detail at St. Andrews

Zero and Positive Sequences Impedances* for Short Circuit Calculations:

(Base MVA=100 and Base kV=220)

Source Circuit	Positive Sequence (PU)		Zero Sequence (PU)		Three Phase X/R ratio
	R ⁺	X ⁺	R ⁰	X ⁰	
St. Andrew N6 115kV	0.00390	0.03736	0.00958	0.04418	9.579
St. Andrew N7 115kV	0.00393	0.03750	0.00910	0.04477	9.542

*Report: Hydro One Networks Inc. June30, 2006

The above parameters are converted at 115 kV, 100 MVA system base. The pu conversion with respect to new voltage base (115 kV) is accomplished with the following formula:

$$Z_{pu_new} = Z_{pu_old} \times \frac{V_{kv_old}^2}{MVA_{old}} \times \frac{MVA_{new}}{V_{kv_new}^2}$$

And the new base is defined as:

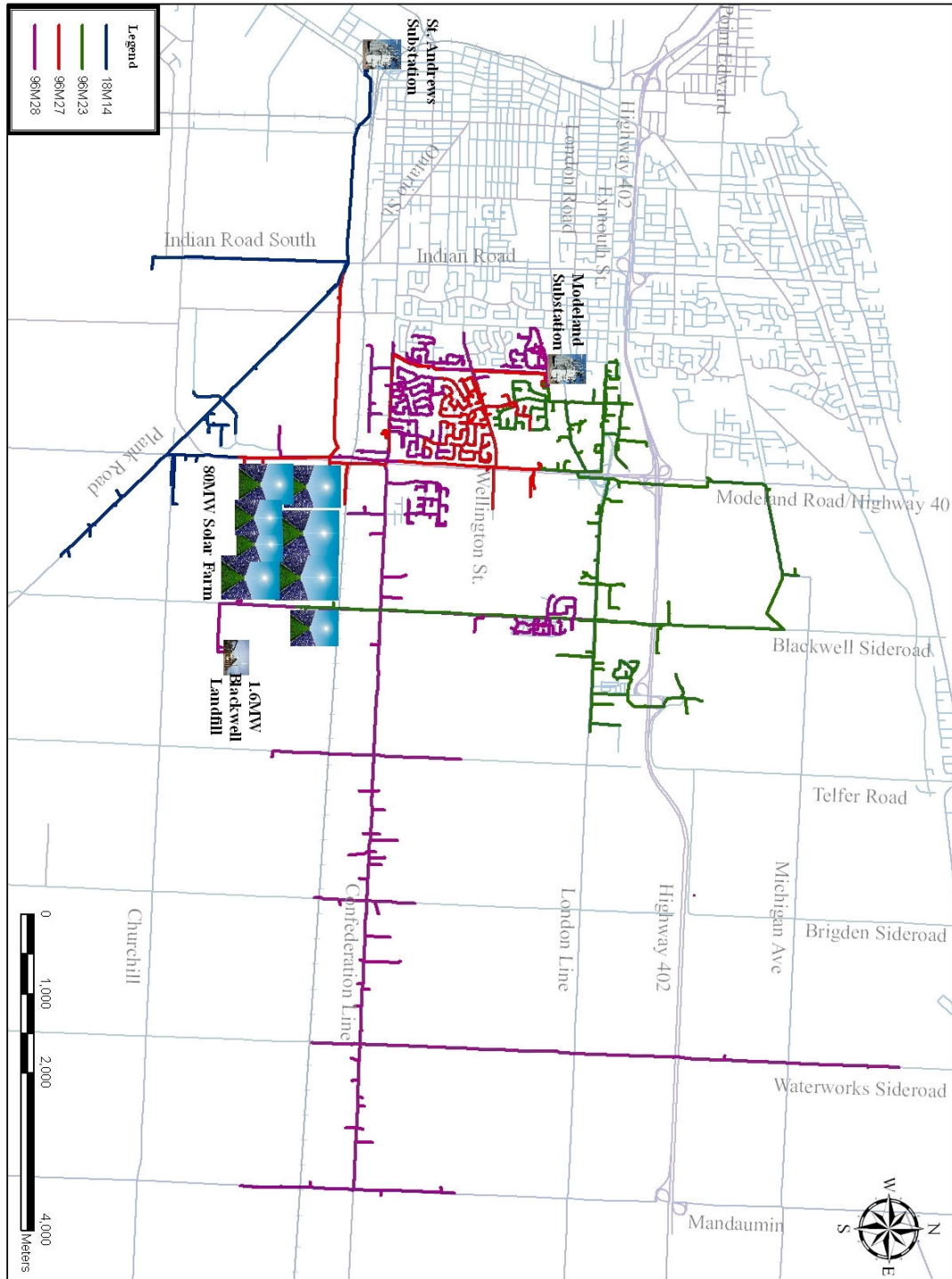
$$Z_{base_new} = \frac{V_{kv_new}^2}{MVA_{new}}$$

The Reactors at each transformer have a zero sequence impedance of 4.74 ohms per phase and 4.78 ohms per phase.

The substation transformer impedances of 12.4% (ONS)/16.5% (ONP)/20.7% (OFP) for the ratings 50/66.6/83.3 MVA respectively at 110/28.4 kV is calculated as 0.43 pu, based on 100 MVA base value at given operating voltage.

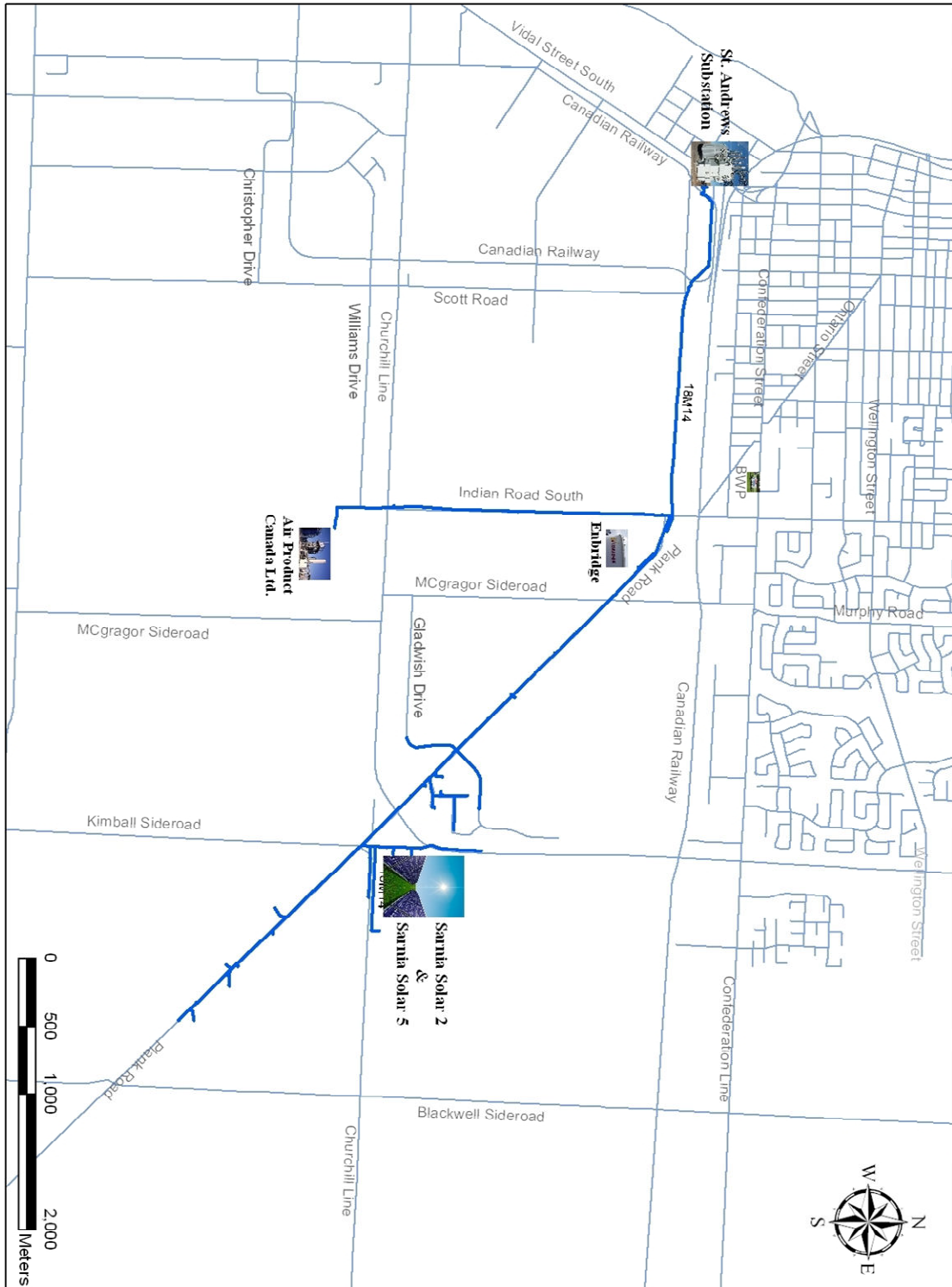
E.2 GIS map for 80MW solar farm location and the feeders.

E.2.1. Four feeders at a glance



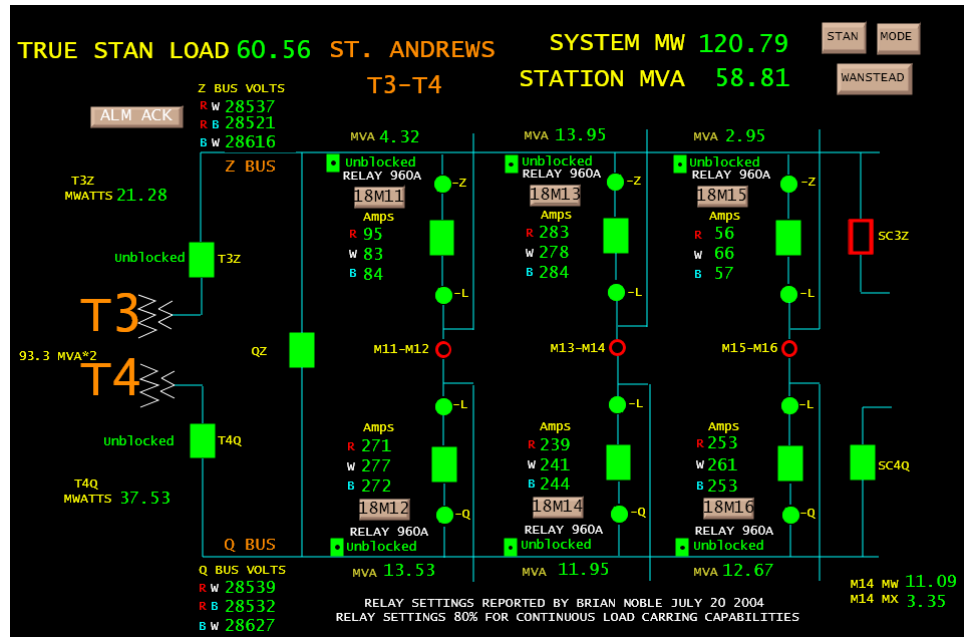
Four Feeders and Generation Stations at a Glance

E. 2. 2. Feeder 18M14



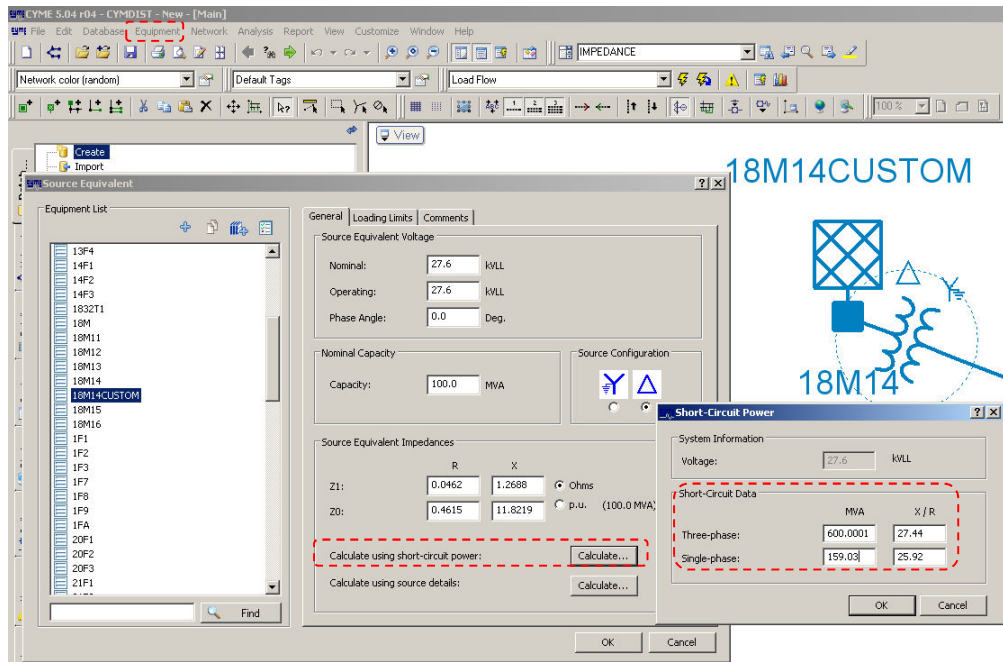
Feeder 18M14

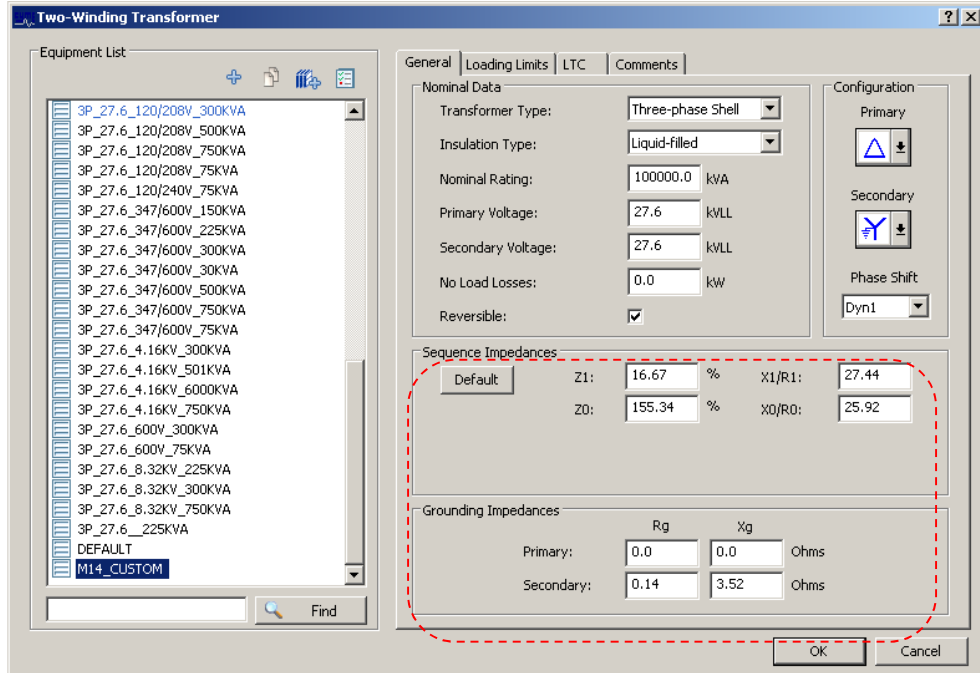
E.3 SCADA snapshot for St. Andrews Substation (Courtesy: BWP SCADA)



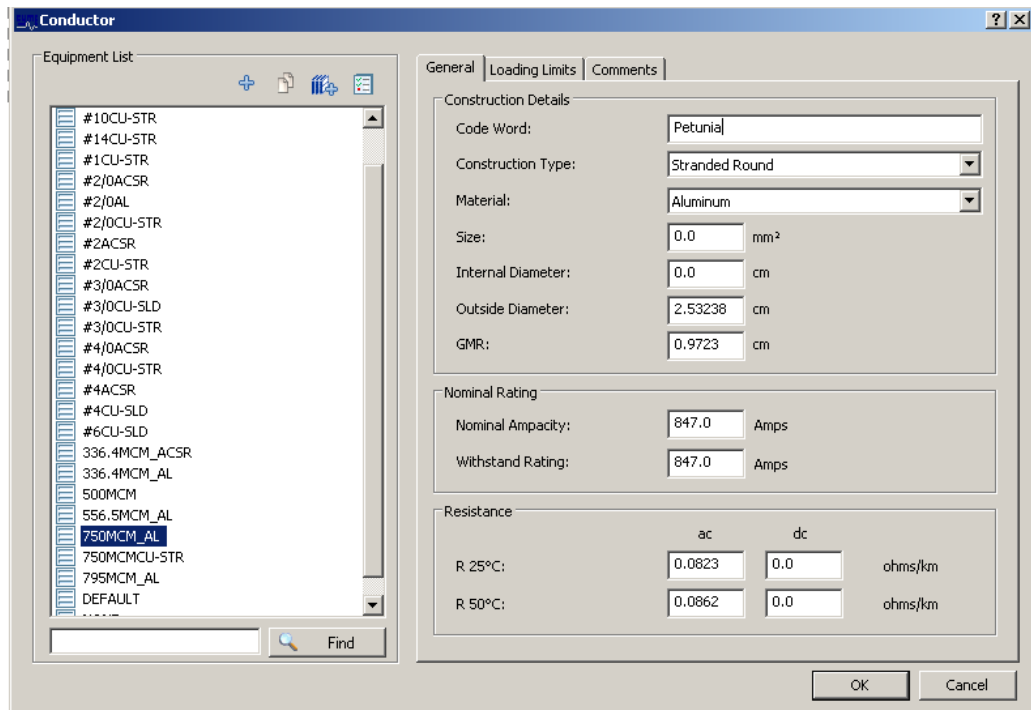
E.4 CYME snapshots for modeling

E.4.1 Substation Modeling and calculation of source impedance from short circuit data and X/R ratio.

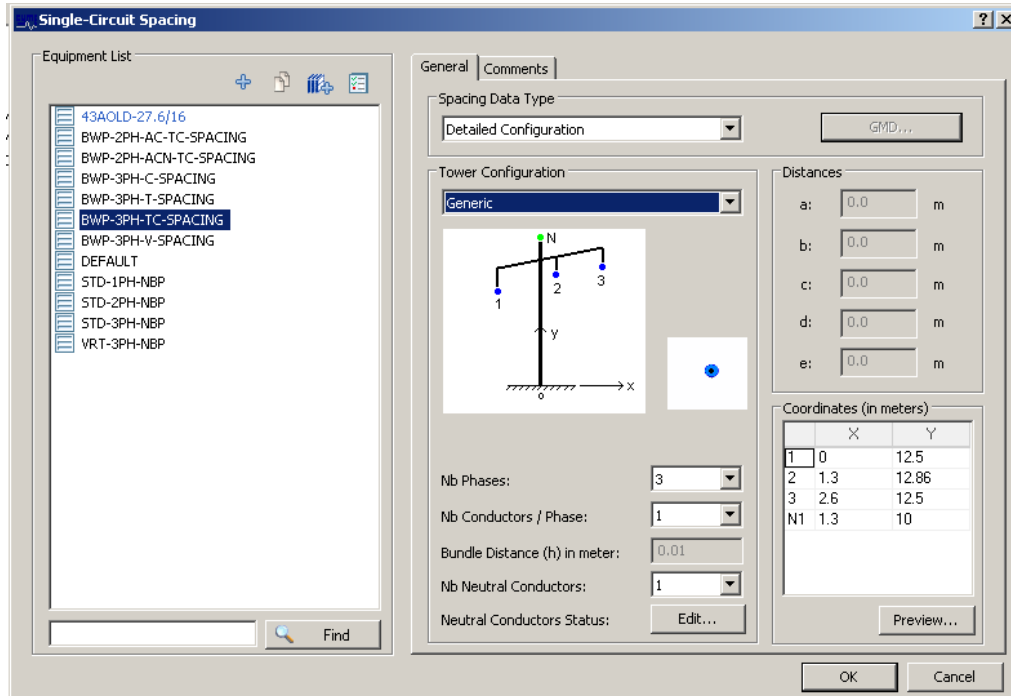




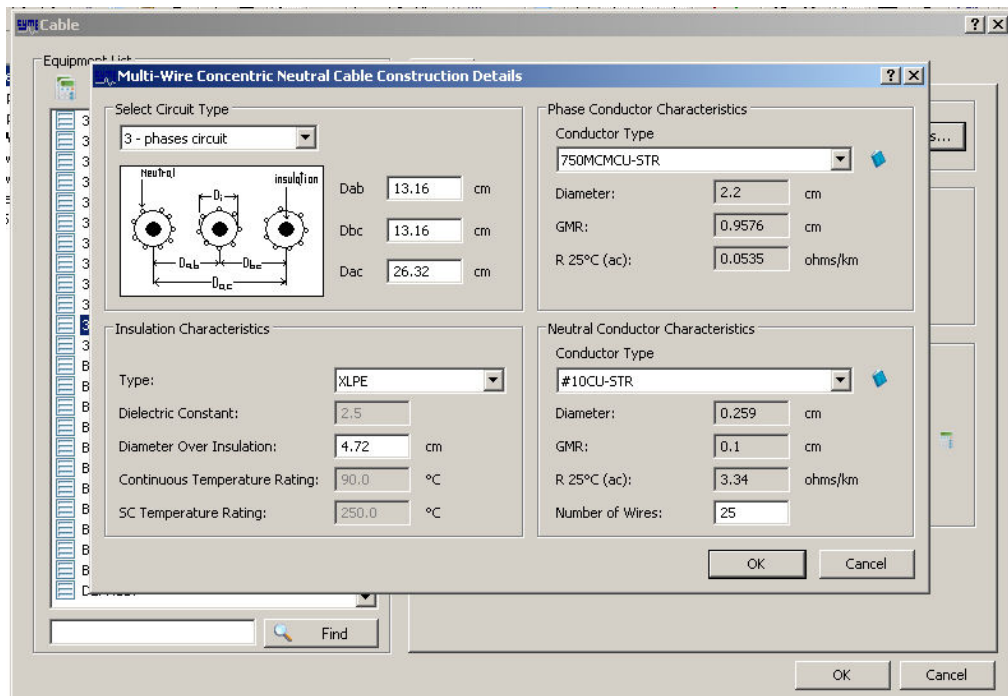
E.4.2 Conductor modeling



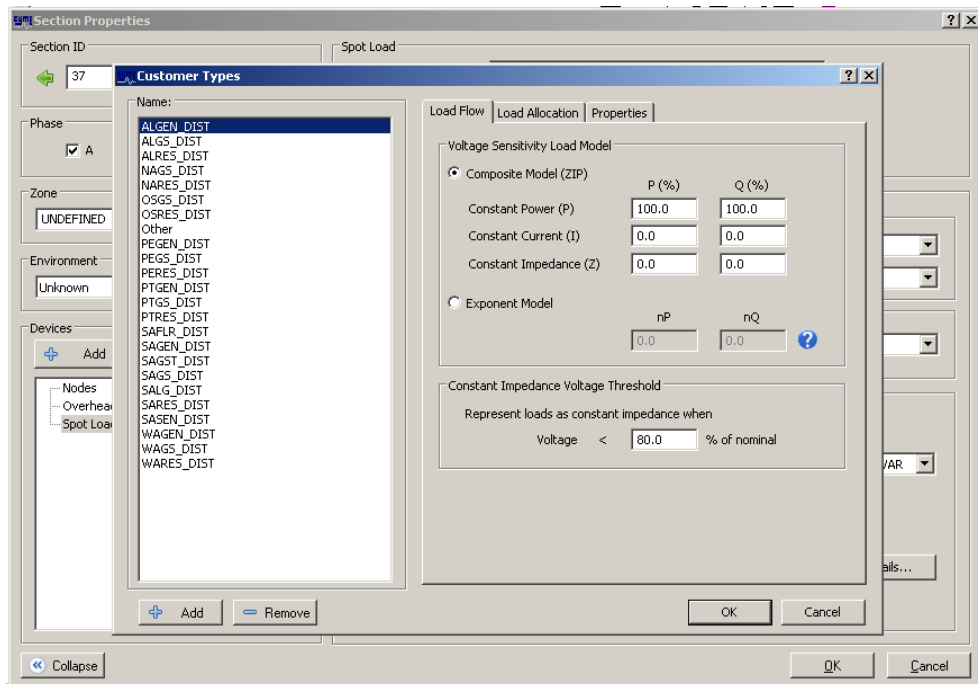
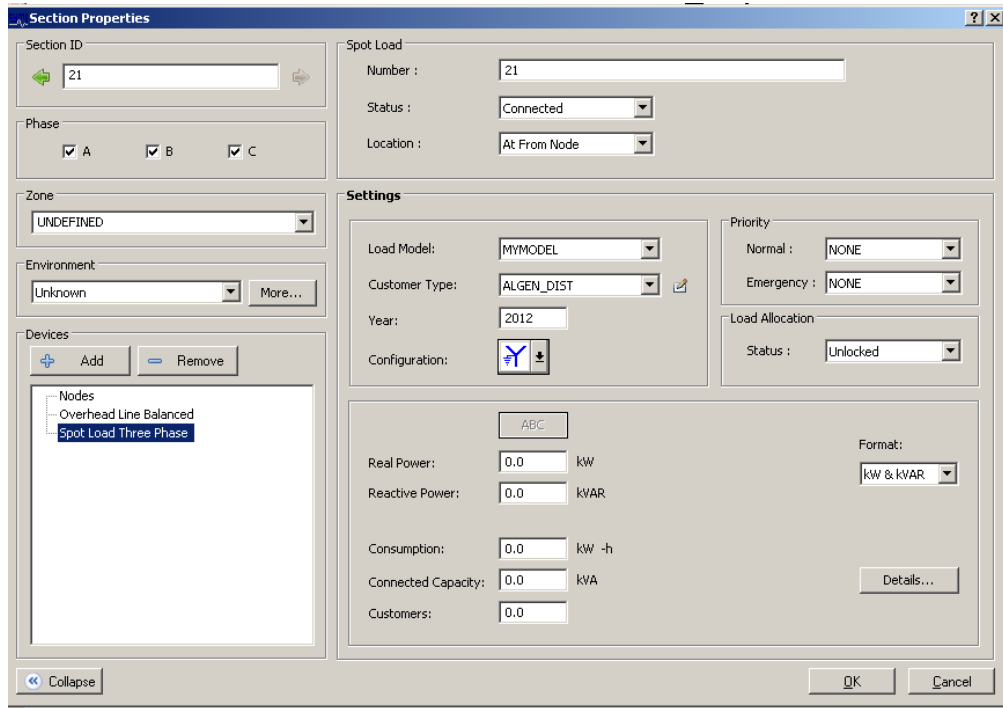
E.4.3 Overhead line space modeling



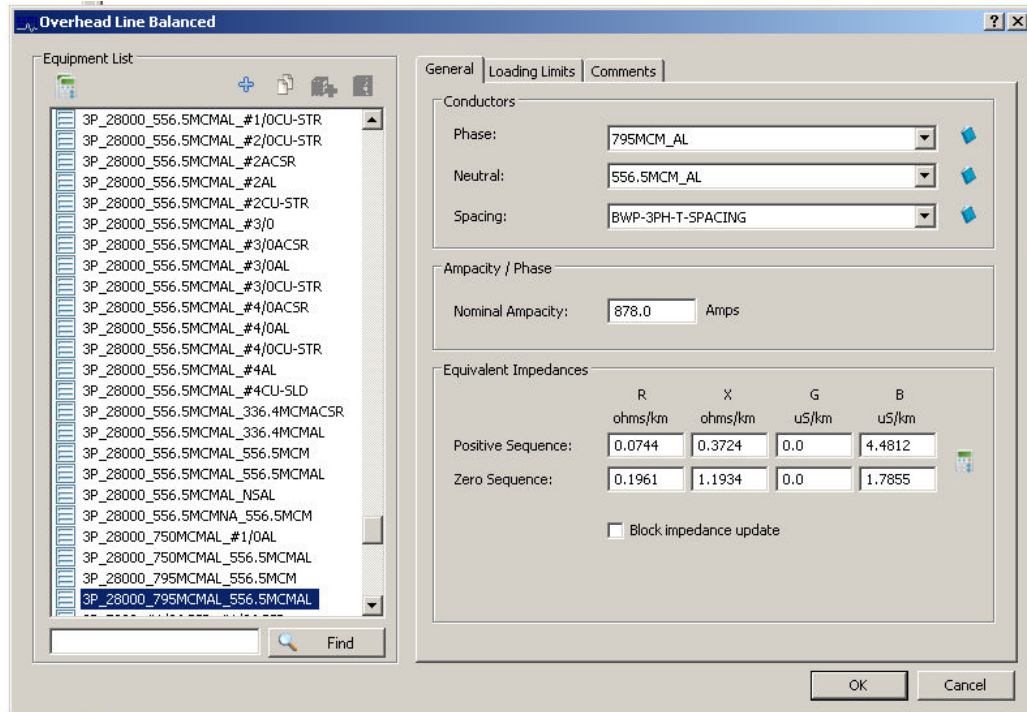
E.4.4 Underground cable modeling



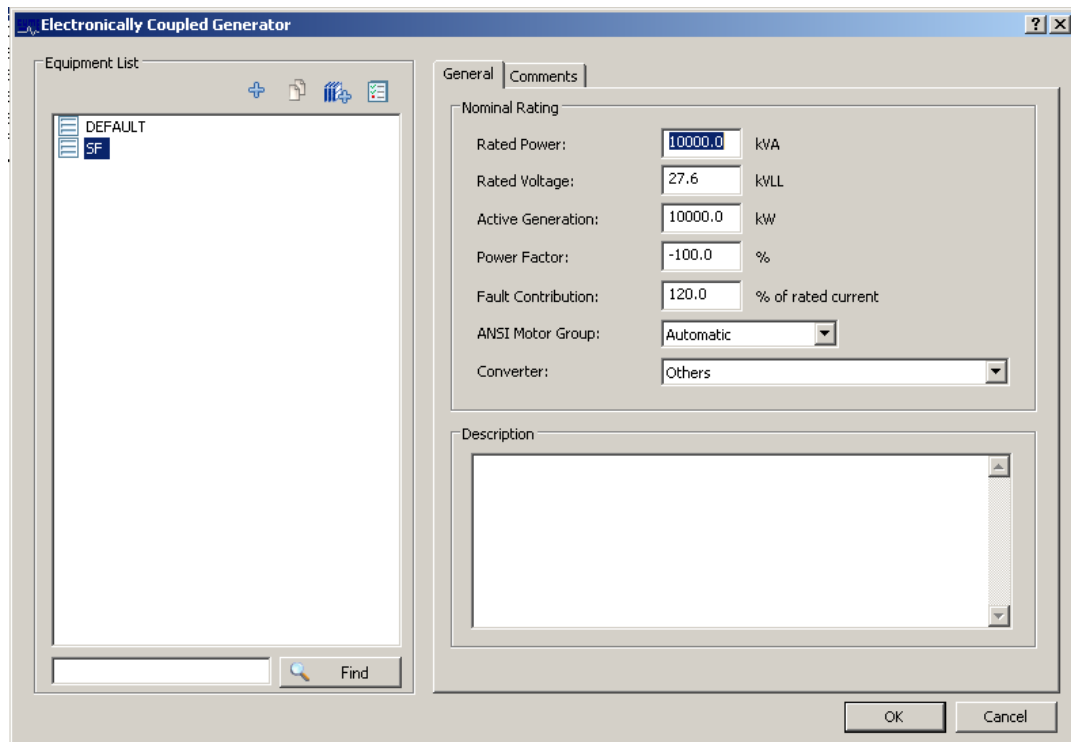
E.4.5 Spot load modeling



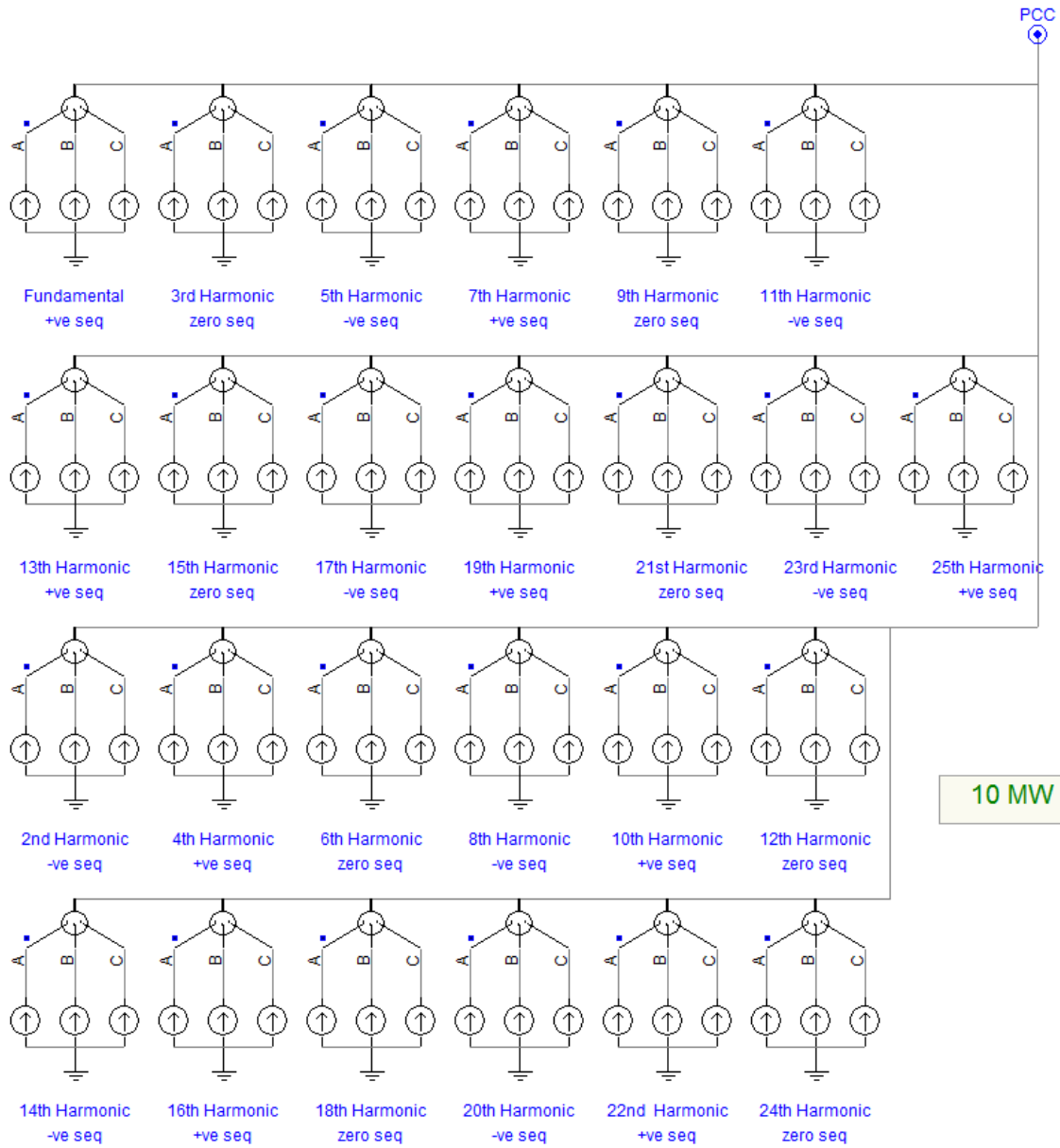
E.4.6 Overhead line modeling from conductor and line space modeling



E.4.7 Solar farm modeling



E.5 Harmonic Source Model in EMTDC/PSCAD for 10MW PV System



Curriculum Vitae

Name: Shah Arifur Rahman

Post-secondary Education and Degrees: Western University
London, Ontario, Canada
2008-2012 Ph.D. in Electric Power Engineering.

Bangladesh Institute of Technology
Chittagong, Bangladesh.
1994-1999 B.Sc in Electrical and Electronics Engineering.

Honours and Awards: Natural Science and Engineering Research Council (NSERC-IPS2)
Canada. 2011-2012

Natural Science and Engineering Research Council (NSERC-IPS1)
Canada. 2009-2010.

Western Graduate Scholarship, Canada
2008

University Merit Based Scholarship, Bangladesh
1994-1999

Related Work Experience Research Associate
Bluewater Power Generation Corporation, Sarnia, ON
2009-2012.

Teaching Assistant
The University of Western Ontario
2008.

Research Associate
Hexaformer AB, Gothenburg, Sweden
2007.

Publications

Patents:

[P.1] Rajiv Varma and **Shah Arifur Rahman**, “Fault Detection and Short Circuit Current Management Technique for Inverter Based Distributed Generators (DG)”, US Provisional Patent Application No. 61/706,387 Filed on September 27, 2012.

[P.2] Rajiv K. Varma and **Shah Arifur Rahman**, “Novel Control of Inverter based DGs as FACTS (DGFACTS) for Enhancing Grid Power Transmission Limits, US Provisional Patent application No. 61/309,612 filed 2nd March 2010.

[P.3] Rajiv K. Varma, Vinod Khadkikar and **Shah Arifur Rahman**, "Utilization of Distributed Generator Inverters as STATCOM" PCT Patent application PCT/CA2010/001419 (for worldwide coverage) filed on 15 September, 2010

- f. Chinese National Phase Entry Application: 201080038759.9
- g. US National Phase Entry Application: 13/391,699
- h. India National Phase Entry Application: 1641/DELNP/2012
- i. Europe Regional Phase Entry Application: 10816511.9
- j. Canada National Phase Entry Application: 2,768,101

E. Journals:

[J.1] Rajiv K. Varma, **Shah Arifur Rahman** and Tim Vanderheide, "New Control of PV Solar Farm as STATCOM (PV-STATCOM) for Increasing Grid Power Transmission Limits During Night and Day," Submitted to IEEE Transaction on Power Delivery, Manuscript ID: TPWRD-01030-2011.R2. (2nd revision submitted).

F. Conferences:

[C.1] Rajiv K. Varma, **Shah Arifur Rahman** and Ravi Seethapathy, "Novel Control of Grid Connected Photovoltaic (PV) Solar Farm for Improving Transient Stability and Transmission Limits Both During Night and Day," in *Proc. 21st World Energy Congress*, Montreal, September, 2010.

[C.2] **Shah A. Rahman**, and R.K. Varma, "PSCAD/EMTDC Model of a 3-Phase Grid Connected Photovoltaic Solar System," in *Proc. 2011 43rd North American Power Symposium, Boston, U.S.A.*, pp. 1-5.

[C.3] Rajiv K. Varma, **Shah Arifur Rahman**, Vinay Sharma, Tim Vanderheide, "Novel Control of a PV Solar System as STATCOM (PV-STATCOM) for Preventing Instability of Induction Motor Load," in *Proc. IEEE CCECE 2012 conference*, April 30-May 2, 2012, Montreal, Quebec.

[C.4] Rajiv K. Varma, **Shah Arifur Rahman** and A.C. Mahendra, "Novel Nighttime Application of PV Solar Farms as STATCOM (PV-STATCOM)," in *Proc. 2012 IEEE PES GM 2012*, San Diego, CA, U.S.A. pp. 1-8.

[C.5] Rajiv K. Varma, **Shah Arifur Rahman** and Wayne H. Litzemberger, "Bibliography of FACTS: 2008 Part I IEEE Working Group Report," in *Proc. IEEE 2010, Power and Energy Society General Meeting*, Minneapolis, MN, U.S.A. pp. 1-7.

[C.6] **Shah Arifur Rahman**, Rajiv K. Varma and Wayne H. Litzemberger, "Bibliography of FACTS: 2008 Part II IEEE Working Group Report," in *Proc. IEEE 2010, Power and Energy Society General Meeting*, Minneapolis, MN, U.S.A. pp. 1-8.

[C.7] Rajiv K. Varma, **Shah Arifur Rahman** and Wayne H. Litzemberger, "Bibliography of FACTS: 2008 Part III IEEE Working Group Report," in *Proc. IEEE 2010, Power and Energy Society General Meeting*, Minneapolis, MN, U.S.A. pp. 1-7.

[C.8] **Shah Arifur Rahman**, Rajiv K. Varma, and Wayne H. Litzemberger, "Bibliography of FACTS Applications for Grid Integration of Wind and PV Solar Power Systems: 1995-2010, IEEE Working Group Report", in *Proc. of IEEE PES General Meeting*, Detroit, MI, U.S.A. 2011.

[C.9] **Shah Arifur Rahman**, Rajiv K. Varma, Wayne H. Litzemberger and Jon Berge "Bibliography of FACTS 2011: Part I; IEEE Working Group Report," in *Proc. 2012 IEEE PES GM 2012*, San Diego, CA, U.S.A. pp. 1-6.